TUM School of Computation, Information and Technology
Technische Universität München

Passivity-Based Force/Motion Planning and Control for Tactile Manipulation

Erfan Shahriari

Vollständiger Abdruck der von der TUM School of Computation, Information and Technology der Technischen Universität München zur Erlangung des akademischen Grades eines

Doktors der **Ingenieur**wissenschaften **(Dr.-Ing.)**

genehmigten Dissertation.

Vorsitz:
Prof. Dr.-Ing. Eckehard Steinbach

Prüfer der Dissertation:
1. Prof. Dr.-Ing. Sami Haddadin
2. Prof. Dr. Neville Hogan
3. Prof. Dr. Oussama Khatib

Die Dissertation wurde am 19.02.2024 bei der Technischen Universität München eingereicht und durch die TUM School of Computation, Information and Technology am 18.07.2024 angenommen.

Passivity-Based Force/Motion Planning and Control for Tactile Manipulation

Erfan Shahriari

Acknowledgement

I extend my heartfelt gratitude to Prof. Sami Haddadin for the countless learning experiences and challenges I encountered while working alongside him. It is a rare privilege to collaborate closely with such an inspiring and intellectually diligent individual. Sami, I am profoundly thankful for the knowledge and insights gained throughout these years, and eagerly look forward to the future opportunities to embark on shared journeys together.

Furthermore, I would like to express my sincere appreciation to Prof. Neville Hogan for the wealth of knowledge I gained from him. Our discussions on rehabilitation robotics, as well as his invaluable lectures on human neuromotor control and physical system modeling, have profoundly enriched my understanding. Thank you, Prof. Hogan. I eagerly anticipate further opportunities to learn from you.

Throughout the past years, I have been fortunate to receive invaluable support from numerous external collaborators. From the Jožef Stefan Institute, my sincere appreciation goes to Prof. Aleš Ude, Prof. Andrej Gams, and Prof. Aljaž Kramberger for our collaborative efforts on the ReconCell and ReconCycle projects. At the Czech Technical University in Prague, I extend my gratitude to Prof. Matej Hoffmann and Dr. Petr Svarny for their unwavering support, especially in projects involving computer vision. Special recognition is owed to the individuals at Reactive Robotics GmbH, notably Dr. Alexander Koenig and Dr. Helfried Peyrl, for graciously hosting me throughout the journey toward developing and certifying our successful robot-aided rehabilitation solution. The moment when I witnessed its positive impact on patients stands out as one of the highlights of my research career. I am also deeply grateful to the team at Schön Klinik Bad Aibling Hospital, especially Dr. Friedemann Müller, for their invaluable insights that contributed to this achievement. I extend my heartfelt thanks to the development team at Franka Emika GmbH for the opportunity to spend time there, enabling me to refine my algorithms. Lastly, I express my heartfelt gratitude to the wonderful individuals at the Newman lab, especially Dr. Johannes Lachner, for fostering an exceptionally warm and enriching environment during my time at MIT.

Among my colleagues, foremost, I want to express my appreciation to the *Hanover Crew*. Our resettlement in Munich would not have been as smooth without each other's support. Among those, I would like to thank Ali Baradaran for our countless crazy R&D nights, as well as Dennis Knobbe, Johannes Ringwald, Johannes Kühn, Mazin Hamad, Jonathan Vorndamme, Tingli Hu, my legendary office mates Fernando Diaz and Lars Johannsmeier, and of course, Alexander Tödtheide. Among those whom I had the privilege to mentor, I extend my heartfelt thanks to Dinmukhamed (Dash) Zardykhan and Anselm Nicklas for their exceptional contributions, notably in the development of the Future of Work demonstration setup. My sincere appreciation goes to Kim Kristin Peper and Dr. Elisabeth Jensen for their invaluable contributions to the clinical studies of the rehabilitation robot and their generous support throughout these years.

Lastly, I want to express my deepest gratitude to my family for their unwavering support throughout my entire life. My heartfelt gratitude and love are reserved for my wife, Maryam, for standing by my side every step of the way over the years. Together, we form an unbreakable rope team where only the beauty of the scenery matters.

Abstract

A key requirement for seamlessly integrating robots into our daily lives lies not only in their ability for skillful manipulation but also in their nuanced capacity for physical interaction with the environment, including humans. Tactile manipulation, the term encompassing both, remains a challenge. So far, only task-specific solutions have been implemented, often necessitating complete task remodeling and pursuing new solutions when there are changes in manipulation objectives or the task environment. To enable the execution of diverse real-world tasks, robots should be equipped with a control framework that facilitates the generalizability of solutions in a robust and stable manner. This dissertation hypothesizes that constructing a transferable and scalable solution hinges on identifying a minimal set of fundamental elements. Accordingly, a modular architecture is pursued, building on the paradigm of force-motion controllers and policies ultimately grounded in an energy-based framework. Embarking from these classical concepts and building on the recent rise of energy-based interaction control, the developed framework achieves high-performance manipulation objectives with minimal complexity.

The foundation of constructing the proposed framework is based on the premise that effective tactile manipulation relies on carefully controlled force and motion. Despite decades of research on force or motion control, the simultaneous control of both has consistently encountered stability-related constraints, including space reciprocity or the necessity for a flawless environment model. Here, by employing the passivity concept, the consolidation of the two standard interaction controllers—impedance control and force control—into a unified system has been generalized to the tracking case. This step overcomes the aforementioned constraints and forms the core of the proposed framework. Generally, achieving entirely independent control of force and motion is not possible in the absence of reciprocity. In fact, if both control objectives do not inherently support each other, a decision must be made regarding their respective priority. In this regard, this dissertation extends the standard unified force-impedance control by introducing a compliance adaptation law that dynamically determines dominance, thereby forging a modular multi-manual control architecture tailored to the task of object manipulation.

Upon achieving robust control of force and motion, the execution of manipulation tasks relies on the proper planning of desired force and motion trajectories, i.e., policy design. Beyond the foundational policies that enable the accomplishment of various tactile manipulation tasks, this dissertation introduces a set of novel reactive policies tailored to navigate more intricate scenarios, particularly those entailing human involvement in the loop. These human-robot interaction challenges span from situations requiring the avoidance of collisions with intended body parts to scenarios involving continuous contact, encompassing aspects such as ergonomic haptic guidance of robot motion or support-adaptive robot-aided movement rehabilitation. A crucial aspect in crafting these policies involves the incorporation of an auxiliary one-dimensional variable—phase. This not only enables the consideration of geometric task constraints but also minimizes the planning space, thereby facilitating a more straightforward derivation of adaptive policies. Lastly, it is also shown that force-motion policies can be accepted by purely impedance-controlled robots using a preceding interpretable coupling term.

Force and motion are typical instances of effort and flow within the Port-Hamiltonian framework, where their dual product determines the transferred power. This forms the root concept underlying the passivity-based approach employed throughout this dissertation, wherein the proposed systems are represented as a well-structured modular network of energy entities. Such energy-based modeling serves not only as a powerful tool for stability analysis and stabilization, e.g., via virtual tank augmentation, but also provides a robust means to perceive the manipulation tasks from an alternative perspective. In this context, with the goal of enhancing previous energy-aware manipulation control, this dissertation extends the conventional concept of virtual energy tanks by introducing valves that can be modulated to regulate the energy flow in the system. Furthermore, various approaches are introduced to derive and learn the required budget and evolution of energy in robot behaviors, a core ability to deal with unknown environments.

In essence, this dissertation generalizes the classical encoding of manipulation tasks from motion to include not only force but also phase and energy under the passivity-based paradigm umbrella. With this unified approach, one can express the complex nature of tactile manipulation with an elegant yet rigorous formalism. This claim is substantiated by experimentally solving challenging manipulation problems with surprisingly simple implementations. Owing to its interpretable and constructive nature, the developed unified approach allows for future seamless integration with data-driven methods, such as foundation models, offering a synergy that captures the best of both worlds.

Zusammenfassung

Eine wesentliche Anforderung für die nahtlose Integration von Robotern in unseren Alltag liegt nicht nur darin ihnen die Fähigkeit zur geschickten Manipulation zu geben, sondern auch zur physischen Interaktion mit der Umgebung, vor allem mit dem Menschen. Taktile Manipulation, der Begriff, der beide Aspekte umfasst, bleibt eine Herausforderung. Bisher wurden nur aufgabenbezogene Lösungen gefunden, die bei Änderung des Manipulationsziel oder der Aufgabenumgebung stets komplett neue Lösungen benötigen. Um die Ausführung vielfältiger realer Aufgaben zu ermöglichen, sollten Roboter jedoch mit einer Regelungsarchitektur ausgestattet sein, die die Verallgemeinerbarkeit von Lösungen auf robuste und stabile Weise erleichtert. Diese Dissertation postuliert, dass die Konstruktion einer transferrier- und skalierbaren Lösung die Identifikation einer minimalen Menge grundlegender Funtionselemente benötigt. Zudiesem Zweck wird eine modulare Architektur angestrebt, die im Paradigma der Kraft-Bewegungsreglung und -Policies fusst, die wiederum Teil des energiebasierten Frameworks sind. Ausgehend von diesen methodischen Konzepten und aufbauend auf dem Erfolg der jüngst aufgekommenen energiebasierten Interaktionsregelung erreicht das entwickelte Framework hochperformante Manipulation bei minimaler Komplexität selbst für anspruchsvolle Manipulationsaufgaben.

Die Grundlage der Methodik beruht auf der Annahme, dass eine effektive taktile Manipulation auf sorgfältig gleichzeitig geregelter Kraft und Bewegung beruht. Trotz jahrzehntelanger Forschung zur Kraft- oder Bewegungsregelung stieß die gleichzeitige Regelung beider immer wieder auf Stabilitätsbeschränkungen, einschließlich Raumrekursivität oder der Notwendigkeit eines fehlerfreien Umgebungsmodells. Unter Nutzung des Passivitätskonzepts wird in dieser Arbeit die Fusion der beiden Standard-Interaktionsregler - Impedanzregelung und Kraftregelung - zu einem einheitlichen Ansatz für den Führungsfall verallgemeinert. Hiermit werden die genannten Beschränkungen überwunden und das Herzstück des vorgeschlagenen Frameworks gebildet. Im Allgemeinen ist es nicht möglich, eine völlig unabhängige Steuerung von Kraft und Bewegung ohne Reziprozität zu erreichen. Tatsächlich muss, wenn beide Regelziele sich nicht inhärent gegenseitig unterstützen, eine Entscheidung über ihre jeweilige Priorität getroffen werden. In diesem Kontext erweitert die vorliegende Dissertation die traditionelle vereinheitlichte Kraft-Impedanz-Regelung durch die Einbindung einer Nachgiebigkeitsadaption. Dieses Gesetz bestimmt dynamisch die Dominanz und ermöglicht somit die Schaffung einer modularen multimanualen-Steuerungsarchitektur für die Manipulation von Objekten.

Nachdem die robuste Steuerung von Kraft und Bewegung erreicht wurde, beruht die Ausführung von Manipulationsaufgaben auf der richtigen Planung gewünschter Kraft- und Bewegungstrajektorien, d.h. der Policies. Neben den grundlegenden Richtlinien, die die Durchführung verschiedener taktiler Manipulationsaufgaben ermöglichen, führt diese Dissertation eine Reihe neuartiger reaktiver Richtlinien ein, die darauf abzielen, komplexere Szenarien mit besonderem Fokus auf die physische Mensch-Roboter Interaktion zu bewältigen. Mit diesem Ansatz werden die Kollisionsvermeidung mit Menschen, Aufgaben mit kontinuierlichem Kontakts, die ergonomisch haptische manuelle Führung der Roboterbewegung, oder unterstützend-adaptive robotergestützte Bewegungsrehabilitation gelöst. Ein Augenmerk bei der Entwicklung dieser Policies liegt auf der Integration einer zusätzlichen eindimensionalen Variable - der Phase. Diese Integration erlaubt nicht nur die Berücksichtigung geometrischer Aufgabenbeschränkungen, sondern reduziert auch den Planungsraum und erleichtert hiermit die Entwicklung der adaptiven Policies. Schließlich wird demonstriert, dass sogar rein impedanzgesteuerte Roboter mit Kraft-Bewegungs-Policies durch einen interpretierbaren Kopplungsterm verbunden werden können.

Kraft und Bewegung sind typische Beispiele für *Aufwand* und *Fluss* im Kontext des Port-Hamiltonischen Frameworks, wobei ihr duales Produkt die übertragene Leistung bestimmt. Dies bildet das Grundkonzept des passivitätsbasierten Ansatzes, der in dieser Dissertation durchgehend verwendet wird, in der die vorgeschlagenen Systeme als gut strukturiertes modulares Netzwerk von Energieeinheiten dargestellt werden. Eine solche energiebasierte Modellierung dient nicht nur als leistungsfähiges Werkzeug für Stabilitätsanalyse und Stabilisierung, z.B. mittels Augmentierung durch virtuelle Energietanks, sondern bietet auch eine robuste Möglichkeit, die Manipulationsaufgaben aus einer alternativen Perspektive zu interpretieren. In diesem Kontext, mit dem Ziel, die bisherige energiebasierte Manipulationsregelung zu verbessern, erweitert diese Dissertation das konventionelle Konzept virtueller Energietanks durch die Einführung von Ventilen. Diese können moduliert werden, um so den Energiefluss im System aktiv zu steuern. Darüber hinaus werden verschiedene Ansätze vorgestellt, um das erforderliches Energiebudget und Energietrajektorie des Roboters abzuleiten und zu lernen; eine Kernfähigkeit für die Interaktion mit unbekannten Umgebungen.

Im Wesentlichen verallgemeinert diese Dissertation die klassische Kodierung von Manipulationsaufgaben in Bewegung auf die Integration von Kraft unter dem Dach des passivitätsbasierten Paradigmas. Darüber hinaus werden auch auch Phase und Energie gleichermaßen berücksichtigt. Mit diesem vereinheitlichten Ansatz kann die komplexe Natur der taktilen Manipulation mit einem äußerst eleganten und gleichzeitig strengen Formalismus ausgedrückt werden. Diese Behauptung wird durch die erfolgreiche experimentelle Umsetzung anspruchsvoller Manipulationsaufgaben mit überraschend einfachen Implementierungen untermauert. Aufgrund seines interpretierbaren und konstruktiven Charakters ermöglicht der entwickelte einheitliche Ansatz eine zukünftige nahtlose Integration mit datengesteuerten Methoden, wie z. B. Foundation Models, und bietet so ein Synergiepotential, die beiden Welten vereinen kann.

Contents

No AI-generated figure is used in this dissertation.
The drawings are created by Shiva Fallahi and Erfan Shahriari.

Notation

Symbol	**Dim.**	**Description**
Assoc.	—	Associated with the
CDMP	—	Coupled Dynamic Movement Primitive
CoR	—	Center of rotation, usually coinciding with the end-effector unless explicitly defined otherwise
DMP	—	Dynamic Movement Primitive
DoF	—	Degrees of freedom
EMG	—	Electromyography
ee	—	End-effector
ns.	—	If not specified
$\boldsymbol{I}_\square$	—	Identity matrix of size $\square$
$\mathbf{1}_{\square\times\triangle}$	—	Matrix of ones with size $\square \times \triangle$
$\mathbf{0}_{\square\times\triangle}$	—	Matrix of zeros with size $\square \times \triangle$
$\mathrm{diag}(\square)$	—	Diagonal matrix of vector $\square$
$N_\square$	—	Number of dimensions of the space assoc. $\square$
$\square^T$	—	Transpose of the matrix $\square$
$\square^{-1}$	—	Inverse (or if not invertible, right-hand Moore-Penrose pseudo-inverse) of the matrix $\square$
$[\square]_\times$	—	Skew-symmetric matrix representation of vector $\square$
$\square \circ \triangle$	—	Element-wise multiplication of vectors $\square$ and $\triangle$
$\|\square\|$	—	Absolute value of $\square$
$\\|\square\\|$	—	Euclidean 2-norm of the vector $\square$
$\dot{\square}$	—	Time-derivative of $\square$ (except for $\dot{\boldsymbol{x}}_\square$ representing a twist)
$\ddot{\square}$	—	Second time-derivative of $\square$
$\bar{\square}$	—	Average **or** normalized value of $\square$
$\tilde{\square}$	—	Error variable ($\square_d - \square$), exception: $\tilde{\boldsymbol{f}} = \boldsymbol{f}_d + \boldsymbol{f}_\text{ext}$
$\square^\dagger$	—	Nominal reference (e.g., initially demonstrated) value of $\square$
$\square'$	—	Adapted $\square$ according to the passivity-based control
$\breve{\square}$	—	Controller variable before applying the shaping function ($\square \in \{{}^{\text{ee}}\boldsymbol{K}_{C,v},\ \boldsymbol{f}_f,\ {}^{\text{ee}}f_o\}$)

$\square^*$	—	Shaped component in the context of the flexible-joint robot ($\square \in \{\boldsymbol{\tau}_j, \boldsymbol{B}_m, \boldsymbol{D}_j\}$)
$\square_a$	—	Assoc. admittance control
$\square_C$	—	Assoc. **or** represented in the Cartesian space
$\square_c$	—	Assoc. compliance control **or** Coulomb friction
$\square_d$	—	Desired value of $\square$
$\square_{\text{diss}}$	—	Assoc. energy dissipation effect
$\square_{\text{ee}}$	—	Assoc. end-effector
$\square_{\text{env}}$	—	Assoc. environment
$\square_{\text{ext}}$	—	Assoc. external effects (e.g., external wrenches)
$\square_f$	—	Assoc. force control
$\square_{\text{fri}}$	—	Assoc. friction effect
$\square_{fu}$	—	Assoc. collision-preventing fused approach
$\square_g$	—	Assoc. gravity effect
$\square_h$	—	Assoc. human
$\square_i$	—	Assoc. impedance control **or** index i
$\square_{\text{in}}$	—	Assoc. input
$\square_{io}$	—	Assoc. collision-preventing Impulse Orb approach
$\square_j$	—	Assoc. flexible-joint robots
$\square_m$	—	Assoc. robot motors **or** human muscles
$\square_{\text{max}}$	—	Maximum value of $\square$
$\square_{\text{min}}$	—	Minimum value of $\square$
$\square_o$	—	Assoc. force control for grasping an object
$\square_{pw}$	—	Assoc. collision-preventing Prognosis Window approach
$\square_{r_\triangle}$	$\mathbb{R}$	Rotational component of $\square$ along $\triangle$ axis ($\triangle \in \{\text{x}, \text{y}, \text{z}\}$)
$\square_{\text{sys}}$	—	Assoc. overall system (without an augmented energy tank)
$\square_T$	—	Assoc. virtual energy tank
$\square_{t_\triangle}$	$\mathbb{R}$	Translational component of $\square$ along $\triangle$ axis ($\triangle \in \{\text{x}, \text{y}, \text{z}\}$)
$\square_v$	—	Assoc. variable impedance control **or** Viscous friction
a_m	$\mathbb{R}$	Muscle activation component
$\hat{a}_m$	$\mathbb{R}_{\geq 0}$	EMG measurement
$\hat{a}_{m,0}$	$\mathbb{R}$	Quiescent EMG baseline
$\boldsymbol{B}_m$	$\mathbb{R}^{n \times n}$	Motor inertia matrix
$\boldsymbol{C}_\square$	$\mathbb{R}^{N_\square \times N_\square}$	Coriolis and centrifugal matrix assoc. $\square$ (ns.: rigid-body robot dynamics model in joint space)

$\boldsymbol{C}_z$	$\mathbb{R}^{m\times m}$	Coupling matrix in a CDMP
$\boldsymbol{c}_z$	$\mathbb{R}^{m}$	Coupling term in a CDMP
c_ϕ	$\mathbb{R}$	Phase-based non-linear term coefficient
$\boldsymbol{D}_\square$	$\mathbb{R}^{N_\square\times N_\square}$	Damping matrix assoc. $\square$
d_a	$\mathbb{R}_{>0}$	Damping coefficient of a 1-dimensional admittance law
$\boldsymbol{d}_c$	$\mathbb{R}^{m}$	Coulomb friction coefficient vector
$\boldsymbol{d}_h$	$\mathbb{R}^{n_h}$	Human limb (with n_h DoF) dissipation vector
$\boldsymbol{d}_v$	$\mathbb{R}^{m}$	Viscous friction coefficient vector
d_ϕ	$\mathbb{R}_{>0}$	Phase-based damping coefficient
E	$\mathbb{R}_{\geq 0}$	Phase-based deviation metric
$E_{\square i}$	$\mathbb{R}_{\geq 0}$	Velocity adaptation threshold of index i in the positive/negative side of the cascading shaped map ($\square \in \{P, N\}$)
$\hat{E}$	$\mathbb{R}$	Path-centric patient physical effect metric
$\boldsymbol{e}_T$	$\mathbb{R}^{N_T}$	Effort variable assoc. potentially passivity-violating power
$\boldsymbol{f}_\square$	$\mathbb{R}^{m}$	Wrench vector assoc. $\square$ (ns.: net torque represented in the Cartesian space)
f_{ma}	$\mathbb{R}$	Active muscle force
$\boldsymbol{f}_N$	$\mathbb{R}^{m}$	Normal wrench to the surface
f_s	$\mathbb{R}$	Steering force in phase-based admittance law
$\boldsymbol{f}_T$	$\mathbb{R}^{N_T}$	Flow variable assoc. potentially passivity-violating power
$\boldsymbol{f}_z$	$\mathbb{R}^{m}$	Forcing term in DMP formulation
f_ϕ	$\mathbb{R}$	External wrench mapped into the phase domain
$\boldsymbol{g}_z$	$\mathbb{R}^{m}$	DMP goal
$\boldsymbol{H}_s$	$\mathbb{R}^{3n\times 3n}$	Matrix function used in the state-space representation of a rigid-body robot
$\boldsymbol{h}_{s,\square}$	$\mathbb{R}^{3n\times 1}$	Vector function assoc. state-space representation (ns.: assoc. rigid-body robot)
${}^{\square}_{\bigcirc}\boldsymbol{J}_{\triangle}$	$\mathbb{R}^{N_\triangle\times N_\bigcirc}$	Jacobian matrix from space $\bigcirc$ (ns.: joint) to space $\triangle$ (ns.: CoR) represented in $\square$ (ns.: CoR) frame
$\boldsymbol{K}_\square$	$\mathbb{R}^{N_\square\times N_\square}$	Stiffness matrix assoc. $\square$
$\boldsymbol{K}_{f,\square}$	$\mathbb{R}^{m\times m}$	Force control proportional/integral/derivative gain matrix ($\square \in \{p, i, d\}$)
$k_{\square_\triangle}$	$\mathbb{R}_{\geq 0}$	Translational/rotational stiffness coefficient along x/y/z axis ($\square \in \{t, r\}, \triangle \in \{\mathrm{x}, \mathrm{y}, \mathrm{z}\}$)
k_C	$\mathbb{R}_{\geq 0}$	Diagonal stiffness matrix elements with equal values
$k_{C,\phi}$	$\mathbb{R}_{>0}$	Cartesian stiffness mapped into phase domain

$\boldsymbol{k}_h$	$\mathbb{R}^{n_h}$	Human limb musculo-tendon elasticity vector
k_ϕ	$\mathbb{R}_{>0}$	Coefficient of the phase-based deviation metric
l	$\mathbb{R}_{\geq 0}$	Projection norm (i.e., pseudo-ellipsoid radius)
l_d	$\mathbb{R}_{>0}$	Length of the desired path
l_i	$\mathbb{R}$	Projection length assoc. ellipsoid i-th principal radius
l_{mf}	$\mathbb{R}_{>0}$	Muscle fiber length
$\boldsymbol{M}$	$\mathbb{R}^{n\times n}$	Mass matrix in joint space
$M_\square$	—	Set of agonist/antagonist muscles ($\square \in \{\text{ag}, \text{ant}\}$)
$\boldsymbol{M}_a$	$\mathbb{R}^{m\times m}$	Admittance control mass
m	$\mathbb{N}$	Dimensions number of the Cartesian space ($m \leq 6$)
$m_{C,\phi}$	$\mathbb{R}_{>0}$	Cartesian mass mapped into phase domain
m_a	$\mathbb{R}_{>0}$	Mass coefficient of a 1-dimensional admittance law
m_ϕ	$\mathbb{R}_{>0}$	Phase-based mass coefficient
$N_\square$	$\mathbb{N}$	Dimensions number of the frame **or** space $\square$
n	$\mathbb{N}$	Number of DoF in an articulated body
n_Λ	$\mathbb{R}_{>0}$	Number of non-zero eigenvalues of the matrix Λ
$P_\square$	$\mathbb{R}$	Power assoc. $\square$
P_T	$\mathbb{R}$	Potentially passivity violating power
$P_T^\square$	$\mathbb{R}$	Tank lower/upper power limit ($\square \in \{\text{low}, \text{up}\}$)
$P_T^{\square_i}$	$\mathbb{R}$	Tank lower/upper power limit for the port i ($\square \in \{\text{low}, \text{up}\}$)
p	$[0, 1]$	P-value (statistical measure)
${}^{\square}_{\bigcirc}\boldsymbol{p}_{\triangle}$	$\mathbb{R}^{N_\square}$	Translation from point $\bigcirc$ (ns.: base) to point $\triangle$ (ns.: CoR) represented in $\square$ (ns.: base) frame ($N_\square \leq m$)
p_i	$\mathbb{R}$	Value of the i-th region in the reference power trajectory
$\boldsymbol{q}$	$\mathbb{R}^n$	Vector of joint angles
${}^{\square}_{\bigcirc}\boldsymbol{R}_{\triangle}$	$\mathbb{R}^{N_\square}$	Rotation from frame $\bigcirc$ (ns.: base) to frame $\triangle$ (ns.: CoR) represented in $\square$ (ns.: base) frame ($N_\square \leq m$)
R^2	$[0, 1]$	Coefficient of determination (statistical measure)
$r_{\square,\triangle}$	$\mathbb{R}_{>0}$	Radius of the inner/outer sphere ($\square \in \{\text{in}, \text{out}\}$) in approach $\triangle$ of the collision-preventing policy ($\triangle \in \{io, pw\}$)
r_i	$\mathbb{R}_{\geq 0}$	Length of the ellipsoid i-th principal radius
$S_\square$	$\mathbb{R}_{\geq 0}$	Storage function assoc. $\square$ (ns.: storage function of a general system **or** support level of a rehabilitation robot)
$S_{T,\square}$	$\mathbb{R}_{\geq 0}$	Storage function of tank assoc. with $\square$ (ns.: general tank)
$S_T^\square$	$\mathbb{R}_{\geq 0}$	Tank energy lower/upper energy limit ($\square \in \{\text{low}, \text{up}\}$)
S_T^Δ	$\mathbb{R}_{\geq 0}$	Tank energy lower limit threshold

S_ϕ	$\mathbb{R}_{\geq 0}$	Storage function of the phase-based admittance law
$S_{h,l}$	$\mathbb{R}_{\geq 0}$	Storage function of the human limb
$S_{h,l,\square}$	$\mathbb{R}_{\geq 0}$	Value of the human limb storage function at the beginning/end of a motion cycle ($\square \in \{\text{start}, \text{end}\}$)
$\boldsymbol{S}_j$	$\mathbb{R}^{n \times n}$	Matrix representing the inertial coupling between the rotors and the preceding link in a flexible-joint robot chain
T	$\mathbb{R}_{\geq 0}$	Kinetic energy
U	$\mathbb{R}_{\geq 0}$	Potential energy
W_m	$\mathbb{R}_{\geq 0}$	Active work performed on the human limb by the human
$\hat{W}_{m,\square}$	$\mathbb{R}_{\geq 0}$	Estimation of the active work by the human, provided by the robot or EMG sensors ($\square \in \{\text{rob}, \text{emg}\}$)
$\hat{W}^*_{m,\text{emg}}$	$\mathbb{R}_{\geq 0}$	Estimation of the active work by the human, provided by EMG sensors for $f_{ma,\max} = 1$, $\kappa_m = 1$, $\hat{a}_{m,0} = 0$
$\boldsymbol{x}_\square$	$\mathbb{R}^m$	Pose vector assoc. $\square$ (ns.: CoR)
$\boldsymbol{x}_{\text{ell}}$	$\mathbb{R}^m$	Points on the surface of the manipulability ellipsoid
$\boldsymbol{x}_\theta$	$\mathbb{R}^m$	Motor position vector represented in the Cartesian space
$\boldsymbol{x}_\psi$	$\mathbb{R}^m$	Auxiliary vector for control design in flexible-joint robots
$\dot{\boldsymbol{x}}_\square$	$\mathbb{R}^m$	Twist vector assoc. $\square$ (ns.: CoR)
$\boldsymbol{z}_z$	$\mathbb{R}^m$	assoc. DMP velocity
$\boldsymbol{z}_{z,c}$	$\mathbb{R}^m$	Auxiliary variable in CDMP formulation
α_z	$\mathbb{R}_{>0}$	Gain term in DMP formulation
$\beta_{\square,pw}$	$\mathbb{R}_{\geq 0}$	Inner/outer braking boundaries ($\square \in \{\text{in}, \text{out}\}$) in the collision-preventing prognosis window approach
β_z	$\mathbb{R}_{>0}$	Gain term in DMP formulation
Γ_l	$\mathbb{R}$	Term for sensitivity analysis of the pseudo-ellipsoid radius
Γ_r	$\mathbb{R}$	Term for sensitivity analysis of the ellipsoid radius
γ_{diss}	$[0, 1]$	Tank valve gain for dissipation power
γ_{low}	$[0, 1]$	Tank valve gain for lower energy limit
γ_p	$[0, 1]$	Tank valve gain for total power limit
γ_{p_i}	$[0, 1]$	Tank valve gain for power limit of port i
γ_T	$[0, 1]$	Tank overall valve gain
γ_{up}	$[0, 1]$	Tank valve gain for upper energy limit
Δ_{pw}	$[0, 1]$	Length of the prognosis window
$\delta_\square$	$\mathbb{R}_{\geq 0}$	Shaping function maximum distance parameter for control law $\square$ ($\square \in \{i, f, o\}$) **or** Estimated joint angle variation assoc. manipulability ellipsoid and pseudo-ellipsoid approaches ($\square \in \{r, l\}$)

$\epsilon_{\square i}$	$\mathbb{R}_{\geq 0}$	Multiplier relating robot support level to $E_{\square i}$
ε_{pw}	$[0, 1]$	Length of prognosis window sections
$\eta_{\square}$	$[0, 1]$	Phase braking gain variable assoc. approach $\square$ ($\square \in \{io, pw, fu, rsz\}$)
$\boldsymbol{\theta}$	$\mathbb{R}^n$	Motor position vector
θ_h	$\mathbb{R}$	Angle between the robot desired velocity and the vector to the human
θ_i	$\mathbb{R}$	Angle between the path direction vector and the manipulability ellipsoid principal radius of index i
$\kappa_{\square}$	$\mathbb{R}_{\geq 0}$	Learning/forgetting factor ($\square \in \{l, f\}$)
κ_m	$\mathbb{R}_{>0}$	Scaling factor for EMG measurement
$\boldsymbol{\Lambda}$	$\mathbb{R}^{m \times m}$	Core matrix of the manipulability ellipsoid
λ_i	$\mathbb{R}_{\geq 0}$	Eigenvalue of index i
μ	$\mathbb{R}_{\geq 0}$	Rate limiter of the admittance mass adaptation
$\boldsymbol{\mu}_{\text{env}}$	$\mathbb{R}^{2 \times 2}$	Coulomb friction coefficient matrix of the environment
$\boldsymbol{\nu}$	$\mathbb{R}^m$	Unit-vector along the encoded path
$\boldsymbol{\nu}_i$	$\mathbb{R}^m$	Eigenvector of index i
$\xi_{\square}$	$\mathbb{R}_{\geq 0}$	Weight of each approach in the collision-preventing fused approach ($\square \in \{io, pw\}$)
$\xi_{\square, io}$	$\mathbb{R}_{>0}$	Radius of the inner/outer sphere ($\square \in \{\text{in}, \text{out}\}$) in the Impulse Orb approach for a unit-norm desired velocity
$\xi_{i, pw}$	$\mathbb{R}_{\geq 0}$	Weight of i-th section in a prognosis window
$\xi_{T, i}$	$\mathbb{R}_{\geq 0}$	Weight (priority) of the i-th port of a tank
$\boldsymbol{\rho}$	$\mathbb{R}^n$	Momentum vector
$\rho_{\square, \triangle}$	$[0, 1]$	Shaping function gain for control law $\square$ ($\square \in \{i, f, o\}$), for the translational/rotational terms ($\triangle \in \{t, r\}$)
$\sigma_{\square}$	$\mathbb{R}$	Phase velocity adaptation gain corresponding to policy $\square$ ($\square \in \{\text{CDMP}, \text{coll}, \text{aan}\}$)
$\sigma_{\square, \max}$	$\mathbb{R}_{\geq 0}$	Maximum value of phase velocity adaptation gain in the positive/negative directions ($\square \in \{P, N\}$)
$\boldsymbol{\tau}_{\square}$	$\mathbb{R}^n$	Torque vector assoc. $\square$ (ns.: net torque) acting on links
$\boldsymbol{\Upsilon}$	$\mathbb{R}^{m \times m}$	Inner matrix of the manipulability ellipsoid's core matrix
Φ_i	—	Phase region of index i
ϕ	$[0, 1]$	Phase variable
ϕ_i	$[0, 1]$	Starting phase value of the i-th phase region
ϕ_{Δ}	$[0, 1]$	Margin length of phase regions
$\psi_{i, pw}$	$\mathbb{R}_{\geq 0}$	Weighted proximity of the i-th section in a prognosis window

ψ_{pw}	$\mathbb{R}_{\geq 0}$	Overall weighted proximity of the Prognosis Window approach
Ω	$\mathbb{R}$	Phase velocity (equivalent to the DMP velocity)

1 Introduction

Today's world is experiencing transformative technological advancements in Artificial Intelligence (AI) and Robotics. Since 2003, the annual growth rate of publications related to AI has consistently outpaced global scientific activity, indicating an accelerating academic interest in these transformative fields [1]. The advancements made by AI and robotics in industry are equally noteworthy. In 2022, the industry produced nearly ten times the number of significant machine learning models compared to academia, marking a continuous progression [2]. The industrial sector has experienced remarkable growth in the deployment of AI and robotics, with the number of operational industrial robots nearly tripling since 2011 [2]. The current global robot-to-human ratio in the manufacturing industry, at 1 to 71, is projected to increase rapidly, underscoring the transformative impact of these technologies on industrial operations [3]. Forecasts indicate that by 2027, approximately 75 percent of companies will have adopted AI, with 50 percent integrating robotics into their operations [4]. These substantial shifts are also evident from a marketing perspective. In 2022, the robotics industry generated a staggering \$32.41 billion in revenue, a substantial increase from \$18.47 billion in 2016, with projections reaching \$43.32 billion by 2027 [5]. Meanwhile, the AI market is poised for a compound annual growth rate of 17.3 percent until 2030 [6]. The profound influence of Artificial Intelligence and Robotics has become integral to global affairs, as exemplified by their inclusion in the 2023 World Economic Forum top 10 list of impactful technologies [7]. This significance has been further underscored in recent statements from G20 and G7 summits [8, 9], emphasizing the crucial need for the responsible global deployment of these technologies to ensure ethical and sustainable progress.

Despite the strides in technological progress, our present reality still falls short of the Earth 2023, as witnessed by Susan Calvin[1], where mankind was no longer alone. The journey to a world where intelligent robots coexist harmoniously with humans is still a considerable distance away. Along this path, the advancement of AI appears to outpace that of robotics. Each day, we become increasingly accustomed to the rapidly expanding array of AI applications in our lives. These range from conversational AI models like ChatGPT to our smartphones seamlessly converting images to text, social media offering personalized recommendations, and the integration of AI in smart homes. Nevertheless, witnessing a mechanical arm adeptly preparing a salad in our kitchen is still a surreal image. Despite recent advances, only a small subset of robots—designed for specific tasks and environments—can achieve performance levels comparable to average humans [10]. Hence, robots have not yet fulfilled their mission of enhancing productivity in our actual lives [11]. The observed and persistent decline in labor productivity rates could present substantial long-term challenges for the global economy [12]. Specifically, across G7 nations, productivity growth has exhibited a slowdown since 2005, with the majority of countries witnessing declines ranging from

---

[1] Referring to the interview (year 2057) with Dr. Susan Calvin, a fictional well-known roboticist in Isaac Asimov's collection "I, Robot,", particularly from the short story "Little Lost Robot."

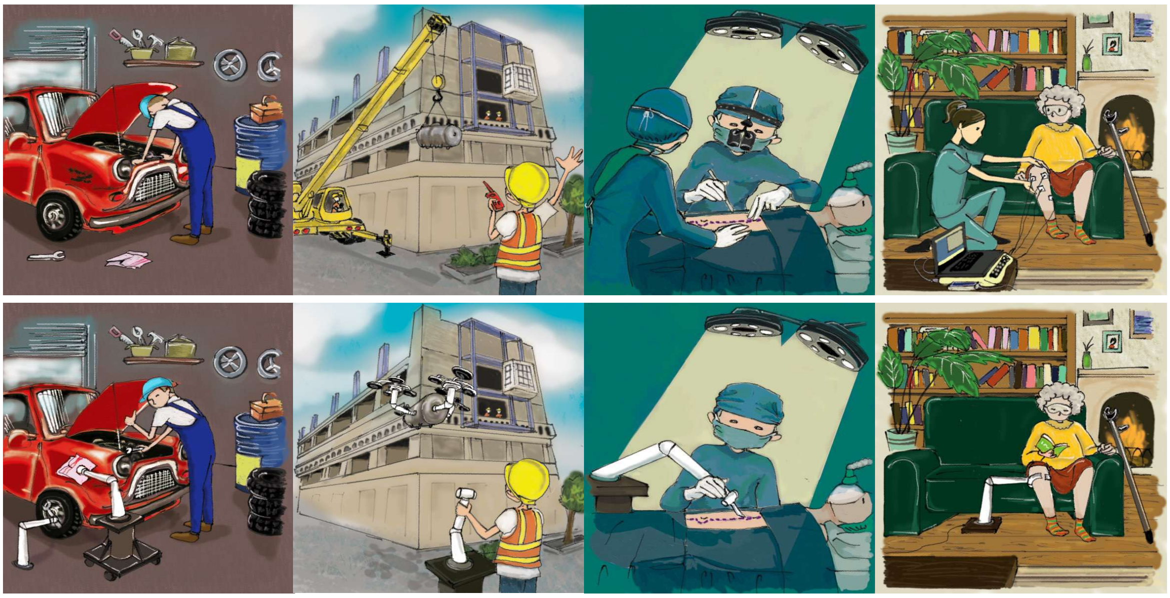

Figure 1.1: Diverse scenarios where robots could enhance daily life challenges.

0.6 to 1.6 percentage points [13]. A major contributor to low productivity is confirmed to be the shortage of skilled workers [14], a well-known challenge of our era. It is anticipated that by 2030, the world will experience a shortage of human talent exceeding 85 million people, approximately equivalent to the population of Germany [15]. Measures addressing skill shortages, evident even in more developed regions such as Europe [16], re-emphasize the importance of employing robots to fill the gaps. According to the World Economic Forum, technologies like AI and automation not only have the potential to address the challenge of labor scarcity but also to create additional jobs and opportunities [17].

Given the recognized benefits, along with dedicated attention and substantial investment, a pertinent question arises: why have we not yet witnessed robots at the anticipated level in our everyday lives? What factors have hindered robots from more prominently undertaking tasks either autonomously or in collaboration with humans, and what strategies can be implemented to overcome these barriers? Exploring these questions involves considering diverse perspectives, ranging from technical challenges such as mechanical or mechatronics design to managerial and production-related aspects. However, a prevailing approach to addressing the current challenges in robotics is from the control perspective. To date, the conventional method for designing a control algorithm for a robotic task is to initially understand the task objective and its environment and then derive the algorithms accordingly. Yet, this approach often results in isolated solutions. Altering the task goal or conditions necessitates the design of alternative algorithms from the ground up, significantly compromising robustness and confining robots to laboratory settings. For robots to effectively perform a wide range of real-world tasks, they need a framework that promotes the efficient generalization of solutions, addressing both control objectives as well as robustness and stability.

For a solution to be effectively generalizable, it should minimize the number of involved elements to avoid unnecessary implementation complexity while ensuring that these elements remain fundamental enough to address a broad spectrum of task objectives. This dissertation contends that the essential, minimal set of building blocks required to address tactile manipulation can be established by drawing upon core concepts from physics. In his book[2] "Principia," Isaac Newton demonstrated that force and motion are the two vital elements for modeling physical interactions. Accordingly, for a robot to seamlessly interact with its environment—regardless of its mechanical or mechatronics design—it must ultimately possess the capacity to deliver the requisite levels of interaction force and motion. This fundamental observation serves as the core principle in constructing a modular planning and control framework centered on the pivotal pair of force and motion and their dynamic interplay. In line with this perspective, this dissertation endeavors to develop minimal yet effective elementary modules for the execution of a wide range of tactile manipulation tasks. Further referring to Newtonian mechanics, any physical interaction can be associated with an exchange of energy, which can be explicitly characterized by the interaction force and motion (i.e., wrench and twist), yielding the transferred power. Such energy-based observation, utilizing a variety of dual variables, forms the bedrock for an intuitive yet potent stability investigation method known as passivity analysis. Consistent with this approach, in constructing the proposed framework, energy—a domain-independent entity—serves as an intrinsic yet pivotal element for developing and interconnecting the involved building blocks across diverse domains.

Building upon the fundamental concepts related to force and motion, their dynamic interplay, and their energy-based attributes is already a well-established practice in robot control. Indeed, the initial studies on these principles form the foundation of classical approaches in robotics dating back to the 1980s and 1990s. Yet, this dissertation aims to harness insights from past achievements in the field in the quest for a generalizable and scalable solution. By standing on the shoulders of giants, it endeavors to construct a modular, expandable framework capable of robustly addressing diverse tactile manipulation problems in real-world settings. The goal is to progressively build a minimal control architecture rooted in classical concepts, capable, on the one hand, of executing manipulation tasks involving robust physical interactions and, on the other hand, serving as a suitable core for future integration into data-driven methods.

---

[2] Philosophiæ Naturalis Principia Mathematica, Isaac Newton, Royal Society in London, 1687.

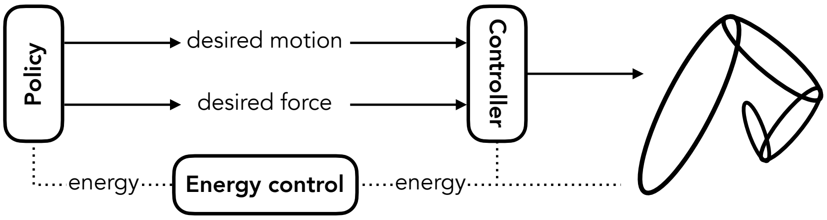

Figure 1.2: High-level architecture of the proposed framework.

1.1 Problem Statement

In the pursuit of versatile robots capable of diverse physical interactions with their environment, the primary challenge in this dissertation lies in determining how to construct a modular control framework utilizing the fundamental concepts from physics. In particular, how can a minimal set of reusable building blocks[3] be formed and interconnected through the concept of energy, ultimately yielding stable and scalable solutions for a wide range of real-world tactile manipulation tasks?

In essence, such a foundational research problem can be broken down into three main challenges. First, considering the role of force and motion in shaping physical interactions, the question is how to enable a robot to robustly deliver the intended interaction force and motion (developing controller blocks). Second, given a robot capable of simultaneously controlling force and motion, the challenge is how to determine the appropriate desired values fulfilling the task objectives (developing policy blocks). Finally, for enhanced task performance and assured stability, how can the developed modules be structured and integrated with an energy-aware approach? Figure 1.2 illustrates a schematic representation of the envisioned framework.

Guided by this categorization, the dissertation systematically develops the proposed framework, beginning with the fundamental challenges of controlling force and motion. The framework is then progressively expanded to encompass a range of applications, from autonomous control in industrial and service robotics to human-centered robotics, addressing critical aspects such as safety, ergonomics, and rehabilitation. Each step is meticulously aligned with a well-defined objective, supported by identified gaps in the existing state-of-the-art related work. The next section articulates these objectives through ten precisely formulated research questions derived from a thorough literature review.

---

[3] Conceptualized as energy capsules.

1.2 Related Work

Navigating through the related literature follows the framework's bottom-up construction policy. Accordingly, the relevant studies are systematically classified into three primary categories aligned with the three key elements of the proposed framework: control, policy, and energy; see Figure 1.2.

The review initially focuses on approaches enabling the *control* of force and motion. In this context, simultaneous force-motion controllers are explored in the *Force/Motion Control for Interaction* section. To illustrate how the control block can be expanded for more intricate objectives, the *Multi-Manual Object Manipulation* section scrutinizes relevant works, addressing scenarios where multiple cooperating robots manipulate an object. With a controller facilitating force and motion commands, the subsequent step involves determining their desired values by designing policy blocks aligned with the task objective. Yet, if the command of only one value (either force or motion) is allowed, such as when using only a motion controller, these policies become impractical. The *Force-Encoded Motion Policies* section outlines various approaches addressing this specific challenge when only the desired motion can be commanded to the robot controller.

Subsequently, the focus of the literature review shifts to designing *policies* for complex scenarios, incorporating humans into the loop. Initially focusing on safe collision-free human-robot collaboration in confined spaces, such as small workshops, the *Human-Robot Collision Avoidance in Confined Spaces* section details relevant works. Presuming geometrical constraints, the following scenario involves continuous interaction for haptically guiding robot motion by humans. The *Haptic Motion Guidance with Geometric Constraints* section explores related works, followed by the *Manipulability Analysis for Ergonomic Human-Robot Interaction* section, covering methods using the manipulability concept to enhance human ergonomics in continuous human-robot interaction scenarios. The next stage considers robot-aided rehabilitation with a patient-centric approach. The *Support-Adaptive Robot-Aided Movement Rehabilitation* section enumerates various methods for adapting the robot control behavior to enhance the rehabilitation process.

The third aspect of the literature review revolves around the concept of *energy*. The emphasis is first on utilizing energy to ensure stability. The *Energy Tanks in Passivity-Based Robot Control* section delves into stability analysis methods, focusing on tank-based approaches. Expanding energy-based approaches, the *Energy-Based Reference Behaviors* section explores more advanced concepts in this context. Finally, to incorporate energy into a more real-world application, robot-aided rehabilitation is revisited in the *Performance Monitoring in Movement Rehabilitation* section, aiming to monitor the patient's involvement level in the rehabilitation task to indicate recovery progress.

In this extensive literature review, the objective is to identify significant research gaps that the proposed framework seeks to address. These gaps are translated into three sets of targeted research questions, with each set associated with one of the three main components of the framework. Each question is posed at the end of the corresponding literature review section. The overarching goal of this dissertation is to systematically develop a generalizable framework, addressing identified challenges in a simple yet robust manner and extending its applicability to effectively handle tactile manipulation scenarios not explicitly covered within the confines of this study.

Controller

The initial focus of the literature review revolves around approaches concerning the control of force and motion. The ultimate aim is to facilitate the simultaneous commanding of force and motion for the controlled robot. The research gaps identified in this section give rise to three research questions enumerated as C.1, C.2, and C.3.

Force/Motion Control for Physical Interactions

The ability to physically interact with the environment is fundamental in today's robot design. Position-controlled robots were not capable of doing so because they could not provide the necessary compliance for physical contacts, let alone the ability to track a desired wrench profile. As a result, over the past decades, continuous progress has been made in both hardware and software design to enable reliable force and motion control suitable for contact/non-contact scenarios. One of the most significant advancements came with the introduction of *Impedance Control* in [18], enabling torque-controlled robots not only to follow desired trajectories in free space but also to establish and shape desired interaction behaviors when in physical contact. Additionally, if the task is to regulate the interaction wrench, one approach is to shape the impedance or the desired trajectory based on the sensed wrench, known as *Indirect Force Control* [19–21]. Yet, to avoid energy over-accumulation in the motion controller's compliance, the *Direct Force Control* approach, where the robot input torque is directly linked to the wrench error, can be used [22–24]. The similarity and distinction between these two approaches are highlighted in [25] and [26], respectively.

As the diversity of tasks that a robot should perform autonomously increases, having a single interaction controller capable of controlling both motion and force can eliminate the need for constant controller switching and the associated instability issues [27]. Moreover, there are numerous manipulation tasks where force and motion must be controlled simultaneously. Therefore, the development of simultaneous force-motion controllers has drawn considerable attention for a long time. One of the most well-known approaches is the *Hybrid Force-Motion Control*, initially introduced in [28], where the output of a direct force control is superimposed onto the motion controller output. The approach was further improved in subsequent works. In [29] and [30], the dynamics effects of the manipulator and the force sensor were incorporated into the motion control loop. The singularity-related instabilities of the motion control were tackled by incorporating the robot dynamics in [31], adjusting motion controller gains in [32], and implementing null space controllers in [33]. In [34], an impedance controller was employed in the motion control loop. This was the case also for more recent works [35, 36] for fully actuated aerial vehicles. In [37], the robot desired motion was defined in the joint space. Finally, another common approach is based on the use of indirect force control, known as the external force feedback loop [38–42]. In this method, the force is regulated in an outer loop, and its output is added to the input of the inner loop motion controller.

Irrespective of the specific controller used, a fundamental restriction exists in simultaneously regulating force and motion: it is generally not possible to independently control both in the same direction [18]. This limitation led to the incorporation of the *Selection Ma-*

trices[4] right from the earliest attempts in simultaneous force-motion control designs. The selection matrix ensures that the force and motion control tasks are performed in orthogonal (reciprocal) spaces. Typically, force control is applied in the direction of the environment constraints, while motion is controlled in unconstrained directions [44].

Using a selection matrix introduces some inherent issues. First, as expounded in [45], the investigation of orthogonality between force and motion spaces is subject to fundamental limitations, notably the dependence on the choice of units and reference frames. Moreover, the selection matrix must be compatible with the constraints imposed by the environment, necessitating a precise model of the environment for its derivation. However, as stated in [46], one of the biggest challenges in force-motion control is the lack of a perfect environment constraint model. That is why another class of controllers, known as *Parallel* force-motion controllers, was introduced. These controllers relax the strict requirement for orthogonality by imposing higher priority on either the force or motion control task. Examples include [47–51], where the force controller takes higher priority by incorporating an integrator part in the feedback loop. Such a policy is not always practical. Specifically, if the force controller takes over in an unconstrained direction (e.g., during a contact loss), the robot can accelerate, resulting in a hazardous situation. Similarly, if the motion controller takes higher priority in a constrained direction, significant penetration of the setpoint into the surface can lead to extreme contact wrenches. Hence, to avoid such unstable scenarios, it is crucial to incorporate a good enough environment model even in the parallel control policies.

There have been adaptive force-impedance control approaches aimed at addressing uncertainties in the environment model. One of the pioneering examples is [52], where the selection matrix continuously changes according to the newly imposed constraints. In [53], an adaptive hybrid controller is proposed, and the environment geometry is continuously estimated under certain assumptions, such as the maximum slope on the surface. In [54, 55], a soft hemispherical tip is assumed for the robot end-effector, and an adaptive term is introduced in the control input to handle uncertainties in the estimated surface normal direction. Other recent works on handling uncertainties in the environment model when using impedance control include [56–58].

Existing Gaps: Simultaneous control of force and motion may result in two distinct stability-compromising actions: force control in unconstrained directions and motion control in constrained directions. Traditionally, addressing these challenges involves decoupling force and motion control into two reciprocal spaces, aligning with environmental constraints. However, apart from reservations about the space reciprocity concept, a significant drawback to this approach lies in its reliance on a precise environmental model. This model must either be pre-existing or learned during the task. The dependence on the environmental model knowledge poses a limitation, mainly when dealing with diverse and unpredictable real-world scenarios featuring unknown non-ideal environments, therefore significantly eroding system robustness. The concept of *Unified Force-Impedance Control* (UFIC) ensures stable simultaneous force and impedance control. Nevertheless, in existing works, stability is guaranteed only for the regulation case. Hence, scenarios that encompass desired motions not reciprocating with the intended or actual interaction wrenches remain unexplored.

---

[4] Also known as the *Task Specification* matrices in the *Operational Space Control* terminology [43].

Research Question C.1: How can the Unified Force-Impedance Control concept be extended to include not only regulation but also tracking tasks for both rigid-body and flexible-joint robots?

Achieving stable control over interaction forces and motion is pivotal for executing a myriad of tactile manipulation tasks. The subsequent question that arises is whether the control block can be expanded to tackle more intricate scenarios, such as orchestrating a team of robot arms to manipulate an object collaboratively.

Multi-Manual Object Manipulation

For decades, impedance control [59] has been the established method for governing the behavior of manipulators during movement and interaction with their surrounding environment. This concept has found extensive use in scenarios involving multi-manual manipulation [60]. In the early stages of this exploration, [61] represents one of the pioneering works where the desired impedance is defined between the manipulated object and the environment. Subsequently, in [62] and [63], additional impedance behavior is introduced between the arms' end-effectors and the object. This modification in the control strategy aims to prevent the accumulation of large forces imposed on the object by adapting the desired trajectories. Following a similar approach, [64] defines desired admittance dynamics for the possible surface deformation of the object at the contact points, leading to the adaptation of the robot trajectories to enhance the overall grasp. Lastly, in [65], an impedance is designed between the contact force and the desired trajectory for each arm. This impedance is then integrated into the control law to enforce trajectory adaptation implicitly. Imposing a desired impedance between the object and its surrounding environment typically involves incorporating the object dynamics into the control policy. Nevertheless, when the objective is to manipulate unknown objects, such a dependency diminishes robustness.

An alternative application of the impedance control concept in multi-manual systems involves regulating the relative pose of end-effectors with respect to each other, maintaining a desired coupled impedance. In one of the earliest instances, [66] introduces a virtual spring model between the end-effectors of a set of leader/follower arms. In this setup, while the leader arms follow their designated trajectories, the follower arms pursue them correspondingly. In [67], relative impedance in a dual-arm system is utilized to control the motion of one arm relative to the other, enabling the execution of cooperative tasks independent of the absolute motions of the arms (e.g., one arm drawing on a board attached to another moving arm). A dual-arm control architecture is presented in [68], featuring conventional impedance for each arm and coupling impedance between them. However, the authors caution against potential interference between these two types of impedance characteristics, emphasizing the importance of choosing compatible parameters, such as rest lengths and stiffness. This architecture is later applied to various bimanual systems [69]. Similarly, [70] employs a similar approach with an additional force coordination factor to limit the applied force on the object. In [71], coupled impedance is modeled as a damper that maps the object deformation force into the arm velocity. Additionally, in [72], a spring-damper system is considered between the two end-effectors of a dual-arm system to update the desired trajectories. The role of coupling impedance is generally to secure the object during manipulation [73]. However, this requires the desired impedance to align with the object size and dynamics, which can compromise the robustness of the policy. Furthermore, maintaining continuous coupling between arms may lead to computational and communication overload when the number of cooperating arms is large. Additionally, there remains a compatibility constraint between the coupling impedance and the individual motion control laws.

In principle, an object manipulation control law may involve two cooperating main components: one to move the object and one to hold the object during movements. In this context, [74] stands as one of the earliest works that segmented object contact forces into manipulating force and grasping force for a multi-fingered robotic hand. This concept was further expanded in [75] by introducing the notion of *Internal Forces* as the object contact forces that do not contribute to object motion. Subsequently, in [76], the concept was further analyzed, and the internal forces were defined as the end-effector wrenches belonging to the null space of the grasp matrix, for which the total virtual work is zero. Several works have delved into determining the proper internal force for effective object grasping. In [77], an online algorithm was developed to derive the minimum desired internal force. An admittance controller in [78] increased the internal force upon detecting object slip. Similarly, [79] developed a tactile sensor for slip detection, using position-based force control to adjust the internal force accordingly. Additionally, in [80], an online approach was proposed to determine the internal force preventing object deformation. Finally, in [81], a model-based approach was presented for deriving both the required internal force and the motion-inducing force. Integrating force control for the establishment and maintenance of grasp with impedance control for the movements gives rise to a distinct class of controllers known as *Hybrid Controllers*.

An early example of hybrid controllers in the context of multi-manual object manipulation is proposed in [82], where a model-based motion controller is coupled with a PI force controller. The same control law is employed in [83], where the internal force is initially represented using the concept of a virtual truss model [84]. In [85], a decentralized control architecture is defined for each arm using the concept of virtual linkage [86] as a model of internal forces associated with multi-grasp manipulation. In [87], the authors justify that the desired force to grasp an object can be a constant value under the condition of being perpendicular to the desired motion. Building on this assumption, they present a linearizable hybrid control algorithm. The multi-manual system in [88] incorporates an arm enhanced with the object dynamics model to compensate for its gravity, while the other arms utilize a hybrid control policy. In [89], contact forces are categorized into two orthogonal groups, active and passive forces, based on their ability to perform work on the object. Each manipulator employs a null space motion controller alongside the hybrid motion/force controller. In another work [90], the concept of squeeze force is introduced for a dual-arm system based on the internal force concept, accompanied by a hybrid controller. However, in the experimental results, the force feedback loop is circumvented in the force controller. As highlighted in several works, a primary limitation of force/motion hybrid control policies in object manipulation is the potential conflict between the desired force and the desired motion. For instance, in a scenario where the desired motion opposes the grasp force, pursuing the desired motion could lead to a loss of contact with the object and, consequently, potential grasp failure.

Existing Gaps: For the complex task of multi-manual object manipulation, model-based approaches prove impractical when confronted with unknown arbitrary objects due to their reliance on the object dynamics model. Similarly, control approaches rooted in the concept of coupled impedance encounter two primary challenges: (i) the coupling diminishes modularity, making the addition or removal of arms during a task challenging; (ii) if the desired motion conflicts with the coupled impedance wrench, it compromises either the motion-following or grasp-maintenance task. This latter issue also persists in hybrid control approaches, particularly when the force control action required to sustain the grasp opposes the intended motion.

> **Research Question C.2:** How can the force-motion control law extend into a modular single-arm controller, empowering a team of robots to manipulate objects robustly while mitigating potential conflicts between grasp and movement actions?

A versatile force-motion controller facilitates the accomplishment of diverse tactile manipulation tasks. This is achieved by defining desired force and motion trajectories through the design of appropriate policy blocks. A follow-up inquiry arises: Can these policies remain effective when the control block is constrained to a singular command value, such as desired motion, as might occur when employing only a motion controller?

Force-Encoded Motion Policies

In scenarios where the robot is restricted to motion commands only, controlling force can be achieved indirectly by modulating the motion trajectory based on the desired and sensed wrenches. In principle, online trajectory adaptation can serve different goals, as elaborated in [91]. However, as originally demonstrated in [59], one objective can be to use force feedback as an input to a virtual system (e.g., with standard mechanical characteristics) for determining the motion command. Since then, the concept of *Admittance Control* has become a standard in robotics [92]. To enable the control of both force and motion, several works in the literature employ a parallel architecture [93–95]. One loop comprises an admittance control in series with a position controller, while the parallel loop incorporates an impedance controller. A switch consistently determines which loop should be active based on the task objective. However, for simultaneous control of force and motion, such a switching policy becomes impractical.

To systematically use an admittance law to adapt the desired motion, standard motion generators can be employed. One of the most well-established ones is the *Dynamics Movement Primitive* (DMP), introduced in [96]. Over the past two decades, DMPs have been a common method for encoding desired trajectories [97]. Aligned with the objective above, the adaptation of the DMP output based on the interaction wrench has already been addressed in the literature. In [98], a coupling term defined at the acceleration level, driven by force feedback, demonstrated the robot's ability to grasp an object even with deviations from the predicted position. A similar approach was applied in [99] using a sequence of movement primitives to handle larger uncertainties. Other works, such as [100] and [101], used coupling terms with parametric temporal probabilistic models, respectively. The coupling term was defined at the velocity level in [102] and was used to adapt to unmodeled curved surfaces in [103]. Although the interaction wrench can modify the motion command in all these works, none of them incorporated a physically interpretable formulation, such as an admittance behavior, for trajectory adaptation.

Existing Gaps: Integrating force information into the motion trajectory allows the utilization of force-motion policies, even when the controller block accepts only the motion command. Admittance control stands out as a robust and physically interpretable approach for determining or adjusting the desired motion trajectory based on a specified force profile. Despite its efficacy, standard motion generators have yet to systematically incorporate the admittance policy in a manner that ensures stability. Notably, well-established motion generators like DMP have successfully integrated force information in various works, but none have employed the admittance law.

Research Question C.3: How can an admittance law be seamlessly integrated into the DMP formulation with guaranteed stability, ensuring the encoding of both desired force and motion information into the generated motion command?

Throughout the dissertation, the focus of the control aspect will be on addressing the enumerated three research questions. The remainder of the literature review will delve into the other two aspects of the proposed framework, namely, policy and energy.

Policy

Expanding beyond the basic policy elements that are already effective for numerous manipulation tasks, this part concentrates on crafting policies for scenarios involving humans. Consequently, four research questions are posed regarding the policy aspect of the proposed framework, enumerated as P.1–4. In the initial scenario envisioned, a robot is engaged in manipulation tasks within a confined workspace, e.g., a small workshop, alongside a human. In this context, the primary emphasis is on the robot executing tasks without collisions, ensuring the safety of both the human and the environment.

Human-Robot Collision Avoidance in Confined Spaces

According to ISO standard regulations [104, 105], one of the four designated modes for human-robot interactions addressing safety is known as *Speed and Separation Monitoring* (SSM). This mode stipulates the maintenance of a protective separation distance at all times, ensuring that the robot halts before a potential collision can occur. This separation distance is determined by considering the relative speed between the robot and the human, often relying on worst-case values for added precaution. Effectively implementing SSM necessitates the integration of robust human detection and distance evaluation methods with swift robot control mechanisms to facilitate prompt reactions. Notably, various approaches in this domain leverage vision-based systems, as comprehensively reviewed in [106]. The current landscape also witnesses the introduction of integrated devices dedicated to human detection [107] or supporting robot evasion and speed limitation [108]. Many of these approaches trace their origins to the *Potential Field* approach for obstacle avoidance [109, 110]. This methodology has evolved to incorporate obstacle-based repulsive fields, which, in the context of physical human-robot interaction, have been further refined into robot-based repulsive vectors or danger fields [111, 112]. Repulsive vectors find application in humanoid robotics, particularly in conjunction with peripersonal space representations [113]. To dynamically calculate the necessary separation distances, these approaches take into account various system properties such as velocities, stopping times, and distances [114, 115]. An alternative approach, the *Kinetostatic Danger Field* (KDF) [116, 117], employs a precalculated safety field updated with the robot velocity and the human position to generate appropriate evasive actions. Another strategy involves swept volumes based on a human kinematic model, predicting the space occupied by the human. This predictive model enables the robot to generate effective evasive trajectories [118].

Existing Gaps: In confined spaces, generating or adjusting evasive trajectories based on repulsive fields around the tracked human body could inadvertently lead to collisions with the surrounding environment. A potential remedy involves concurrently applying the earlier-mentioned collision avoidance strategies to multiple entities, encompassing both the human body and the environment. However, this approach becomes impractical when obtaining a precise geometric model of the environment proves challenging.

Research Question P.1: How can collision prevention policies be devised for human interactions without necessitating geometric modifications in robot motion?

In tasks where motion compliance is crucial, such as those involving geometric constraints, the robot can assist in achieving the required precision. In scenarios where the trajectory cannot be predetermined, the human may guide the motion. This guidance can occur through continuous physical contact, with the human haptically steering the robot motion. The next section delves into instances where the robot accuracy in adhering to geometric constraints can be integrated with human guidance.

Haptic Motion Guidance with Geometric Constraints

Human motion guidance intentions can be conveyed to robots through various interfaces, such as smartphone applications [119], speech commands [120], visual cues [121], brain-computer interfaces [122], haptic joysticks [123], pedals [124], and essentially any teleoperation system [125–128]. Unlike the aforementioned methods, several alternative approaches eliminate the need for supplementary interfaces to provide guidance. In these methods, operators can convey their guidance intentions by directly interacting with the guided robot. For instance, in [129], an intention recognition approach is proposed based on the grip force applied by the human when using a walking helper. A similar strategy is employed in [130], where the estimated handle grasp force exerted by the human is utilized to infer their intention. Several studies have introduced trajectory modification policies based on human-applied wrenches. For instance, in [131], the robot intended motion is altered whenever the operator applies force, causing the robot to deviate from its predefined path. Similarly, the robot is kinesthetically taught in [132], and the control parameters are adjusted to ensure adherence to task-oriented constraints. In [133], a quadratic optimization approach is employed to modify the trajectory of an impedance-controlled exoskeleton in response to the human-applied wrenches. Likewise, in [134], a trajectory modification approach is presented aiming at minimizing both motion-tracking errors and interaction force magnitudes. In [135], various motion policies are proposed based on the designated level of human guidance. In all these methods, the applied wrench either selects a predefined motion policy or modifies the desired trajectory. Thus, they do not allow for enabling exhaustive guidance by the operator.

A commonly embraced strategy to facilitate motion guidance involves the utilization of admittance controllers [136], where an input wrench results in the generation of a desired motion. A thorough overview of the application of admittance control in scenarios involving physical human-robot interaction can be found in [137]. Recent developments in the use of admittance control for motion guidance include works such as [138], where control parameters are adjusted to modify the robot compliance in critical areas, especially close to singularities. In [139], the standard admittance controller is extended by damping feedback to decrease peak contact force during collisions with the environment. In [140], a variable admittance controller is employed to navigate a cluttered environment, especially when the operator's view is obstructed. In [141], collision detection schemes are incorporated into the guidance policy, while in [142], adaptation policies are used to handle uncertainties, such as an unknown payload. In these approaches, although the operator can guide the robot motion, they do not account for the imposition of stringent geometric constraints that the robot must adhere to.

Numerous works in the literature have delved into constraining robot motion. A well-established approach is the use of *Virtual Fixtures*, as initially introduced in [143] and expanded upon in [144]. In this approach, a repulsive wrench, normal to a predefined surface, is virtually applied to the robot. Typically, the magnitude of the wrench is proportional to the inverse of the distance between the robot and the surface. For instance, in [145], a virtual fixture defined along the spinal cord prevents the robot from getting too close, particularly in the context of robot-aided orthopedic surgery. Similarly, in [146], virtual fixtures are employed to counteract surgeon hand tremors during delicate micro-surgeries. In situations where the geometric constraint is exceptionally stringent, requiring the robot to adhere to a specific path strictly, the application of a repelling force, as employed in these methods, becomes impractical. For such scenarios, the adapted concept of virtual fixtures, referred to as *Virtual Guides*, can be utilized. Virtual guides offer a more relevant framework for maintaining the robot trajectory along a predefined path. One of the pioneering works in this context is [147], where desired motion directions are determined based on a predetermined path. In this approach, admittance control gains are adjusted such that high gains are applied when the force aligns with the desired direction, and low (ideally zero) gains are used otherwise. This method has two primary drawbacks. First, in practical scenarios, adjusting admittance controller gains based on path direction, especially with frequent changes or slight communication delays, does not guarantee that the output trajectory remains precisely on the constrained path. Second, typically in these approaches, when the robot deviates from the path, e.g., due to controller compliance, the robot is redirected to the nearest point on the predefined path while being guided by the human [148]. However, accurately determining the suitable point on the path to establish the desired direction can be challenging. This challenge is shared by approaches like [149] and [150], where motion control gains along the path are adapted for user-guided robot movement. Continuous assessment of the robot actual pose in relation to the intended path is necessary to verify its alignment and, if not maintained, to select the nearest path point for adjusting controller gains. This process adds computational burden, and in some cases, identifying the closest path point is nontrivial. For instance, consider the robot end-effector falling on the bisector of an angular line along the intended path, resulting in two potential closest points.

To kinesthetically teach geometric constraints, virtual guides were combined with 6D XSplines in [151], Gaussian mixture models in [152], and dynamic movement primitives in [153]. Lastly, a practical approach for representing rotational virtual guides was proposed by [154]. The concept of virtual guides has evolved into *Virtual Mechanisms*, initially introduced in the context of teleoperation in [155]. This approach treats the setpoint as a massless particle positioned on the constrained path linked to the robot end-effector through a spring-damper system. When the human applies force to the robot end-effector, this force is transferred to the particle, allowing it to glide along the path. However, a limitation of this approach is its lack of modularity; it is tightly coupled with the employed motion controller. Consider a scenario where the human is not guiding the robot, yet there is an offset between the setpoint and the robot end-effector. Ideally, the motion controller would move the robot toward the setpoint. However, the virtual spring force could still influence the setpoint, even without actual human input. A similar consideration is made in [156], where the impact of the virtual mechanism force on the robot is shaped based on a reference velocity profile. This approach aims to reduce human guidance when the robot speed is excessive and enhance it when the speed is too slow. To keep the modularity of the guidance policy in the presence of geometrical constraint, [157] presents a strategy for minimally invasive surgery by dividing the robot joint space into constrained and unconstrained subspaces, effectively filtering out admittance-generated motions conflicting with the specified constraints. Similarly, in [158], any change in the orientation of the output motion from the admittance control is neglected, particularly in the context of a drilling task. Nevertheless, these approaches do not ensure that the robot setpoint invariably conforms to a stringent geometric constraint, such as a predefined path.

Existing Gaps: Within the existing literature, motion guidance methods granting the human operator full control over the robot motion commonly do not address stringent geometric constraints, like adhering to a predetermined path. On the contrary, guidance policies tailored to handle such constraints are often closely intertwined with the motion controller, compromising practicality due to a lack of modularity.

Research Question P.2: How can a modular haptic motion guidance policy be developed in such a way that the generated desired trajectory for the robot is guaranteed to adhere to stringent geometric constraints, such as a predefined path?

Continuous interaction with a human, especially during manipulation tasks that may induce changes in the body configuration, requires consideration of human ergonomics. One approach is through manipulability analysis, as explored in the next section.

Manipulability Analysis for Ergonomic Human-Robot Interaction

While one of the earliest articles on the concept of ergonomics is [159], the term[5] was introduced later in 1949, with an emphasis on equipment and workspace design [160]. However, modern ergonomics also contribute to the design and evaluation of work systems and products [161], leading to standards and guidelines such as [162], which studies ergonomics in

---

[5] The Greek term εργος means work and νομος means law.

manual pushing and pulling. Other related conventions for the evaluation of ergonomics include the *Rapid Upper Limb Assessment* (RULA) [163], evaluating the exposure of individual workers to ergonomic risk factors associated with upper limbs, the *National Institute for Occupational Safety and Health* (NIOSH) guidelines [164], assessing ergonomics in weight lifting tasks, the *Rapid Entire Body Assessment* (REBA) [165], a scoring system for muscle activity caused by static, dynamic, or unstable postures, and finally, the *Strain Index* (SI) [166], evaluating tasks based on exerted force, movement frequency, and wrist posture. An ergonomics assessment toolkit was created in [167] based on standard analysis methods for a virtual manufacturing environment. Alternatively, [168] conducted movement analysis along with inverse dynamics modeling of a set of tasks to build a dataset for upper limb joint involvement during daily-life tasks. Furthermore, user studies have been conducted to evaluate the comfort level for basic tasks such as mouse or joystick guidance [169] or hand tool grips [170].

A recent literature review on the use cases of ergonomics in human-robot interaction from both physical and cognitive perspectives can be found in [171]. Similarly, [172] analyzes typical ergonomics-endangering factors in human-robot collaboration scenarios, with a focus on agriculture. In the realm of human-robot interaction scenarios, most ergonomics assessment tools rely on standard metrics. For example, the NIOSH equation is employed for an ergonomics-aware task planning policy in [173]. The assessment in [174] incorporates NIOSH and RULA, along with considerations of muscle strains and human recovery time after task execution, to evaluate enhanced ergonomics within their proposed robotic assembly cell. In [175], a gesture control system is evaluated according to the RULA metric, as well as through questionnaires addressing physical workload, intuitiveness, and comfort. Additionally, REBA is utilized for human ergonomic posture assessment in [176], and the SI is applied to assess human physical stress in [177] and [178]. Most of the aforementioned techniques for assessing human ergonomics are offline [179]. In [180] and [181], Electromyography (EMG) sensors measure individual muscle fatigue in real time, allowing for the assessment of task ergonomics. In [182] and [183], the ergonomics evaluation factor is human joint torque overload, estimated by monitoring body posture with either a wearable sensory suit or a vision system, respectively. Additionally, learned task-specific minimized musculoskeletal simulations, as discussed in [184], can be employed for computationally efficient ergonomics evaluation.

The *Manipulability* concept, introduced in [185] and further developed in [186], has been a valuable tool for evaluating the effectiveness of the force/motion mapping between different spaces (e.g., operational and actuator spaces) of a manipulator. Over time, it has been applied to more sophisticated systems, including dual-arm setups [187] and parallel manipulators [188]. One of the earliest applications of this concept to the human body can be found in [189]. In this context, the manipulability metric was introduced in [190] and later used to assess human force exertion ability in [191]. In their subsequent work [192], a strong relationship was demonstrated between the spatial characteristics of force manipulability and so-called *Human Operational Comfort.* In another study [193], a high correlation was found between human manipulability and muscle activation determined by EMG signals. Manipulability, represented as an ellipsoid, has more recently found application in human-centered robotics. In [180] and [194], the robot task frame was assigned based on the direction of the human force manipulability ellipsoid. Similarly, in [195], robot motion controller gains were adjusted based on the configuration of the manipulability ellipsoid. An assistive robot control scheme based on manipulability, aiding the human in applying forces in problematic directions, was presented in [196]. This approach was later extended to human muscular force manipulability in [197] and [198] to consider muscular space ergonomics. In [199], the manipulability ellipsoid volume was used as an assessment metric to optimize multi-arm multi-human collaboration scenarios ergonomically. Finally, in [200], the limitations of the conventional manipulability analysis approach were highlighted and addressed by considering both kinematic and inertial parameters in the derivation of the manipulability ellipsoid. The authors extended their method in [201] by including the inertial parameters of virtual constrained tasks counteracting against the motion.

In human-robot interaction, adapting the robot behavior can enhance human ergonomics. In general, adaptive interaction control design has been a foundational aspect in human-robot interaction scenarios, with examples ranging from early works like [202], where the co-manipulator stiffness adapts according to the desired task, to teleoperation scenarios such as [203], where the guidance dynamics change by adjusting the impedance of the leader robot. In the context of human-controlled robotics applications, [204] proposes an adaptive control policy that shapes the perceived admittance based on the task or user characteristics. An optimization approach for impedance controller adaptation to minimize human control effort while maintaining tracking performance is introduced in [205]. Additionally, an adaptive impedance controller based on the level of human muscle fatigue is proposed in [194] and [206]. Specifically focusing on guidance policies, [134] and [207] propose admittance control gain adaptation laws based on the contact situation with the environment. In [208], admittance controller gains are adapted based on the perceived human steering intention via the interaction forces. Most adaptive steering policies primarily shape the damping part of the guidance law, as seen in [209], which uses a reinforcement learning algorithm to learn the proper damping for minimum jerk movements, or [210], which develops a neural network to estimate the best damping coefficient associated with a minimum jerk.

Existing Gaps: To tailor robot behavior for improved human ergonomics, it is essential to assess human ergonomics first. Manipulability analysis serves as a well-established approach to evaluate the configuration-based manipulation capabilities of articulated bodies. Despite its successful application in robotics, its direct transfer to the assessment of human bodies faces significant challenges. This is primarily attributed to the inherent absence of proprioceptive sensors and, thus, the potential for data inaccuracies in the estimation of the body configuration, upon which manipulability analysis heavily relies. Such limitation has not been adequately addressed in the existing literature.

Research Question P.3: How can manipulability analysis be effectively employed to create a robust approach for assessing human ergonomics that is less sensitive to the body configuration measurement and estimation data?

Another application of human-centered tactile manipulation, which already bears significant relevance in today's society, is robot-aided movement rehabilitation. In this realm, the next mission is to formulate an adaptive policy that empowers a rehabilitation robot to transcend the conventional role of passively moving a patient's limb.

Support-Adaptive Robot-Aided Movement Rehabilitation

Despite significant progress in stroke prevention, the overall incidence of strokes has surged by 70 percent from 1990 to 2019, primarily attributed to population growth [211]. Consequently, acknowledging the pivotal role of rehabilitation in the recovery of stroke survivors [212, 213], an escalating commitment to therapy delivery is imperative year by year. In today's world, physiotherapy and rehabilitation play a crucial role in enhancing recovery and well-being. Specifically, movement rehabilitation is targeted at individuals with movement dysfunction, demonstrating efficacy in treating motor impairments associated with neurological conditions such as post-stroke and Parkinson's disease [214–216]. The significance of repetition in movement therapy cannot be overstated, as studies on neuroplasticity suggest that a high number of repetitions can lead to cortical reorganization and functional improvement [217, 218]. However, as the number of patients and repetitions increases, manually guiding a patient's limb along a therapeutic trajectory can become burdensome for a physiotherapist. This is where rehabilitation robots come into play; leveraging technological advancements, they aim to provide reliable, repetitive movements for physical therapy, alleviating potential burdens often associated with human physiotherapists [219, 220]. For an in-depth exploration of various types of rehabilitation robots, refer to [221]. Numerous studies have refuted the efficacy of relying solely on passive, repetitive movements for patients [222], underscoring the benefits of active patient engagement in the therapeutic process [223–226]. This raises a crucial question: how can patients be encouraged to actively participate in movement exercises when they are already receiving assistance from a robot? One approach is to dynamically adjust the level of assistance based on patient performance, aiming to maintain a *Challenge Point*—providing sufficient support to prevent discouragement but not so much that they become bored and unmotivated. This adaptive modulation of robot assistance, termed *Assist-As-Needed* (AAN) control in the literature [227], strives to deliver only the minimum support necessary to the patient [228].

The adaptive support of the robot is facilitated through various methods, including tunnel-based approaches such as [229, 230], where a virtual tunnel is established within the workspace, e.g., by using multiple force fields. Within this tunnel, a virtual moving wall guides and assists the patient along the therapeutic path. Similarly, in [231, 232], patients are guided within a virtual moving window along the path. Taking a distinct route, [233] determines the remaining effort needed to move the robot based on the estimated human joint torque. Likewise, in [234], the detected torque exerted by the human is amplified to provide support in an arm exoskeleton. Implementing the model-based adaptive controller from [235], the AAN control policies in [228, 236, 237] gradually reduce the feedforward control term. In [238, 239], a motion adaptation law is utilized to minimize interaction torque during gait training. However, the most prevalent approach for adjusting the robot support level has traditionally involved adapting the control parameters of impedance control [240]. Examples include [238, 241–243] for lower-limb rehabilitation and [229, 244–246] for upper-limb rehabilitation scenarios. Generally, in these methodologies, the stiffness of the controller signifies the extent of assistance provided by the robot to the patient. A shared characteristic among the aforementioned approaches is the necessity of online adaptation of the robot controller for adjusting the support level. Consequently, they lack the modularity that would be attained by formulating an approach at a policy level, as opposed to the control level.

A crucial requirement for enhancing recovery is to allow the Central Nervous System to experience the accurate mapping between neural outflow (motor commands) and neural inflow (sensory signals), including an efference copy of its own outflow. This facilitates learning or re-adaptation of how to produce neural outflow to achieve the desired action [247]. Consequently, for effective recovery, a rehabilitation robot should exhibit sufficient *Permissiveness*, i.e., the capacity to facilitate, rather than impede, the patient's intended movement in the correct direction. In essence, enabling unrestricted movements demands minimal impedance from the robot [248]. One strategy involves the utilization of direct-drive electromechanical robots, as exemplified in [249], which demonstrate superior back-drivability and reduced mechanical inertia. Nevertheless, this approach entails a considerable expense, particularly in terms of the torque-to-weight ratio and the time-varying dynamics behavior, particularly inertia. To virtually reduce the mechanical effects of the robot, a common approach involves inertia shaping through joint torque feedback [250]. Alternatively, external wrench feedback can be employed to attain the desired Cartesian impedance behavior [251]. However, compensating for all naturally dynamic effects of a robot demands highly precise measurements and accurate model knowledge. This, in turn, may result in reduced practicality or even instability if these requirements are not sufficiently met [252, 253]. Moreover, even with advanced methods, achieving complete compensation of the robot inertia remains a challenging task in practical applications [254]. As detailed earlier, this limitation can adversely impact the effectiveness of robot-aided rehabilitation therapy, stemming from a deficiency in the necessary permissiveness.

Existing Gaps: In achieving effective robot-aided rehabilitation, the ability to dynamically adjust the level of support proves beneficial. Although this aspect has received attention in the literature, it alone is insufficient. It is equally crucial for the robot to exhibit permissive behavior when the patient moves in an appropriate direction. Existing literature lacks a modular approach that comprehensively addresses the control of both the support and permissiveness aspects of the robot.

Research Question P.4: How can an adaptive movement rehabilitation policy be formulated to systematically adjust and learn the appropriate levels of robot support and permissiveness along a therapeutic path, facilitating an effective recovery?

Having explored the existing literature pertaining to the control and policy blocks, the subsequent review will center on the third aspect—energy.

Energy

In the development of the proposed framework, energy does not merely serve as an independent aspect but is consistently employed as a dual perspective in the construction process of the involved building modules. The following sections explore different facets of energy utilization in the literature, giving rise to three research questions enumerated as E.1–3. Within this context, a recurring application of energy is its role in ensuring stability. The next section delves into this crucial aspect.

Energy Tanks in Passivity-Based Robot Control

Designing a control system requires a comprehensive examination of system stability. Within the existing literature, the *Lyapunov* concept [255] emerges as a widely used method for assessing the stability of controlled robots. Notable applications of the Lyapunov stability theorem include its implementation in adaptive motion control for teleoperation [256], developing adaptive impedance controllers mainly for human-robot interaction [257–259], and designing controllers for robots with Series Elastic Actuators (SEA) [260]. The Lyapunov concept is also utilized for learning adaptive control parameters within motion-constrained human-robot systems [261]. An alternative approach to stability analysis in robot control involves frequency domain analysis. This method was applied to a haptic teleoperation system [262], adaptation of admittance controller parameters [263], and shaping control parameters in response to variations in the stiffness of the interacting environment [264]. Other noteworthy approaches include Nyquist/Bode plots, as demonstrated in teleoperation setups with variable stiffness [265], Root Locus analysis as employed to examine the impedance characteristics of a cooperative robot [266], the absolute stability problem, also known as the Lur'e problem, in [267], and, even experimental stability investigations such as [268].

An increasingly popular approach for investigating the stability of controlled systems is the *Passivity-Based Control* approach. It was initially introduced for adaptive control in robot manipulators in the 80s in [269], followed by [270], and [271]. However, the concept of passivity traces its roots back to the 1950s in the realm of network analysis [272]. Passivity-based control has gained widespread application in robotics as a means to ensure controller stability. Systematic approaches for investigating the passivity of controlled systems are detailed in [273] and [274]. Teleoperation stands out as one of the most common applications of passivity-based approaches. For instance, in [275], passivity is employed to counteract position drift during the remote motion control of a robot. Particularly in scenarios involving time delays, passivity analysis emerges as a robust tool to ensure stability [276–279]. Moreover, passivity-based control is applied in collaborative multi-robot scenarios [280–282]. In the realm of flexible-joint robots, passivity analysis is addressed in [283–285]. In [286], the authors have used the passivity analysis to develop a guidance method allowing the human operator to modify the learned trajectories. In [287], a passivity-based admittance controller is proposed that enhances the robot to have a more natural interaction with an unknown environment. In the domain of humanoid robots, passivity-based control has predominantly been explored in the context of gait stabilization and posture control [288–290]. In the specific realm of impedance-controlled robots, passivity has been scrutinized in contact loss scenarios [291], as well as in cases involving regulation [250]. Finally, in [292], passivity is employed for force and motion regulation when interacting with compliant surfaces.

Passivity analysis serves as a crucial tool for identifying sources of unbounded energy within a controlled system. To guarantee stability, addressing and managing such passivity-violating energy is imperative. A well-established approach involves the utilization of *virtual Energy Tanks*. While the concept of energy tanks was implicitly utilized in [293], one of the pioneering instances of their explicit application was documented in [294]. In this work, virtual energy tanks were employed to ensure the passivity of scattering-based communication channels. The same approach was implicitly applied in [294], incorporating power-continuous control terms to ensure stability. Over time, the concept of energy tanks has gained popularity, finding applications in various control design strategies. In [295], tanks were utilized to stabilize teleoperation setups with time-varying delays. An innovative approach was presented in [296], where dissipated energy was fed back into the tank as part of a two-layered control architecture. In [297], a hierarchical framework is presented, consisting of multiple local and global energy tanks. In general, energy tanks have seen widespread use across different contexts, contributing to the stabilization of cooperative multi-robot systems [298–300], time-varying impedance control [301–305], control of aerial vehicles [36, 306], implementation of controller switching policies [307], and enhancing safety measures [308]. In [309], energy tanks are employed to perceive human guidance, enabling the robot to passively follow the human. To counteract the destabilizing impact of the human's actions, the robot controller parameters are adaptively adjusted based on the observed energy that violates passivity, as explored in [134, 310–312]. Furthermore, a reformulation of the robot's admittance control policy is presented in [313], casting it as an energy optimization problem. Other admittance control policies utilizing energy tanks are outlined in [314–317].

Existing Gaps: In all the referenced works, the primary focus revolves around ensuring stability. For this purpose, passivity analysis is employed to detect any potentially unbounded energy source, and energy tanks are utilized to constrain such energy by deactivating associated control actions. Yet, none of these works extends the use of energy tanks beyond this application. In essence, rather than solely halting the energy flow by deactivating associated actions, the flow can be shaped in alignment with the task objective. This grants the overall framework a distinctive energy-awareness feature.

Research Question E.1: How can the standard configuration of virtual energy tanks be expanded to ensure both stability and active control over the energy flow, imparting enhanced energy awareness to accomplish a broader range of objectives?

The capability to exert control over an entity raises a pivotal question: what should be the reference value for regulating that entity? This crucial query is explored in the subsequent section, particularly within the realm of energy and virtual energy tanks.

Energy-Based Reference Behaviors

One of the earliest instances where the concept of reference energy in the passivity domain was applied is evident in [318], specifically for determining the desired damping term in a haptic teleoperation setup. While this approach saw further development in [319], the original idea of monitoring energy to investigate passivity can be traced back to [276]. The general practice of shaping control parameters to regulate energy and power to desired values has been addressed in numerous robot control works, ranging from seminal contributions like [320] to subsequent works such as [321–325]. More recent contributions, like [326, 327], introduced the concept of energy budgets, for example, to enhance safety in physical human-robot interaction scenarios. Finally, an overview of energy-aware robot control approaches is presented in [328].

Existing Gaps: Possessing the capability to control energy flow within a system raises the immediate question of determining an appropriate reference profile for its regulation. This remains a challenge not fully addressed in the literature, especially in the realm of energy tanks. In this context, insufficient exploration has been undertaken to identify or adapt the associated reference values, which, if addressed, could significantly improve the robustness of interactions with unmodeled environments.

Research Question E.2: How can model-based and learning-based approaches be devised to determine or adapt the reference values and trajectories of virtual energy tanks, thereby enhancing control performance?

Examining yet another application of energy in tactile manipulation, the robot-aided rehabilitation context is revisited. This iteration aims to assess the level of patient participation in the movement, serving as a key indicator of the extent of their recovery.

Performance Monitoring in Movement Rehabilitation

Numerous methods for evaluating patient performance in robot-assisted rehabilitation are available in the literature, with a focus on physiological measurements. In [329], four psychophysiological responses, namely heart rate, respiration, skin conductance, and skin temperature, were employed to assess the physiological state during post-stroke upper extremity rehabilitation. The motor cortex neural drive, the origin of movement, can be theoretically evaluated using Electroencephalography (EEG). At least one research group has demonstrated that EEG can distinguish between active and passive walking with a robotic device [330]. For a more movement-specific measure of neuromotor activity, electromyography (EMG) is widely utilized in laboratory settings [331]. In [236, 332], EMG data is utilized to estimate joint torques during rehabilitation, incorporating it as input for computational models of the musculoskeletal system. This approach allows for the estimation of actual joint torque, which, in turn, aids in determining deficient joint torque [233]. In another study [333], EMG data is fused with interaction forces to assess the patient's condition and establish an exoskeleton control mode for lower-limb rehabilitation in early post-stroke patients. As electrophysiological sensors are deemed impractical for routine use in Intensive Care Unit (ICU) settings [334], it becomes crucial to explore methods that involve sensors integrable into the robotic system only.

In [335], force/torque information is proposed as an alternative to EMG data to circumvent associated preparation complications. This sensory data has been applied in other studies [238, 239] to comprehend the patient's intended motion and respond accordingly in a gait rehabilitation scenario. Another study [336] monitors the alignment of interaction force with the therapeutic path direction as an input for their control adaptation policy. Motion tracking error serves as another method for assessing performance. For instance, in [337, 338], the average tracking error during each movement cycle is employed to adapt the robot support. Similarly, in [339], the tracking error in the velocity domain, and in [340], the total movement duration for reaching the target is considered, respectively. Additionally, model-based approaches [241] utilize combined robot and human dynamics to extract human-generated torque. Another approach [341] estimates gains of the assumed PD controller of the human, while in [342], a musculoskeletal model of the human is employed to estimate required assistance. Estimating active participation becomes challenging when relying solely on force or motion sensing, particularly when the robot support undergoes changes. For example, variations in interaction force may become less apparent when support is low, and a similar phenomenon occurs with motion observation metrics when support is high.

Existing Gaps: The existing methods for assessing patient performance, based on robot sensors, are confined to either force or motion data. However, in instances of altered control behavior, depending solely on either type of information proves impractical. A resolution to this challenge entails the integration of both force and motion data into a holistic metric, such as energy. The concept of transferred power, introduced in [343] for analyzing human-robot interaction, is utilized in [229] within the context of rehabilitation as a feedback metric to iteratively adjust robot control parameters. However, the current literature lacks a comprehensive approach for the derivation and validation of an energy-based patient performance monitoring metric through a systematic clinical study.

Research Question E.3: How can an energy-based method be developed for a rehabilitation robot to continuously monitor the active participation of the patient in therapeutic motion?

In pursuit of the overall ten research questions within the three considered main aspects, the objective of this dissertation is to construct a modular control framework progressively. Addressing these inquiries results in a series of contributions and impacts provided by this dissertation, as enumerated in the following section.

1.3 Contribution and Impact

This dissertation endeavors to build upon the existing groundwork in the field and extend standard approaches in robot control. The ultimate goal is to construct a well-organized framework capable of effectively addressing diverse real-world manipulation and physical interaction scenarios. Through this endeavor, the dissertation aims to make several contributions to the state of the art, as highlighted in the following, leading to various real-world impacts.

Contribution

Addressing the research questions raised in accordance with the identified gaps during the literature review yields the following contributions to the field.

As the foundational building module in the proposed architecture, aiming to control force and motion during physical interactions, the *Unified Force-Impedance Control framework* (UFIC) is presented and significantly extended in this dissertation. While the basic concept was introduced in earlier work [344], patented [345], and commercialized via the Franka Emika robot [346], the extension made in this dissertation represents the first systematic effort to unify impedance with force control under a single paradigm for a more general class of control tasks, overcoming the conventional limitations typically associated with such integration. In this regard, the expansion encompasses both regulation and tracking tasks for both rigid-body and flexible-joint robots. This serves as the *first* contribution of the dissertation, corresponding to the research question C.1. As the *second* contribution, the UFIC is extended to tackle a complex class of systems—multi-manual object manipulation. In this context, a direction-dependent compliance adaptation law is introduced to alleviate the potential conflict between two actions: maintaining contact and moving opposite to the contact wrench, as outlined in research question C.2. This stiffness-adaptation strategy results in a modular single-arm control law, eliminating the typical coupling between the involved arms and significantly enhancing the scalability of the approach. The *third* contribution of the dissertation, linked to research question C.3, involves enabling the utilization of force-motion policies in scenarios where the robot controller only accepts motion commands. To achieve this, a new type of Dynamic Movement Primitives (DMP), known as *Admittance-Coupled DMP*, is introduced. Unlike other modified DMPs, the coupling term in this approach has a clear physical interpretation, facilitating improved tuning and stability analysis.

The subsequent contributions of the dissertation focus on the design of human-centered policies. A recurring aspect of the targeted research questions is the presence of strict geometrical constraints. To tackle this challenge, the dissertation introduces reactive policies utilizing an auxiliary one-dimensional variable phase, determining the temporal aspect of the desired trajectories while keeping their values intact. This not only ensures that trajectory adaptation avoids violating constraints but also enhances the adaptation process by reducing the space dimension to only one. Following this approach, the *fourth* contribution of the dissertation, associated with research question P.1, introduces two phase modulation policies, namely *Impulse Orb* and *Prgnosis Window.* These policies are defined to prevent collisions with humans while maintaining the robot setpoint on a predefined constrained path. Addressing research question P.2, the *fifth* contribution of the dissertation involves introducing an adaptive phase-based haptic motion guidance policy. This policy enables a human opera-

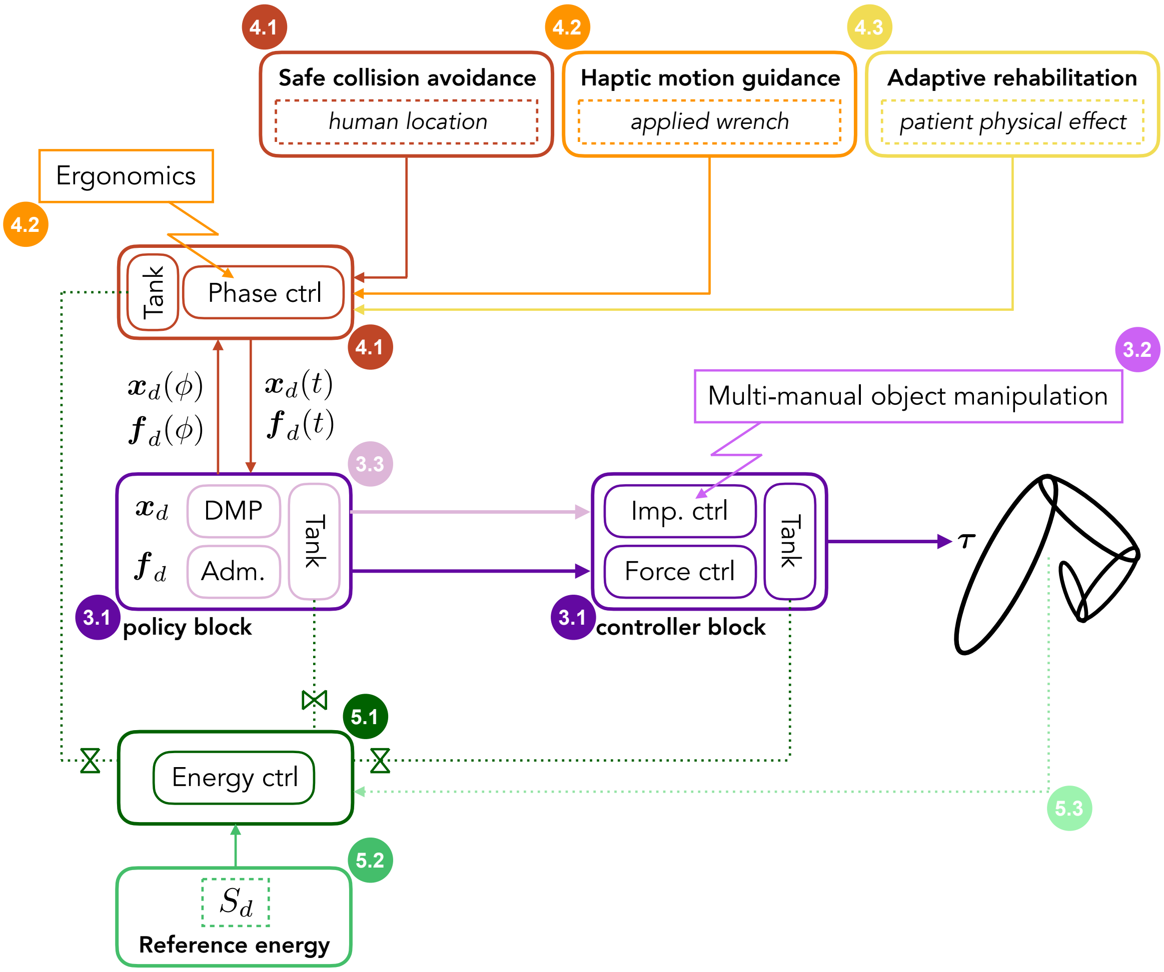

Figure 1.3: Proposed framework architecture – Each building module is annotated with its corresponding section number for clarity. Elements introduced later in the associated chapter are depicted in lighter colors.

tor to steer the robot motion while ensuring that the generated desired trajectory adheres to a constrained path. The guidance law is modular and applicable to any robot equipped with a rigid or compliant motion controller and the capability of sensing or estimating external wrenches. Its formulation is designed such that its actual physical behavior can be likened to a standard mass-damper system, facilitating intuitive online adaptation methods with stability investigation. Leveraging the manipulability analysis approach to evaluate and enhance human ergonomics, particularly during physical human-robot interactions, this dissertation introduces the novel concept of the *Manipulability Pseudo-Ellipsoid* as its *sixth* contribution. As addressed in research question P.3, the objective is to decrease the sensitivity of the conventional manipulability ellipsoid approach to body configuration data. The subsequent, i.e., *seventh*, contribution of the dissertation pertains to the field of robot-aided movement rehabilitation. In response to research question P.4, a phase-based adaptation and learning method is introduced, automatically adjusting the support level of the robot based on the patient's involvement in the therapeutic motion. This approach allows for the fine-tuning of the robot behavior along the therapeutic path, ranging from supportive to permissive. Similar to the aforementioned methods, as the approach operates on the policy level, it is agnostic to the controller choice.

The final set of contributions focuses on the energy aspect. These energy-based methods do not function as independent entities but rather offer a dual theoretical perspective. In this context, energy tanks consistently serve as a tool to ensure the stability of developed blocks. Yet, in this dissertation, for the first time to the best of the authors' knowledge, energy tanks are utilized beyond the scope of ensuring stability. As the *eighth* contribution of the dissertation, associated with research question E.1, a novel class of *Valve-Based Energy Tanks* is defined. The formulation enables the control of energy flow, allowing for energy-based task objectives, such as energy allocation for the prioritization of control actions. The *ninth* contribution of the dissertation involves various explorations in the concepts of reference energy-based behavior. First, model-based estimation methods for initializing energy tanks are introduced. Next, to enhance robustness, learning methods are presented and validated for updating the tank reference power when the robot interacts with a changing environment. These efforts are closely tied to research question E.2. Finally, as the *tenth* contribution of the dissertation, corresponding to research question E.3, energy is utilized to assess and monitor the active participation of a patient during rehabilitation. The validity of the proposed approach is confirmed through a systematic clinical study wherein electromyography (EMG) was employed to assess muscle activation patterns. The approach is independent of the choice of policy and control blocks and does not rely on sophisticated sensory devices such as EMG.

All the contributions outlined in this work underwent rigorous experimental validation to ensure their applicability in real-world scenarios. The stability of the derived control and policy blocks is systematically confirmed through passivity analysis, and virtual energy tanks are designed to rectify the identified passivity-violating components. Each of these contributions addresses a specific facet of the proposed architecture, culminating in the construction of a versatile framework whose use cases are poised to extend beyond the confines of the targeted research questions. The subsequent section delves into the noteworthy impact this framework already had.

Impact

The impact of the control framework proposed in this dissertation spans four distinct perspectives, ranging from applications where a single arm must robustly perform tactile manipulation tasks to more intricate scenarios involving multiple robots or even human-robot interactions.

Single-Robot Tactile Manipulation: The initial set of impacts from this dissertation centers around the concept of UFIC—a robust solution for the simultaneous control of force and motion. Illustrating only a fraction of its potential use cases, particularly in industrial applications, a permanent demonstration setup titled "Future of Work" has been established; see Figure 1.4. This setup incorporates various tactile manipulation tasks and features additional concepts proposed in the dissertation, including energy awareness and safety-enhancing speed adaptation. The Future of Work demonstrator has already been showcased at prestigious technological exhibitions, including the Hannover Messe, one of the world's largest trade fairs dedicated to the topic of industry development, and Automatica, the world's leading trade fair for smart automation and robotics. These exhibitions provided a platform to reach a crucial audience spanning from the scientific to the governmental world. UFIC constitutes the foundational component of the MIRMI Institute's robot control library, MIOS, and numerous recent published research and developments have continually built upon it. UFIC serves as the core component of the European Union project ReconCycle (Nr. 871352), aimed at developing robotic workcells for the recycling of electronic waste (see Figure 1.4). The robust control of force and motion enabled by UFIC facilitates the disassembly of sub-parts that should not undergo the typical crushing process. ReconCycle follows the success of another European Union project, ReconCell (Nr. 680431), focusing on automated assembly processes. Notably, the Admittance-Coupled DMP concept was developed and used in the ReconCell project.

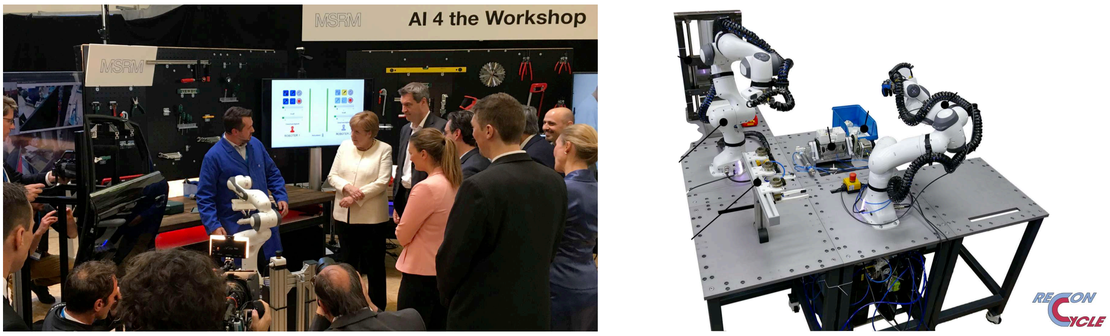

Figure 1.4: UFIC Framework Applications. Left: Future of Work demonstration setup; Right: Electronic waste disassembly work-cell for the ReconCycle project.

Multi-Robot Tactile Manipulation: A consistent approach used throughout the dissertation is energy-based control, with a major application focused on stabilizing the developed systems. This encompasses diverse applications, ranging from a single pneumatic actuator as part of the European project SoftPro (Nr. 688857), aimed at developing assistive devices like prosthetics, to a telepresence setup consisting of two separated arms designed for an infection-free medical examination during the peak of the Covid-19 era, as part of the BMBF national project ProteCT (Nr. 16SV8569), see Figure 1.5. One outcome of the energy-based approach is the introduction of Valve-Based Energy Tanks, enabling the allocation of energy among multiple actions and components. This concept is systematically applied in another national project named VERITAS (Nr. 16SV7987), which focuses on the design of distributed control for dynamically cooperating smart machines. The next analogous scenario in this dissertation, involving multiple cooperative robots, revolves around the challenge of multi-manual object manipulation. The extended UFIC, with the capability of direction-dependent compliance adaptation, offers a highly modular and scalable solution, allowing for the addition or removal of cooperative arms on the fly (see Figure 1.5). This approach has been applied in the national project KoBo34 (Nr. 16SV7987), with the aim of developing bimanual assistive robots.

Figure 1.5: Manipulation tasks demanding multiple arms. Left: Telemedicine setup for the ProteCT project; Right: Multi-Manual Object Manipulation demonstration setup.

Human-Robot Interaction: A crucial aspect considered in the Future of Work demonstrator involves the coexistence of working humans and robots in close proximity. To bolster safety, the phase-modulation approaches introduced in this dissertation are employed to adjust the robot speed based on the proximity of the human intended body part (e.g., the wrist). This proximity is detected by an embedded depth camera in the setup equipped with the OpenCV3 software [347]; see Figure 1.6. These advancements in safe physical human-robot interaction played a pivotal role in the European project ILIAD (Nr. 732737), aiming to safely integrate robotic solutions with existing warehouse facilities. The subsequent human-robot interaction scenario addressed in this dissertation involves the development of the haptic motion guidance law. Utilizing this modular policy allows for human-robot co-manipulation tasks, where the robot strength and accuracy can be combined with human guidance and decision-making capability. A practical application of this approach is demonstrated in a dedicated setup (see Figure 1.6). Furthermore, this approach contributed to the Geriatronics project (Nr. 5140951), which aims to enhance the lives of elderly people through the use of intelligent robotics.

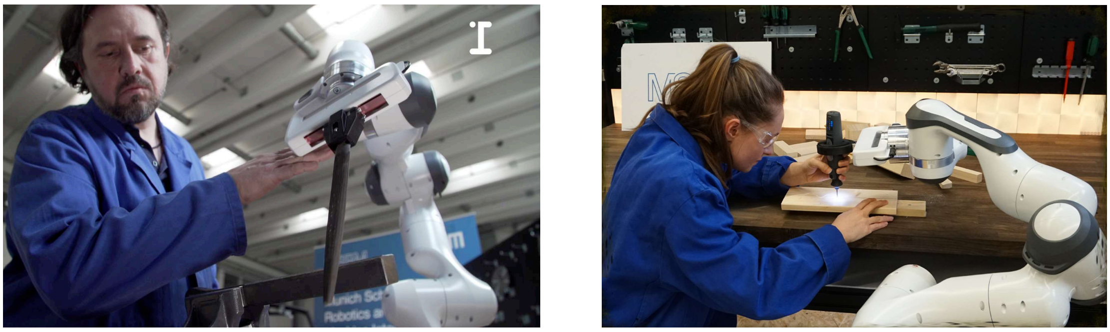

Figure 1.6: Human-robot interaction. Left: Safety-enhancing speed modulation in the Future of Work demonstrator; Right: Precision-improved co-manipulation in wood engraving.

Movement Rehabilitation: The proposed framework has a significant impact on the field of rehabilitation. The novel support-adaptive policy introduced in this dissertation not only facilitates Assist-As-Needed therapy (providing optimum support to the patient) but also enables even minimally back-drivable robots to exhibit permissive behavior—a crucial component in the process of neural recovery. The controller-agnostic nature of the approach, coupled with the absence of a requirement for precise force sensing or additional sensors like Electromyography (EMG), significantly enhances its practicality, making movement rehabilitation more accessible to the growing population in need. This patented invention has been implemented on a lower-limb rehabilitation device (see Figure 1.7), obtained CE certification, been commercialized, and today is globally available. Several subsequent clinical studies have acknowledged the effectiveness of the approach [348]. Among these, this dissertation also investigates the proposed approach through a series of clinical studies utilizing two innovative patient monitoring metrics. With such a learning-based technology, rehabilitation can be conducted by individuals without specialized therapy training, such as those in home care settings. The approach has garnered acknowledgment from governmental and scientific organizations and is recognized with numerous awards, including the annual European Technology Transfer award [349] for the best research-based commercialized technology in Europe. Finally, another impactful contribution to the field of rehabilitation is the development of the energy-based method for observing patient participation in therapeutic motion. This approach alleviates the typical need for sophisticated sensory devices such as EMG, making it practical for environments like the Intensive Care Unit (ICU). These strides in robot-aided rehabilitation have significantly contributed to national projects, including MobIPaR (Nr. 16SV7987), aiming for the mobilization of those in need of intensive care through adaptive robotics, and AI.D (Nr. 16ME0539K), aiming to use robotic devices to help neurologically ill patients regain their motor functions.

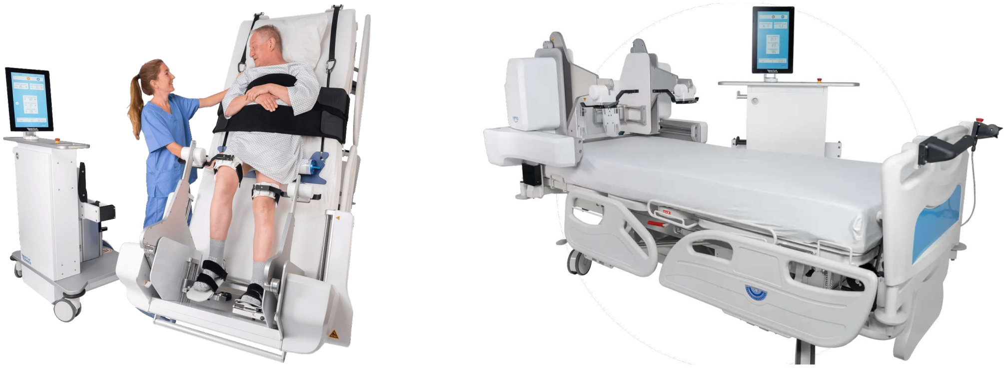

Figure 1.7: VEMOTION®: The commercialized lower-limb rehabilitation robot featuring the innovative CE-certified support adaptation/learning method (Reactive Robotics GmbH).

1.4 Dissertation Structure

The dissertation begins by exploring the foundational concepts in Chapter 2 necessary to build the proposed framework. It then systematically applies these concepts to derive each of the comprising blocks of the framework. Chapter 3 presents the derivation of the controller modules, showcasing how even simple policies can enable the performance of numerous tactile manipulation tasks. In Chapter 4, three phase-based human-centered policies are presented, addressing more intricate objectives. Finally, Chapter 5 presents energy-based methods beyond those used throughout the entire dissertation for stability analysis. The specific details covered in each chapter are outlined in the following.

In Chapter 2, the foundational concepts are introduced. First, in Section 2.1, the terms and preliminaries necessary for modeling rigid-body and flexible-joint manipulators are presented. Next, Section 2.2 outlines the Port-Hamiltonian framework, serving as the cornerstone for the consistently-employed port-based modeling approach. Port-based modeling is crucial for the passivity analysis and the valve-based virtual energy tank augmentation methods presented in Section 2.3. These approaches are pivotal for ensuring the stability of the developed algorithms throughout the dissertation. Chapter 3 focuses on empowering the command of desired force and motion values for a manipulator. To achieve this goal, it introduces an extension and generalization of the unified force-impedance control (UFIC) in Section 3.1 for tracking and regulation tasks applicable to both rigid-body and flexible-joint robots. Moving forward, Section 3.2 further extends UFIC to enable a cooperating team of robots to hold and transport an object. Finally, in Section 3.3, the derivation of admittance-coupled DMPs is presented, allowing the utilization of force-motion policies when the robot controller only accepts motion commands.

In Chapter 4, the focus shifts to planning aspects, particularly in scenarios involving humans. In Section 4.1, the concept of phase is introduced to encode desired force and motion trajectories, rendering them time-independent. Subsequently, two distinct phase modulation methods are introduced in this section to prevent collisions between the robot and the human. In contrast, the phase modulation law introduced in Section 4.2 aims to enable path-constrained haptic motion guidance. This section also introduces the concept of manipulability pseudo-ellipsoid for assessing the ergonomics of the human and adapting the guidance law accordingly. Finally, in Section 4.3, the support-adaptive movement rehabilitation policy is derived using the third phase modulation strategy proposed in the dissertation. In Chapter 5, the challenges of control and planning are approached through a distinct lens: energy. In this context, valve-based virtual energy tanks are used for task prioritization in Section 5.1. Following that, in Section 5.2, both model-based and learning-based methods are presented for planning the reference behaviors of the energy tanks. Ultimately, in Section 5.3, the robot-aided rehabilitation is revisited, introducing an energy-based approach for monitoring the patient participation actively during therapy. Figure 1.3 provides a schematic representation of the proposed control framework constructed throughout the dissertation. Having explored the fundamentals in Chapter 2 and subsequently crafted the proposed framework in Chapters 3 to 5, Chapter 6 concludes the dissertation, encapsulating the key findings and elucidating the avenues for future work.

1.5 Publications and Patents

Below, the publications, peer-reviewed conferences, and patents whose findings significantly contribute to the content of this dissertation are listed. They are categorized according to their relevance to the associated sections.

Section 3.1

- [350] Sami Haddadin, Erfan Shahriari. “Unified Force-Impedance Control.” *The International Journal of Robotics Research (IJRR)*, 43.13 (2024): 2112-2141.

Section 3.2

- [351] Erfan Shahriari, Seyed Ali Baradaran Birjandi, Sami Haddadin. “Passivity-Based Adaptive Force-Impedance Control for Modular Multi-Manual Object Manipulation.” *IEEE Robotics and Automation Letters (RA-L)*, 7, no. 2 (2022): 2194-2201.

Section 3.3

- [352] Erfan Shahriari, Aliaž Kramberger, Andrej Gams, Aleš Ude, Sami Haddadin. “Adapting to Contacts: Energy Tanks and Task Energy for Passivity-Based Dynamic Movement Primitives.” *2017 IEEE-RAS International Conference on Humanoid Robo -tics (Humanoids)*, pp. 136-142.

- [353] Aljaž Kramberger, Erfan Shahriari, Andrej Gams, Bojan Nemec, Aleš Ude, Sami Haddadin. “Passivity Based Iterative Learning of Admittance-Coupled Dynamic Movement Primitives for Interaction with Changing Environments.” *2018 IEEE/RSJ International Conference on Intelligent Robots and Systems (IROS)*, pp. 6023-6028.

Section 4.1

- [354] Dinmukhamed Zardykhan, Petr Svarny, Matej Hoffmann, Erfan Shahriari, Sami Haddadin. “Collision Preventing Phase-Progress Control for Velocity Adaptation in Human Robot Collaboration.” *2019 IEEE-RAS International Conference on Humanoid Robots (Humanoids)*, pp. 266-273.

Section 4.2

- [355] Erfan Shahriari, Petr Svarny, Matej Hoffmann, Sami Haddadin. “Path-Constrained Haptic Motion Guidance via Adaptive Phase-Based Admittance Control.” *IEEE Transactions on Robotics (TRO)*, 41 (2024): 1039-1058.

- [356] Erfan Shahriari, Kim Kristin Peper, Matej Hoffmann, Sami Haddadin. “Enhancing Robustness in Manipulability Assessment: The Pseudo-Ellipsoid Approach.” *2024 IEEE/RSJ International Conference on Intelligent Robots and Systems (IROS)*, pp. 1329-1336.

Section 4.3

- [357] Erfan Shahriari, Dinmukhamed Zardykhan, Alexander Koenig, Elisabeth Jensen, Sami Haddadin. "Energy-Based Adaptive Control and Learning for Patient-Aware Rehabilitation." *2019 IEEE/RSJ International Conference on Intelligent Robots and Systems (IROS)*, pp. 5671-5678.

- [358] Erfan Shahriari, Johannes Lachner, Sami Haddadin, Neville Hogan. "Minimally-Back-Drivable Robots for Rehabilitation: Path-Adherent Permissiveness Control via Trajectory Adaptation." *IEEE Robotics and Automation Letters (RA-L).*

- [359] Marion Egger, Martina Steinböck, Erfan Shahriari, Friedemann Müller. "Robot Assisted Mobilization Therapy with Artificial Intelligence (Robotergestützte Mobilisierungstherapie mit Künstlicher Intelligenz)." *Neuroreha*, 13. no. 1 (2021) 27-31.

- [360] Erfan Shahriari, Sami Haddadin, Dinmukhamed Zardykhan, Alexander Koenig, Helfried Peyrl, Xavier Hildenbrand. "Method for the Open-Loop and Closed-Loop Control of a Device Including a Movement Mmodule During the Interaction of the Device With a Human, and Device Controlled in Such a Manner." *German Patent Office*, DE102020102351A1, *World Intellectual Property Organization*, WO/2021/089087A1 (2021).

Section 5.1

- [361] Erfan Shahriari, Lars Johannsmeier, Sami Haddadin. "Valve-Based Virtual Energy Tanks: A Framework to Simultaneously Passify Controls and Embed Control Objectives." *2018 Annual American Control Conference (ACC)*, pp. 3634-3641.

- [362] Erfan Shahriari, Sami Haddadin. "Incorporation of Control Objectives into Virtual Energy Tanks in Passivity-Based Control (Einbestellung von regelzielen in virtuelle energietanks in der passivitatsbasierten regelung)." *2018 Regelungstechnisches Kolloquium (Control Engineering Colloquium) in Boppard.*

Section 5.2

- [363] Erfan Shahriari, Lars Johannsmeier, Elisabeth Jensen, Sami Haddadin. "Power Flow Regulation, Adaptation, and Learning for Intrinsically Robust Virtual Energy Tanks." *IEEE Robotics and Automation Letters (RA-L)*, 5, no. 1 (2019): 211-218.

Section 5.3

- [364] Elisabeth Jensen, Kim Kristin Peper, Marion Egger, Friedemann Müller, Erfan Shahriari, Sami Haddadin. "Monitoring Active Patient Participation During Robotic Rehabilitation: Comparison Between a Robot-Based Metric and an EMG-Based Metric." *IEEE Transactions on Neural Systems and Rehabilitation Engineering (TNSRE)*, 31, (2023): 4156-4166.


PRINCIPIA
MATHEMATICA
I.S NEWTON
fuel

2 Foundations: Passivity-Based Modeling and Stabilization in Manipulation

To effectively utilize a device, a thorough understanding of its functioning is imperative. This involves identifying a suitable model for the device, which ultimately enables the proper formulation of approaches for its optimal usage. In the case of a manipulator, there are already standard methods for its modeling. Among these, similar to any rigid-body object, a widely used modeling approach involves deriving the dynamic relation between the generalized forces acting on the robot and the resulting motion. Here, this established approach is integrated with another modeling technique known as port-based modeling. Rooted in the port-Hamiltonian paradigm, this methodology not only facilitates the development of a modular architecture comprising the manipulator's physical components but also allows the design and incorporation of virtual components, such as control and policy modules, in a stable manner. The key principle underlying this approach is the conservativity of energy, providing a robust foundation for stability analysis, particularly through the lens of passivity. Passivity analysis offers an intuitive means to verify system stability. For components where stability cannot be guaranteed, straightforward approaches like virtual energy tank augmentation methods can be employed. This chapter introduces fundamental concepts in modeling and passivity analysis, subsequently presenting an innovative enhancement to the virtual energy tank formulation. These concepts are a central tool throughout the dissertation to construct the proposed control architecture.

The chapter initiates with the exploration of kinematics and dynamics modeling, covering both rigid-body and flexible-joint robots. Following this, a brief historical overview of the port-Hamiltonian approach is provided, laying the groundwork for the introduction of its fundamental concepts. Subsequently, the port-based modeling of a flexible-joint manipulator in contact with the environment is systematically derived. The next section introduces the concept of passivity, specifically within the context of port-based modeling. Passivity is then correlated with the well-established Lyapunov stability approach, providing a better understanding of the concept. The chapter culminates in the presentation of the foundational formulation of a novel concept: valve-based virtual energy tanks. Virtual tanks are employed extensively throughout the dissertation for the design and stabilization of control and policy modules.

2.1 Manipulator Modeling

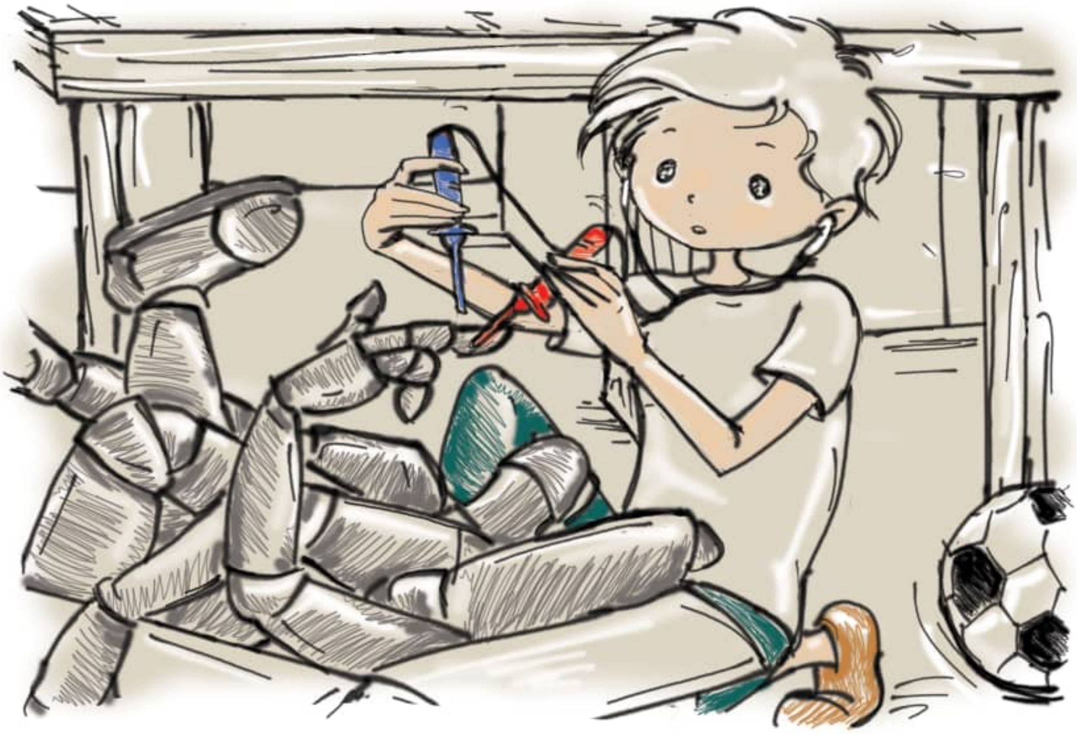

In this section, fundamental concepts related to the kinematics and dynamics modeling of a manipulator are introduced. The discussion begins with the characterization of robot motion in different spaces. Subsequently, the dynamic relation between the generalized forces acting on a robot and the resulting motion is explored through the development of the robot dynamics model. Finally, the potential influence of joint elasticity on the derived models is discussed, presenting a control law that allows for shaping such effects.

2.1.1 Rigid-Body Robot

Consider a robot with n degrees of freedom, as exemplified in Figure 2.1, where its joint angles are indicated by $\boldsymbol{q} \in \mathbb{R}^n$. Additionally, let $\boldsymbol{x} \in \mathbb{R}^m$ represent the pose of the robot center of rotation, defining the robot motion and typically coinciding with the robot end-effector, in an m-dimensional Cartesian space with the origin at the robot base frame. For such a robot, a configuration-dependent Jacobian matrix $\boldsymbol{J}(\boldsymbol{q}) \in \mathbb{R}^{m \times n}$ can be identified from the robot kinematics model, relating the joint velocity $\dot{\boldsymbol{q}} \in \mathbb{R}^n$ to the center of rotation twist $\dot{\boldsymbol{x}} \in \mathbb{R}^m$ via [365]

$$\dot{\boldsymbol{x}} = \boldsymbol{J}(\boldsymbol{q})\dot{\boldsymbol{q}}. \tag{2.1}$$

Please note that throughout the dissertation, rotation matrices[1] $\boldsymbol{R} \in \mathbb{R}^{3\times3}$ are utilized to identify the rotational component of a pose, for instance, in determining the tracking error

---

[1] Elements of the special orthogonal group SO(3); refer to [366].

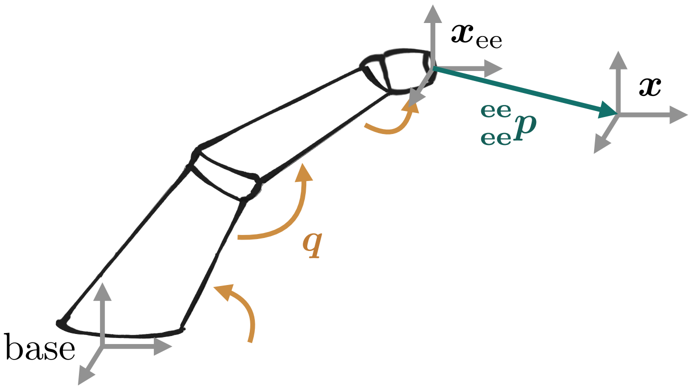

Figure 2.1: Kinematics variables of a manipulator

for motion control. However, for a clearer representation of the derivation of the proposed approaches, a pose is presented as a vector comprising the translational component $\boldsymbol{x}_t \in \mathbb{R}^{m_t}$ as well as the rotational part[2] $\boldsymbol{x}_r \in \mathbb{R}^{m_r}$, using Euler angles as an example. Note that the rotational component of a twist $\dot{\boldsymbol{x}}_r$ (i.e., angular velocity) is related to the rotation matrix via

$$\boldsymbol{R}^T \dot{\boldsymbol{R}} = [\dot{\boldsymbol{x}}_r]_\times \tag{2.2}$$

where $[.]_\times$ is the skew-symmetric matrix representation of a vector. For more information, please refer to [366].

In cases where the robot center of rotation is aligned but not coincident with its end-effector, let $\boldsymbol{x}_{\text{ee}} \in \mathbb{R}^m$ indicate the pose of the end-effector. Additionally, let ${}^{\text{ee}}_{\text{ee}}\boldsymbol{p}_{\text{cr}} \in \mathbb{R}^{m_t}$ be the vector connecting the end-effector to the center of rotation, represented in the end-effector frame. Under this consideration, the Jacobian matrix can be deconstructed as

$$\boldsymbol{J}(\boldsymbol{q}) = {}_{\text{ee}}\boldsymbol{J}\ \boldsymbol{J}_{\text{ee}}(\boldsymbol{q}), \tag{2.3}$$

where $\boldsymbol{J}_{\text{ee}}(\boldsymbol{q}) \in \mathbb{R}^{m \times n}$ is the robot Jacobian matrix to the end-effector such that

$$\dot{\boldsymbol{x}}_{\text{ee}} = \boldsymbol{J}_{\text{ee}}(\boldsymbol{q})\dot{\boldsymbol{q}}, \tag{2.4}$$

with $\dot{\boldsymbol{x}}_{\text{ee}} \in \mathbb{R}^m$ denoting the end-effector twist. Moreover, ${}_{\text{ee}}\boldsymbol{J} \in \mathbb{R}^{m \times m}$ is the Jacobian matrix relating the end-effector twist to the center of rotation twist as

$$\dot{\boldsymbol{x}} = {}_{\text{ee}}\boldsymbol{J}\ \dot{\boldsymbol{x}}_{\text{ee}}, \tag{2.5}$$

which is derived as

$${}_{\text{ee}}\boldsymbol{J} = \begin{bmatrix} \boldsymbol{I}_{m_t} & [{}^{\text{ee}}_{\text{ee}}\boldsymbol{p}]^T_\times \\ \boldsymbol{0}_{m_t \times m_t} & \boldsymbol{I}_{m_t} \end{bmatrix}. \tag{2.6}$$

---

[2] $m_t + m_r = m$.

Considering $\boldsymbol{M}(\boldsymbol{q}), \boldsymbol{C}(\boldsymbol{q}, \dot{\boldsymbol{q}}) \in \mathbb{R}^{n\times n}$ as the symmetric positive-definite mass (inertia) matrix as well as the centrifugal and Coriolis matrix of the robot, respectively, the robot dynamics equation is well-known [367] to be

$$\boldsymbol{M}(\boldsymbol{q})\ddot{\boldsymbol{q}} + \boldsymbol{C}(\boldsymbol{q}, \dot{\boldsymbol{q}})\dot{\boldsymbol{q}} = \boldsymbol{\tau}, \tag{2.7}$$

where $\ddot{\boldsymbol{q}} \in \mathbb{R}^n$ is the joint acceleration vector, and $\boldsymbol{\tau} \in \mathbb{R}^n$ represents the net torque being applied on the robot links derived as

$$\boldsymbol{\tau} = \boldsymbol{\tau}_m + \boldsymbol{\tau}_{\text{ext}} - \boldsymbol{\tau}_{\text{fri}} - \boldsymbol{\tau}_g. \tag{2.8}$$

Here, $\boldsymbol{\tau}_m, \boldsymbol{\tau}_{\text{ext}} \in \mathbb{R}^n$ represent the torques applied to the links by the motors (equivalent to the control input) and the external wrenches, respectively. Additionally, $\boldsymbol{\tau}_{\text{fri}}(\boldsymbol{q}, \dot{\boldsymbol{q}}) \in \mathbb{R}^n$ denotes the friction torque[3], ensuring the satisfaction of

$$\dot{\boldsymbol{q}}^T \boldsymbol{\tau}_{\text{fri}}(\boldsymbol{q}, \dot{\boldsymbol{q}}) \geq 0. \tag{2.9}$$

Finally, with $U_g \in \mathbb{R}_{\geq 0}$ representing the gravitational energy of the links, the gravity torque[4] $\boldsymbol{\tau}_g(\boldsymbol{q}) \in \mathbb{R}^n$ is derived as

$$\boldsymbol{\tau}_g(\boldsymbol{q}) = \frac{\partial U_g}{\partial \boldsymbol{q}}. \tag{2.10}$$

The dynamics equation (2.7) can be expressed in the Cartesian space as [368]

$$\boldsymbol{M}_C(\boldsymbol{q})\ddot{\boldsymbol{x}} + \boldsymbol{C}_C(\boldsymbol{q}, \dot{\boldsymbol{q}})\dot{\boldsymbol{x}} = \boldsymbol{f}, \tag{2.11}$$

in which $\ddot{\boldsymbol{x}} \in \mathbb{R}^m$ denotes the acceleration twist vector of the center of rotation. Additionally, matrices $\boldsymbol{M}_C(\boldsymbol{q})$, $\boldsymbol{C}_C(\boldsymbol{q}, \dot{\boldsymbol{q}}) \in \mathbb{R}^{m\times m}$, and vector $\boldsymbol{f} \in \mathbb{R}^m$ represent the robot mass matrix, Coriolis and centrifugal matrix, and the joint torque vector, respectively, expressed in the Cartesian space and derived as [368]

$$\begin{aligned} \boldsymbol{M}_C(\boldsymbol{q}) &= \boldsymbol{J}^{-T}(\boldsymbol{q})\boldsymbol{M}(\boldsymbol{q})\boldsymbol{J}^{-1}(\boldsymbol{q}), && (2.12)\\ \boldsymbol{C}_C(\boldsymbol{q}, \dot{\boldsymbol{q}}) &= \boldsymbol{J}^{-T}(\boldsymbol{q})\boldsymbol{C}(\boldsymbol{q}, \dot{\boldsymbol{q}})\boldsymbol{J}^{-1}(\boldsymbol{q}) - \boldsymbol{M}_C(\boldsymbol{q})\dot{\boldsymbol{J}}(\boldsymbol{q})\boldsymbol{J}^{-1}(\boldsymbol{q}), && (2.13)\\ \boldsymbol{f} &= \boldsymbol{J}^{-T}(\boldsymbol{q})\boldsymbol{\tau}. && (2.14) \end{aligned}$$

Here, $\dot{\boldsymbol{J}}(\boldsymbol{q}) \in \mathbb{R}^{m\times n}$ is the time derivative, and $\boldsymbol{J}^T(\boldsymbol{q}), \boldsymbol{J}^{-1}(\boldsymbol{q}) \in \mathbb{R}^{n\times m}$ are the transpose and the inverse of the Jacobian matrix, respectively, and $\boldsymbol{J}^{-T}(\boldsymbol{q}) = \left(\boldsymbol{J}^{-1}(\boldsymbol{q})\right)^T$. If the Jacobian matrix is not invertible, one viable option, as suggested in [369], is to employ the right-hand Moore-Penrose pseudo-inverse $\boldsymbol{J}^{-1} = \boldsymbol{J}^T(\boldsymbol{J}\boldsymbol{J}^T)^{-1}$. Furthermore, while acknowledging the non-uniqueness of the centrifugal and Coriolis matrix, as highlighted in [367], in this dissertation, a specific selection is made in such a way that

$$\boldsymbol{C}_C(\boldsymbol{q}, \dot{\boldsymbol{q}}) + \boldsymbol{C}_C^T(\boldsymbol{q}, \dot{\boldsymbol{q}}) = \dot{\boldsymbol{M}}_C(\boldsymbol{q}, \dot{\boldsymbol{q}}), \tag{2.15}$$

---

[3] Please note that, in general, the friction torque can be considered as a function of joint angles and velocities, denoted as $\boldsymbol{\tau}_{\text{fri}}(\boldsymbol{q}, \dot{\boldsymbol{q}})$. However, for the sake of brevity, throughout the dissertation, this dependency is often omitted in its notation, and thus $\boldsymbol{\tau}_{\text{fri}}$ is used.

[4] Please note that the gravity torque is a function of joint angle, denoted as $\boldsymbol{\tau}_g(\boldsymbol{q})$. However, for the sake of brevity, throughout the dissertation, this dependency is often omitted in its notation, and thus $\boldsymbol{\tau}_g$ is used.

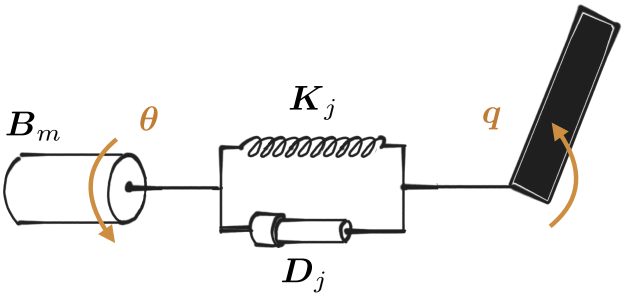

Figure 2.2: A single-link flexible-joint robot

yielding the skew symmetry of the matrix $\dot{\boldsymbol{M}}_C(\boldsymbol{q},\dot{\boldsymbol{q}}) - 2\boldsymbol{C}_C(\boldsymbol{q},\dot{\boldsymbol{q}})$. Finally, akin to (2.8), the vector $\boldsymbol{f}$ in (2.11) can be interpreted as

$$\boldsymbol{f} = \boldsymbol{f}_m + \boldsymbol{f}_{\text{ext}} - \boldsymbol{f}_{\text{fri}} - \boldsymbol{f}_g, \tag{2.16}$$

where $\boldsymbol{f}_m, \boldsymbol{f}_g, \boldsymbol{f}_{\text{fri}} \in \mathbb{R}^m$ denote the motor, gravity, and the friction torques, respectively, represented in the Cartesian space, and $\boldsymbol{f}_{\text{ext}} \in \mathbb{R}^m$ is the external wrench applied to the robot. The individual torque and wrench vectors in (2.8) and (2.16) can be mapped and converted into each other through the Jacobian matrix, as

$$\boldsymbol{\tau}_m = \boldsymbol{J}^T(\boldsymbol{q})\boldsymbol{f}_m, \tag{2.17}$$
$$\boldsymbol{\tau}_{\text{ext}} = \boldsymbol{J}^T(\boldsymbol{q})\boldsymbol{f}_{\text{ext}}, \tag{2.18}$$
$$\boldsymbol{\tau}_{\text{fri}} = \boldsymbol{J}^T(\boldsymbol{q})\boldsymbol{f}_{\text{fri}}, \tag{2.19}$$
$$\boldsymbol{\tau}_g = \boldsymbol{J}^T(\boldsymbol{q})\boldsymbol{f}_g. \tag{2.20}$$

2.1.2 Flexible-Joint Robot

For lightweight or Series Elastic Actuator-type systems, the modeling presented above lacks the necessary precision to describe the inherent dynamics, mainly due to the presence of a flexible transmission. The joint elasticity induced by gears (e.g., Harmonic Drive gear) and integrated joint torque sensors cannot be overlooked and must be considered. Referring to (2.8), while a rigid-body robot directly transmits the motor torque $\boldsymbol{\tau}_m$ to the links, a flexible-joint robot exhibits elasticity between the motors and the links, as discussed in [370]; see Figure 2.2. Consequently, the joint angles $\boldsymbol{q}$ deviate from the motor angles $\boldsymbol{\theta} \in \mathbb{R}^n$, leading to the mass matrix and the centrifugal and Coriolis matrix no longer incorporating the motor inertia. The net torque in the dynamics equation (2.7) is then derived as

$$\boldsymbol{\tau} = \boldsymbol{\tau}_j + \boldsymbol{\tau}_{\text{ext}} - \boldsymbol{\tau}_{\text{fri}} - \boldsymbol{\tau}_g, \tag{2.21}$$

where $\boldsymbol{\tau}_j \in \mathbb{R}^n$ represents the torque generated by the elastic joints, derived as [370]

$$\boldsymbol{\tau}_j = \boldsymbol{K}_j(\boldsymbol{\theta} - \boldsymbol{q}) + \boldsymbol{D}_j(\dot{\boldsymbol{\theta}} - \dot{\boldsymbol{q}}), \tag{2.22}$$

in which $\dot{\boldsymbol{\theta}} \in \mathbb{R}^n$ denotes the motor velocity and $\boldsymbol{K}_j, \boldsymbol{D}_j \in \mathbb{R}^{n\times n}$ are diagonal positive definite matrices representing the lumped joint stiffness and damping, respectively. Lastly, considering $\boldsymbol{B}_m \in \mathbb{R}^{n\times n}$ as the diagonal positive definite motor inertia matrix, the motor angles $\boldsymbol{\theta}$ would evolve according to the motor torque $\boldsymbol{\tau}_m$ and the elastic joint torque $\boldsymbol{\tau}_j$ via

$$\boldsymbol{B}_m \ddot{\boldsymbol{\theta}} = \boldsymbol{\tau}_m - \boldsymbol{\tau}_j. \tag{2.23}$$

Notably, for the sake of simplicity, motor friction is omitted in (2.23).

Inertia Shaping Through Joint Torque Feedback

Flexible-joint robots, when equipped with joint torque sensing, provide the capability to shape both motor inertia and joint damping. This can be achieved by implementing the following low-level control law [283].

$$\boldsymbol{\tau}_m = \boldsymbol{B}_m \boldsymbol{B}_m^{*^{-1}} \boldsymbol{\tau}_{m,j} + \boldsymbol{\tau}_{j,K} + \boldsymbol{D}_j \boldsymbol{K}_{\boldsymbol{j}}^{\boldsymbol{-1}} \dot{\boldsymbol{\tau}}_{j,K} - \boldsymbol{B}_m \boldsymbol{B}_m^{*^{-1}} (\boldsymbol{\tau}_{j,K} + \boldsymbol{D}_j^* \boldsymbol{K}_j^{-1} \dot{\boldsymbol{\tau}}_{j,K}). \tag{2.24}$$

Here, $\boldsymbol{\tau}_{j,K} = \boldsymbol{K}_j(\boldsymbol{\theta} - \boldsymbol{q})$, and $\boldsymbol{B}_m^*, \boldsymbol{D}_j^* \in \mathbb{R}^{n\times n}$ represent the intended shaped values of the motor inertia and joint damping, respectively. Additionally, $\boldsymbol{\tau}_{m,j}^*$ denotes the new auxiliary high-level control input, which can be assigned according to the manipulation task. As a result, the shaped motor and flexible-joint dynamics equations become

$$\boldsymbol{B}_m^* \ddot{\boldsymbol{\theta}} = \boldsymbol{\tau}_{m,j} - \boldsymbol{\tau}_j^*, \tag{2.25}$$

$$\boldsymbol{\tau}_j^* = \boldsymbol{K}_j(\boldsymbol{\theta} - \boldsymbol{q}) + \boldsymbol{D}_j^*(\dot{\boldsymbol{\theta}} - \dot{\boldsymbol{q}}). \tag{2.26}$$

Complete Dynamics Model of a Flexible-Joint Robot

Note that (2.22) and (2.23) are associated with the reduced dynamics model of a flexible-joint robot. The complete model is typically represented as [251, 371]

$$\begin{bmatrix} \boldsymbol{M}_j(\boldsymbol{q}) & \boldsymbol{S}_j(\boldsymbol{q}) \\ \boldsymbol{S}_j^T(\boldsymbol{q}) & \boldsymbol{B}_m \end{bmatrix} \begin{bmatrix} \ddot{\boldsymbol{q}} \\ \ddot{\boldsymbol{\theta}} \end{bmatrix} + \boldsymbol{C}_j(\boldsymbol{q}, \dot{\boldsymbol{q}}) \begin{bmatrix} \dot{\boldsymbol{q}} \\ \dot{\boldsymbol{\theta}} \end{bmatrix} + \begin{bmatrix} \boldsymbol{\tau}_g - \boldsymbol{K}_j(\boldsymbol{\theta} - \boldsymbol{q}) - \boldsymbol{D}_j(\dot{\boldsymbol{\theta}} - \dot{\boldsymbol{q}}) \\ \boldsymbol{K}_j(\boldsymbol{\theta} - \boldsymbol{q}) + \boldsymbol{D}_j(\dot{\boldsymbol{\theta}} - \dot{\boldsymbol{q}}) \end{bmatrix} = \begin{bmatrix} \boldsymbol{\tau}_{\text{ext}} - \boldsymbol{\tau}_{\text{fri}} \\ \boldsymbol{\tau}_m \end{bmatrix}, \tag{2.27}$$

where

$$\boldsymbol{M}_j(\boldsymbol{q}) = \boldsymbol{M}(\boldsymbol{q}) + \boldsymbol{M}_m(\boldsymbol{q}) + \boldsymbol{S}_j(\boldsymbol{q}) \boldsymbol{B}_m^{-1} \boldsymbol{S}_j^T(\boldsymbol{q}). \tag{2.28}$$

Here, $\boldsymbol{M}_m(\boldsymbol{q}) \in \mathbb{R}^{n\times n}$ encompasses the rotor masses and possible rotor inertial components along other principal axes. The matrix $\boldsymbol{S}_j(\boldsymbol{q}) \in \mathbb{R}^{n\times n}$ denotes the inertial couplings between the rotors and the preceding links in the robot chain, and $\boldsymbol{C}_j(\boldsymbol{q}, \dot{\boldsymbol{q}}) \in \mathbb{R}^{2n\times 2n}$ represents the centrifugal and Coriolis matrix of the flexible-joint robot. Note that, similar to (2.23), the effects of motor-side friction are excluded in (2.27).

2.2 Port-Based Modeling in Manipulation

This section explores the port-based modeling approach and its application in modeling a tactile manipulator. Rooted in the port-Hamiltonian framework, the section begins with a brief history of the approach and the fundamental concepts. Subsequently, an exemplary modular architecture is derived, encompassing various elements involved in a flexible-joint manipulator in contact with the environment, utilizing the introduced concepts.

2.2.1 Port-Hamiltonian Systems

The concept of a *port* originated in electrical circuit theory in the late 1940s, introduced by Wheeler and Dettinger [372]. However, it was Henry M. Paynter who extended this notion to encompass arbitrary power ports, applicable universally, and introduced the concept of a *bond* as the connecting line between two ports. Paynter finalized and presented the *bond graph* notation during a lecture in 1959 at the MIT Mechanical Engineering department [373]. This development was inspired by the American philosopher Charles Sanders Peirce, who reversed the conventional interpretation of graphs by associating edges with objects and nodes with operations[5].

A port functions as a conceptual interface facilitating interaction between systems. This interaction, intrinsically tied to the exchange of energy (i.e., power), is symbolized as a (power) bond. Consequently, a bond signifies a bilateral relationship between two ports of the interacting systems. The bidirectional nature of this energy-coupled relation implies the existence

---

[5] See also https://sites.utexas.edu/longoria/hmp.

of two variables associated with the power represented by the bond. These variables, termed *power-conjugate variables*, typically yield transferred power through a product operation and are known as *effort* and *flow* in a domain-independent scenario. In domain-dependent instances, examples of effort and flow encompass voltage and current in the electromagnetic domain, pressure and volume flow in hydraulic and pneumatic domains, entropy flow and temperature in the thermal domain, and force and velocity in the mechanical domain.

In the early 1990s, Maschke and Van der Schaft [374] discovered that by integrating the bond graph formalism with Hamiltonian dynamics, it becomes possible to model and control physical systems interacting with their environment in a well-defined manner. They termed this approach a *port-controlled Hamiltonian system* and demonstrated several advantages of such modeling. Hamiltonian dynamics modeling shares similarities with the Lagrangian method, with a significant advantage in handling a larger number of interacting systems [375]. The key advantage lies in the Hamiltonian formulation's close correlation with energy. Since energy is an accumulative term, Hamiltonian models of a network of subsystems can seamlessly merge into a unified system model. These characteristics suggest inherent similarities between Hamiltonian dynamics modeling and the bond graph formalism. In fact, any bond graph can be associated with a Hamiltonian representation [376]. The integration of Hamiltonian dynamics with the port-based bond graph formalism creates a powerful tool for describing dynamical systems through a generalizable and modular geometric structure [377]. Systems represented using such modeling are referred to as *port-Hamiltonian systems* and prove particularly advantageous in modeling a network of interacting dynamical systems.

Figure 2.3 illustrates a general port-Hamiltonian system. Central to the derivation of port-Hamiltonian systems is the concept of a *Dirac structure*, denoted[6] by $\mathscr{D}$ in Figure 2.3, which unifies the description of interactions in physical systems. Its role is to connect the ports in a *power-conservative* manner, ensuring that the total power associated with the port variables is zero. Considering $\mathscr{F}$ as the finite-dimensional linear space of flows (e.g., $\mathscr{F} = \mathbb{R}^k$), and $\mathscr{E}$ as its dual linear (efforts) space, i.e., $\mathscr{E} := \mathscr{F}^\ddagger$ (e.g., $\mathscr{F} = (\mathbb{R}^k)^\ddagger$), the total space of flow and effort variables is $\mathscr{F} \times \mathscr{F}^\ddagger$. Now, considering $\boldsymbol{f} \in \mathscr{F}$ and $\boldsymbol{e} \in \mathscr{E}$ as the elements of such spaces, the power associated with the total space of port variables is defined as

$$P = \langle \boldsymbol{e} | \boldsymbol{f} \rangle, \qquad (\boldsymbol{f}, \boldsymbol{e}) \in \mathscr{F} \times \mathscr{F}^\ddagger, \tag{2.29}$$

where $\langle . | . \rangle$ denotes the dual product operation. In the case where efforts and flows are defined as column vectors, it becomes

$$\langle \boldsymbol{e} | \boldsymbol{f} \rangle = \boldsymbol{e}^T \boldsymbol{f}. \tag{2.30}$$

A Dirac structure on the space $\mathscr{F} \times \mathscr{F}^\ddagger$ is the largest subspace $\mathscr{D} \subset \mathscr{F} \times \mathscr{F}^\ddagger$ such that for all $(\boldsymbol{f}, \boldsymbol{e}) \in \mathscr{D}$, the associated power is zero (i.e., $\langle \boldsymbol{e} | \boldsymbol{f} \rangle = 0$). Therefore, considering the port variables in Figure 2.3 as column vectors, the depicted Dirac structure $\mathscr{D}$ implies

$$\boldsymbol{e}_S^T \boldsymbol{f}_S + \boldsymbol{e}_R^T \boldsymbol{f}_R + \boldsymbol{e}_P^T \boldsymbol{f}_P = 0. \tag{2.31}$$

Figure 2.3, potentially representing a single physical entity, illustrates three distinct elements with unique physical behavior types, interconnected through the Dirac structure $\mathscr{D}$.

---

[6] Please note that the variables associated with the Dirac structure formulation presented in Section 2.2.1 are not explicitly listed in the Notation section.

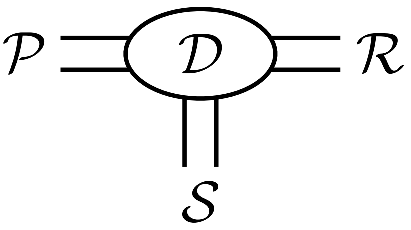

Figure 2.3: Dirac structure $\mathcal{D}$, connecting the energy storage $\mathcal{S}$, energy dissipation $\mathcal{R}$, and external elements $\mathcal{P}$ in a power-conservative manner

This categorization, rooted in fundamental elementary behaviors in physical systems, can significantly enhance the modeling process. According to the bond graph formalism, any physical system (or subsystem) can be perceived as an interconnection of components from a relatively small set of dynamic elements. The three elements in Figure 2.3 represent three energy-based behaviors of a physical system and are explained in the following.

Energy Storage: The energy storage element corresponds to all system components capable of storing energy. Examples specific to domains include the spring and mass in the mechanical domain or the capacitor and inductor in the electrical domain. These elements are characterized by a state space manifold $\mathscr{X}$ with coordinates $\boldsymbol{x}$, and a Hamiltonian function $H : \mathscr{X} \to \mathbb{R}_{\geq 0}$ representing their stored energy. The port variables $\boldsymbol{e}_S, \boldsymbol{f}_S$ are connected to their energy and state variables as follows:

$$\boldsymbol{e}_S = \frac{\partial H(\boldsymbol{x})}{\partial \boldsymbol{x}}, \qquad \boldsymbol{f}_S = -\dot{\boldsymbol{x}}. \tag{2.32}$$

Thus, the power associated with the energy storage ports becomes

$$P_S = \boldsymbol{e}_S^T \boldsymbol{f}_S = -\left(\frac{\partial H(\boldsymbol{x})}{\partial \boldsymbol{x}}\right)^T \dot{\boldsymbol{x}} = -\dot{H}(\boldsymbol{x}), \tag{2.33}$$

indicating that the transferred power from the energy storage element corresponds to the rate of change of stored energy. For instance, in the case of an ideal capacitor, where the state variable is the electrical charge $x = q$ and the stored energy is $H = q^2/2C$ (with C as the capacitance parameter), the effort and flow variables are $e_s = \partial H/\partial x = q/C = v$ and $f_s = -\dot{q} = -i$, where v and i represent the capacitor voltage and electrical current, respectively. The electrical power from the capacitor is then $P_S = -vi = -\dot{H}(x)$.

Energy Dissipation: The energy dissipating (resistive) element corresponds to the behavior of energy dissipation, also known as irreversible energy transformation. Examples include friction in the mechanical domain or resistance in the electrical domain. Typically, the energy dissipation port variables adhere to a static resistive relation $\mathcal{R}(\boldsymbol{e}_R, \boldsymbol{f}_R) = 0$, such that for all $(\boldsymbol{f}_R, \boldsymbol{e}_R)$

$$P_R = \langle \boldsymbol{e}_R | \boldsymbol{f}_R \rangle \leq 0. \tag{2.34}$$

In essence, the energy dissipation element consistently injects negative power into the port-Hamiltonian system. For instance, in the case of an electrical resistor, the port variables

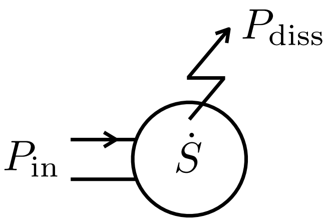

Figure 2.4: Compact port-based representation of a general (passive) system

are $e_R = v = iR$ and $f_R = -i$, where $R \geq 0$ is the resistance parameter. Accordingly, the resistive relation is $\mathcal{R}(e_R, f_R) = e_R + Rf_R = 0$, and the power emanating from the resistor is $P_R = e_R f_R = -Ri^2$, which is consistently negative.

External Ports: In a general context, the energy storage and energy dissipation elements are regarded as the internal components of a port-Hamiltonian system. The system engages with external elements through its external ports, which might be linked to controller actions, energy sources, or other port-Hamiltonian systems. The power corresponding to the external ports is

$$P_P = \boldsymbol{e}_P^T \boldsymbol{f}_P. \tag{2.35}$$

The port-Hamiltonian system, characterized by the state space $\mathscr{X}$ and Hamiltonian H associated with the energy storage port $\mathscr{S}$, energy dissipation port $\mathscr{R}$, external ports $\mathscr{P}$, and the Dirac structure $\mathscr{D}$, can be explicitly represented as $\Sigma = (\mathscr{X}, H, \mathscr{R}, \mathscr{P}, \mathscr{D})$. The dynamics of the port-Hamiltonian system are derived from the constraints imposed by the Dirac structure

$$(\boldsymbol{e}_S, \boldsymbol{f}_S, \boldsymbol{e}_R, \boldsymbol{f}_R, \boldsymbol{e}_P, \boldsymbol{f}_P) \in \mathscr{D}, \tag{2.36}$$

which according to (2.31) and (2.33) results in

$$\dot{H} = \boldsymbol{e}_R^T \boldsymbol{f}_R + \boldsymbol{e}_P^T \boldsymbol{f}_P. \tag{2.37}$$

To construct a more compact representation for a network model of interacting physical systems, the conventional depiction of Figure 2.3 can be replaced. Figure 2.4 illustrates an alternative port-based representation, where the circle corresponds to the storage element of the system with the stored energy $S \in \mathbb{R}_{\geq 0}$, equivalent to the Hamiltonian function H. The zigzag arrow indicates the dissipation power $P_{\text{diss}} \in \mathbb{R}_{\geq 0}$, equivalent to $(-P_R)$ in (2.34), associated with the dissipation element. The system interacts with its outer world via its interaction port(s), through which the transferred power P_{in} is injected into the system. The arrow drawn on the interaction port indicates the power flow direction when the dual product of the port variables has a positive sign. Finally, the dynamics equation (2.37) is rewritten for the new port-based representation as follows:

$$\dot{S} = P_{\text{in}} - P_{\text{diss}}. \tag{2.38}$$

Consistently throughout this dissertation, the geometric structure illustrated in Figure 2.4 and the associated energy dynamics equation (2.38) are employed to construct energy-based system models and design energy-aware, stable controllers.

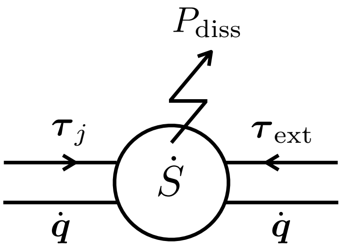

Figure 2.5: Port-based model of a rigid-body robot

2.2.2 Port-Based Modeling of a Tactile Manipulator

In this section, a port-based representation of a flexible-joint[7] manipulator in contact with the environment is developed, along with the associated energy dynamics equations (2.38), following the modeling approach outlined in Section 2.1. As mentioned earlier, modularity is one of the main advantages of port-based modeling. Consequently, the subsystem models involved are derived individually and then interconnected in a power-conservative manner.

Rigid-Body Robot: The energy storage element of a rigid-body robot, similar to any rigid-body object, is associated with two energy types: kinetic energy[8] T and gravitational potential energy U_g. Accordingly, the storage function S becomes

$$S = T + U = \frac{1}{2}\dot{\boldsymbol{q}}^T \boldsymbol{M}(\boldsymbol{q})\dot{\boldsymbol{q}} + g_0 \sum_{i=1}^{n} m_i h_i(\boldsymbol{q}), \tag{2.39}$$

where $g_0 \approx 9.81$ m/s^2 is the gravity acceleration. For the i-th link, $m_i \in \mathbb{R}_{>0}$ is the weight, and $h_i \in \mathbb{R}_{\geq 0}$ is the height of its center of mass. The energy dissipation element is associated with the friction torque, and considering (2.9), the dissipation power becomes

$$P_{\text{diss}} = \dot{\boldsymbol{q}}^T \boldsymbol{\tau}_{\text{fri}}. \tag{2.40}$$

Finally, considering (2.21) and (2.23), the external ports of the rigid-body robot represent its interaction with the joints and the surrounding environment. The associated power is

$$P_{\text{in}} = \dot{\boldsymbol{q}}^T \boldsymbol{\tau}_j + \dot{\boldsymbol{q}}^T \boldsymbol{\tau}_{\text{ext}}. \tag{2.41}$$

---

[7] The port-based model of a flexible-joint manipulator encompasses the rigid-body manipulator model.

[8] Please note that, in this context, without compromising the validity of the approach, the robot velocity was utilized in the derivation of the kinetic energy instead of the generalized momenta vector $\boldsymbol{\rho} = \boldsymbol{M}(\boldsymbol{q})\dot{\boldsymbol{q}}$.

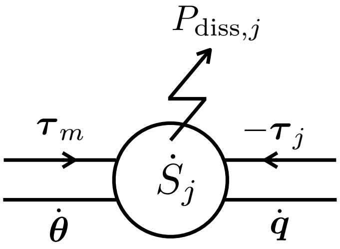

Figure 2.6: Port-based model of a flexible joint

The energy dynamics (2.38) should be consistent with the derived storage function and powers. To confirm this, the time evolution of the storage function S can be analyzed.

$$\begin{aligned}
\dot{S} &= \dot{T} + \dot{U}_g && (2.42)\\
&= \frac{1}{2}\dot{\boldsymbol{q}}^T\dot{\boldsymbol{M}}(\boldsymbol{q})\dot{\boldsymbol{q}} + \dot{\boldsymbol{q}}^T\boldsymbol{M}(\boldsymbol{q})\ddot{\boldsymbol{q}} + \dot{\boldsymbol{q}}^T\frac{\partial U_g}{\partial \boldsymbol{q}} && (2.43)\\
&= \frac{1}{2}\dot{\boldsymbol{q}}^T\dot{\boldsymbol{M}}(\boldsymbol{q})\dot{\boldsymbol{q}} - \dot{\boldsymbol{q}}^T\boldsymbol{C}(\boldsymbol{q},\dot{\boldsymbol{q}})\dot{\boldsymbol{q}} + \dot{\boldsymbol{q}}^T\boldsymbol{\tau} + \dot{\boldsymbol{q}}^T\boldsymbol{\tau}_g && (2.44)\\
&= \underbrace{\frac{1}{2}\dot{\boldsymbol{q}}^T\left(\dot{\boldsymbol{M}}(\boldsymbol{q}) - 2\boldsymbol{C}(\boldsymbol{q},\dot{\boldsymbol{q}})\right)\dot{\boldsymbol{q}}}_{0} + \underbrace{\dot{\boldsymbol{q}}^T\boldsymbol{\tau}_j + \dot{\boldsymbol{q}}^T\boldsymbol{\tau}_{\text{ext}}}_{P_{\text{in}}} - \underbrace{\dot{\boldsymbol{q}}^T\boldsymbol{\tau}_{\text{fri}}}_{P_{\text{diss}}} \underbrace{- \dot{\boldsymbol{q}}^T\boldsymbol{\tau}_g + \dot{\boldsymbol{q}}^T\boldsymbol{\tau}_g}_{0} && (2.45)\\
&= P_{\text{in}} - P_{\text{diss}}. && (2.46)
\end{aligned}$$

Here, (2.7) and (2.10) are used to derive (2.44), and the skew-symmetry of the matrix $\left(\dot{\boldsymbol{M}}(\boldsymbol{q}) - 2\boldsymbol{C}(\boldsymbol{q},\dot{\boldsymbol{q}})\right)$ is considered in (2.45). Moreover, the non-negativity of P_{diss} in (2.46) is observed in (2.9). Figure 2.5 shows the port-based modeling of the rigid-body robot.

Flexible Joint: The storage element of the flexible joint system, as explained in Section 2.1, is associated with the motor inertia $\boldsymbol{B}_m$ and the joint elasticity $\boldsymbol{K}_j$, with the storage function S_j as

$$S_j = \frac{1}{2}\dot{\boldsymbol{\theta}}^T\boldsymbol{B}_m\dot{\boldsymbol{\theta}} + \frac{1}{2}(\boldsymbol{\theta} - \boldsymbol{q})^T\boldsymbol{K}_j(\boldsymbol{\theta} - \boldsymbol{q}). \tag{2.47}$$

The dissipation element corresponds to the joint damping $\boldsymbol{D}_j$, with the dissipation power

$$P_{\text{diss},j} = (\dot{\boldsymbol{\theta}} - \dot{\boldsymbol{q}})^T\boldsymbol{D}_j(\dot{\boldsymbol{\theta}} - \dot{\boldsymbol{q}}) \geq 0. \tag{2.48}$$

Finally, the external ports are connected to the motor and the rigid-body robot with the following input power to the flexible joint.

$$P_{\text{in},j} = \dot{\boldsymbol{\theta}}^T\boldsymbol{\tau}_m - \dot{\boldsymbol{q}}^T\boldsymbol{\tau}_j. \tag{2.49}$$

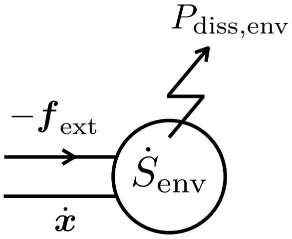

Figure 2.7: Port-based model of a viscoelastic surface

Accordingly, the derivative of the storage function S_j becomes

$$\begin{aligned}
\dot{S}_j &= \dot{\boldsymbol{\theta}}^T \boldsymbol{B}_m \ddot{\boldsymbol{\theta}} + (\dot{\boldsymbol{\theta}} - \dot{\boldsymbol{q}})^T \boldsymbol{K}_j (\boldsymbol{\theta} - \boldsymbol{q}) && (2.50)\\
&= \dot{\boldsymbol{\theta}}^T (\boldsymbol{\tau}_m - \boldsymbol{\tau}_j) + (\dot{\boldsymbol{\theta}} - \dot{\boldsymbol{q}})^T \Big(\boldsymbol{\tau}_j - \boldsymbol{D}_j(\dot{\boldsymbol{\theta}} - \dot{\boldsymbol{q}})\Big) && (2.51)\\
&= \dot{\boldsymbol{\theta}}^T \boldsymbol{\tau}_m \underbrace{- \dot{\boldsymbol{\theta}}^T \boldsymbol{\tau}_j + \dot{\boldsymbol{\theta}}^T \boldsymbol{\tau}_j}_{0} - \dot{\boldsymbol{q}}^T \boldsymbol{\tau}_j - (\dot{\boldsymbol{\theta}} - \dot{\boldsymbol{q}})^T \boldsymbol{D}_j (\dot{\boldsymbol{\theta}} - \dot{\boldsymbol{q}}) && (2.52)\\
&= P_{\text{in},j} - P_{\text{diss},j}, && (2.53)
\end{aligned}$$

where (2.23) and (2.21) are considered to derive (2.51). The port-based modeling of the flexible joint system is illustrated in Figure 2.6.

Contact: Here, a simplified model of a spring-damper system is considered to be used in modeling the contact surface of the environment (e.g., a wall) that is touched by the robot. Let $\boldsymbol{x}_{\text{env}} \in \mathbb{R}^m$ represent the stationary rest pose of the contact surface (i.e., $\dot{\boldsymbol{x}}_{\text{env}} = \boldsymbol{0}$), and $\boldsymbol{K}_{\text{env}}, \boldsymbol{D}_{\text{env}} \in \mathbb{R}^{m \times m}$ denote the stiffness and damping matrices of the surface, respectively. The external wrench applied to the robot is then given by

$$\boldsymbol{f}_{\text{ext}} = \boldsymbol{K}_{\text{env}}(\boldsymbol{x}_{\text{env}} - \boldsymbol{x}) - \boldsymbol{D}_{\text{env}} \dot{\boldsymbol{x}}, \tag{2.54}$$

where $\boldsymbol{x}$ is the robot end-effector pose in the Cartesian space. The storage function of such a contact model is

$$S_{\text{env}} = \frac{1}{2}(\boldsymbol{x}_{\text{env}} - \boldsymbol{x})^T \boldsymbol{K}_{\text{env}} (\boldsymbol{x}_{\text{env}} - \boldsymbol{x}), \tag{2.55}$$

and the dissipation power associated with the contact damping is

$$P_{\text{diss,env}} = \dot{\boldsymbol{x}}^T \boldsymbol{D}_{\text{env}} \dot{\boldsymbol{x}} \geq 0. \tag{2.56}$$

Moreover, the input power injected into the system through its external port is

$$P_{\text{in,env}} = -\dot{\boldsymbol{x}}^T \boldsymbol{f}_{\text{ext}}. \tag{2.57}$$

Finally, the time evolution of the storage function becomes

$$\begin{aligned}
\dot{S}_{\text{env}} &= (\underbrace{\dot{\boldsymbol{x}}_{\text{env}}}_{\boldsymbol{0}} - \dot{\boldsymbol{x}})^T \boldsymbol{K}_{\text{env}} (\boldsymbol{x}_{\text{env}} - \boldsymbol{x}) && (2.58)\\
&= -\dot{\boldsymbol{x}}^T \left(\boldsymbol{f}_{\text{ext}} + \boldsymbol{D}_{\text{env}} \dot{\boldsymbol{x}}\right) && (2.59)\\
&= -\dot{\boldsymbol{x}}^T \boldsymbol{f}_{\text{ext}} - \dot{\boldsymbol{x}}^T \boldsymbol{D}_{\text{env}} \dot{\boldsymbol{x}} && (2.60)\\
&= P_{\text{in,env}} - P_{\text{diss,env}}, && (2.61)
\end{aligned}$$

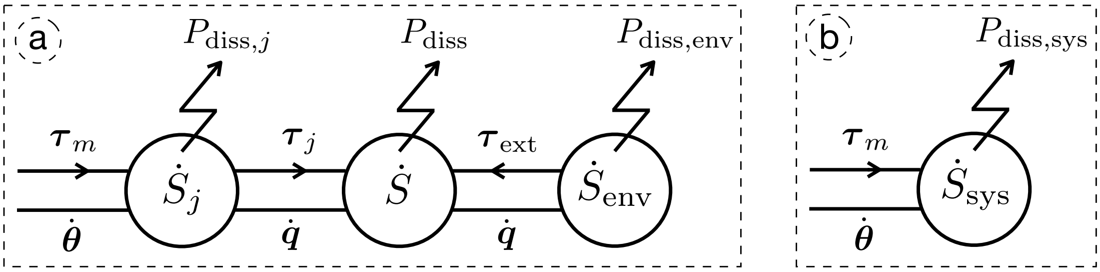

Figure 2.8: Two equivalent port-based models of a flexible-joint robot in contact; note that $(S_j + S + S_{\text{env}})$ in model ⓐ is equal to S_{sys} in model ⓑ.

where (2.54) is taken into account to achieve (2.59). Figure 2.7 depicts the port-based representation of the contact model.

Having derived the three subsystems, the overall system can now be constructed by interconnecting them in a power-conservative manner. To achieve this, the external ports of the subsystems need to be made compatible with each other. For the rigid-body robot model, the existing representation is retained. However, for the flexible joint model, the power flow direction associated with the external port $(\dot{\boldsymbol{q}}, -\boldsymbol{\tau}_j)$ in Figure 2.6 is reversed by changing the port variables notation to $(\dot{\boldsymbol{q}}, \boldsymbol{\tau}_j)$. This results in the new port-based representation without affecting the input power $P_{\text{in,j}}$ in (2.49) and the energy dynamics equation (2.53). Similarly, for the contact model, the external port variables $(\dot{\boldsymbol{x}}, -\boldsymbol{f}_{\text{ext}})$ are replaced with $(\dot{\boldsymbol{q}}, \boldsymbol{\tau}_{\text{ext}})$, resulting in a reversed power flow direction with respect to Figure 2.7. Now, the port-based models of the three subsystems can be merged into a unified model. As shown in Figure 2.8, there is a Jacobian conversion between the external ports of the rigid robot and the contact models. Considering (2.1) and (2.18), this conversion has no effect on the power flow and does not violate the power-conservation constraint.

$$\dot{\boldsymbol{x}}^T \boldsymbol{f}_{\text{ext}} = \dot{\boldsymbol{q}}^T \boldsymbol{J}^T(\boldsymbol{q}) \boldsymbol{f}_{\text{ext}} = \dot{\boldsymbol{q}}^T \boldsymbol{\tau}_{\text{ext}}. \tag{2.62}$$

Finally, the overall system can be represented as a compact port-based model with the storage function S_{sys} defined as

$$S_{\text{sys}} = S_j + S + S_{\text{env}}. \tag{2.63}$$

Taking into account the equations (2.41), (2.46), (2.49), (2.53), (2.57), (2.61) and (2.62), the time evolution of the storage function S_{sys} becomes

$$\begin{aligned} \dot{S}_{\text{sys}} &= \dot{S}_j + \dot{S} + \dot{S}_{\text{env}} && (2.64)\\ &= P_{\text{in},j} + P_{\text{in}} + P_{\text{in,env}} - P_{\text{diss},j} - P_{\text{diss}} - P_{\text{diss,env}} && (2.65)\\ &= \dot{\boldsymbol{\theta}}^T \boldsymbol{\tau}_m \underbrace{- \dot{\boldsymbol{q}}^T \boldsymbol{\tau}_j + \dot{\boldsymbol{q}}^T \boldsymbol{\tau}_j}_{0} + \underbrace{\dot{\boldsymbol{q}}^T \boldsymbol{\tau}_{\text{ext}} - \dot{\boldsymbol{q}}^T \boldsymbol{\tau}_{\text{ext}}}_{0} - (P_{\text{diss},j} + P_{\text{diss}} + P_{\text{diss,env}}). && (2.66) \end{aligned}$$

Now, considering $P_{\text{in,sys}}$ and $P_{\text{diss,sys}}$ as the input power and dissipation power of the overall system, respectively, and defining them as

$$\begin{aligned} P_{\text{in,sys}} &= \dot{\boldsymbol{\theta}}^T \boldsymbol{\tau}_m, && (2.67)\\ P_{\text{diss,sys}} &= P_{\text{diss},j} + P_{\text{diss}} + P_{\text{diss,env}}, && (2.68) \end{aligned}$$

the energy dynamics equation for the compact port-based model of a flexible-joint manipulator in contact becomes

$$\dot{S}_{\text{sys}} = P_{\text{in,sys}} - P_{\text{diss,sys}}. \tag{2.69}$$

Its schematic representation is also depicted in Figure 2.7. The interpretation of such a model is as follows: The input power $\dot{\boldsymbol{\theta}}^T \boldsymbol{\tau}_m$ coming from the motors is partially dissipated due to the damping effects of the flexible joints and the contact surface, along with robot friction. The remaining power is used to alter the energy levels stored as kinetic energy in the motor and the links, gravitational energy in the links, and elastic energy in the flexible joints and the contact surface. This provides a comprehensive view of the power flow and energy transformations within the interconnected system.

2.3 Stabilization via Passivity-Based Control

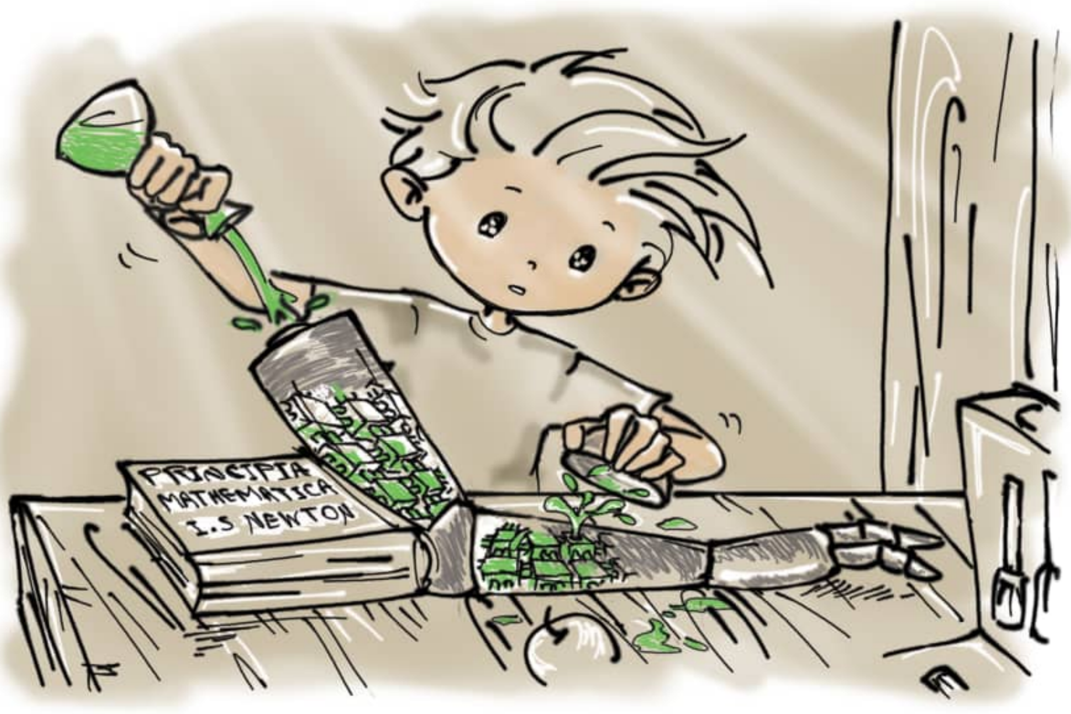

Energy, a fundamental element in the port-based modeling approach, offers the opportunity to investigate system stability through an intuitive yet powerful method—passivity analysis. This section introduces the concept of passivity and its relation to the well-established Lyapunov stability analysis. Additionally, an enhanced formulation of the well-known virtual energy tanks is introduced to ensure stability in non-passive systems.

2.3.1 Passivity Analysis

Consider a system with the state variable $\boldsymbol{x}_s \in \mathbb{R}^k$, and the state space model

$$\dot{\boldsymbol{x}}_s = \boldsymbol{h}_{s,1}(\boldsymbol{x}_s, \boldsymbol{u}_s), \tag{2.70}$$

$$\boldsymbol{y}_s = \boldsymbol{h}_{s,2}(\boldsymbol{x}_s, \boldsymbol{u}_s), \tag{2.71}$$

where $\boldsymbol{u}_s, \boldsymbol{y}_s \in \mathbb{R}^s$ are the system input and output, respectively. The system is said to be *passive* with respect to the pair $(\boldsymbol{u}_s, \boldsymbol{y}_s)$, if there exists a continuously differentiable positive semi-definite so-called *storage function* $S : \mathbb{R}^k \rightarrow \mathbb{R}_{\geq 0}$ such that for all inputs $\boldsymbol{u}_s(t = \sigma)$, with $\sigma \in \mathbb{R}_{>0}$, and for all initial states $\boldsymbol{x}_s(t = 0)$, the following holds [274].

$$S(\boldsymbol{x}_s(\sigma)) - S(\boldsymbol{x}_s(0)) \leq \int_0^\sigma \boldsymbol{y}_s^T(t)\boldsymbol{u}_s(t)dt. \tag{2.72}$$

Thus, considering (2.72), to establish the passivity of the system (2.70)–(2.71) with respect to the pair $(\boldsymbol{u}_s, \boldsymbol{y}_s)$, it is imperative to identify an appropriate storage function $S(\boldsymbol{x}_s)$ such that

$$\forall(\boldsymbol{x}_s, \boldsymbol{u}_s), \qquad \dot{S}(\boldsymbol{x}_s) \leq \boldsymbol{u}_s^T \boldsymbol{y}_s. \tag{2.73}$$

Remark: For a rigid-body robot, the system state can be chosen as $\boldsymbol{x}_s = [\dot{\boldsymbol{q}}^T, \boldsymbol{q}^T]^T$. Accordingly, considering (2.7) and (2.8), by assigning $\boldsymbol{u}_s = \boldsymbol{\tau}_m + \boldsymbol{\tau}_{\text{ext}}$ and $\boldsymbol{y}_s = \dot{\boldsymbol{q}}$, the system dynamics equations (2.70) and (2.71) can be combined into the following representation [325]:

$$\begin{bmatrix} \dot{\boldsymbol{x}}_s \\ \boldsymbol{y}_s \end{bmatrix} = \boldsymbol{H}_s(\boldsymbol{x}_s) \begin{bmatrix} \boldsymbol{x}_s \\ \boldsymbol{u}_s \end{bmatrix} + \boldsymbol{h}_s(\boldsymbol{x}_s), \tag{2.74}$$

where

$$\boldsymbol{H}_s(\boldsymbol{x}_s) = \begin{bmatrix} -\boldsymbol{M}^{-1}(\boldsymbol{q})\boldsymbol{C}(\boldsymbol{q}, \dot{\boldsymbol{q}}) & \boldsymbol{0}_{n\times n} & \boldsymbol{M}^{-1}(\boldsymbol{q}) \\ \boldsymbol{I}_{n\times n} & \boldsymbol{0}_{n\times n} & \boldsymbol{0}_{n\times n} \\ \boldsymbol{I}_{n\times n} & \boldsymbol{0}_{n\times n} & \boldsymbol{0}_{n\times n} \end{bmatrix}, \tag{2.75}$$

and

$$\boldsymbol{h}_s(\boldsymbol{x}_s) = \begin{bmatrix} -\boldsymbol{M}^{-1}(\boldsymbol{q})\left(\boldsymbol{\tau}_g(\boldsymbol{q}) + \boldsymbol{\tau}_{\text{fri}}(\boldsymbol{q}, \dot{\boldsymbol{q}})\right) \\ \boldsymbol{0}_{n\times 1} \\ \boldsymbol{0}_{n\times 1} \end{bmatrix}. \tag{2.76}$$

Considering the storage function S derived in (2.39) and replacing the input torque $\boldsymbol{\tau}_j$ with $\boldsymbol{\tau}_m$ in the derivation of the storage function's time evolution (2.45), it can be deduced that

$$\dot{S} \leq \boldsymbol{u}_s^T \boldsymbol{y}_s, \tag{2.77}$$

demonstrating the passivity of a rigid-body robot.

Considering the storage function S as the stored energy of a port-Hamiltonian system whose input port variables are $(\boldsymbol{u}_s, \boldsymbol{y}_s)$, i.e., $P_{\text{in}} = \boldsymbol{u}_s^T \boldsymbol{y}_s$, the energy dynamics equation (2.38) simplifies to (2.73). Thus, Figure 2.4 represents a passive system with respect to its input port. The fundamental concepts of port-based modeling introduced in the previous section are also applicable to passivity analysis. For instance, assembling N individual systems with the storage functions $\{S_1, \ldots, S_N\}$, each passive with respect to the input powers $\{P_{\text{in},1}, \ldots, P_{\text{in},N}\}$, results in a new system with the storage function $(\sum_{i=1}^{N} S_i)$, which is passive with respect to the input power $(\sum_{i=1}^{N} P_{\text{in},i})$. In case some input powers cancel each other out, i.e., when $\sum_{i=j}^{M} P_{\text{in},i} = 0$, the overall system becomes passive with respect to fewer input ports. The composite system of a flexible-joint manipulator in contact with a viscoelastic surface, presented in the previous section, is an example of this situation. Considering (2.66), while the flexible joint, the rigid-body robot, and the surface contact each represent a passive system with respect to its individual input port(s), the overall system is also passive, yet with respect to only one input port, i.e., $(\boldsymbol{\tau}_m, \dot{\boldsymbol{\theta}})$. In a more special case, if all input powers cancel each other out, the overall system would not have any input port. Such a system is called an *autonomous* passive system for which, considering (2.72), the overall stored energy $\sum_{i=1}^{N} S_i$ is never larger than the initial energy $\sum_{i=1}^{N} S_i\left(\boldsymbol{x}_i(0)\right)$. In other words, a system is said to be autonomously passive if its storage function always satisfies the following condition:

$$\forall \boldsymbol{x}_s, \qquad \dot{S}(\boldsymbol{x}_s) \leq 0. \tag{2.78}$$

Equivalently, considering (2.73), a system is autonomously passive if the input power to the system is always non-positive.

In passivity-based control design, two aspects should be considered. First, the storage functions should be selected in a way that their minimum values correspond to the states associated with the desired control behavior. Second, the control framework should be designed in such a way that the overall controlled system is guaranteed to be autonomously passive. This ensures that there is no positive input power, causing the storage function to increase. As a result, the system states would not simultaneously diverge from their desired values. While there is no unique solution for finding a suitable storage function that satisfies the first condition, the main challenge arises from the second condition. What if the autonomous passivity of the controlled system is not guaranteed? As discussed in the following section, there are standard approaches to address this problem. Yet, before delving into the next section, it is worthwhile to compare the passivity analysis approach with another standard stability investigation method, i.e., the Lyapunov stability.

Lyapunov Stability vs. Passivity

Consider an autonomous system with the state variable $\boldsymbol{x}_s \in \mathbb{R}^k$, and the *equilibrium point* $\boldsymbol{x}_e \in \mathbb{R}^k$ defined as

$$\dot{\boldsymbol{x}}_s = \boldsymbol{f}_s(\boldsymbol{x}_s), \tag{2.79}$$

$$\boldsymbol{f}_s(\boldsymbol{x}_e) = \boldsymbol{0}. \tag{2.80}$$

This system is said [378] to be *Lyapunov stable* at $\boldsymbol{x}_s = \boldsymbol{x}_e$, if for all $t \in \mathbb{R}_{\geq 0}$

$$\forall \epsilon \in \mathbb{R}_{>0}, \quad \exists \delta \in \mathbb{R}_{>0}, \quad \text{s.t.} \quad \|\boldsymbol{x}_s(0) - \boldsymbol{x}_e\| < \delta \implies \|\boldsymbol{x}_s(t) - \boldsymbol{x}_e\| < \epsilon. \tag{2.81}$$

Moreover, such system is called *asymptotically stable* at $\boldsymbol{x}_s = \boldsymbol{x}_e$, if it is stable, and:

$$\exists \delta \in \mathbb{R}_{>0}, \quad \text{s.t.} \quad \|\boldsymbol{x}_s(0) - \boldsymbol{x}_e\| < \delta \implies \lim_{t\to\infty} \boldsymbol{x}_s(t) = \boldsymbol{x}_e. \tag{2.82}$$

Finally, the system is considered *globally asymptotically stable* if it is asymptotically stable for any initial state $\boldsymbol{x}_s(0)$. Intuitively speaking [379], if the system's initial state $\boldsymbol{x}_s(0)$ is close enough to the equilibrium $\boldsymbol{x}_e$, the Lyapunov stability condition (2.81) implies that it will remain near $\boldsymbol{x}_e$, and the asymptotic stability condition (2.82) implies that it will converge to $\boldsymbol{x}_e$. The global asymptotic stability condition, however, waives the requirement for the initial state to be close to the equilibrium.

The *Lyapunov theorem* enables the verification of system stability without explicitly finding the system solutions. Given a continuously differentiable Lyapunov function defined as $V(\boldsymbol{x}_s) : \mathbb{R}^k \to \mathbb{R}$, with $V(\boldsymbol{x}_e) = 0$ and $V(\boldsymbol{x}_s \neq \boldsymbol{x}_e) > 0$, the system (2.79)-(2.80) is stable, if [378]

$$\forall \boldsymbol{x}_s, \quad \dot{V}(\boldsymbol{x}_s) \leq 0, \tag{2.83}$$

and is asymptotically stable if in addition to (2.83),

$$\forall \boldsymbol{x}_s \backslash \{\boldsymbol{x}_e\}, \quad \dot{V}(\boldsymbol{x}_s) < 0. \tag{2.84}$$

Finally, the system is globally asymptotically stable if, in addition to (2.83) and (2.84), the following condition holds.

$$\lim_{|\boldsymbol{x}_s| \to \infty} V(\boldsymbol{x}_s) = \infty. \tag{2.85}$$

Given a storage function $S(\boldsymbol{x}_s)$ whose minimum value is only at the system equilibrium $\boldsymbol{x}_e$, by setting $\boldsymbol{x}_s = \boldsymbol{x}_s$, the following Lyapunov candidate function can be defined.

$$V_s(\boldsymbol{x}_s) = S(\boldsymbol{x}_s) - S(\boldsymbol{x}_e). \tag{2.86}$$

Function $V_s(\boldsymbol{x}_s)$ is a proper Lyapunov function as $V_s(\boldsymbol{x}_e) = 0$ and $V_s(\boldsymbol{x}_s \neq \boldsymbol{x}_e) > 0$. Its time derivative for a stationary equilibrium state $\boldsymbol{x}_e$ becomes

$$\dot{V}(\boldsymbol{x}_s) = \dot{S}(\boldsymbol{x}_s). \tag{2.87}$$

Considering (2.78), the time derivative of the proposed Lyapunov function is always non-negative. Thus, it can be deduced that an autonomous passive system is Lyapunov stable. Considering (2.38) with $P_{\text{in}} = 0$, in case there is always a non-zero dissipation effect (i.e., $P_{\text{diss}} \neq 0$) for non-equilibrium states, inequality (2.78) becomes a strict inequality. In that scenario, the time derivative of the proposed Lyapunov function consistently remains negative, except for the equilibrium, indicating that an autonomous passive system is asymptotically stable. Finally, if the storage function is defined such that the condition (2.85) holds[9], an autonomous passive system can be assumed to be globally asymptotically stable.

2.3.2 Valve-Based Virtual Energy Tanks

When a system cannot be proven to be autonomously passive, the question arises: How can its passivity be ensured? Consider a passive system with the storage function $S_{\text{sys}} \in \mathbb{R}_{\geq 0}$ such that

$$\dot{S}_{\text{sys}} \leq P_T, \tag{2.88}$$

where $P_T \in \mathbb{R}$ is the power being transferred to the system. Considering (2.78), if $P_T \leq 0$, the system autonomous passivity condition holds. However, for a positive P_T, this is not the case. One way to ensure that the system always remains autonomously passive is to only allow non-negative values of P_T and damp out any positive value. This approach, however, would significantly affect the system's behavior. Another possibility is to allow positive power P_T yet in a limited way. This can be done by attaching a secondary passive system with the storage function $S_T \in \mathbb{R}_{\geq 0}$ such that

$$\dot{S}_T \leq -P_T. \tag{2.89}$$

By defining the storage function $S = S_{\text{sys}} + S_T$ for the combination of these two systems, the following can be deduced considering (2.88) and (2.89).

$$\dot{S} = \dot{S}_{\text{sys}} + \dot{S}_T \leq 0. \tag{2.90}$$

---

[9] This is usually the case due to the common quadratic form of the storage functions, e.g., in (2.39), (2.47), and (2.55).

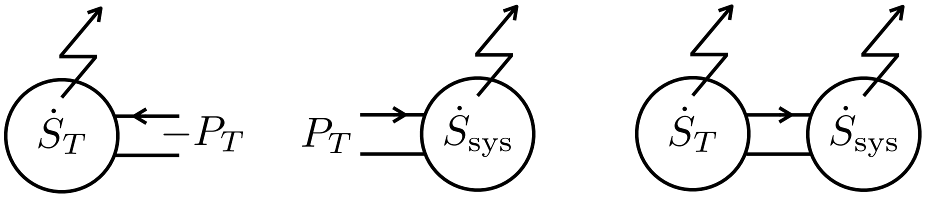

Figure 2.9: From left to right: virtual energy tank, passive system, autonomous passive system with tank augmentation

Therefore, the overall system is autonomously passive; see Figure 2.9. In the literature, the secondary system with the storage function S_T is referred to as a *virtual energy tank*.

The stabilization procedure using the virtual tank augmentation method involves the initial derivation of an appropriate storage function S_{sys} for the system. Subsequently, as it is essential to confirm the non-positivity of its time derivative $\dot{S}_{\text{sys}}$ to ensure passivity, the potentially passivity-violating power P_T that could lead to positive $\dot{S}_{\text{sys}}$ should be identified. Following this, a virtual tank is defined with the storage function S_T, representing the energy within the tank. This limited energy serves to supply the positive power P_T requested by the system, and once the tank energy is depleted, no further positive P_T can be provided.

Remark: A notable limitation of the conventional tank augmentation approach is the sudden reduction of power P_T to zero when the tank energy is fully depleted. Such an abrupt change may lead to inappropriate system behavior in practice. To address this issue, this dissertation introduces an enhancement to virtual energy tanks through the incorporation of valves. This improvement not only prevents sudden changes in input power to the system but also, as discussed in Chapter 5, enables various energy-aware control methods. Therefore, in the following, for better readability, the novel formulation of *Valve-Based Virtual Energy Tanks* is introduced, which differs from standard methods such as [275, 297, 301]. This formulation is further extended in Chapter 5 to encompass a broader range of objectives beyond ensuring stability.

Considering $\boldsymbol{e}_T, \boldsymbol{f}_T \in \mathbb{R}^{N_T}$ as the effort and flow of the tank's external port such that $P_T = \boldsymbol{e}_T^T \boldsymbol{f}_T$, a valve-based virtual energy tank can be augmented to a system by shaping the effort variable via the tank overall valve gain $\gamma_T \in [0, 1]$ such that

$$\boldsymbol{e}'_T = \gamma_T \boldsymbol{e}_T, \tag{2.91}$$

where γ_T is continuously derived as the multiplication of various individual valve gains, i.e.,

$$\gamma_T = \prod_{i \in \Gamma_T} \gamma_i, \qquad \Gamma_T = [\text{low}, \text{up}, \text{diss}, \ldots]. \tag{2.92}$$

Accordingly, the tank energy dynamics becomes

$$\dot{S}_T = -\gamma_T P_T, \tag{2.93}$$

which is consistent with (2.89). In the following, three main types of valve gains are presented. More advanced types are discussed in Section 5.1.

The most important valve gain is γ_{low}, whose role is to ensure that the tank energy is always above its lower limit $S_T^{\mathrm{low}} \in \mathbb{R}_{\geq 0}$. This guarantees the passivity of the tank. The gain value is consistently determined via

$$\gamma_{\mathrm{low}} = \begin{cases} 0 & \text{if } \; S_T \leq S_T^{\mathrm{low}} \quad \wedge \quad 0 < P_T, \\ \frac{1}{2}\left(1 - \cos\left(\frac{S_T - S_T^{\mathrm{low}}}{S_T^{\Delta}}\pi\right)\right) & \text{if } \; S_T^{\mathrm{low}} < S_T \leq S_T^{\Delta} \quad \wedge \quad 0 < P_T, \\ 1 & \text{else,} \end{cases} \tag{2.94}$$

where $S_T^{\Delta} \in \mathbb{R}_{\geq 0}$ is the threshold above the lower limit S_T^{low} from which the valve gain value smoothly reduces to 0.

The purpose of the optional valve gain γ_{up} is to maintain the tank energy below the upper limit $S_T^{\mathrm{up}} \in \mathbb{R}_{\geq 0}$. It is derived as

$$\gamma_{\mathrm{up}} = \begin{cases} 0 & \text{if } \; S_T^{\mathrm{up}} \leq S_T \quad \wedge \quad P_T < 0, \\ 1 & \text{else.} \end{cases} \tag{2.95}$$

Another optional valve gain is γ_{diss}, designed to prevent any increase in the tank energy and thus to enforce a dissipative behavior. The gain value is determined through

$$\gamma_{\mathrm{diss}} = \begin{cases} 0 & \text{if } \; P_T < 0, \\ 1 & \text{else.} \end{cases} \tag{2.96}$$

Throughout the dissertation, to ensure the stability of the proposed control and policy modules, passivity analysis is consistently employed to identify potentially passivity-violating powers. Subsequently, various energy tanks are augmented to guarantee stability, and their effectiveness is thoroughly investigated through numerous experiments.


IPIA
TICA
ON
Wiping
sanding
screwing
filing
welding
carving

3 Passivity-Based Interaction Control

To successfully perform manipulation tasks, a robot must effectively execute commanded values via its controller. In scenarios involving physical interaction, controlling motion alone is insufficient; addressing the interaction wrench is also imperative. However, simultaneously controlling force and motion encounters stability challenges, particularly regarding the reciprocal nature of force and motion spaces. This reciprocity constraint often requires careful planning of force and motion commands, relying on knowledge of the environment model.

To address these challenges, the Unified Force-Impedance Control (UFIC) framework, initially introduced in [344] and subsequently generalized in this dissertation, leverages the concept of passivity to ensure stability, even in scenarios where these constraints are not fully met. The original UFIC formulation was designed primarily for regulation tasks, i.e., when the motion setpoint is stationary. In this chapter, the UFIC is extended to include tracking tasks. Moreover, in the case of flexible-joint robots, the UFIC is formulated in this chapter by incorporating a novel impedance characteristic that considers the influence of joint elasticity on overall stability. Generally, achieving independent control of motion and wrench in the same direction is impractical due to constraints imposed by the interacting environment. For tasks where force and motion commands violate this limitation, a method to determine the dominance of each is crucial. In this context, this chapter introduces a modular compliance adaptation methodology, taking the UFIC framework a step further.

The ability to command force and motion to the robot controller facilitates the formulation of manipulation tasks as force-motion policies. However, what if the robot controller can only accept motion commands? This limitation arises, for example, when the robot is equipped solely with a position controller or an impedance controller, thereby restricting the utilization to motion policies only. To address this challenge, this chapter explores the enhancement of one of the most well-known motion policies, Dynamic Movement Primitive (DMP), with indirect force control capability. This modification, namely Admittance-Coupled Dynamic Movement Primitive (CDMP), enables the utilization of force-motion policies even when the robot controller only accepts motion commands. Finally, the chapter introduces the concept of reference power, which is thoroughly elaborated later in Chapter 5. It demonstrates how reference power can enhance the stabilization process for tactile manipulation tasks through force-motion policies.

3.1 Unified Force-Impedance Control

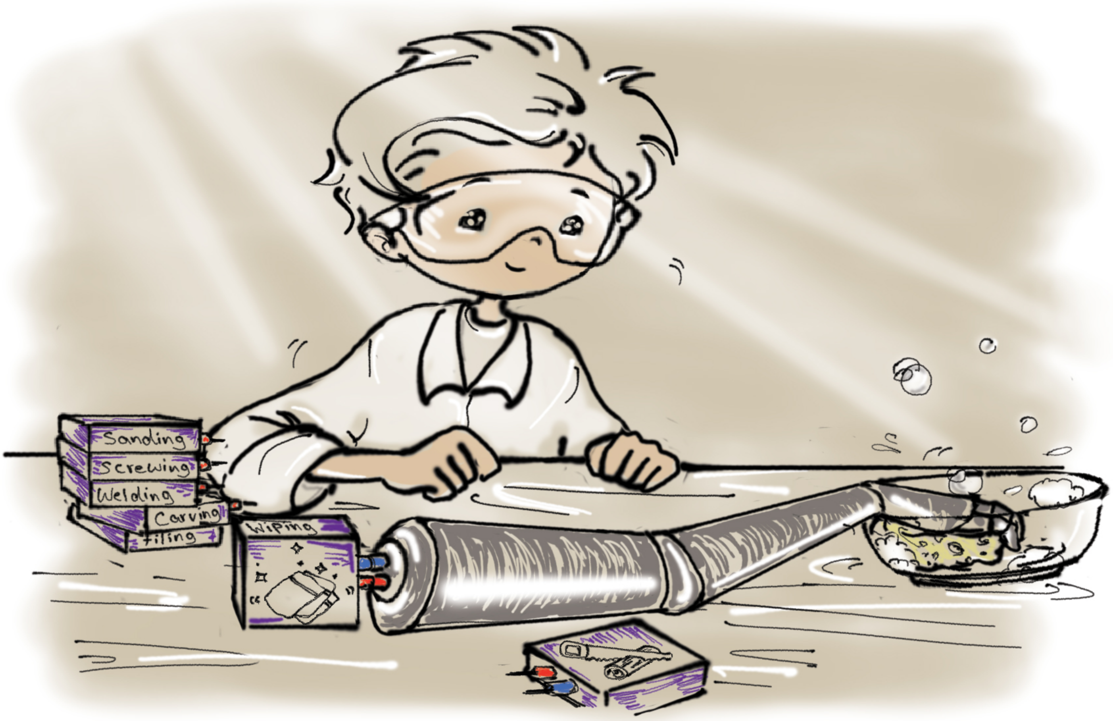

Effectively controlling the physical interaction of a robot with its environment requires addressing both force and motion. Traditionally, simultaneous control of force and motion faces two fundamental challenges: the spaces of force and motion control need to be reciprocal, and the model of the interacting environment should be known precisely. However, real-world scenarios do not always allow these two constraints to be satisfied; see Figure 3.1. The *Unified Force-Impedance Control* (UFIC) can mitigate these constraints using the concept of passivity. In this section, a generalized formulation of UFIC is introduced, which also covers tactile tasks with motion tracking for both rigid-body and flexible-joint robots.

3.1.1 Control Design for Rigid-Body Robots

The UFIC system couples impedance control and force control in a manner that ensures the stability and robustness of the controlled robot. This section presents the involved components and the derivation of UFIC for a rigid-body robot.

Cartesian Impedance Control

For a rigid-body robot with dynamics given by (2.11), it is well-known that to achieve a closed-loop Cartesian impedance behavior with the desired stiffness $\boldsymbol{K}_C \in \mathbb{R}^{m \times m}$ and damping $\boldsymbol{D}_C \in \mathbb{R}^{m \times m}$ with inertia identical[1] to the actual Cartesian robot mass $\boldsymbol{M}_C(\boldsymbol{q})$

---

[1] No inertia shaping is considered here.

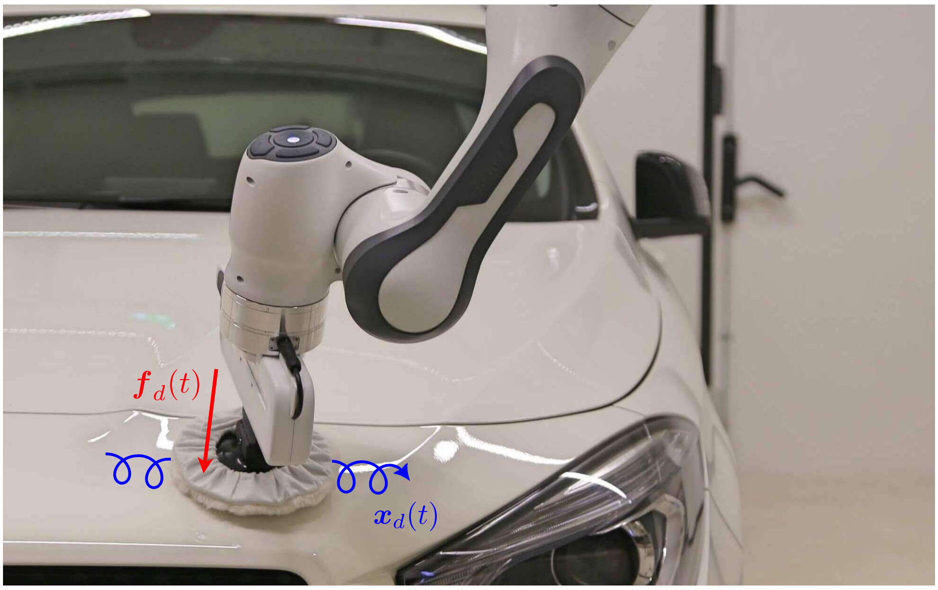

Figure 3.1: Achieving high-performance interaction control over complex, discontinuous, and possibly compliant surfaces necessitates precise yet robust control of both force and motion.

defined in (2.12), the control law is derived as [291]

$$\boldsymbol{\tau}_i = \boldsymbol{J}^T(\boldsymbol{q})\boldsymbol{f}_i, \tag{3.1}$$

$$\boldsymbol{f}_i = \boldsymbol{K}_C\tilde{\boldsymbol{x}} + \boldsymbol{D}_C\dot{\tilde{\boldsymbol{x}}} + \boldsymbol{M}_C(\boldsymbol{q})\ddot{\boldsymbol{x}}_d + \boldsymbol{C}_C(\boldsymbol{q},\dot{\boldsymbol{q}})\dot{\boldsymbol{x}}_d + \boldsymbol{f}_g(\boldsymbol{q}), \tag{3.2}$$

$$\tilde{\boldsymbol{x}} = \boldsymbol{x}_d - \boldsymbol{x}, \tag{3.3}$$

where $\boldsymbol{x}_d \in \mathbb{R}^m$ denotes the differentiable desired Cartesian pose. It is important to note that throughout the dissertation, in order to obtain the rotational component of the error $\tilde{\boldsymbol{x}}$ in (3.3), rotation matrices are employed instead of using Euler angles. Specifically, considering $\boldsymbol{R}_d, \boldsymbol{R} \in \mathbb{R}^{m_r \times m_r}$ as the rotation matrices associated with $\boldsymbol{x}_d$ and $\boldsymbol{x}$ respectively, first the error rotation matrix $\boldsymbol{R}_d\boldsymbol{R}^T$ is identified. Subsequently, the rotational component of the vector $\tilde{\boldsymbol{x}}$ is constructed using the axis-angle representation. For more detailed information, please refer to [378].

In case the desired pose is stationary ($\dot{\boldsymbol{x}}_d = \boldsymbol{0}$), the control law (3.1) reduces to the well-known compliance control law

$$\boldsymbol{\tau}_c = \boldsymbol{J}^T(\boldsymbol{q})\boldsymbol{f}_c, \tag{3.4}$$

$$\boldsymbol{f}_c = \boldsymbol{K}_C\tilde{\boldsymbol{x}} - \boldsymbol{D}_C\dot{\boldsymbol{x}} + \boldsymbol{f}_g(\boldsymbol{q}). \tag{3.5}$$

Force Control

To control the interaction wrench, first, a direct PID force control law with a feedforward term can be defined in the Cartesian space, as follows:

$$\breve{\boldsymbol{f}}_f = \boldsymbol{K}_{f,p}(\boldsymbol{f}_d + \boldsymbol{f}_{\text{ext}}) + \boldsymbol{K}_{f,i}\left(\int_0^t (\boldsymbol{f}_d(\varepsilon) + \boldsymbol{f}_{\text{ext}}(\varepsilon))\, d\varepsilon\right) + \boldsymbol{K}_{f,d}(\dot{\boldsymbol{f}}_d + \dot{\boldsymbol{f}}_{\text{ext}}) + \boldsymbol{f}_d + \boldsymbol{f}_{FF}, \tag{3.6}$$

with $\boldsymbol{f}_d \in \mathbb{R}^m$ as the desired interaction wrench applied by the robot to the environment[2], $\boldsymbol{K}_{f,p}, \boldsymbol{K}_{f,i}, \boldsymbol{K}_{f,d} \in \mathbb{R}^{m\times m}$ being the diagonal positive definite gain matrices and finally $\boldsymbol{f}_{FF} \in \mathbb{R}^m$ as the feedforward term which could be chosen arbitrarily. The control torque can then be derived as

$$\boldsymbol{\tau}_f = \boldsymbol{J}^T(\boldsymbol{q})\boldsymbol{f}_f, \tag{3.7}$$

$$\boldsymbol{f}_f = \boldsymbol{\rho}_f \circ \breve{\boldsymbol{f}}_f. \tag{3.8}$$

Here, $\circ$ represents the element-wise vector multiplication operator, and $\boldsymbol{\rho}_f$ denotes the safety-enhancing shaping function vector, playing a role in deactivating force control components that might otherwise excessively deviate the robot from the setpoint. It is defined as

$$\boldsymbol{\rho}_f = [\rho_{f,t}\ \mathbf{1}_{1\times m_t},\ \rho_{f,r}\ \mathbf{1}_{1\times m_r}]^T, \tag{3.9}$$

where $\rho_{f,t}$ and $\rho_{f,r}$ are associated with the translational and rotational components, respectively. They are defined as smooth functions according to

$$\rho_{f,t} = \begin{cases} 1 & \text{if} \quad 0 \le \frac{\boldsymbol{f}_{d,t}}{\|\boldsymbol{f}_{d,t}\|}\tilde{\boldsymbol{x}}_t, \\ \frac{1}{2}\left(1 + \cos\left(\frac{\|\tilde{\boldsymbol{x}}_t\|}{\delta_{f,t}}\pi\right)\right) & \text{if} \ -\delta_{f,t} \le \frac{\boldsymbol{f}_{d,t}}{\|\boldsymbol{f}_{d,t}\|}\tilde{\boldsymbol{x}}_t < 0, \\ 0 & \text{else.} \end{cases} \tag{3.10}$$

and

$$\rho_{f,r} = \begin{cases} 1 & \text{if} \quad 0 \le \frac{\boldsymbol{f}_{d,r}}{\|\boldsymbol{f}_{d,r}\|}\tilde{\boldsymbol{x}}_r, \\ \frac{1}{2}\left(1 + \cos\left(\frac{\|\tilde{\boldsymbol{x}}_r\|}{\delta_{f,r}}\pi\right)\right) & \text{if} \ -\delta_{f,r} \le \frac{\boldsymbol{f}_{d,r}}{\|\boldsymbol{f}_{d,r}\|}\tilde{\boldsymbol{x}}_r < 0, \\ 0 & \text{else.} \end{cases} \tag{3.11}$$

Here, $\boldsymbol{f}_{d,t}, \tilde{\boldsymbol{x}}_t \in \mathbb{R}^{m_t}$ represent the translational components of the desired wrench and the error vectors $\boldsymbol{f}_d$ and $\tilde{\boldsymbol{x}}$, respectively. Similarly, $\boldsymbol{f}_{d,r}, \tilde{\boldsymbol{x}}_r \in \mathbb{R}^{m_r}$ denote the rotational components of these vectors. Finally, $\delta_{f,t}$ and $\delta_{f,r}$ are the user-defined translational and rotational thresholds, respectively, along which the shaping function smoothly reduces to zero to deactivate the force controller.

Remark: Typically, force control is defined in the end-effector frame. In this case, as elaborated in Section 2.1, the involved signals should also be represented in the end-effector frame as ${}^{\text{ee}}\boldsymbol{f}_d$, ${}^{\text{ee}}\boldsymbol{f}_{\text{ext}}$, ${}^{\text{ee}}\boldsymbol{f}_f$, and ${}^{\text{ee}}\tilde{\boldsymbol{x}}$. Moreover, in the control law (3.7), the Jacobian matrix ${}^{\text{ee}}\boldsymbol{J}(\boldsymbol{q})$ should be used. Please note that such a change in the coordinate frame does not violate the passivity analysis derivations in the following sections.

---

[2] Please note that the direction of the external wrench $\boldsymbol{f}_{\text{ext}}$ is defined to be from the environment to the robot, i.e., opposite to the desired wrench $\boldsymbol{f}_d$.

Unified Force-Impedance Control Before Stabilization

To enable the simultaneous utilization of impedance and force control, the control laws (3.1) and (3.7) can be combined. As a result, the input torque $\boldsymbol{\tau}_m$ in (2.8) becomes

$$\boldsymbol{\tau}_m = \boldsymbol{\tau}_f + \boldsymbol{\tau}_i. \tag{3.12}$$

Considering (2.11), (2.16), (2.17), (2.20), (3.1), (3.2), and (3.7), and neglecting the friction torque $\boldsymbol{\tau}_{\mathrm{fri}}$ in (2.19), applying the control law (3.12) yields the following closed-loop behavior.

$$\boldsymbol{M}_C(\boldsymbol{q})\ddot{\tilde{\boldsymbol{x}}} + \boldsymbol{C}_C(\boldsymbol{q},\dot{\boldsymbol{q}})\dot{\tilde{\boldsymbol{x}}} + \boldsymbol{D}_C\dot{\tilde{\boldsymbol{x}}} + \boldsymbol{K}_C\tilde{\boldsymbol{x}} + \boldsymbol{f}_f + \boldsymbol{f}_{\mathrm{ext}} = \boldsymbol{0}. \tag{3.13}$$

3.1.2 Stabilization

The passivity analysis approach introduced in Section 2.3 is utilized here to investigate stability. For this purpose, a storage function is defined for the controlled robot as

$$S_i = \frac{1}{2}\dot{\tilde{\boldsymbol{x}}}^T\boldsymbol{M}_C(\boldsymbol{q})\dot{\tilde{\boldsymbol{x}}} + \frac{1}{2}\tilde{\boldsymbol{x}}^T\boldsymbol{K}_C\tilde{\boldsymbol{x}}. \tag{3.14}$$

To investigate passivity, the time evolution of S_i is derived as

$$\dot{S}_i = \dot{\tilde{\boldsymbol{x}}}^T\boldsymbol{M}_C(\boldsymbol{q})\ddot{\tilde{\boldsymbol{x}}} + \frac{1}{2}\dot{\tilde{\boldsymbol{x}}}^T\dot{\boldsymbol{M}}_C(\boldsymbol{q},\dot{\boldsymbol{q}})\dot{\tilde{\boldsymbol{x}}} + \dot{\tilde{\boldsymbol{x}}}^T\boldsymbol{K}_C\tilde{\boldsymbol{x}} \tag{3.15}$$

$$= \dot{\tilde{\boldsymbol{x}}}^T\left(-\boldsymbol{f}_{\mathrm{ext}} - \boldsymbol{f}_f - \boldsymbol{C}_C(\boldsymbol{q},\dot{\boldsymbol{q}})\dot{\tilde{\boldsymbol{x}}} - \boldsymbol{D}_C\dot{\tilde{\boldsymbol{x}}} - \cancel{\boldsymbol{K}_C\tilde{\boldsymbol{x}}}\right) + \frac{1}{2}\dot{\tilde{\boldsymbol{x}}}^T\dot{\boldsymbol{M}}_C(\boldsymbol{q},\dot{\boldsymbol{q}})\dot{\tilde{\boldsymbol{x}}} + \cancel{\dot{\tilde{\boldsymbol{x}}}^T\boldsymbol{K}_C\tilde{\boldsymbol{x}}} \tag{3.16}$$

$$= -\dot{\tilde{\boldsymbol{x}}}^T(\boldsymbol{f}_{\mathrm{ext}} + \boldsymbol{f}_f) - \dot{\tilde{\boldsymbol{x}}}^T\boldsymbol{D}_C\dot{\tilde{\boldsymbol{x}}} + \frac{1}{2}\underbrace{\dot{\tilde{\boldsymbol{x}}}^T\left(\dot{\boldsymbol{M}}_C(\boldsymbol{q},\dot{\boldsymbol{q}}) - 2\boldsymbol{C}_C(\boldsymbol{q},\dot{\boldsymbol{q}})\right)\dot{\tilde{\boldsymbol{x}}}}_{=0} \tag{3.17}$$

$$= \dot{\boldsymbol{x}}^T\boldsymbol{f}_{\mathrm{ext}} + \dot{\boldsymbol{x}}^T\boldsymbol{f}_f - \dot{\boldsymbol{x}}_d^T(\boldsymbol{f}_f + \boldsymbol{f}_{\mathrm{ext}}) - \underbrace{\dot{\tilde{\boldsymbol{x}}}^T\boldsymbol{D}_C\dot{\tilde{\boldsymbol{x}}}}_{\geq 0}. \tag{3.18}$$

Note that (3.16) is obtained by considering the closed-loop dynamics (3.13), and the skew-symmetry of the matrix $\dot{\boldsymbol{M}}_C(\boldsymbol{q},\dot{\boldsymbol{q}}) - 2\boldsymbol{C}_C(\boldsymbol{q},\dot{\boldsymbol{q}})$, resulting from (2.15), is taken into account in (3.17). Accordingly, the following assumption can be deduced.

$$\dot{S}_i \leq \dot{\boldsymbol{x}}^T\boldsymbol{f}_{\mathrm{ext}} + \dot{\boldsymbol{x}}^T\boldsymbol{f}_f - \dot{\boldsymbol{x}}_d^T(\boldsymbol{f}_f + \boldsymbol{f}_{\mathrm{ext}}). \tag{3.19}$$

This implies that the rigid-body robot system with control input (3.12) is passive with respect to the pairs $(\boldsymbol{f}_{\mathrm{ext}}, \dot{\boldsymbol{x}})$, $(\boldsymbol{f}_f, \dot{\boldsymbol{x}})$ and $\big(-(\boldsymbol{f}_{\mathrm{ext}} + \boldsymbol{f}_f), \dot{\boldsymbol{x}}_d\big)$. Please note that the shaping function (3.9) or any damping adaptation would not affect the system passivity. Moreover, in the absence of a force controller in (3.12), (3.19) simplifies to

$$\boldsymbol{f}_f = \boldsymbol{0} \implies \dot{S}_i \leq \dot{\boldsymbol{x}}^T\boldsymbol{f}_{\mathrm{ext}} - \dot{\boldsymbol{x}}_d^T\boldsymbol{f}_{\mathrm{ext}}. \tag{3.20}$$

Considering a passive environment with the storage function S_{env} satisfying

$$\dot{S}_{\mathrm{env}} \leq -\dot{\boldsymbol{x}}^T\boldsymbol{f}_{\mathrm{ext}}, \tag{3.21}$$

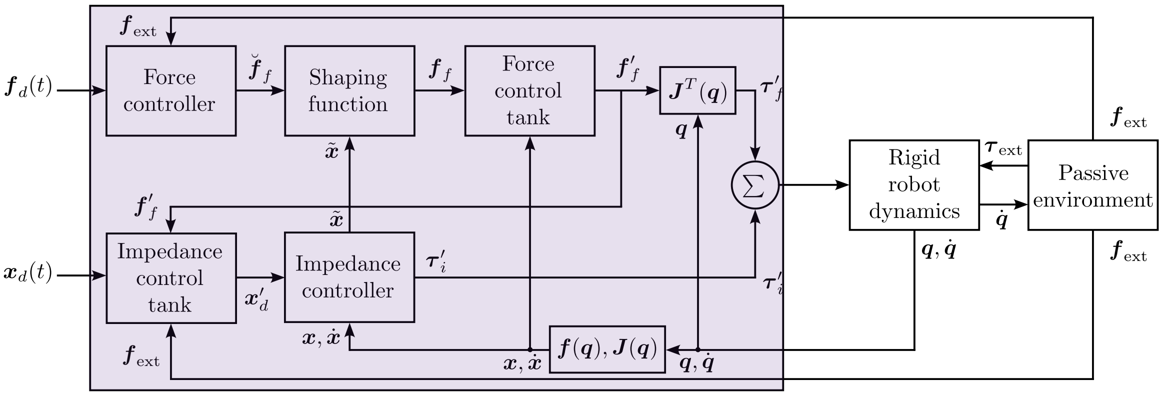

Figure 3.2: Block diagram of the UFIC (highlighted) used for a robot interacting with a passive environment.

the overall storage function for the controlled robot in contact with the environment becomes

$$S_{\text{sys}} = S_{\text{env}} + S_i. \tag{3.22}$$

Given (3.19) and (3.21), the following can be deduced.

$$\dot{S}_{\text{sys}} \leq \cancel{-\dot{\boldsymbol{x}}^T \boldsymbol{f}_{\text{ext}}} + \cancel{\dot{\boldsymbol{x}}^T \boldsymbol{f}_{\text{ext}}} + \dot{\boldsymbol{x}}^T \boldsymbol{f}_f - \dot{\boldsymbol{x}}_d^T (\boldsymbol{f}_f + \boldsymbol{f}_{\text{ext}}) \tag{3.23}$$

$$\leq \underbrace{\dot{\boldsymbol{x}}^T \boldsymbol{f}_f}_{P_{T,f}} \underbrace{- \dot{\boldsymbol{x}}_d^T (\boldsymbol{f}_f + \boldsymbol{f}_{\text{ext}})}_{P_{T,i}}. \tag{3.24}$$

To ensure the autonomous stability of the overall system, two virtual energy tanks can be augmented for the powers $P_{T,f}$ and $P_{T,i}$, with the associated controllable variables $\boldsymbol{f}_f$ and $\dot{\boldsymbol{x}}_d$, corresponding to the force control and impedance control, respectively. The control law (3.12) is then modified to

$$\boldsymbol{\tau}'_m = \boldsymbol{\tau}'_f + \boldsymbol{\tau}'_i, \tag{3.25}$$

with

$$\boldsymbol{\tau}'_f = \boldsymbol{J}^T(\boldsymbol{q}) \boldsymbol{f}'_f, \tag{3.26}$$

$$\boldsymbol{f}'_f = \gamma_{T,f} \ \boldsymbol{f}_f, \tag{3.27}$$

and

$$\boldsymbol{\tau}'_i = \boldsymbol{J}^T(\boldsymbol{q}) \boldsymbol{f}'_i, \tag{3.28}$$

$$\boldsymbol{f}'_i = \boldsymbol{K}_C \tilde{\boldsymbol{x}}' + \boldsymbol{D}_C \dot{\tilde{\boldsymbol{x}}}' + \boldsymbol{M}_C(\boldsymbol{q}) \ddot{\boldsymbol{x}}'_d + \boldsymbol{C}_C(\boldsymbol{q}, \dot{\boldsymbol{q}}) \dot{\boldsymbol{x}}'_d + \boldsymbol{f}_g(\boldsymbol{q}), \tag{3.29}$$

$$\tilde{\boldsymbol{x}}' = \boldsymbol{x}'_d - \boldsymbol{x}, \tag{3.30}$$

in which

$$\dot{\boldsymbol{x}}'_d = \gamma_{T,i} \ \dot{\boldsymbol{x}}_d. \tag{3.31}$$

Here, $\gamma_{T,f}, \gamma_{T,i} \in [0, 1]$ denote the valve gains associated with the force control and impedance control tanks, respectively. For their derivations, please refer to Section 2.3. Through the augmentation of the two virtual energy tanks, the overall system remains stable. The architecture of UFIC is depicted in Figure 3.2.

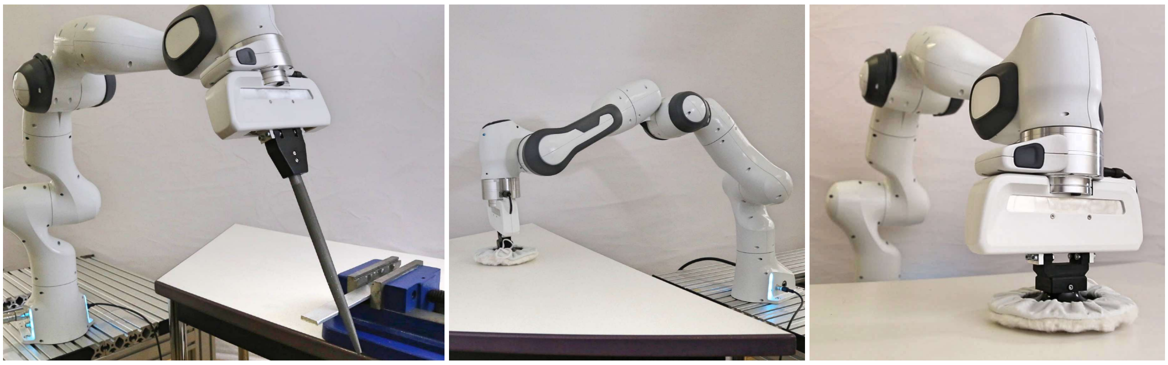

Figure 3.3: Experimental setup with Franka Emika robot.

Remark: Please note that the design of the impedance control tank can include the power associated with the damping effect, and it can be expressed as follows:

$$P_{T,i} = -\dot{\boldsymbol{x}}_d^T(\boldsymbol{f}_f + \boldsymbol{f}_{\text{ext}}) - \dot{\tilde{\boldsymbol{x}}}^T \boldsymbol{D}_C \dot{\tilde{\boldsymbol{x}}}. \tag{3.32}$$

Finally, if a compliance control law (3.5) is used instead of an impedance controller (3.1), the corresponding storage function becomes

$$S_c = \frac{1}{2}\dot{\boldsymbol{x}}^T \boldsymbol{M}_C(\boldsymbol{q})\dot{\boldsymbol{x}} + \frac{1}{2}\tilde{\boldsymbol{x}}^T \boldsymbol{K}_C \tilde{\boldsymbol{x}}, \tag{3.33}$$

with the following time evolution.

$$\begin{aligned}
\dot{S}_c &= \dot{\boldsymbol{x}}^T \boldsymbol{M}_C(\boldsymbol{q})\ddot{\boldsymbol{x}} + \frac{1}{2}\dot{\boldsymbol{x}}^T \dot{\boldsymbol{M}}_C(\boldsymbol{q},\dot{\boldsymbol{q}})\dot{\boldsymbol{x}} + \dot{\tilde{\boldsymbol{x}}}^T \boldsymbol{K}_C \tilde{\boldsymbol{x}} && (3.34)\\
&= \dot{\boldsymbol{x}}^T \left(\boldsymbol{f}_{\text{ext}} + \boldsymbol{f}_f - \boldsymbol{C}_C(\boldsymbol{q},\dot{\boldsymbol{q}})\dot{\boldsymbol{x}} - \boldsymbol{D}_C\dot{\boldsymbol{x}} + \cancel{\boldsymbol{K}_C\tilde{\boldsymbol{x}}}\right) + \frac{1}{2}\dot{\boldsymbol{x}}^T \dot{\boldsymbol{M}}_C(\boldsymbol{q},\dot{\boldsymbol{q}})\dot{\boldsymbol{x}} - \cancel{\dot{\tilde{\boldsymbol{x}}}^T \boldsymbol{K}_C \tilde{\boldsymbol{x}}} && (3.35)\\
&= \dot{\boldsymbol{x}}^T \boldsymbol{f}_{\text{ext}} + \dot{\boldsymbol{x}}^T \boldsymbol{f}_f - \underbrace{\dot{\boldsymbol{x}}^T \boldsymbol{D}_C \dot{\boldsymbol{x}}}_{\geq 0}. && (3.36)
\end{aligned}$$

As a result, no impedance control tank would be required.

3.1.3 Experiments

For experimental validation, six experiments are conducted using a 7-DoF Franka Emika robot; see Figure 3.3. For Experiments 1-5, a wool-covered 3D-printed plate is used to perform a polishing task. In Experiment 6, a metal file is mounted to the end-effector to perform a filing task. The control parameters can be found in Table 3.1. In the force control law (3.6), the external wrench $\boldsymbol{f}_{\text{ext}}$ is estimated via the robot interoceptive momentum-based observer [380], and no feedforward term is used (i.e., $\boldsymbol{f}_{FF} = \boldsymbol{0}$). The force control gains in directions where no force control is intended are set to zero. The Cartesian damping $\boldsymbol{D}_C$ in (3.2) is continuously adapted to achieve critical damping [381]. For all experiments, the tank energy associated with the impedance control tank is denoted by $S_{T,i}$ and is derived according to (3.32). Its upper and lower limits set as $S_{T,i}^{\text{up}} = 20$ J and $S_{T,i}^{\text{low}} = 0.01$ J, respectively. Similarly, the tank energy associated with the force control tank is denoted by $S_{T,f}$. While its upper limit is consistently set to $S_{T,f}^{\text{up}} = 0.20$ J, its lower limit is adjusted to $S_{T,f}^{\text{low}} = 0.01$ J for Experiments 1–4 and 6, and $S_{T,f}^{\text{low}} = 5$ J for Experiment 5.

	f_{d,t_z} [N]	f_{d,r_y} [N.m]	$\boldsymbol{K}_C$ [N/m, N.m/rad]	$\boldsymbol{K}_{f,p}$	$\boldsymbol{K}_{f,d}$ [1/s]	$\boldsymbol{K}_{f,i}$ [s]
Exp. 1	25	—	$\mathrm{diag}([3000, 3000, 100, 300, 300, 300])$	$\boldsymbol{I}_6$	$\boldsymbol{0}_{6\times6}$	$2.5\boldsymbol{I}_6$
Exp. 2	30	—	$\mathrm{diag}([3000, 3000, 100, 300, 300, 300])$	$\boldsymbol{I}_6$	$\boldsymbol{0}_{6\times6}$	$2.5\boldsymbol{I}_6$
Exp. 3	var	—	$\mathrm{diag}([3000, 3000, 100, 300, 300, 300])$	$\boldsymbol{I}_6$	$\boldsymbol{0}_{6\times6}$	$2.5\boldsymbol{I}_6$
Exp. 4	15	—	$\mathrm{diag}([3000, 3000, 10, 0, 50, 300])$	$\boldsymbol{I}_6$	$\boldsymbol{0}_{6\times6}$	$4\boldsymbol{I}_6$
Exp. 5	25	—	$\mathrm{diag}([3000, 3000, 10, 0, 50, 300])$	$\boldsymbol{I}_6$	$\boldsymbol{0}_{6\times6}$	$4\boldsymbol{I}_6$
Exp. 6	—	-1	$\mathrm{diag}([3000, 3000, 3000, 300, 0, 300])$	$\boldsymbol{I}_6$	$\boldsymbol{0}_{6\times6}$	$2.5\boldsymbol{I}_6$

Table 3.1: Experimental gains and parameters.

Experiment 1: Controlling Force and Motion During Polishing

In the initial experiment, the objective is to regulate the normal force exerted on the surface while performing circular motions upon it. Figure 3.4 depicts the experiment results.

In stage ①, the contact is established using only impedance control. In stage ②, UFIC is activated to apply a 25 N force while the motion setpoint remains stationary. In stage ③, the desired pose follows a circular motion, and thus, the robot starts to move on the surface to perform the polishing task. Due to the low effective velocity in the z-direction, the change in force control tank energy is negligible. However, the energy in the impedance control tank increases due to the damping effect of the impedance controller according to (3.32).

In stage ④, the energy level of the impedance control tank reaches its upper limit, and thus, the corresponding tank valve $\gamma_{\mathrm{up},i}$ changes to zero according to (2.95). As can be seen in Figure 3.4, this does not affect the behavior of the robot. Overall, the task is executed accurately and robustly. During the dynamic polishing motion, the force control error remains approximately 1 N.

Experiment 2: Contact Loss Handling by the Shaping Function

To demonstrate how the force control shaping function (3.9) handles unexpected contact loss, the motion command is intentionally set so that the robot moves to the edge of the table, as shown in Figure 3.6. In stage ① (corresponding to ⓐ and ⓑ in Figure 3.6), the robot applies a desired force to the surface while moving in the x-direction. In stage ② (corresponding to ⓒ or ⓓ in Figure 3.6), contact is lost.

The experiment is conducted with two parameterizations. In the first case (corresponding to ⓒ in Figure 3.6), the shaping function is activated with $\delta_{f,t} = 0.05$ m. As observed in Figure 3.5, immediately after the contact is lost, $\rho_{f,t}$ smoothly decreases from 1 to 0. Despite the force error ramping up to ≈ 30 N, the system does not exhibit abrupt motion, and the robot position x_{t_x} comes to a halt. This slight movement in the direction of the desired force leads to a small energy drop for the force controller tank.

In the second case (corresponding to ⓒ in Figure 3.6), no shaping function is present. Consequently, when contact is lost, the effect of the force controller in the z-direction is much more significant than the impedance control due to its low stiffness. As a result, the robot accelerates in the direction of the commanded force. Due to such high acceleration,

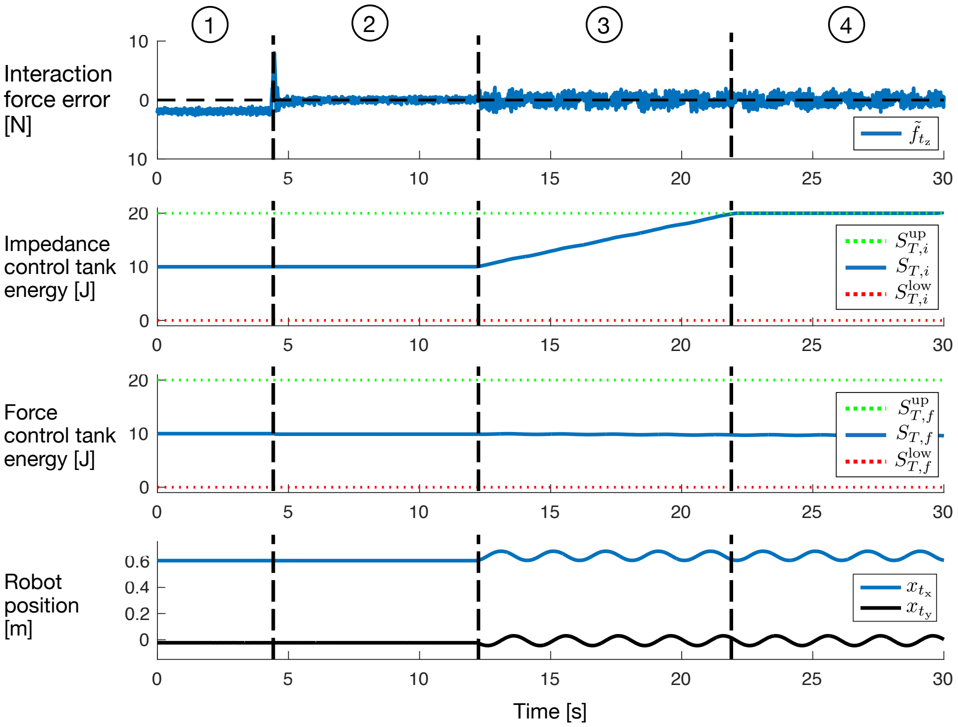

Figure 3.4: Experiment 1 – Force error, tank energy, and robot position during a polishing task.

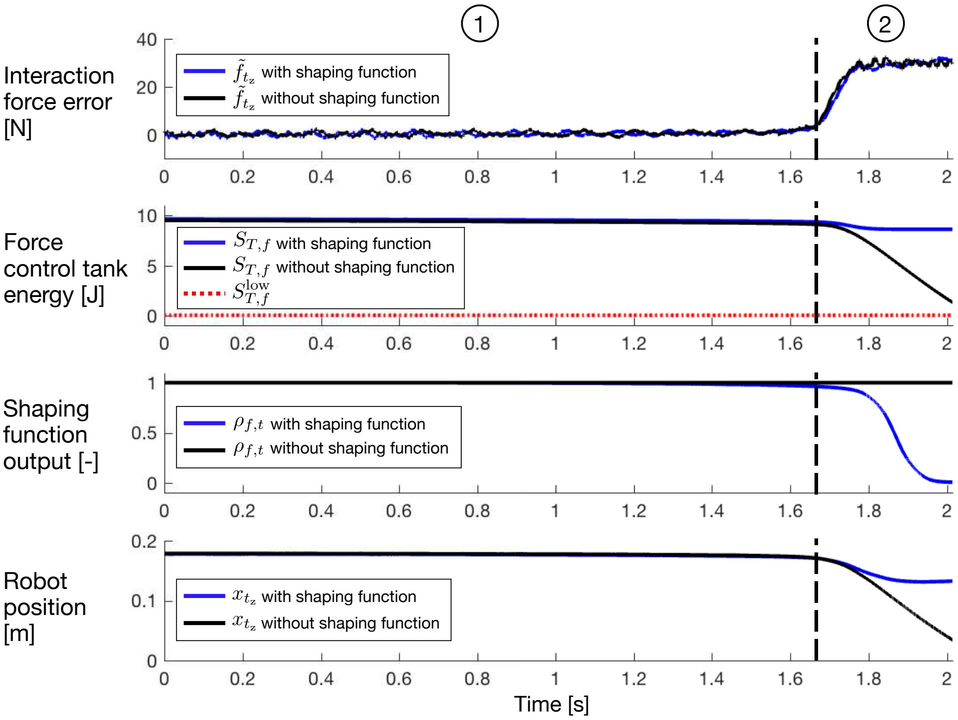

Figure 3.5: Experiment 2 – The robot exhibits two distinct behaviors during contact loss, depending on the presence of the force controller's shaping function.

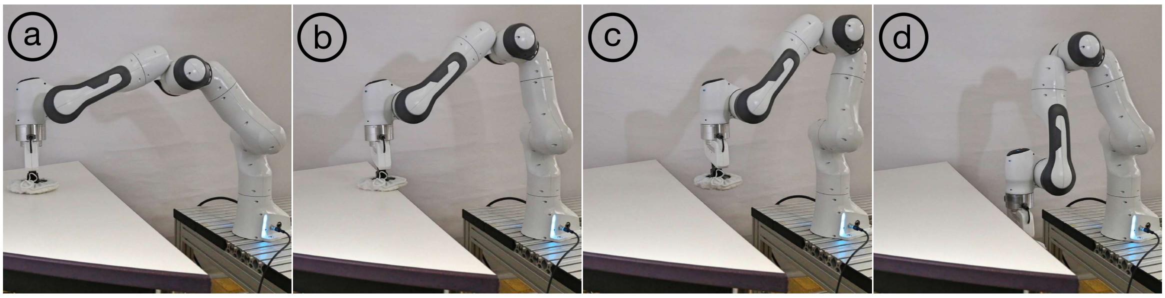

Figure 3.6: Experiment 2 – The robot loses contact when moving beyond the edge of the table.

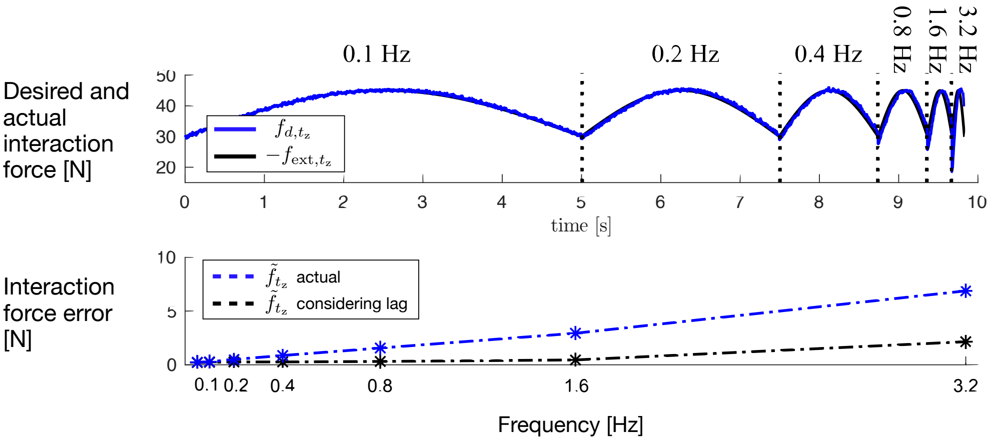

Figure 3.7: Experiment 3 – Force tracking performance at various frequencies, considering the time lag between the actual and desired values.

the tank energy depletes toward the lower limit. This undesirable and dangerous behavior can be mitigated by a well-tuned shaping function.

Experiment 3: Force Tracking

To experimentally assess the force tracking bandwidth, a sinusoidal trajectory with increasing frequency is utilized as a desired force while maintaining the impedance controller setpoint constant. Figure 3.7 (upper) illustrates the tracking behavior for half a period of a sine wave at different frequencies. This time-domain plot is constructed from the concatenation of results from different experiments after several periods for each experiment. Figure 3.7 (lower) presents the mean absolute error measured for different frequencies, with and without considering the phase lag. High tracking accuracy can be achieved up to 3.2 Hz. However, for frequencies beyond the mechanical system bandwidth, the phase lag starts causing significant tracking errors.

Experiment 4: Controlling Force and Motion Under Heavy Disturbance

To demonstrate how a robot equipped with UFIC can robustly adapt to an unknown environment even under unexpected heavy disturbances and contact loss, a seesaw setup is

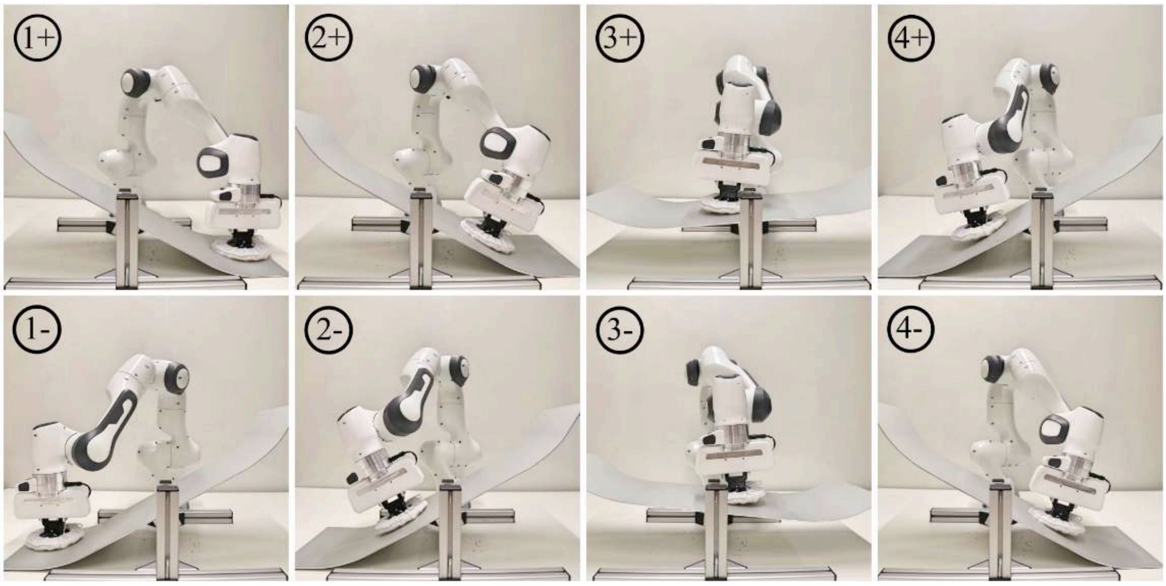

Figure 3.8: Experiment 4 and 5 – The orientation of the robot adapts according to the surface inclination due to the low rotational stiffness of the impedance control.

utilized; see Figure 3.8. The environment is neither modeled nor is there a vision system or other external sensors to monitor the seesaw inclination. Similar to the first experiment, the task goal is to polish a surface at a constant normal force; however, in this experiment, the surface is not always horizontal.

To handle the disturbances associated with the seesaw inclination changes, the impedance control task is defined in the robot base frame, while the force control task is defined in the robot end-effector frame. Additionally, the rotational stiffness of the impedance control is set to zero (see Table 3.1) to let the end-effector—and thus the polishing plate—passively align with the surface. Consequently, while the impedance controller moves the robot along the table, the force controller applies a perpendicular wrench to the seesaw surface.

Figure 3.9 depicts the experiment results. The robot starts from an initial position ⓪ and initiates sinusoidal motion in the x-direction and linear motion in the y-direction. The initial setpoint is set to be slightly below the table surface. During the motion ①–②, the end-effector pose swiftly adjusts to the inclination of the seesaw, while the robot maintains a perpendicular force on the seesaw surface. After crossing the unknown natural equilibrium point of the seesaw, it tilts abruptly ③, and the robot needs to regulate the force again. A momentary force deviation occurs due to the absence of a counterforce, but it is quickly resolved after contact is established in ④.

Experiment 5: The Influence of Energy Tank Limits

To illustrate the effect of a tank with insufficient energy, the previous experiment is conducted multiple times in a more dynamic setting. Three modifications are introduced: the lower tank limit is increased from 0 J to 5 J, the desired velocity in the y-direction is higher than before, and a higher force is commanded, resulting in more energy drained during the

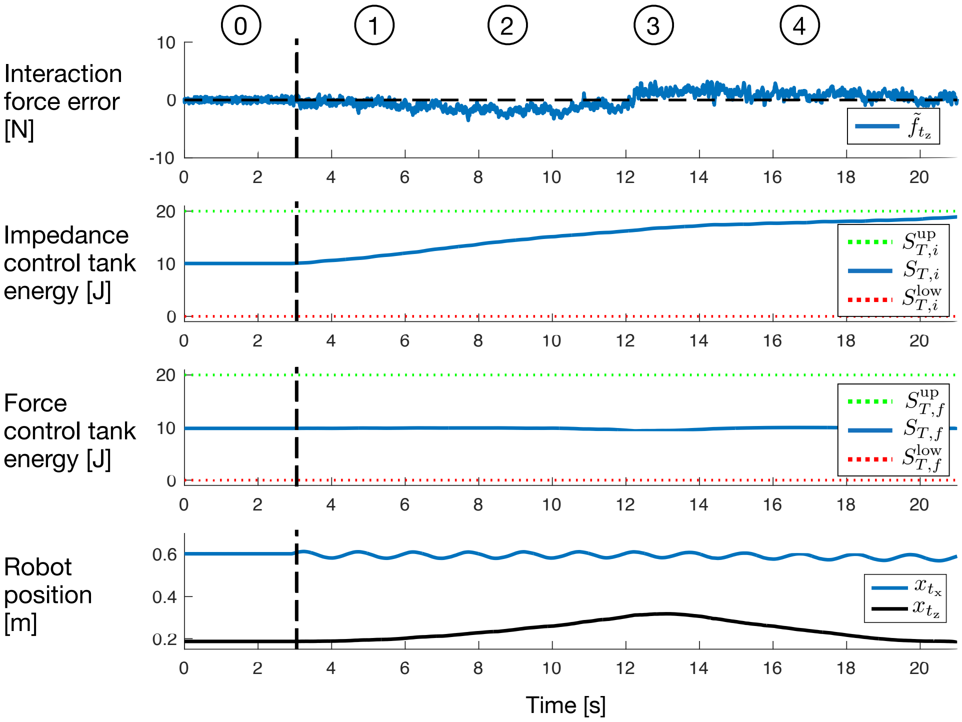

Figure 3.9: Experiment 4 – The impact of disturbances induced by a changeable contact surface, i.e., an aluminum seesaw.

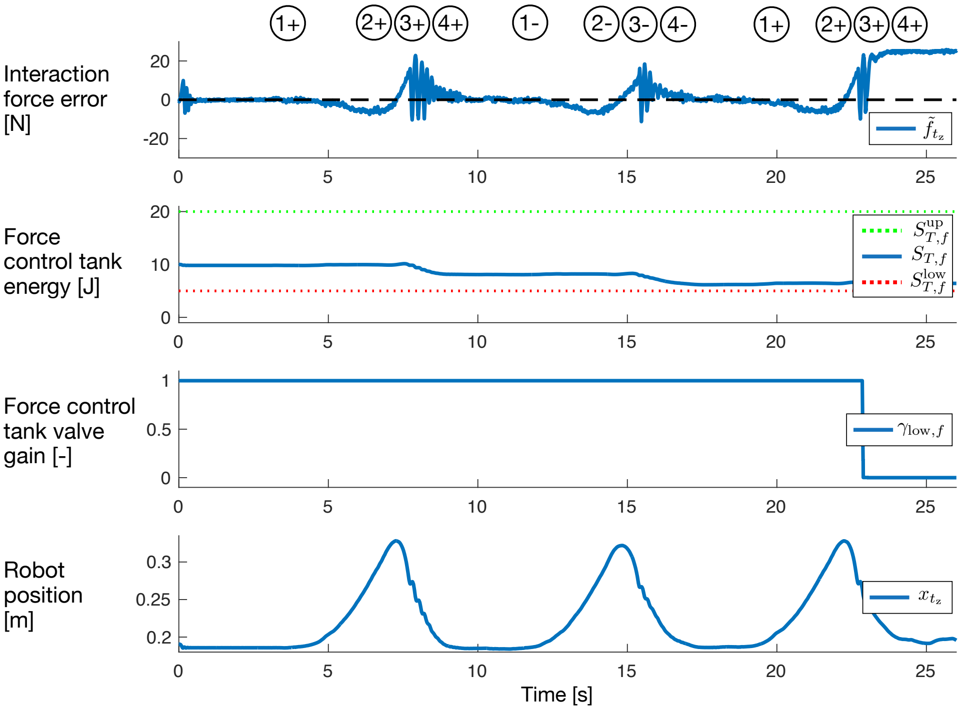

Figure 3.10: Experiment 5 – Several iterations of Experiment 4 in a more dynamic setting, incorporating more conservative tank limits.

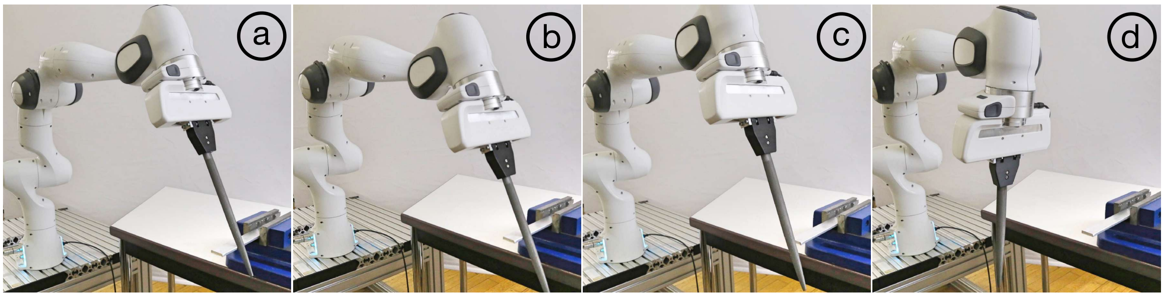

Figure 3.11: Experiment 6 – Contact is lost as the robot moves beyond the edge of the metal piece.

experiment. Examining Figure 3.10, it is evident that during the third iteration around $t \approx 23$ s, the force controller tank energy is depleted. This leads $\gamma_{\mathrm{low},f}$ to switch from 1 to 0. Hence, the force controller is deactivated, and the force error reaches 25 N.

In practical scenarios where force control is applied without solid contact, unintended robot motion in the direction of the desired wrench may occur. Through tank augmentation, the associated energy and potentially hazardous motion can be constrained. This is particularly crucial in situations involving contact loss and without a well-tuned shaping function. Failing to restrict the resulting robot acceleration could lead to an unsafe impact. The same rationale applies to the impedance control tank, as penetration of the desired trajectory into a contact may generate a significant interaction wrench, posing a potential hazard to both the robot and its environment. As demonstrated in this experiment, the tank effectively prevents such occurrences.

Experiment 6: Controlling Moment and Motion During Filing

The final experiment focuses on the control of moments. A real-world metal filing application serves as the evaluation task with the desired moment of $\boldsymbol{f}_{d,r_{\mathrm{y}}} = -1$ Nm (see Figure 3.11). Simultaneously, a linear motion in the y-direction and an orthogonal sinusoidal motion along the z-direction are commanded. Consequently, the robot, while regulating the desired moment, moves toward the edge of the metal piece. Both cases with and without an activated shaping function are considered. The shaping function threshold $\delta_{f,r}$ is set to 2°. Figure 3.12 depicts the experiment results.

After losing contact (i.e., stage ③ in Figure 3.12) in the first case (corresponding to ⓒ in Figure 3.11), the shaping function smoothly deactivates the force control. For the second case (corresponding to ⓓ in Figure 3.11), the robot accelerates further around the y-axis, causing an undesired and dangerous situation.

For both experiments, the moment is almost perfectly regulated during stage ①. During the rapid filing process at stage ②, the moment error increases due to dynamic process forces. As the motion in the direction of the desired moment is negligible, the tank energy does not change significantly. When contact is lost in stage ③, the moment error reaches -1 Nm for both cases. While the energy level with the shaping function remains almost constant, energy is consistently drained without the shaping function.

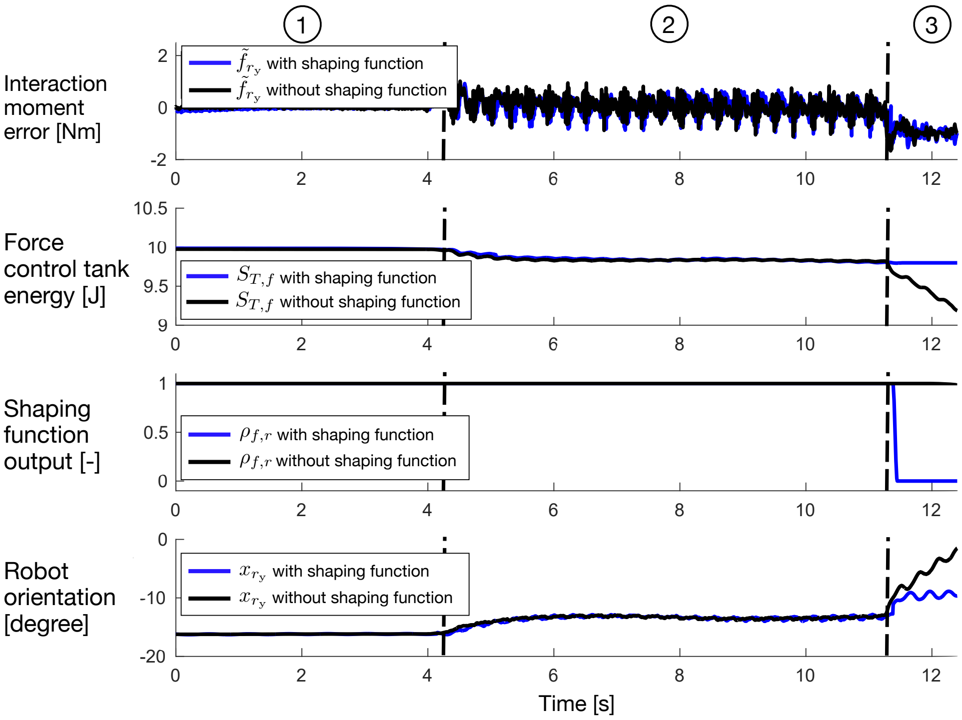

Figure 3.12: Experiment 6 – The robot exhibits two distinct behaviors during contact loss, depending on the presence of the shaping function.

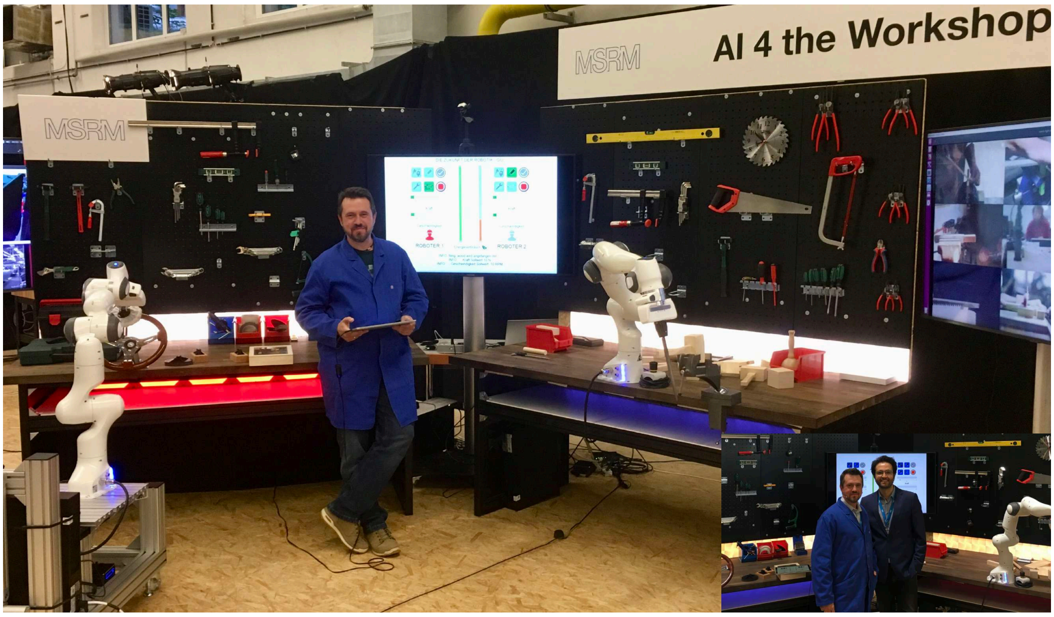

Figure 3.13: Future of Work demonstration setup – a collaborative human-robot environment for performing diverse tactile manipulation tasks.

Figure 3.14: Graphical User Interface for interacting with robots. The magnitude of the desired wrench (Kraft) and velocity (Geschwindigkeit) can be adjusted in real time.

3.1.4 Future of Work Demonstration Setup

The unified force-impedance control (UFIC) framework offers a robust and stable approach to controlling force and motion without the typical limitations associated with force and motion space reciprocity or the need for precise knowledge of the environment model. Noticeably, it is fully integrated into the Robot Control Unit (RCU) of the Franka Emika robots [346]. The extended UFIC, as presented in this section, takes a step further by allowing for tracking tasks (i.e., where $\dot{\boldsymbol{x}}_d \neq \boldsymbol{0}$). It serves as the foundational module of the control architecture developed in this dissertation and has been employed in various research projects associated with this work. To demonstrate its capabilities, a dedicated permanent setup named "Future of Work" has been established at the Chair of Robotics and Systems Intelligence, Technical University of Munich, as illustrated in Figure 3.13.

The setup comprises two Franka Emika robots, one fixed on a table and the other mounted on a mobile base. Its purpose is to showcase a collaborative human-robot environment where robots assist a human operator in various workshop tasks that involve physical interaction with the environment, such as polishing a car door, filing a metal piece, and wiping a steering wheel. Different task-guiding methods are implemented based on the chosen task, including Imitation Learning with Dynamic Movement Primitives, allowing the operator to teach the robot motion. To enhance safety, the speed reduction policy introduced in Section 4.1 is applied to both robots. This involves a vision system that utilizes the OpenPose library [382] and two Intel RealSense D435 RGB-D cameras mounted on the setup to detect the proximity of a human to the robot end-effectors. A Graphic User Interface (GUI) is designed to enable the operator to choose, run, and stop intended tasks, as illustrated in Figure 3.14. The GUI also allows manual adjustment of control variables such as the magnitude of the desired wrench or velocity. Additionally, the energy level of the dedicated virtual tank for each task and the proximity of a human to the robots can be monitored.

The demonstration setup is designed to be intuitive, allowing anyone, even with no technical background, to utilize it. This user-friendly design has been showcased in various exhibitions, including Hannover Messe, one of the world's largest trade fairs dedicated to the

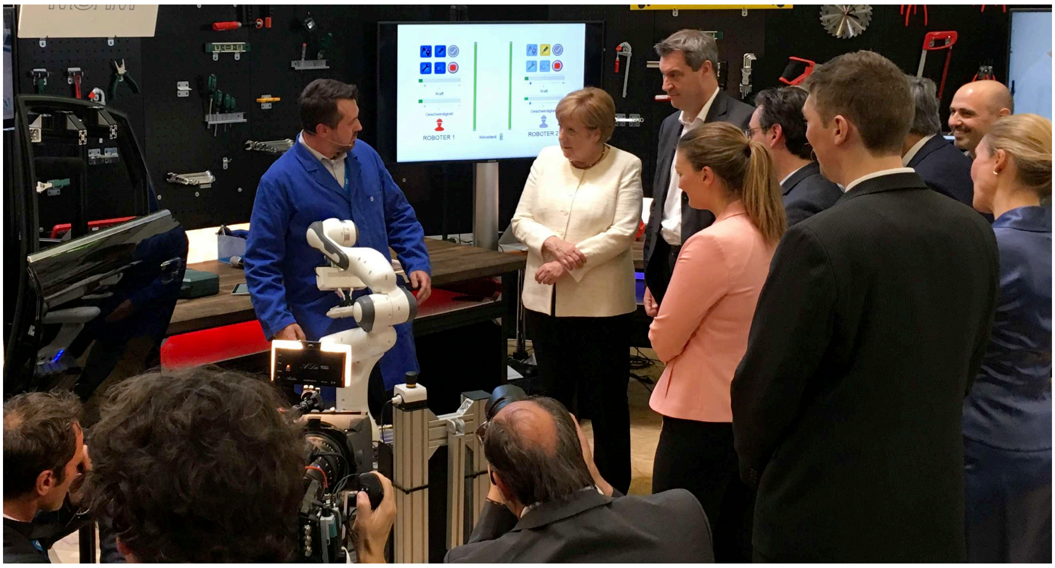

Figure 3.15: A staff craftsman, despite having no background in robotics, demonstrates the intuitive process of guiding the robot to polish a car door.

topic of industry development, and Automatica, the world's leading trade fair for smart automation and robotics. The setup received attention from well-known audiences, as depicted in Figure 3.15.

3.1.5 Control Design and Stabilization for Flexible-Joint Robots

Due to the presence of elasticity in flexible-joint robots, the desired impedance behavior and the corresponding stability proof differ from those applicable to rigid-body robots.

Representation of Joint Parameters in the Cartesian Space

The shaped motor inertia matrix $\boldsymbol{B}_m^*$ and the joint stiffness and shaped damping matrices $\boldsymbol{K}_j, \boldsymbol{D}_j^*$ introduced in Section 2.1, can be represented in the Cartesian space as follows:

$$\boldsymbol{B}_{m,C}(\boldsymbol{q}) := \boldsymbol{J}^{-T}(\boldsymbol{q})\boldsymbol{B}_m^*\boldsymbol{J}^{-1}(\boldsymbol{q}), \tag{3.37}$$

$$\boldsymbol{K}_{j,C}(\boldsymbol{q}) := \boldsymbol{J}^{-T}(\boldsymbol{q})\boldsymbol{K}_j\boldsymbol{J}^{-1}(\boldsymbol{q}), \tag{3.38}$$

$$\boldsymbol{D}_{j,C}(\boldsymbol{q}) := \boldsymbol{J}^{-T}(\boldsymbol{q})\boldsymbol{D}_j^*\boldsymbol{J}^{-1}(\boldsymbol{q}). \tag{3.39}$$

Considering $\boldsymbol{\theta}$ as the motor angle, its corresponding representation in the Cartesian space can be defined as

$$\boldsymbol{x}_\theta := \boldsymbol{J}(\boldsymbol{q})\,(\boldsymbol{\theta} - \boldsymbol{q}) + \boldsymbol{x}. \tag{3.40}$$

Consequently, under the assumption $\dot{\boldsymbol{J}}(\boldsymbol{q}) \approx \boldsymbol{0}$, it follows

$$\dot{\boldsymbol{x}}_\theta \approx \boldsymbol{J}(\boldsymbol{q})\dot{\boldsymbol{\theta}}, \tag{3.41}$$

$$\ddot{\boldsymbol{x}}_\theta \approx \boldsymbol{J}(\boldsymbol{q})\ddot{\boldsymbol{\theta}}. \tag{3.42}$$

As a result, the following relations can be deduced.

$$\boldsymbol{B}_m^* \ddot{\boldsymbol{\theta}} = \boldsymbol{J}^T(\boldsymbol{q}) \left(\boldsymbol{B}_{m,C}(\boldsymbol{q}) \ddot{\boldsymbol{x}}_\theta \right), \tag{3.43}$$

$$\boldsymbol{K}_j \left(\boldsymbol{\theta} - \boldsymbol{q} \right) = \boldsymbol{J}^T(\boldsymbol{q}) \left(\boldsymbol{K}_{j,C}(\boldsymbol{q}) \left(\boldsymbol{x}_\theta - \boldsymbol{x} \right) \right), \tag{3.44}$$

$$\boldsymbol{D}_j^* (\dot{\boldsymbol{\theta}} - \dot{\boldsymbol{q}}) = \boldsymbol{J}^T(\boldsymbol{q}) \left(\boldsymbol{D}_{j,C}(\boldsymbol{q}) \left(\dot{\boldsymbol{x}}_\theta - \dot{\boldsymbol{x}} \right) \right). \tag{3.45}$$

Considering (2.11), (2.16), (2.22) and (2.21), and by neglecting the friction torque $\boldsymbol{\tau}_{\text{fri}}$ in (2.21), the dynamics equation of a flexible-joint robot in the Cartesian space can be represented as

$$\boldsymbol{K}_{j,C}(\boldsymbol{q}) \left(\boldsymbol{x}_\theta - \boldsymbol{x} \right) + \boldsymbol{D}_{j,C}(\boldsymbol{q}) \left(\dot{\boldsymbol{x}}_\theta - \dot{\boldsymbol{x}} \right) = \boldsymbol{M}_C(\boldsymbol{q}) \ddot{\boldsymbol{x}} + \boldsymbol{C}_C(\boldsymbol{q}, \dot{\boldsymbol{q}}) \dot{\boldsymbol{x}} + \boldsymbol{f}_g(\boldsymbol{q}) - \boldsymbol{f}_{\text{ext}}. \tag{3.46}$$

Controller Design

The force control law is similar to the one used for the rigid-body robot (3.8).

$$\boldsymbol{\tau}_{f,j} = \boldsymbol{J}^T(\boldsymbol{q}) \boldsymbol{f}_{f,j}, \tag{3.47}$$

$$\boldsymbol{f}_{f,j} = \boldsymbol{f}_f. \tag{3.48}$$

To derive the impedance control law, an auxiliary variable $\boldsymbol{x}_\psi \in \mathbb{R}^m$ is first defined, which can be continuously obtained by solving the following differential equation.

$$\boldsymbol{K}_{j,C}(\boldsymbol{q}) \left(\boldsymbol{x}_\psi - \boldsymbol{x}_d \right) + \boldsymbol{D}_{j,C}(\boldsymbol{q}) \left(\dot{\boldsymbol{x}}_\psi - \dot{\boldsymbol{x}}_d \right) = \boldsymbol{M}_C(\boldsymbol{q}) \ddot{\boldsymbol{x}}_d + \boldsymbol{C}_C(\boldsymbol{q}, \dot{\boldsymbol{q}}) \dot{\boldsymbol{x}}_d. \tag{3.49}$$

The Cartesian impedance control law for the flexible-joint robots is then defined as

$$\boldsymbol{\tau}_{i,j} = \boldsymbol{J}^T(\boldsymbol{q}) \boldsymbol{f}_{i,j}, \tag{3.50}$$

$$\boldsymbol{f}_{i,j} = \boldsymbol{K}_C \tilde{\boldsymbol{x}} + \boldsymbol{D}_C \dot{\tilde{\boldsymbol{x}}}_\theta + \boldsymbol{M}_C(\boldsymbol{q}) \ddot{\boldsymbol{x}}_d + \boldsymbol{C}_C(\boldsymbol{q}, \dot{\boldsymbol{q}}) \dot{\boldsymbol{x}}_d + \boldsymbol{B}_{m,C}(\boldsymbol{q}) \ddot{\boldsymbol{x}}_\psi + \boldsymbol{f}_g(\boldsymbol{q}). \tag{3.51}$$

Similar to rigid-body robots, the control input $\boldsymbol{\tau}_{m,j}$ in (2.24) can be derived by incorporating (3.47) and (3.50) as

$$\boldsymbol{\tau}_{m,j} = \boldsymbol{\tau}_{f,j} + \boldsymbol{\tau}_{i,j} \tag{3.52}$$

Defining $\tilde{\boldsymbol{x}}_\theta := \boldsymbol{x}_\psi - \boldsymbol{x}_\theta$ the closed-loop dynamics of a flexible-joint robot equipped with the control law (3.52) becomes

$$\boldsymbol{M}_C(\boldsymbol{q}) \ddot{\tilde{\boldsymbol{x}}} + \boldsymbol{C}_C(\boldsymbol{q}, \dot{\boldsymbol{q}}) \dot{\tilde{\boldsymbol{x}}} + \boldsymbol{D}_C \dot{\tilde{\boldsymbol{x}}} + \boldsymbol{K}_C \tilde{\boldsymbol{x}} + \boldsymbol{B}_{m,C} \ddot{\tilde{\boldsymbol{x}}}_\theta + \boldsymbol{f}_f + \boldsymbol{f}_{\text{ext}} = \boldsymbol{0}. \tag{3.53}$$

Control Behavior in the Quasi-Static Scenario

Considering the flexible joint dynamics (2.25) and (2.26) represented in the Cartesian space for the quasi-static case (i.e., for when $\dot{\boldsymbol{\theta}} \approx \dot{\boldsymbol{q}} \approx \dot{\boldsymbol{x}}_\psi \approx \dot{\boldsymbol{x}}_d \approx \boldsymbol{0}$), and given (3.44), (3.48), and (3.51), utilizing the control law (3.52) yields

$$\boldsymbol{K}_{j,C}(\boldsymbol{q}) \left(\boldsymbol{x}_\theta - \boldsymbol{x} \right) \approx \boldsymbol{K}_C \tilde{\boldsymbol{x}} + \boldsymbol{f}_f + \boldsymbol{f}_g(\boldsymbol{q}). \tag{3.54}$$

Moreover, in the quasi-static condition, (3.49) reduces to

$$\boldsymbol{K}_{j,C}(\boldsymbol{q})\left(\boldsymbol{x}_\psi - \boldsymbol{x}_d\right) \approx \boldsymbol{0} \implies \boldsymbol{x}_\psi \approx \boldsymbol{x}_d. \tag{3.55}$$

Therefore, it can be deduced that

$$\begin{aligned}
\dot{\tilde{\boldsymbol{x}}}_\theta^T\left(\boldsymbol{K}_C\tilde{\boldsymbol{x}} + \boldsymbol{f}_f + \boldsymbol{f}_g(\boldsymbol{q})\right) &= \underbrace{\dot{\boldsymbol{x}}_\psi^T}_{\approx\dot{\boldsymbol{x}}_d^T}\left(\boldsymbol{K}_C\tilde{\boldsymbol{x}} + \boldsymbol{f}_f + \boldsymbol{f}_g(\boldsymbol{q})\right) - \dot{\boldsymbol{x}}_\theta^T\left(\underbrace{\boldsymbol{K}_C\tilde{\boldsymbol{x}} + \boldsymbol{f}_f + \boldsymbol{f}_g(\boldsymbol{q})}_{\approx\boldsymbol{K}_{j,C}(\boldsymbol{q})(\boldsymbol{x}_\theta - \boldsymbol{x})}\right)\\
&\approx \dot{\boldsymbol{x}}_d^T\left(\boldsymbol{K}_C\tilde{\boldsymbol{x}} + \boldsymbol{f}_f + \boldsymbol{f}_g(\boldsymbol{q})\right) - \dot{\boldsymbol{x}}_\theta^T\boldsymbol{K}_{j,C}(\boldsymbol{q})\left(\boldsymbol{x}_\theta - \boldsymbol{x}\right)\\
&= \dot{\boldsymbol{x}}_d^T\left(\boldsymbol{K}_C\tilde{\boldsymbol{x}} + \boldsymbol{f}_f + \boldsymbol{f}_g(\boldsymbol{q})\right) - \left(\dot{\boldsymbol{x}}_\theta - \dot{\boldsymbol{x}}\right)^T\boldsymbol{K}_{j,C}(\boldsymbol{q})\left(\boldsymbol{x}_\theta - \boldsymbol{x}\right)\\
&\quad - \dot{\boldsymbol{x}}^T\left(\underbrace{\boldsymbol{K}_{j,C}(\boldsymbol{q})\left(\boldsymbol{x}_\theta - \boldsymbol{x}\right)}_{\approx\boldsymbol{K}_C\tilde{\boldsymbol{x}} + \boldsymbol{f}_g(\boldsymbol{q}) + \boldsymbol{f}_f}\right)\\
&\approx \dot{\tilde{\boldsymbol{x}}}^T\left(\boldsymbol{K}_C\tilde{\boldsymbol{x}} + \boldsymbol{f}_f + \boldsymbol{f}_g(\boldsymbol{q})\right) - \left(\dot{\boldsymbol{x}}_\theta - \dot{\boldsymbol{x}}\right)^T\boldsymbol{K}_{j,C}(\boldsymbol{q})\left(\boldsymbol{x}_\theta - \boldsymbol{x}\right).
\end{aligned} \tag{3.56}$$

Energy Dynamics

By incorporating the gravity vector into the closed-loop dynamics (3.53), the following can be obtained.

$$\begin{aligned}
&\dot{\tilde{\boldsymbol{x}}}_\theta^T\Big(\boldsymbol{M}_C(\boldsymbol{q})\ddot{\tilde{\boldsymbol{x}}} + \boldsymbol{C}_C(\boldsymbol{q}, \dot{\boldsymbol{q}})\dot{\tilde{\boldsymbol{x}}} + \boldsymbol{K}_C\tilde{\boldsymbol{x}} + \boldsymbol{D}_C\dot{\tilde{\boldsymbol{x}}}_\theta + \boldsymbol{B}_{\theta C}(\boldsymbol{q})\ddot{\tilde{\boldsymbol{x}}}_\theta + \boldsymbol{f}_f + \boldsymbol{f}_{\text{ext}} + \boldsymbol{f}_g(\boldsymbol{q})\Big)\\
&\quad = \dot{\tilde{\boldsymbol{x}}}_\theta^T\boldsymbol{f}_g(\boldsymbol{q}).
\end{aligned} \tag{3.57}$$

Considering (3.46) and (3.49), (3.57) results in

$$\begin{aligned}
&\dot{\tilde{\boldsymbol{x}}}_\theta^T\overbrace{\left(\boldsymbol{M}_C(\boldsymbol{q})\ddot{\boldsymbol{x}}_d + \boldsymbol{C}_C(\boldsymbol{q}, \dot{\boldsymbol{q}})\dot{\boldsymbol{x}}_d\right)}^{\boldsymbol{K}_{j,C}(\boldsymbol{q})(\boldsymbol{x}_\psi - \boldsymbol{x}_d) + \boldsymbol{D}_{j,C}(\boldsymbol{q})(\dot{\boldsymbol{x}}_\psi - \dot{\boldsymbol{x}}_d)} - \dot{\tilde{\boldsymbol{x}}}_\theta^T\overbrace{\left(\boldsymbol{M}_C(\boldsymbol{q})\ddot{\boldsymbol{x}} + \boldsymbol{C}_C(\boldsymbol{q}, \dot{\boldsymbol{q}})\dot{\boldsymbol{x}} + \boldsymbol{f}_g(\boldsymbol{q}) - \boldsymbol{f}_{\text{ext}}\right)}^{\boldsymbol{K}_{j,C}(\boldsymbol{q})(\boldsymbol{x}_\theta - \boldsymbol{x}) + \boldsymbol{D}_{j,C}(\boldsymbol{q})(\dot{\boldsymbol{x}}_\theta - \dot{\boldsymbol{x}})}\\
&+ \dot{\tilde{\boldsymbol{x}}}_\theta^T\left(\boldsymbol{K}_C\tilde{\boldsymbol{x}} + \boldsymbol{D}_C\dot{\tilde{\boldsymbol{x}}}_\theta + \boldsymbol{B}_{m,C}(\boldsymbol{q})\ddot{\tilde{\boldsymbol{x}}}_\theta + \boldsymbol{f}_f + \boldsymbol{f}_g(\boldsymbol{q})\right) = \boldsymbol{0}.
\end{aligned} \tag{3.58}$$

Consequently

$$\begin{aligned}
&\dot{\tilde{\boldsymbol{x}}}_\theta^T\left(\boldsymbol{K}_{j,C}(\boldsymbol{q})\left(\tilde{\boldsymbol{x}}_\theta - \tilde{\boldsymbol{x}}\right) + \boldsymbol{D}_{j,C}(\boldsymbol{q})\left(\dot{\tilde{\boldsymbol{x}}}_\theta - \dot{\tilde{\boldsymbol{x}}}\right)\right)\\
&+ \dot{\tilde{\boldsymbol{x}}}_\theta^T\left(\boldsymbol{K}_C\tilde{\boldsymbol{x}} + \boldsymbol{D}_C\dot{\tilde{\boldsymbol{x}}}_\theta + \boldsymbol{B}_{m,C}(\boldsymbol{q})\ddot{\tilde{\boldsymbol{x}}}_\theta + \boldsymbol{f}_f + \boldsymbol{f}_g(\boldsymbol{q})\right) = \boldsymbol{0},
\end{aligned} \tag{3.59}$$

resulting in

$$\begin{aligned}
&\left(\dot{\tilde{\boldsymbol{x}}}_\theta - \dot{\tilde{\boldsymbol{x}}}\right)^T\left(\boldsymbol{K}_{j,C}(\boldsymbol{q})\left(\tilde{\boldsymbol{x}}_\theta - \tilde{\boldsymbol{x}}\right) + \boldsymbol{D}_{j,C}(\boldsymbol{q})\left(\dot{\tilde{\boldsymbol{x}}}_\theta - \dot{\tilde{\boldsymbol{x}}}\right)\right)\\
&+ \dot{\tilde{\boldsymbol{x}}}^T\left(\boldsymbol{K}_{j,C}(\boldsymbol{q})\left(\tilde{\boldsymbol{x}}_\theta - \tilde{\boldsymbol{x}}\right) + \boldsymbol{D}_{j,C}(\boldsymbol{q})\left(\dot{\tilde{\boldsymbol{x}}}_\theta - \dot{\tilde{\boldsymbol{x}}}\right)\right)\\
&+ \dot{\tilde{\boldsymbol{x}}}_\theta^T\left(\boldsymbol{K}_C\tilde{\boldsymbol{x}} + \boldsymbol{D}_C\dot{\tilde{\boldsymbol{x}}}_\theta + \boldsymbol{B}_{m,C}(\boldsymbol{q})\ddot{\tilde{\boldsymbol{x}}}_\theta + \boldsymbol{f}_f + \boldsymbol{f}_g(\boldsymbol{q})\right) = \boldsymbol{0}.
\end{aligned} \tag{3.60}$$

Therefore

$$\begin{aligned}
&\left(\dot{\tilde{\boldsymbol{x}}}_\theta - \dot{\tilde{\boldsymbol{x}}}\right)^T \boldsymbol{K}_{j,C}(\boldsymbol{q}) \left(\tilde{\boldsymbol{x}}_\theta - \tilde{\boldsymbol{x}}\right) + \left(\dot{\tilde{\boldsymbol{x}}}_\theta - \dot{\tilde{\boldsymbol{x}}}\right)^T \boldsymbol{D}_{j,C}(\boldsymbol{q}) \left(\dot{\tilde{\boldsymbol{x}}}_\theta - \dot{\tilde{\boldsymbol{x}}}\right) \\
&+ \dot{\tilde{\boldsymbol{x}}}^T \left(\overbrace{\boldsymbol{K}_{j,C}(\boldsymbol{q}) \left(\boldsymbol{x}_\psi - \boldsymbol{x}_d\right) + \boldsymbol{D}_{j,C}(\boldsymbol{q}) \left(\dot{\boldsymbol{x}}_\psi - \dot{\tilde{\boldsymbol{x}}}_d\right)}^{\boldsymbol{M}_C(\boldsymbol{q})\ddot{\boldsymbol{x}}_d + \boldsymbol{C}_C(\boldsymbol{q},\dot{\boldsymbol{q}})\dot{\boldsymbol{x}}_d}\right) \\
&- \dot{\tilde{\boldsymbol{x}}}^T \left(\underbrace{\boldsymbol{K}_{j,C}(\boldsymbol{q}) \left(\boldsymbol{x}_\theta - \boldsymbol{x}\right) + \boldsymbol{D}_{j,C}(\boldsymbol{q}) \left(\dot{\boldsymbol{x}}_\theta - \dot{\boldsymbol{x}}\right)}_{\boldsymbol{M}_C(\boldsymbol{q})\ddot{\boldsymbol{x}} + \boldsymbol{C}_C(\boldsymbol{q},\dot{\boldsymbol{q}})\dot{\boldsymbol{x}} + \boldsymbol{f}_g(\boldsymbol{q}) - \boldsymbol{f}_{\text{ext}}}\right) \qquad (3.61) \\
&+ \dot{\tilde{\boldsymbol{x}}}_\theta^T \left(\boldsymbol{K}_C\tilde{\boldsymbol{x}} + \boldsymbol{D}_C\dot{\tilde{\boldsymbol{x}}}_\theta + \boldsymbol{B}_{m,C}(\boldsymbol{q})\ddot{\tilde{\boldsymbol{x}}}_\theta + \boldsymbol{f}_f + \boldsymbol{f}_g(\boldsymbol{q})\right) = \boldsymbol{0},
\end{aligned}$$

which after a rearrangement yields

$$\begin{aligned}
&\left(\dot{\tilde{\boldsymbol{x}}}_\theta - \dot{\tilde{\boldsymbol{x}}}\right)^T \boldsymbol{K}_{j,C}(\boldsymbol{q}) \left(\tilde{\boldsymbol{x}}_\theta - \tilde{\boldsymbol{x}}\right) + \dot{\tilde{\boldsymbol{x}}}^T \boldsymbol{M}_C(\boldsymbol{q})\ddot{\tilde{\boldsymbol{x}}} + \dot{\tilde{\boldsymbol{x}}}^T \boldsymbol{C}_C(\boldsymbol{q},\dot{\boldsymbol{q}})\dot{\tilde{\boldsymbol{x}}} - \dot{\tilde{\boldsymbol{x}}}^T \boldsymbol{f}_g(\boldsymbol{q}) + \dot{\tilde{\boldsymbol{x}}}_\theta^T \boldsymbol{B}_{m,C}(\boldsymbol{q})\ddot{\tilde{\boldsymbol{x}}}_\theta \\
&+ \dot{\tilde{\boldsymbol{x}}}_\theta^T \left(\boldsymbol{K}_C\tilde{\boldsymbol{x}} + \boldsymbol{f}_f + \boldsymbol{f}_g(\boldsymbol{q})\right) = -\dot{\tilde{\boldsymbol{x}}}^T \boldsymbol{f}_{\text{ext}} - \left(\dot{\tilde{\boldsymbol{x}}}_\theta - \dot{\tilde{\boldsymbol{x}}}\right)^T \boldsymbol{D}_{j,C}(\boldsymbol{q}) \left(\dot{\tilde{\boldsymbol{x}}}_\theta - \dot{\tilde{\boldsymbol{x}}}\right) - \dot{\tilde{\boldsymbol{x}}}_\theta^T \boldsymbol{D}_C\dot{\tilde{\boldsymbol{x}}}_\theta. \qquad (3.62)
\end{aligned}$$

In the quasi-static mode, (3.56) can be employed. As a result, (3.62) results in

$$\begin{aligned}
&\left(\dot{\tilde{\boldsymbol{x}}}_\theta - \dot{\tilde{\boldsymbol{x}}}\right)^T \boldsymbol{K}_{j,C}(\boldsymbol{q}) \left(\tilde{\boldsymbol{x}}_\theta - \tilde{\boldsymbol{x}}\right) + \dot{\tilde{\boldsymbol{x}}}^T \boldsymbol{M}_C(\boldsymbol{q})\ddot{\tilde{\boldsymbol{x}}} + \dot{\tilde{\boldsymbol{x}}}^T \boldsymbol{C}_C(\boldsymbol{q},\dot{\boldsymbol{q}})\dot{\tilde{\boldsymbol{x}}} - \cancel{\dot{\tilde{\boldsymbol{x}}}^T \boldsymbol{f}_g(\boldsymbol{q})} + \dot{\tilde{\boldsymbol{x}}}_\theta^T \boldsymbol{B}_{m,C}(\boldsymbol{q})\ddot{\tilde{\boldsymbol{x}}}_\theta \\
&+ \dot{\tilde{\boldsymbol{x}}}^T \boldsymbol{K}_C\tilde{\boldsymbol{x}} + \cancel{\dot{\tilde{\boldsymbol{x}}}^T \boldsymbol{f}_g(\boldsymbol{q})} - \left(\dot{\boldsymbol{x}}_\theta - \dot{\boldsymbol{x}}\right)^T \boldsymbol{K}_{j,C}(\boldsymbol{q}) \left(\boldsymbol{x}_\theta - \boldsymbol{x}\right) \\
&= -\dot{\tilde{\boldsymbol{x}}}^T \boldsymbol{f}_f - \dot{\tilde{\boldsymbol{x}}}^T \boldsymbol{f}_{\text{ext}} - \left(\dot{\tilde{\boldsymbol{x}}}_\theta - \dot{\tilde{\boldsymbol{x}}}\right)^T \boldsymbol{D}_{j,C}(\boldsymbol{q}) \left(\dot{\tilde{\boldsymbol{x}}}_\theta - \dot{\tilde{\boldsymbol{x}}}\right) - \dot{\tilde{\boldsymbol{x}}}_\theta^T \boldsymbol{D}_C\dot{\tilde{\boldsymbol{x}}}_\theta. \qquad (3.63)
\end{aligned}$$

Stabilization

The following storage function is proposed for the controlled flexible-joint robot.

$$\begin{aligned}
S_{i,j} =&\frac{1}{2}\left(\tilde{\boldsymbol{x}}_\theta - \tilde{\boldsymbol{x}}\right)^T \boldsymbol{K}_{j,C}(\boldsymbol{q}) \left(\tilde{\boldsymbol{x}}_\theta - \tilde{\boldsymbol{x}}\right) + \frac{1}{2}\dot{\tilde{\boldsymbol{x}}}_\theta^T \boldsymbol{B}_{m,C}(\boldsymbol{q})\dot{\tilde{\boldsymbol{x}}}_\theta - \frac{1}{2}\left(\boldsymbol{x}_\theta - \boldsymbol{x}\right)^T \boldsymbol{K}_{j,C}(\boldsymbol{q}) \left(\boldsymbol{x}_\theta - \boldsymbol{x}\right) \\
&+ \frac{1}{2}\dot{\tilde{\boldsymbol{x}}}^T \boldsymbol{M}_C(\boldsymbol{q})\dot{\tilde{\boldsymbol{x}}} + \frac{1}{2}\tilde{\boldsymbol{x}}^T \boldsymbol{K}_C\tilde{\boldsymbol{x}}. \qquad (3.64)
\end{aligned}$$

Its time evolution can be derived as

$$\begin{aligned}
\dot{S}_{i,j} = &\left(\dot{\tilde{\boldsymbol{x}}}_\theta - \dot{\tilde{\boldsymbol{x}}}\right)^T \boldsymbol{K}_{j,C}(\boldsymbol{q}) \left(\tilde{\boldsymbol{x}}_\theta - \tilde{\boldsymbol{x}}\right) + \dot{\tilde{\boldsymbol{x}}}_\theta^T \boldsymbol{B}_{m,C}(\boldsymbol{q})\ddot{\tilde{\boldsymbol{x}}}_\theta - \left(\dot{\boldsymbol{x}}_\theta - \dot{\boldsymbol{x}}\right)^T \boldsymbol{K}_{j,C}(\boldsymbol{q}) \left(\boldsymbol{x}_\theta - \boldsymbol{x}\right) \\
&+ \dot{\tilde{\boldsymbol{x}}}^T \boldsymbol{M}_C(\boldsymbol{q})\ddot{\tilde{\boldsymbol{x}}} + \underbrace{\dot{\tilde{\boldsymbol{x}}}^T \boldsymbol{C}_C(\boldsymbol{q},\dot{\boldsymbol{q}})\dot{\tilde{\boldsymbol{x}}}}_{\frac{1}{2}\dot{\tilde{\boldsymbol{x}}}^T \dot{\boldsymbol{M}}_C(\boldsymbol{q})\dot{\tilde{\boldsymbol{x}}}} + \dot{\tilde{\boldsymbol{x}}}^T \boldsymbol{K}_C\tilde{\boldsymbol{x}}, \qquad (3.65)
\end{aligned}$$

where the skew-symmetry of the matrix $\dot{\boldsymbol{M}}_C(\boldsymbol{q},\dot{\boldsymbol{q}}) - 2\boldsymbol{C}_C(\boldsymbol{q},\dot{\boldsymbol{q}})$ due to the condition (2.15) was taken into account. Considering (3.63), (3.65) reduces to

$$\dot{S}_{i,j} = \dot{\boldsymbol{x}}^T \boldsymbol{f}_{\text{ext}} + \underbrace{\dot{\boldsymbol{x}}^T \boldsymbol{f}_f}_{P_{T,f}} \underbrace{- \dot{\boldsymbol{x}}_d^T (\boldsymbol{f}_f + \boldsymbol{f}_{\text{ext}})}_{P_{T,i}} - \underbrace{\dot{\tilde{\boldsymbol{x}}}_\theta^T \boldsymbol{D}_C\dot{\tilde{\boldsymbol{x}}}_\theta}_{\geq 0} - \underbrace{\left(\dot{\tilde{\boldsymbol{x}}}_\theta - \dot{\tilde{\boldsymbol{x}}}\right)^T \boldsymbol{D}_{j,C}(\boldsymbol{q}) \left(\dot{\tilde{\boldsymbol{x}}}_\theta - \dot{\tilde{\boldsymbol{x}}}\right)}_{\geq 0}. \qquad (3.66)$$

Similar to the stabilization of the rigid-body robot, by considering a passive environment satisfying (3.21) and augmenting the two energy tanks for the powers $P_{T,f}$ and $P_{T,i}$ yielding (3.27) and (3.31), respectively, the overall system can be assumed to be passive. The port-based model of a flexible-joint robot equipped with a unified force-impedance control is depicted in Figure 3.16.

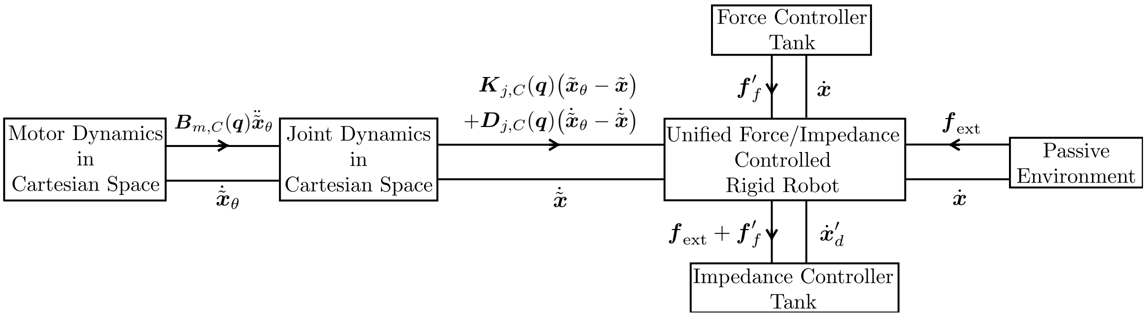

Figure 3.16: Port-based representation of the closed-loop UFIC system for flexible joint robots

Remark: In the passivity proof, rather than assuming the quasi-static condition, the following approximation can be considered.

$$\dot{\tilde{\boldsymbol{x}}}_\theta^T \left(\boldsymbol{K}_C\tilde{\boldsymbol{x}} + \boldsymbol{f}_f + \boldsymbol{f}_g(\boldsymbol{q})\right) = \dot{\tilde{\boldsymbol{x}}}^T \left(\boldsymbol{K}_C\tilde{\boldsymbol{x}} + \boldsymbol{f}_f + \boldsymbol{f}_g(\boldsymbol{q})\right). \tag{3.67}$$

Consequently, an additional energy tank can be augmented for the potential passivity-violating power associated with such an approximation, derived as

$$P_{T,j} = (\dot{\tilde{\boldsymbol{x}}}_\theta - \dot{\tilde{\boldsymbol{x}}})^T \left(\boldsymbol{K}_C\tilde{\boldsymbol{x}} + \boldsymbol{f}_f + \boldsymbol{f}_g(\boldsymbol{q})\right). \tag{3.68}$$

3.2 Unified Force-Impedance Control with Variable Stiffness

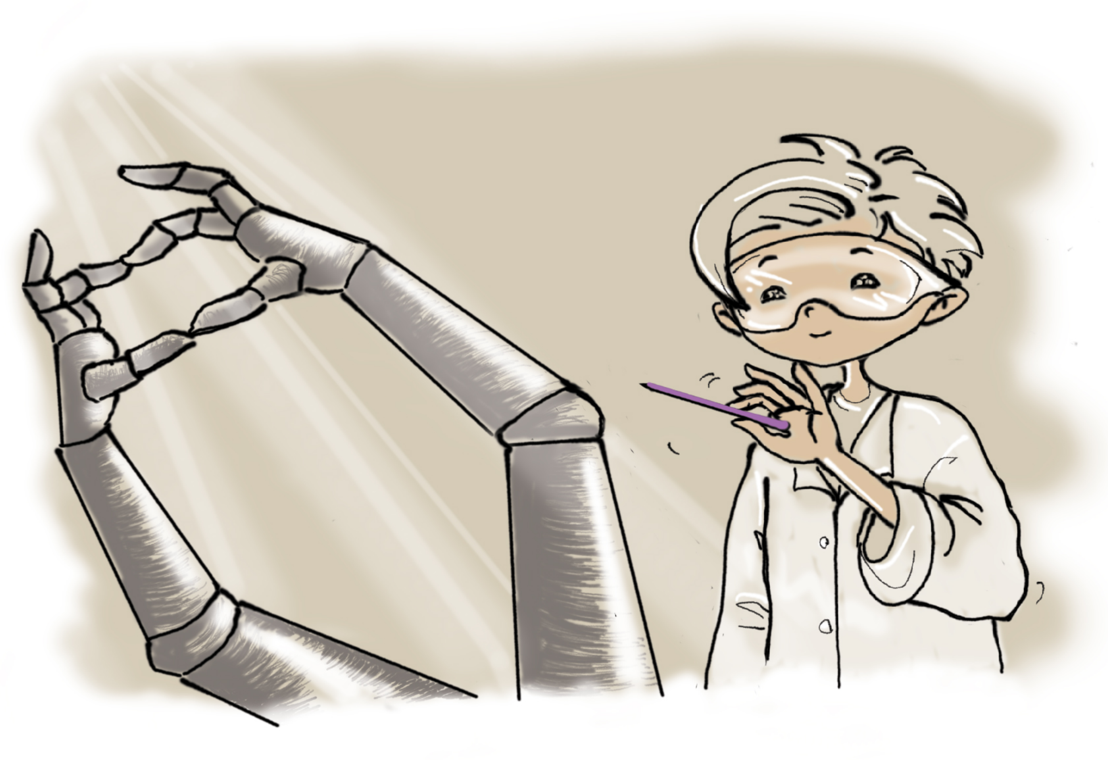

Arbitrarily controlling force and motion in the same direction is typically challenging due to constraints imposed by the impedance characteristics of the interacting environment. However, certain tasks necessitate simultaneous control of both motion and force in a particular direction, such as when a robot must maintain controlled contact with a moving object. In such scenarios, it becomes crucial to determine the dominance of either force control or motion control. One approach involves adjusting the strength of motion control by adapting its compliance. This section introduces a method for the online adaptation of impedance controller stiffness within the unified force-impedance control framework outlined in the previous section.

3.2.1 Direction-Dependent Compliance for Multi-Manual Manipulation

Consider a scenario where a team of robots is tasked with collaboratively transporting an object; see Figure 3.17. To address potential situations where the control of force (for maintaining object grasp) and motion (for moving the object) align in the same direction, this section introduces a compliance adaptation method. The derivation of this method is entirely modular, allowing for the dynamic addition or removal of cooperative arms on the fly. Consequently, the subsequent presentation outlines the control law for a single robot. As demonstrated in the experiments section, implementing this control law independently on each robot enables effective cooperative object manipulation.

Figure 3.17: A multi-manual system manipulating a large box.

Problem Formulation

Consider ${}^{\text{TF}}\boldsymbol{x}_d(t) \in \mathbb{R}^m$ as the desired trajectory defined in a task frame TF for an object being held by n_r robots. Assuming that the location of contact points on the object account for the grasp matrix condition [76] (or similarly the virtual linkage model [86]), each robot is supposed to exert a certain normal force ${}^{\text{ee}}f_{d,t_\text{z}} \in \mathbb{R}_{>0}$ to maintain the grasp. Without loss of generality, the following proposed control algorithm is derived for one n-DoF manipulator whose base frame is rotated by the rotation matrix ${}^{\text{TF}}\boldsymbol{R}$ with respect to the task frame TF. The other cooperative arms also use the same algorithm with their associated rotation matrices, as shown in Figure 3.17 and Figure 3.18.

Assuming a stable contact between the manipulator end-effector and the object, the vector ${}^{\text{ee}}_{\text{ee}}\boldsymbol{p}_{\text{cr}} \in \mathbb{R}^{m_t}$ can be defined in the robot end-effector frame, connecting the end-effector pose $\boldsymbol{x}_{\text{ee}} \in \mathbb{R}^m$ to the object center of rotation pose $\boldsymbol{x} \in \mathbb{R}^m$ (see Figure 3.18). The associated Jacobian matrices are defined according to (2.3)–(2.6), satisfying the following relations.

$$\dot{\boldsymbol{x}}_{\text{ee}} = \boldsymbol{J}_{\text{ee}}(\boldsymbol{q})\dot{\boldsymbol{q}}, \tag{3.69}$$

$$\dot{\boldsymbol{x}} = {}_{\text{ee}}\boldsymbol{J}\ \dot{\boldsymbol{x}}_{\text{ee}}, \tag{3.70}$$

$$\dot{\boldsymbol{x}} = \underbrace{{}_{\text{ee}}\boldsymbol{J}\ \boldsymbol{J}_{\text{ee}}(\boldsymbol{q})}_{\boldsymbol{J}(\boldsymbol{q})}\,\dot{\boldsymbol{q}}. \tag{3.71}$$

Here, $\boldsymbol{q} \in \mathbb{R}^n$ denotes the robot joint angles, and ${}_{\text{ee}}\boldsymbol{J} \in \mathbb{R}^{m\times m}$ is derived as a function of ${}^{\text{ee}}_{\text{ee}}\boldsymbol{p}_{\text{cr}}$ according to (2.6).

Variable Impedance Controller

For the incorporated Cartesian impedance controller, the same control law as (3.1) is used, but with a variable stiffness matrix denoted as $\boldsymbol{K}_{C,v} \in \mathbb{R}^{m\times m}$, as opposed to the constant

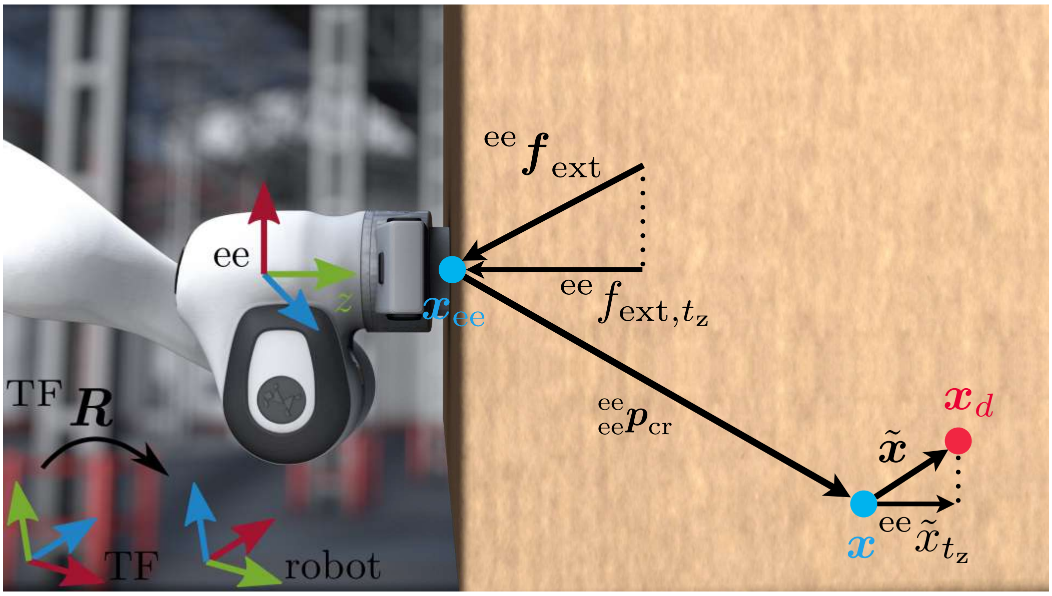

Figure 3.18: Variables associated with each arm. The scalars ${}^{\mathrm{ee}}f_{\mathrm{ext},t_{\mathrm{z}}}$ and ${}^{\mathrm{ee}}\tilde{x}_{t_{\mathrm{z}}}$ are the projections of the external wrench ${}^{\mathrm{ee}}\boldsymbol{f}_{\mathrm{ext}}$ and the pose error $\tilde{\boldsymbol{x}}$, respectively, on the z-axis of the end-effector frame.

stiffness matrix $\boldsymbol{K}_C$ in (3.2). For its derivation, the stiffness matrix is first defined in the end-effector frame as a diagonal matrix ${}^{\mathrm{ee}}\boldsymbol{K}_{C,v}$, as

$$ {}^{\mathrm{ee}}\boldsymbol{K}_{C,v} = \mathrm{diag}([{}^{\mathrm{ee}}k_{t_{\mathrm{x}}},\ {}^{\mathrm{ee}}k_{t_{\mathrm{y}}},\ \rho_{i,t}\ {}^{\mathrm{ee}}k_{t_{\mathrm{z}}},\ {}^{\mathrm{ee}}k_{r_{\mathrm{x}}},\ {}^{\mathrm{ee}}k_{r_{\mathrm{y}}},\ {}^{\mathrm{ee}}k_{r_{\mathrm{z}}}]), \tag{3.72} $$

where $k_{t_{\mathrm{x}}}, k_{t_{\mathrm{y}}}, k_{t_{\mathrm{z}}}, k_{r_{\mathrm{x}}}, k_{r_{\mathrm{y}}}, k_{r_{\mathrm{z}}} \in \mathbb{R}_{\geq 0}$ are the user-defined translational and rotational stiffness coefficients. Additionally, $\rho_{i,t} \in [0,1]$ denotes the impedance control shaping function variable defined as a smooth function according to

$$ \rho_{i,t} = \begin{cases} 1 & \text{if } \ \delta_{i,t} \leq \ {}^{\mathrm{ee}}\tilde{x}_{t_{\mathrm{z}}}, \\ \frac{1}{2}\left(1 - \cos\left(\pi \frac{{}^{\mathrm{ee}}\tilde{x}_{t_{\mathrm{z}}}}{\delta_{i,t}}\right)\right) & \text{if } \ 0 \ \leq \ {}^{\mathrm{ee}}\tilde{x}_{t_{\mathrm{z}}} < \delta_{i,t}, \\ 0 & \text{else}, \end{cases} \tag{3.73} $$

with ${}^{\mathrm{ee}}\tilde{x}_{t_{\mathrm{z}}}$ representing the pose error $\tilde{\boldsymbol{x}}$ rotated by ${}^{\mathrm{ee}}\boldsymbol{R}^T$ along the end-effector z-direction, and $\delta_{i,t} \in \mathbb{R}_{>0}$ serving as the threshold along the end-effector z-direction, from which the stiffness begins to adapt. The rationale behind this shaping function is to increase compliance whenever the robot setpoint is behind its end-effector, ensuring that (i) no backward motion interferes with the force control maintaining the grasp and (ii) robots on the other side of the object can take the lead and move the robot by pushing the object while the grasp is maintained.

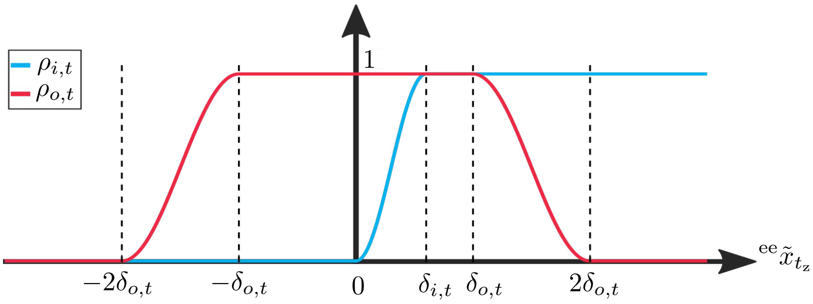

Figure 3.19: Shaping function variables; The role of $\rho_{o,t}$ is to activate the force controller only when the position error along the z-axis of the end-effector frame is not too large, whereas the role of $\rho_{i,t}$ is to engage the motion controller along the end-effector z-axis only when the robot is supposed to move forward (i.e. when ${}^{\mathrm{ee}}\tilde{x}_{t_\mathrm{z}} > 0$).

The diagonal matrix ${}^{\mathrm{ee}}\boldsymbol{K}_{C,v}$ in (3.72) is continuously transformed from the end-effector frame to the robot base frame, yielding the stiffness matrix $\boldsymbol{K}_{C,v}$ in the control law

$$\boldsymbol{\tau}_v = \boldsymbol{J}^T(\boldsymbol{q})\boldsymbol{f}_v, \tag{3.74}$$

$$\boldsymbol{f}_v = \boldsymbol{K}_{C,v}\tilde{\boldsymbol{x}} + \boldsymbol{D}_C\dot{\tilde{\boldsymbol{x}}} + \boldsymbol{M}_C(\boldsymbol{q})\ddot{\boldsymbol{x}}_d + \boldsymbol{C}_C(\boldsymbol{q},\dot{\boldsymbol{q}})\dot{\boldsymbol{x}}_d + \boldsymbol{f}_g(\boldsymbol{q}), \tag{3.75}$$

$$\tilde{\boldsymbol{x}} = \boldsymbol{x}_d - \boldsymbol{x}. \tag{3.76}$$

Force Controller for Object Grasp

The employed force control is similar to (3.7), but only a 1-dimensional force is supposed to be controlled to maintain the object's grasp. As mentioned before, to hold the object, each manipulator should establish a contact force ${}^{\mathrm{ee}}f_{d,t_\mathrm{z}}$ along the z-direction of their end-effector frame. Thus, considering ${}^{\mathrm{ee}}f_{\mathrm{ext},t_\mathrm{z}} \in \mathbb{R}$ as the external force along the end-effector z-direction, the proposed force control law is

$$\boldsymbol{\tau}_o = {}^{\mathrm{ee}}\boldsymbol{J}^T(\boldsymbol{q})\;{}^{\mathrm{ee}}\boldsymbol{f}_o, \tag{3.77}$$

$${}^{\mathrm{ee}}\boldsymbol{f}_o = [0,\ 0,\ \rho_{o,t}\;{}^{\mathrm{ee}}\breve{f}_o,\ 0,\ 0,\ 0]^T, \tag{3.78}$$

where

$${}^{\mathrm{ee}}\breve{f}_o = {}^{\mathrm{ee}}f_{d,t_\mathrm{z}} + k_{f,p}\;{}^{\mathrm{ee}}\tilde{f}_{t_\mathrm{z}} + k_{f,i}\int_0^t {}^{\mathrm{ee}}\tilde{f}_{t_\mathrm{z}}(\varepsilon)\;d\varepsilon + k_{f,d}\;{}^{\mathrm{ee}}\dot{\tilde{f}}_{t_\mathrm{z}}, \tag{3.79}$$

$${}^{\mathrm{ee}}\tilde{f}_{t_\mathrm{z}} = {}^{\mathrm{ee}}f_{d,t_\mathrm{z}} + {}^{\mathrm{ee}}f_{\mathrm{ext},t_\mathrm{z}}, \tag{3.80}$$

with $k_{f,p}, k_{f,i}, k_{f,d} \in \mathbb{R}_{\geq 0}$ denoting the PID gains. Additionally, $\rho_{o,t}$ represents the force control shaping function variable defined as a smooth function as follows:

$$\rho_{o,t} = \begin{cases} 0 & \text{if } 2\delta_{o,t} \leq\ |{}^{\mathrm{ee}}\tilde{x}_{t_\mathrm{z}}|, \\ \frac{1}{2}\left(1+\cos\left(\pi(\frac{{}^{\mathrm{ee}}\tilde{x}_{t_\mathrm{z}}}{\delta_{o,t}}-1)\right)\right) & \text{if }\ \delta_{o,t} \leq\ |{}^{\mathrm{ee}}\tilde{x}_{t_\mathrm{z}}| < 2\delta_{o,t}, \\ 1 & \text{else.} \end{cases} \tag{3.81}$$

Here $\delta_{o,t} \in \mathbb{R}_{>0}$ is the shaping function threshold, from which the force control is smoothly deactivated to avoid any hazardous behavior. Figure 3.19 depicts the evolution of the impedance control and force control shaping function variables based on the pose error along the end-effector z-axis.

Final controller

The robot input torque $\boldsymbol{\tau}_m$ in (2.8) is derived by incorporating the variable impedance control and object grasp control laws, as

$$\boldsymbol{\tau}_m = \boldsymbol{\tau}_v + \boldsymbol{\tau}_o. \tag{3.82}$$

Considering (2.11), (2.16), (2.17), (2.20), (3.74) and (3.77), the closed-loop dynamics of the robot equipped with the input torque (3.82) in the absence of joint friction becomes

$$\boldsymbol{M}_C(\boldsymbol{q})\ddot{\tilde{\boldsymbol{x}}} + \boldsymbol{C}_C(\boldsymbol{q},\dot{\boldsymbol{q}})\dot{\tilde{\boldsymbol{x}}} + \boldsymbol{D}_C\dot{\tilde{\boldsymbol{x}}} + \boldsymbol{K}_{C,v}\tilde{\boldsymbol{x}} + {}_{\mathrm{ee}}\boldsymbol{J}^{-T}\left(\boldsymbol{f}_o + \boldsymbol{f}_{\mathrm{ext}}\right) = \boldsymbol{0}. \tag{3.83}$$

3.2.2 Stabilization

For investigating stability, the passivity analysis approach introduced in Section 2.3 is utilized here. The proposed storage function is similar to (3.14), and is defined as

$$S_v = \frac{1}{2}\dot{\tilde{\boldsymbol{x}}}^T\boldsymbol{M}_C(\boldsymbol{q})\dot{\tilde{\boldsymbol{x}}} + \frac{1}{2}\tilde{\boldsymbol{x}}^T\boldsymbol{K}_{C,v}\tilde{\boldsymbol{x}}. \tag{3.84}$$

Its time evolution is derived as

$$\begin{aligned}
\dot{S}_v &= \dot{\tilde{\boldsymbol{x}}}^T\boldsymbol{M}_C(\boldsymbol{q})\ddot{\tilde{\boldsymbol{x}}} + \frac{1}{2}\dot{\tilde{\boldsymbol{x}}}^T\dot{\boldsymbol{M}}_C(\boldsymbol{q},\dot{\boldsymbol{q}})\dot{\tilde{\boldsymbol{x}}} + \dot{\tilde{\boldsymbol{x}}}^T\boldsymbol{K}_{C,v}\tilde{\boldsymbol{x}} + \frac{1}{2}\tilde{\boldsymbol{x}}^T\dot{\boldsymbol{K}}_{C,v}\tilde{\boldsymbol{x}} && (3.85)\\
&= -\dot{\tilde{\boldsymbol{x}}}^T\ {}_{\mathrm{ee}}\boldsymbol{J}^{-T}(\boldsymbol{f}_o + \boldsymbol{f}_{\mathrm{ext}}) + \frac{1}{2}\tilde{\boldsymbol{x}}^T\dot{\boldsymbol{K}}_{C,v}\tilde{\boldsymbol{x}} - \dot{\tilde{\boldsymbol{x}}}^T\boldsymbol{D}_C\dot{\tilde{\boldsymbol{x}}} && (3.86)\\
&= \dot{\boldsymbol{x}}_{\mathrm{ee}}^T\boldsymbol{f}_{\mathrm{ext}} \underbrace{-\dot{\tilde{\boldsymbol{x}}}^T\ {}_{\mathrm{ee}}\boldsymbol{J}^{-T}\boldsymbol{f}_o - \dot{\boldsymbol{x}}_d^T\ {}_{\mathrm{ee}}\boldsymbol{J}^{-T}\boldsymbol{f}_{\mathrm{ext}} + \frac{1}{2}\tilde{\boldsymbol{x}}^T\dot{\boldsymbol{K}}_{C,v}\tilde{\boldsymbol{x}}}_{P_T} - \underbrace{\dot{\tilde{\boldsymbol{x}}}^T\boldsymbol{D}_C\dot{\tilde{\boldsymbol{x}}}}_{\geq 0}. && (3.87)
\end{aligned}$$

Considering n_r as the total number of robots and assuming a passive object in a passive environment, the following assumptions can be made.

$$\dot{S}_{\mathrm{env}} \leq \sum_{i=1}^{n_r} -\dot{\boldsymbol{x}}_{\mathrm{ee},i}^T\boldsymbol{f}_{\mathrm{ext},i}. \tag{3.88}$$

Here, $S_{\mathrm{env}} \in \mathbb{R}_{\geq 0}$ denotes the storage function associated with the object and the environment. Accordingly, the storage function associated with the overall system of n_r manipulator holding the object becomes

$$S_{\mathrm{sys}} = \sum_{i=1}^{n_r} S_{v,i} + S_{\mathrm{env}}. \tag{3.89}$$

Parameter	Experiment 1	Experiment 2
${}^{\mathrm{ee}}_{\mathrm{ee}}\boldsymbol{p}_{\mathrm{cr}}$ [m]	$[0, 0, 0.225]^T$	
$k_{t_\mathrm{x}}, k_{t_\mathrm{y}}, k_{t_\mathrm{z}}$ [N/m]	1000	
$k_{r_\mathrm{x}}, k_{r_\mathrm{y}}, k_{r_\mathrm{z}}$ [Nm/rad]	150	
$\boldsymbol{D}_C$	Critical damping [381]	
$\delta_{i,t}, \delta_{o,t}$ [m]	$0.01, 0.05$	
${}^{\mathrm{ee}}f_{d,t_\mathrm{z}}$ [N]	10	15
$k_{f,p}, k_{f,i}, k_{f,d}$ [-]	$1.5, 0.3, 0$	$1, 0.3, 0$
$S_T(t=0), S_{\mathrm{env}}(t=0)$ $[J]$	$7, 1$	

Table 3.2: Controller parameters for each arm.

Given (3.87) and (3.88), it follows

$$\dot{S}_{\mathrm{sys}} \leq \sum_{i=1}^{n_r} P_{T,i}. \tag{3.90}$$

In order to ensure passivity, a virtual energy tank with the storage function $S_T \in \mathbb{R}_{\geq 0}$ can be defined such that

$$\dot{S}_T = -\sum_{i=1}^{n_r} P_{T,i}. \tag{3.91}$$

Considering (3.87), the tank has three ports for each robot with controllable variables $\boldsymbol{f}_o$, $\dot{\boldsymbol{K}}_{C,v}$, and $\dot{\boldsymbol{x}}_d$. As elaborated in Section 2.3, to guarantee the passivity of the overall system, the tank valve gain γ_{low} associated with its lower energy plays a crucial role. As soon as the tank energy is fully drained, γ_{low} and accordingly, all the controllable variables change to zero. The passivity of the overall system, including the virtual energy tank, can be observed according to (3.90) and (3.91), via

$$S = S_{\mathrm{sys}} + S_T \leq 0. \tag{3.92}$$

3.2.3 Experiments

In order to evaluate the proposed approach, a bi-manual setup consisting of two 7-DoF Franka Emika robots is prepared. For a better contact force establishment, foam balls are cut and attached to the robot end-effectors, as shown in Figure 3.20 and Figure 3.22. The external wrench $\boldsymbol{f}_{\mathrm{ext}}$ for each robot is estimated via the interoceptive momentum-based observer [380]. The manipulated object is a wooden beam with weight and length of 0.9 kg and 0.45 m, respectively.

Two experiments are carried out. In the first one, the robots are supposed to grasp and carry the object along a predefined trajectory. In the second experiment, the desired motion is determined by a human operator interacting with a third robot remotely. For grasping the

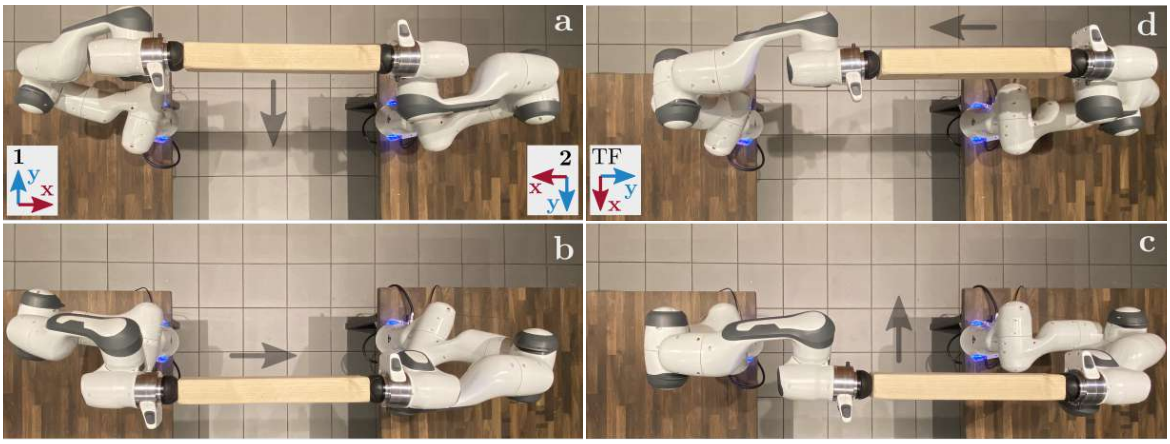

Figure 3.20: Experiment 1 – The object follows a rectangular path in the xy-plane. Figures ⓐ, ⓑ, ⓒ and ⓓ correspond to the beginning of the stages ②, ③, ④ and ⑤, respectively.

object, in both experiments, the robot end-effectors are aligned with and facing each other, thus meeting the grasp matrix condition [76]. The controller parameters for both robots are empirically tuned and set according to Table 3.2.

Experiment 1: Object Manipulation Along a Rectangular Path

In this experiment, the bi-manual system is supposed to first grasp the object with the desired contact force $^{\mathrm{ee}}f_{d,t_z} = 10$ N. Thereafter, the object is supposed to move with a velocity of 0.1 m/s along a square with a side length of 0.25 m on the xy-plane of the task frame TF, as shown in Figure 3.20.

As depicted in Figure 3.21, during the grasp stage ①, the motion controller stiffness along the end-effector z-axis is zero ($\rho_{i,t} = 0$), and the force controllers perfectly establish the contact force of 10 N. The initial oscillations are due to the elasticity of the end-effectors' surface. During stage ②, the robots move along their y-axes. Due to the initial zero stiffness on the robots x-axes (i.e., end-effector z-axis), the robots, and accordingly the object, start to slightly drift toward robot 1 (left robot in Figure 3.20). This behavior increases the value of $^{\mathrm{ee}}\tilde{x}_{t_z}$ for robot 1, and as a result, the variable $\rho_{i,t}$ slightly increases. Consequently, the increased stiffness of robot 1 prevents any further object drifting. Throughout stage ③, as the desired pose $\boldsymbol{x}_d$ for robot 1 moves ahead of its end-effector, the variable $\rho_{i,t}$ becomes 1. As a result, the controller's high stiffness pushes the object toward robot 2 and the contact force increases. As the stiffness of robot 2 along its end-effector z-axis is still zero ($\rho_{i,t} = 0$), its force controller is able to maintain the contact force of 10 N by moving the robot backward. During stage ④, similar to stage ②, the variable $\rho_{i,t}$ for robot 1 slightly increases to stop any possible object drifting behavior. Finally, in stage ⑤, the stiffness of robot 2 increases ($\rho_{i,t} = 1$), and the robot pushes the object toward its initial position to complete the rectangular path.

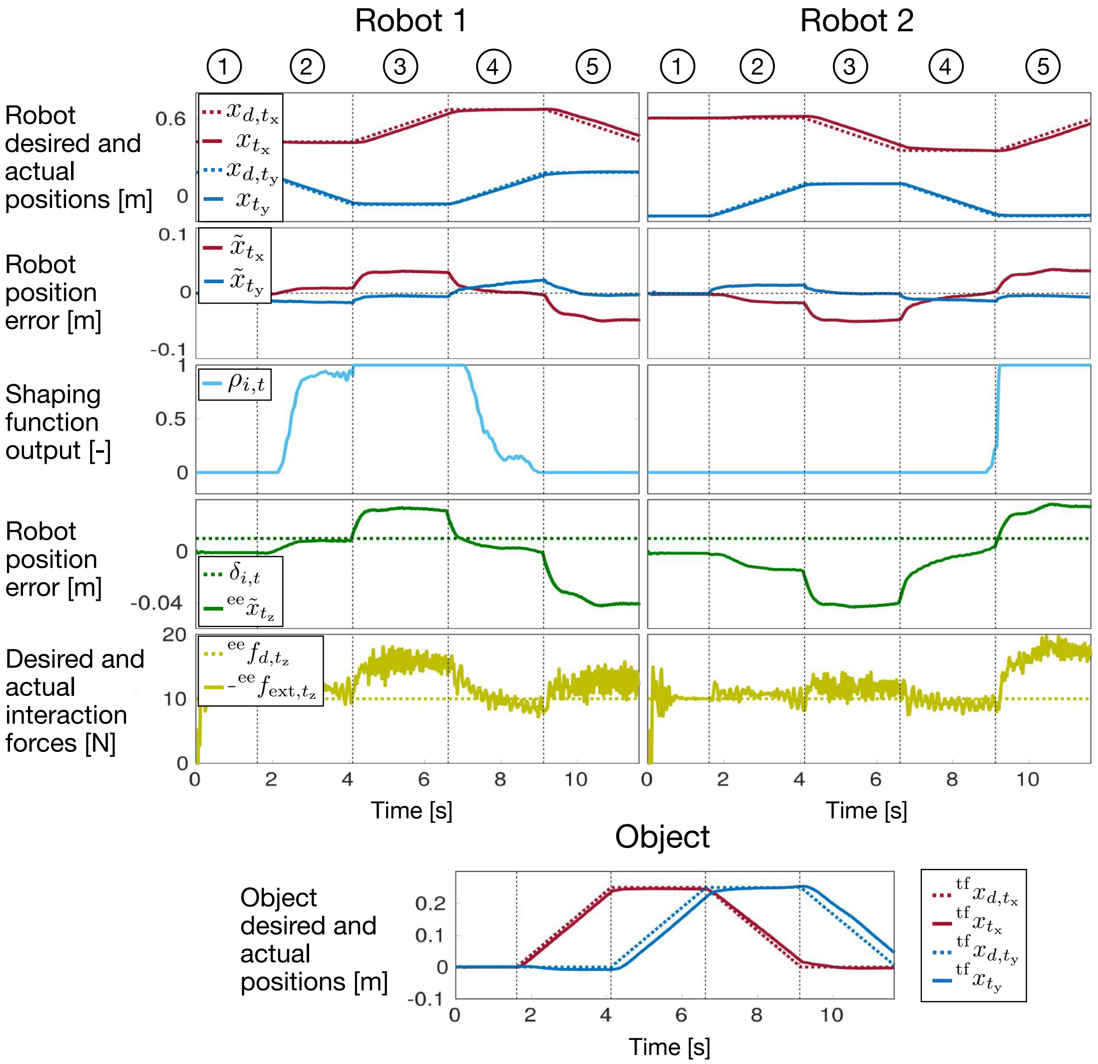

Figure 3.21: Experiment 1 – To manipulate the object, each robot independently follows its desired force and motion in its own frame. The variable $\rho_{i,t}$ adapts based on the desired motion direction. Through this cooperative approach, the object moves within its own frame.

Figure 3.22: Experiment 2 – An operator is remotely manipulating the object by moving the guiding robot in the yz-plane.

Experiment 2: Energy Evolution During Teleoperation

In this experiment, another robot is employed as a guidance interface, through which a human operator commands the desired motion of the object, as shown in Figure 3.22. The guiding robot motion is constrained such that the operator can only move it in the yz-plane of the task frame TF. Additionally, the initial pose of the robot is perceived as the actual initial pose of the object (Figure 3.22.a). The human operator moves the guiding robot first along its y-axis (between time 2 and 4 s in Figure 3.21) and then along the z-axis (between time 4 and 6 s). The aim of this experiment is to monitor the evolution of the power and energy signals introduced during the stability analysis.

In order to better analyze the energy evolution, the following signals are introduced for each robot.

$$E_{T,v} := \int_0^t \frac{1}{2}\tilde{\boldsymbol{x}}^T \dot{\boldsymbol{K}}_{C,v}\tilde{\boldsymbol{x}}\ d\varepsilon, \tag{3.93}$$

$$E_{T,o} := \int_0^t -\dot{\tilde{\boldsymbol{x}}}^T\ {}_{\mathrm{ee}}\boldsymbol{J}^{-T}\boldsymbol{f}_o\ d\varepsilon, \tag{3.94}$$

$$E_{T,i} := \int_0^t -\dot{\boldsymbol{x}}_d^T\ {}_{\mathrm{ee}}\boldsymbol{J}^{-T}\boldsymbol{f}_{\mathrm{ext}}\ d\varepsilon, \tag{3.95}$$

$$E_T := E_{T,v} + E_{T,o} + E_{T,i} \tag{3.96}$$

$$E_{\mathrm{ext}} := \int_0^t \dot{\boldsymbol{x}}^T\ {}_{\mathrm{ee}}\boldsymbol{J}^{-T}\boldsymbol{f}_{\mathrm{ext}}\ d\varepsilon. \tag{3.97}$$

Note that these values do not necessarily correspond to energy, as they can become negative.

Initially, with no desired motion, the stiffness value along the x-axes is zero for both robots. As the human moves the guiding robot to the right, the stiffness for robot 1 increases to push the object to the right. The stiffness remains nonzero even when the human moves the guiding robot upward to restrict any object drifting behavior. Despite the rapid change in stiffness $\dot{\boldsymbol{K}}_C$ at around 2 s, the relatively small pose error $\tilde{\boldsymbol{x}}$ results in low values for $E_{T,v}$. This value remains zero for robot 2, as its stiffness does not change during the experiment. Similarly, due to the comparatively low velocity-error $\dot{\tilde{\boldsymbol{x}}}$, the value $E_{T,o}$ remains low for both robots. However, $E_{T,i}$ is the major component of E_T. In fact, considering (3.87) and (3.95), as the desired velocity $\dot{\boldsymbol{x}}_d$ and the interaction force $\boldsymbol{f}_{\mathrm{ext}}$ for robot 1 have opposite directions, $E_{T,i}$ corresponds to the main potentially passivity-violating power. This is not the case for Robot 2, as at least during the first part of the motion, $E_{T,i}$ is continuously decreasing.

Figure 3.23 depicts the evolution of the physical power exchanged between each robot and the environment. Pushing the object is equivalent to some work being done on the environment. Therefore, E_{ext} for robot 1 is continuously decreasing. In contrast, work is done on robot 2 for the same motion as the environment pushes this robot. Considering the overall behavior, it is observed that throughout the experiment, the tank energy S_T drains. In fact, its energy is either being dissipated by the Cartesian controller damping or contributing to the energy evolution of the storage functions $S_{v,i}$ and $S_{v,2}$ and the environment energy S_{env}. Moreover, the transferred energy to the environment is either stored as the object's gravitational potential energy or dissipated (e.g., via the friction effects that have been ignored in the modeling).

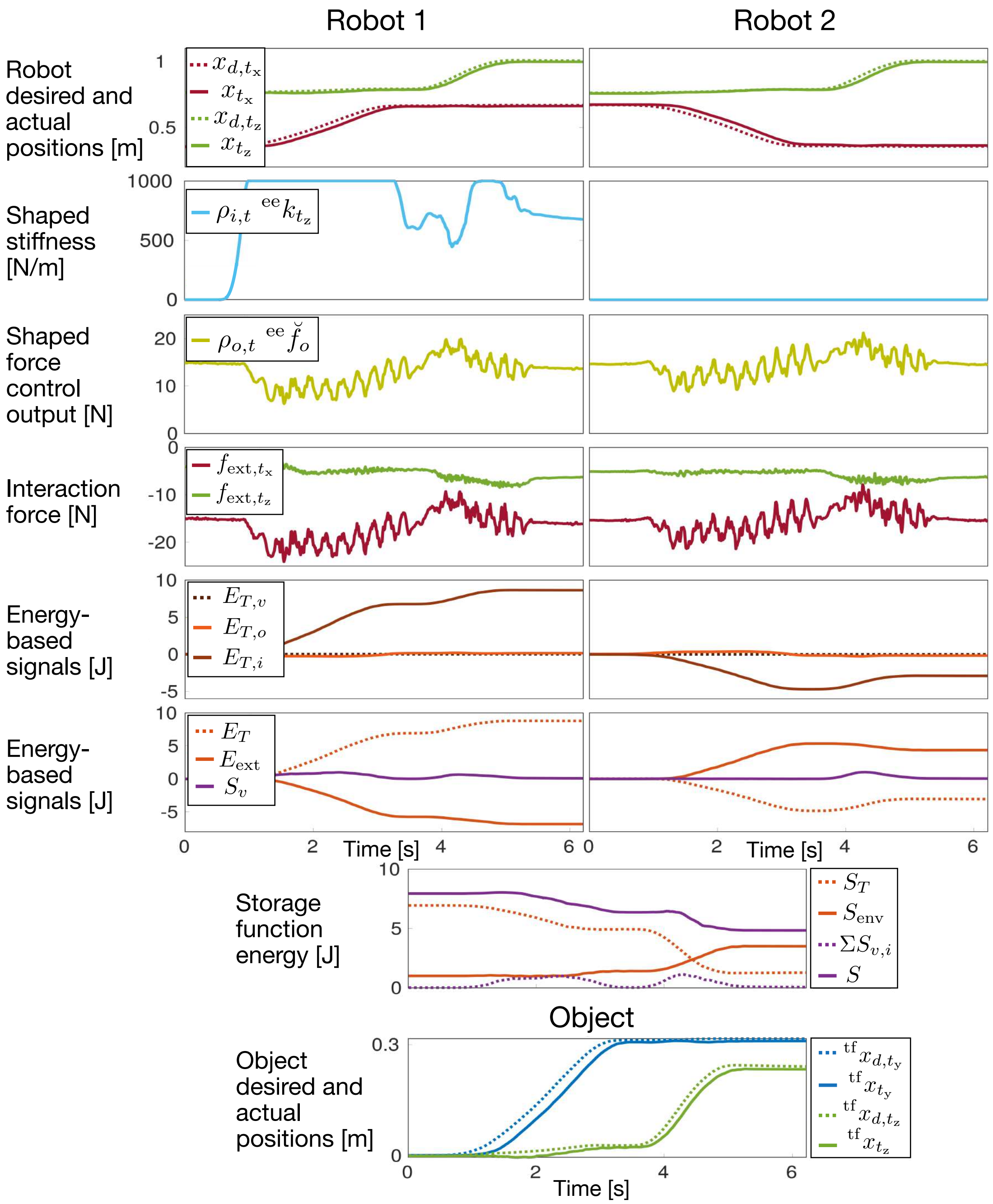

Figure 3.23: Experiment 2 – The cooperative object manipulation is achieved through power exchanges among various components. Despite these dynamic interactions, the overall storage function S remains bounded throughout the experiment.

3.3 Force-Encoded Motion Policies for Interaction Control

When a robot is equipped solely with a motion controller[3], the direct control of the interaction wrench, as in the unified force-impedance control, becomes unattainable. In such scenarios, where only the desired motion can be commanded to the robot, the application is restricted to utilizing a motion policy. This section introduces a modification to one of the most well-established motion policies, Dynamic Movement Primitives (DMP). Traditionally, DMPs are effective tools for encoding desired motions into a dynamical system formulation. With this innovative modification, DMPs are empowered with an indirect force control capability. These modified DMPs, known as *Admittance-Coupled Dynamic Movement Primitives* (CDMP), facilitate intuitive energy modeling due to their physically interpretable formulation. This ultimately enables the utilization of the concept of reference power to ensure stability with respect to a nominal (e.g., demonstrated) task.

3.3.1 Indirect Force Control via Trajectory Modification

Considering $\boldsymbol{x}_{d,0}(t) \in \mathbb{R}^m$ as the desired motion trajectory in an m-dimensional Cartesian space without incorporating force control intentions, the modified trajectory $\boldsymbol{x}_d(t)$ for the robot controller can be formulated

$$\boldsymbol{x}_d(t) = \boldsymbol{x}_{d,0}(t) + \boldsymbol{x}_a(t), \tag{3.98}$$

---

[3] The motion controller employed in this context can be either a rigid motion controller, such as in the case of position control, or a compliant motion controller, as seen in the case of impedance control.

where $\boldsymbol{x}_a(t) \in \mathbb{R}^m$ represents the modification trajectory for indirect force control achievable through the following admittance dynamics.

$$\boldsymbol{f}_d + \boldsymbol{f}_{\text{ext}} = \boldsymbol{M}_a \ddot{\boldsymbol{x}}_a + \boldsymbol{D}_a \dot{\boldsymbol{x}}_a + \boldsymbol{K}_a \boldsymbol{x}_a. \tag{3.99}$$

Here, $\boldsymbol{f}_d, \boldsymbol{f}_{\text{ext}} \in \mathbb{R}^m$ are the robot desired wrench to the environment and the actual external wrench from the environment to the robot, respectively. Additionally, $\boldsymbol{M}_a, \boldsymbol{D}_a, \boldsymbol{K}_a \in \mathbb{R}^{m \times m}$ denote the admittance mass, damping, and stiffness positive-definite matrices, respectively.

3.3.2 Admittance-Coupled Dynamic Movement Primitives

The standard formulation of a Dynamic Movement Primitive (DMP) is represented by the following dynamical system [383]:

$$\dot{\boldsymbol{z}}_z = \Omega \left(\alpha_z \left(\beta_z (\boldsymbol{g}_z - \boldsymbol{x}_{\text{DMP}}) - \boldsymbol{z}_z \right) + \boldsymbol{f}_z(\phi) \right), \tag{3.100}$$

where $\boldsymbol{x}_{\text{DMP}} \in \mathbb{R}^m$ denotes the system state representing the encoded motion trajectory, $\boldsymbol{g}_z \in \mathbb{R}^m$ is the goal state, and $\alpha_z, \beta_z \in \mathbb{R}_{\geq 0}$ are DMP gains. Additionally, $\boldsymbol{f}_z(\phi) \in \mathbb{R}^m$ is the nonlinear forcing term, $\phi \in [0, 1]$ is the phase variable (i.e., the state representing the movement progress), and $\Omega \in \mathbb{R}$ is the phase velocity determining how fast the motion progresses via

$$\Omega = \dot{\phi}. \tag{3.101}$$

Finally, $\boldsymbol{z}_z \in \mathbb{R}^m$ is associated with the DMP velocity such that

$$\dot{\boldsymbol{x}}_{\text{DMP}} = \Omega \boldsymbol{z}_z. \tag{3.102}$$

Similar to (3.98)–(3.99), the DMP formulation can be extended to facilitate simultaneous indirect control of interaction wrenches using an admittance law. This leads to a variant known as Admittance-Coupled Dynamic Movement Primitives (CDMP), formulated as

$$\begin{aligned}
\dot{\boldsymbol{z}}_{z,c} &= \Omega \left(\alpha_z \left(\beta_z (\boldsymbol{g}_z + \boldsymbol{c}_z - \boldsymbol{x}_{\text{CDMP}}) - \boldsymbol{z}_{z,c} \right) + \boldsymbol{f}_z(\phi) \right), && (3.103) \\
\dot{\boldsymbol{x}}_{\text{CDMP}} &= \Omega \boldsymbol{z}_{z,c} + \boldsymbol{c}_z, && (3.104) \\
\dot{\boldsymbol{c}}_z &= \boldsymbol{D}_z (\boldsymbol{f}_d + \boldsymbol{f}_{\text{ext}}). && (3.105)
\end{aligned}$$

Here, $\boldsymbol{c}_z \in \mathbb{R}^m$ represents the coupling term integrated into the original DMP trajectory. By setting $\boldsymbol{D}_z = \boldsymbol{D}_a^{-1}$, the coupling term $\boldsymbol{c}_z$ becomes identical to $\boldsymbol{x}_a$ in (3.99) where no mass $\boldsymbol{M}_a$ or stiffness $\boldsymbol{K}_a$ are employed in the admittance formulation. Figure 3.24 demonstrates the generalized architecture of an impedance-controlled manipulator equipped with a CDMP.

3.3.3 Stabilization

To broaden the scope of the stability analysis, the general admittance formulation (3.99) is considered, which, as mentioned earlier, can be simplified to the coupling relation (3.105) in the CDMP formulation. Consequently, (3.98) can be rewritten as

$$\boldsymbol{x}_{\text{CDMP}} = \boldsymbol{x}_{\text{DMP}} + \boldsymbol{x}_a. \tag{3.106}$$

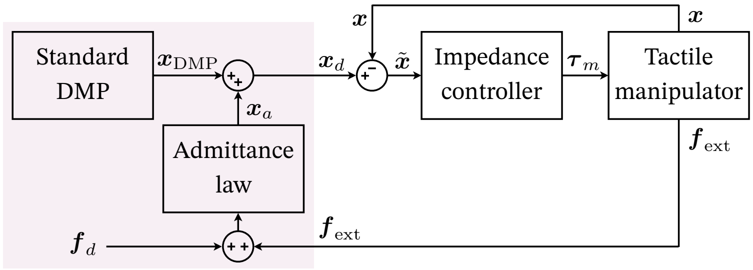

Figure 3.24: The highlighted blocks represent the generalized architecture of an Admittance-Coupled Dynamic Movement Primitive (CDMP).

The proposed storage function for the admittance system (3.99) is

$$S_a = \frac{1}{2}\dot{\boldsymbol{x}}_a^T \boldsymbol{M}_a \dot{\boldsymbol{x}}_a + \frac{1}{2}\boldsymbol{x}_a^T \boldsymbol{K}_a \boldsymbol{x}_a, \tag{3.107}$$

with the time evolution derived as

$$\dot{S}_a = \dot{\boldsymbol{x}}_a^T(\boldsymbol{M}_a \ddot{\boldsymbol{x}}_a + \boldsymbol{K}_a \boldsymbol{x}_a) \tag{3.108}$$

$$= \dot{\boldsymbol{x}}_a(\boldsymbol{f}_d + \boldsymbol{f}_{\mathrm{ext}}) - \underbrace{\dot{\boldsymbol{x}}_a^T \boldsymbol{D}_a \dot{\boldsymbol{x}}_a}_{\geq 0}, \tag{3.109}$$

$$\implies \dot{S}_a \leq \dot{\boldsymbol{x}}_a^T \boldsymbol{f}_d + \dot{\boldsymbol{x}}_a^T \boldsymbol{f}_{\mathrm{ext}}. \tag{3.110}$$

The inequality (3.110) demonstrates the passivity of the admittance system (3.99) with respect to the pairs $(\boldsymbol{f}_d, \dot{\boldsymbol{x}}_a)$ and $(\boldsymbol{f}_{\mathrm{ext}}, \dot{\boldsymbol{x}}_a)$.

Considering a Cartesian impedance controller with the control law given by (3.1) for the motion control of the robot and the associated storage function S_i defined in (3.14), and assuming a passive environment with the storage function S_{env}, the storage function of the overall system can be defined as

$$S_{\mathrm{sys}} = S_{\mathrm{env}} + S_i + S_a. \tag{3.111}$$

By considering (3.19) in the absence of a force controller (i.e., $\boldsymbol{f}_f = \boldsymbol{0}$), along with (3.21) and (3.110), the following observation can be made regarding the time evolution of S_{sys}:

$$\dot{S}_{\mathrm{sys}} \leq \overbrace{-\dot{\boldsymbol{x}}^T \boldsymbol{f}_{\mathrm{ext}}}^{\dot{S}_{\mathrm{env}} \leq} + \overbrace{\dot{\boldsymbol{x}}^T \boldsymbol{f}_{\mathrm{ext}} - \dot{\boldsymbol{x}}_d^T \boldsymbol{f}_{\mathrm{ext}}}^{\dot{S}_i \leq} + \overbrace{\dot{\boldsymbol{x}}_a^T \boldsymbol{f}_d + \dot{\boldsymbol{x}}_a^T \boldsymbol{f}_{\mathrm{ext}}}^{\dot{S}_a \leq} \tag{3.112}$$

$$\leq \cancel{-\dot{\boldsymbol{x}}^T \boldsymbol{f}_{\mathrm{ext}}} + \cancel{\dot{\boldsymbol{x}}^T \boldsymbol{f}_{\mathrm{ext}}} - \dot{\boldsymbol{x}}_{\mathrm{DMP}}^T \boldsymbol{f}_{\mathrm{ext}} - \cancel{\dot{\boldsymbol{x}}_a^T \boldsymbol{f}_{\mathrm{ext}}} + \dot{\boldsymbol{x}}_a^T \boldsymbol{f}_d + \cancel{\dot{\boldsymbol{x}}_a^T \boldsymbol{f}_{\mathrm{ext}}} \tag{3.113}$$

$$\leq \underbrace{\dot{\boldsymbol{x}}_a^T \boldsymbol{f}_d - \dot{\boldsymbol{x}}_{\mathrm{DMP}}^T \boldsymbol{f}_{\mathrm{ext}}}_{P_T}. \tag{3.114}$$

Referring to (3.114), the overall system demonstrates passivity with respect to the pairs $(\boldsymbol{f}_d, \dot{\boldsymbol{x}}_a)$ and $(\boldsymbol{f}_{\mathrm{ext}}, \dot{\boldsymbol{x}}_{\mathrm{DMP}})$; see Figure 3.25. To guarantee the autonomous passivity of the overall system, an energy tank can be designed for the potentially passivity-violating power P_T. Yet, as elaborated in the following, the concept of reference power is employed before tank augmentation.

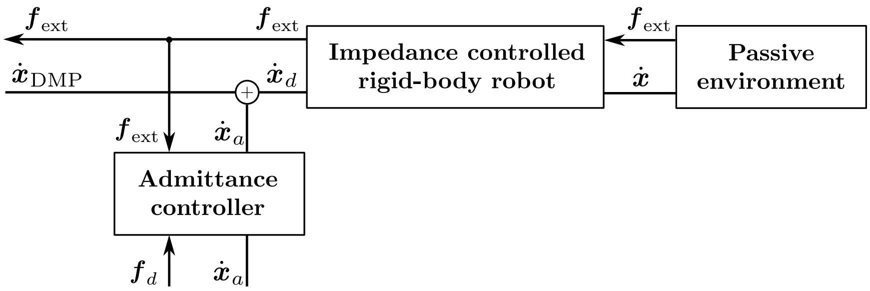

Figure 3.25: Port-based representation of an impedance-controlled robot in contact with a passive environment and equipped with CDMP.

Reference Power

As previously explained, a common use case for DMPs is imitation learning, where an operator demonstrates a trajectory that is then encoded into the DMP formulation. Consider a scenario where, before a task, an operator showcases the desired trajectories for motion and interaction wrench, denoted as $\boldsymbol{x}^{\dagger}_{\mathrm{DMP}}$ and $\boldsymbol{f}^{\dagger}_{d}$, respectively. These values may represent the actual trajectories during the demonstration stage. Consequently, a reference power trajectory $P_d \in \mathbb{R}$ can be determined as

$$P_d = \dot{\boldsymbol{x}}^{\dagger T}_{\mathrm{DMP}} \boldsymbol{f}^{\dagger}_{d}. \tag{3.115}$$

A virtual passive system with the storage function $S_d \in \mathbb{R}_{\geq 0}$ can then be associated with the reference power P_d such that

$$\dot{S}_d = -P_d. \tag{3.116}$$

By combining S_d with the storage function S_{sys} in (3.111), a new storage function denoted as $S_{\mathrm{sys}'} \in \mathbb{R}_{\geq 0}$ can be defined such that

$$S_{\mathrm{sys}'} = S_{\mathrm{sys}} + S_d. \tag{3.117}$$

Given (3.114) and (3.116), the time evolution of $S_{\mathrm{sys}'}$ becomes

$$\dot{S}_{\mathrm{sys}'} = \dot{S}_{\mathrm{sys}} + \dot{S}_d \tag{3.118}$$

$$\leq \underbrace{\overbrace{\dot{\boldsymbol{x}}_a^T \boldsymbol{f}_d - \dot{\boldsymbol{x}}_{\mathrm{DMP}}^T \boldsymbol{f}_{\mathrm{ext}}}^{P_T} - \dot{\boldsymbol{x}}^{\dagger T}_{\mathrm{DMP}} \boldsymbol{f}^{\dagger}_{d}}_{P'_T}. \tag{3.119}$$

Zero values of P'_T indicate that during the task, the potentially passivity-violating power P_T in (3.114) remains equal to the reference power P_d in (3.115). However, in reality, this is not always the case. Nonzero P'_T indicates that the system is either demanding more or less power than the reference power. Considering (3.114) and (3.119), to keep P'_T close to zero, the power P_T can be continuously adapted by modifying the amplitudes of $\dot{\boldsymbol{x}}_a$ and $\dot{\boldsymbol{x}}_{\mathrm{DMP}}$. This adaptation can be achieved by adjusting the phase velocity Ω in (3.101). Assuming

$\Omega^\dagger$ as the phase velocity associated with the nominal trajectories $\boldsymbol{x}^\dagger_{\text{DMP}}$ and $\boldsymbol{f}^\dagger_d$, the phase velocity adaptation law can be expressed as

$$\Omega = \Omega^\dagger - \sigma_{\text{CDMP}} P'_T, \tag{3.120}$$

where $\sigma_{\text{CDMP}} \in \mathbb{R}_{\geq 0}$ is a user-defined phase velocity adaptation gain for the CDMP. Considering (3.120), when P'_T is positive (indicating P_T is greater than P_d), Ω decreases to reduce the amplitudes of $\dot{\boldsymbol{x}}_a$ and $\dot{\boldsymbol{x}}_{\text{DMP}}$, thereby decreasing P_T. Conversely, when P'_T is negative (indicating P_T is smaller than P_d), Ω increases. This approach motivates the system to consume the reference power P_d in a more optimal manner.

To address positive values of P'_T and ensure system passivity, a virtual energy tank with the storage function $S_T \in \mathbb{R}_{\geq 0}$ is introduced, defined as

$$S_T = -P'_T. \tag{3.121}$$

The tank can influence the phase velocity through its valve gain γ_T as follows:

$$\Omega' = \gamma_T \Omega. \tag{3.122}$$

Considering the storage function $S \in \mathbb{R}_{\geq 0}$ defined as

$$S = S_T + S_{\text{sys}'}, \tag{3.123}$$

and given (3.119) and (3.121), the overall system maintains passivity according to

$$\dot{S} = \dot{S}_T + \dot{S}_{\text{sys}'} \leq 0. \tag{3.124}$$

3.3.4 Experiments

To validate the proposed approach, a 7-DoF Kuka LWR-4 robot equipped with an impedance controller is employed for a polishing task on a surface with changing configurations, as illustrated in Figure 3.26. An additional ATI force/torque sensor is mounted on the robot wrist to determine the external wrenches $\boldsymbol{f}_{\text{ext}}$. The task involves applying a vertical force with $f_{d,t_z} = 10$ N. The desired motion, perpendicular to the desired force, is initially demonstrated by an operator. Thus, according to (3.115), the reference power P_d remains consistently zero due to the reciprocity of $\dot{\boldsymbol{x}}^\dagger_{\text{DMP}}$ and $\boldsymbol{f}^\dagger_d$. The upper and lower energy limits for the virtual tank are defined as $S^{\text{up}}_T = 0.6$ J and $S^{\text{low}}_T = 0$ J, respectively. Experimental results in Figure 3.27 capture the four stages of the task. In stage ①, P'_T stays at zero, driven by the negligible admittance velocity $\dot{\boldsymbol{x}}_a$ and the minimal external wrench in the direction of $\boldsymbol{x}_{\text{DMP}}$. Stage ② involves lifting one corner of the surface, leading to periodic variations in P'_T, Ω, and S_T as $\dot{\boldsymbol{x}}_a$ varies periodically. As the other corner of the surface is lifted in stage ③, reestablishing contact, P'_T remains at zero. In stage ④, as the surface tilts again, positive P'_T decreases the phase velocity, ultimately depleting the tank energy and halting the phase progress. These results showcase the capability to robustly control both motion and force, relying solely on a motion policy—the Admittance-Coupled Dynamic Movement Primitive.

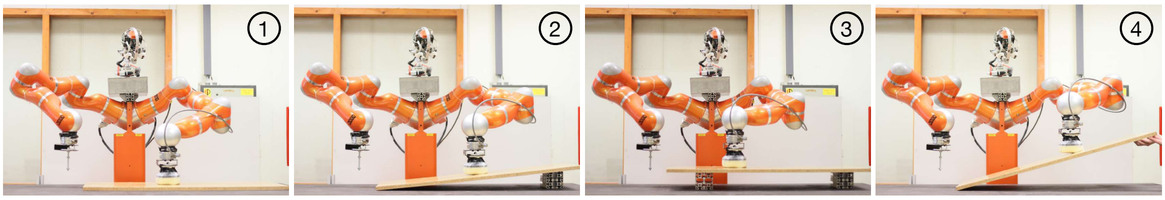

Figure 3.26: Four consecutive stages during the surface polishing experiment.

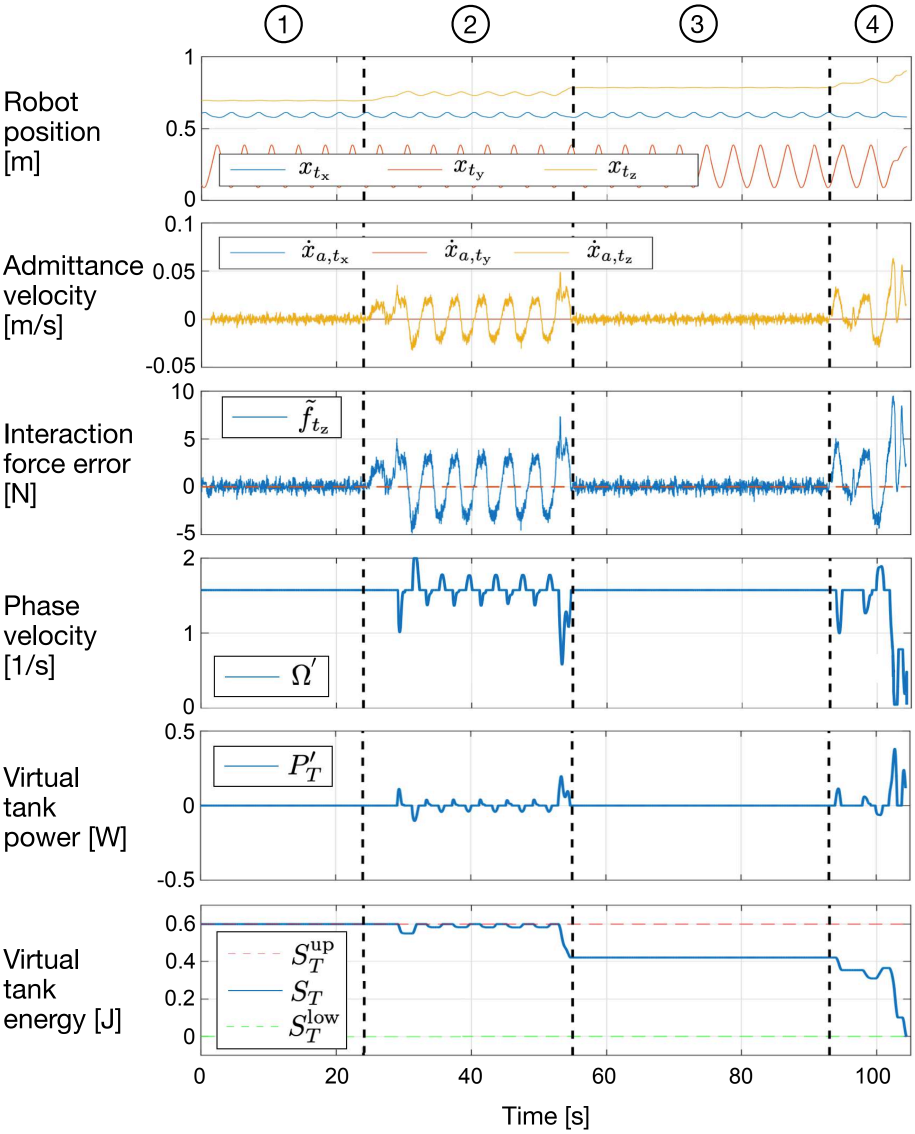

Figure 3.27: Positive values of the power P_T' lead to a reduction in phase velocity and, ultimately, the depletion of the tank energy.

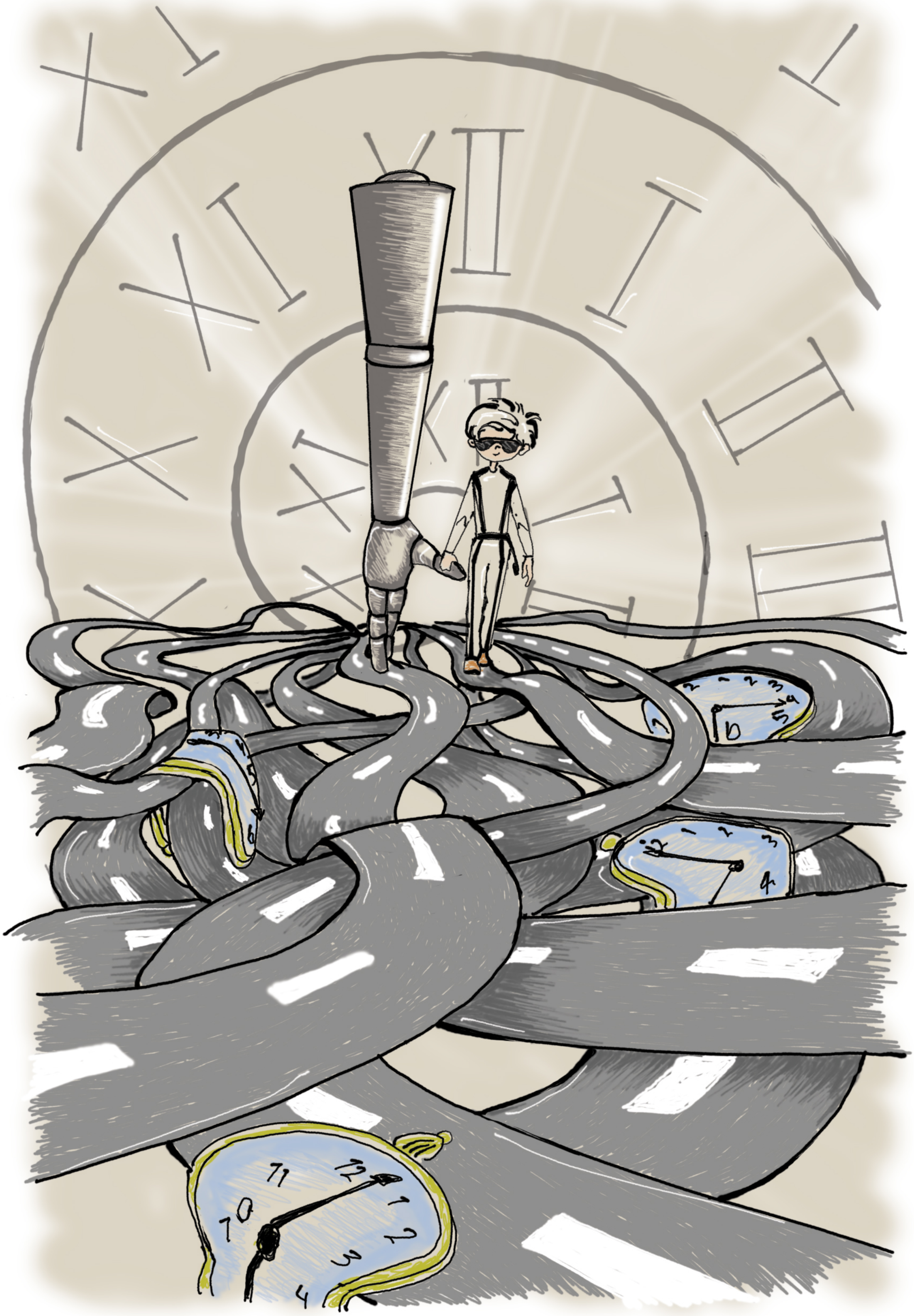

4 Reactive Phase-Based Planning for Path-Centric Manipulation

Once a controller is implemented and fine-tuned, the next crucial step is to determine the desired values that the controller should regulate. In tactile manipulation tasks, where controlling both interaction wrench and motion is vital, this step involves formulating the desired force and motion trajectories. Trajectory formulation can be approached in various ways. However, ultimately, a desired trajectory is communicated to the robot controller as a sequence of setpoints with specific timing characteristics.

In a general context, a trajectory can be considered to consist of two essential components: a set of setpoints and their timing. Manipulating either of these components can have a distinct impact on the robot's behavior. Some manipulation tasks require addressing these components independently. For example, in tasks where setpoints must remain unchanged due to constraints, such as adhering to a specified path during a motion-following task, the adjustment of timing becomes particularly crucial. This chapter focuses on designing policies with this consideration in mind.

To regulate only the timing behavior of a trajectory, an auxiliary variable, referred to as phase, can be introduced. The setpoint values can then be defined as functions of phase, and similarly, the phase value as a function of time, yielding a phase trajectory. Consequently, by adapting the phase trajectory, the timing characteristic of the setpoints sequence can be altered while keeping their values unchanged. This concept, named phase trajectory generation and adaptation, is the central theme of this chapter.

The utilization of a phase variable is a familiar concept in the existing literature. For example, in the formulation of a Dynamic Movement Primitive (DMP) discussed in Chapter 3, a phase variable is employed as the state of the incorporated canonical system. However, despite the presence of features such as overall time-scaling within DMPs, explicit regulation of phase dynamics is not incorporated there.

This chapter proposes three path-centric policies with distinct objectives utilizing the concept of phase. First, it illustrates how the timing characteristic of a trajectory can be adjusted to avoid collisions, such as those with a particular human body part. Next, it introduces a phase trajectory generation law incorporating human haptic input to facilitate motion guidance along a path. Finally, the concept of phase modulation is applied in the context of rehabilitation, allowing for the adjustment of the robot level of support to the patient along the therapeutic path to enhance recovery.

4.1 Collision-Preventing Phase Progress Control

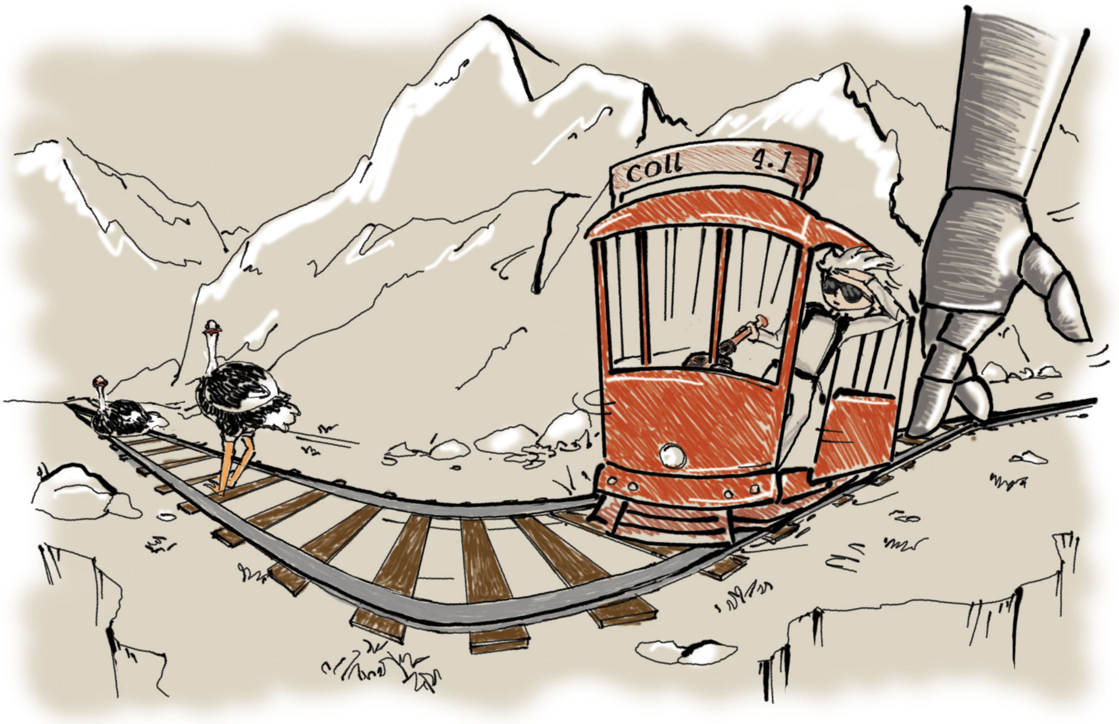

In real-world settings, acquiring an accurate stationary model of the environment for collision-free motion planning is often challenging. As a result, numerous trajectory adaptation methods have been proposed in the literature with the aim of collision avoidance. The common rationale behind these methods is that when an obstacle, such as a human, approaches a moving robot, the robot should adjust its trajectory to avoid a collision. However, there are scenarios where such trajectory adjustments, or drifting, may not be feasible. For example, it could lead to undesirable collisions with other parts of the environment. This is particularly relevant in confined environments with a geometrically constrained workspace for the robot. To tackle this challenge, instead of adapting the entire desired trajectory, its timing characteristics can be altered while keeping the trajectory setpoint values unchanged. This can be achieved by encoding the desired trajectory using a phase variable. The phase trajectory is then adapted based on an estimation of collision, taking into account the configuration of the obstacle with respect to the encoded path.

4.1.1 Phase: Unleashing Time from Trajectory

A trajectory, such as a desired motion trajectory $\boldsymbol{x}_d(t)$, regardless of its encoding process, can be viewed as a sequence of setpoints $\boldsymbol{x}_d$ with associated time stamps. In certain situations, it may be necessary to retain the setpoint values while adjusting (or entirely redefining) their timing. Conventional trajectory adaptation methods might not be practical, as for

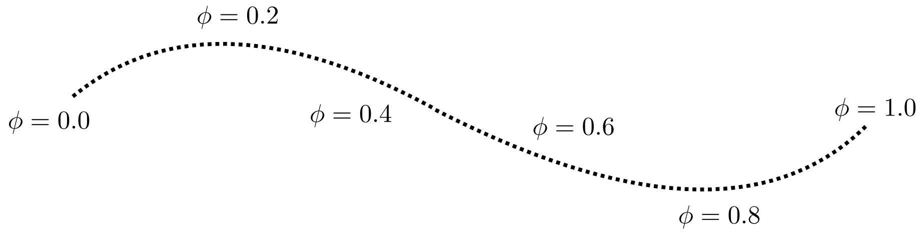

Figure 4.1: A representative association of the phase variable with path progress, where $\phi = 0$ corresponds to the initial point on the path, and $\phi = 1$ corresponds to the final point.

our objective, only the timing characteristic of the trajectory needs to be controlled in a decoupled manner. To achieve this, an auxiliary variable, namely phase, can be employed.

Let $\phi \in [0, 1]$ be a one-dimensional phase variable[1], where $\phi = 0$ corresponds to the initial setpoint, and $\phi = 1$ corresponds to the final one; see Figure 4.1. By associating a desired timing behavior with the phase value, a phase trajectory $\phi(t)$ can be generated. As the setpoints are functions of phase, this phase trajectory can yield the desired trajectory, i.e., $\boldsymbol{x}_d(\phi(t)) = \boldsymbol{x}_d(t)$ for the desired motion. Adjusting (or defining) the phase trajectory allows the timing characteristic of the desired trajectory to be modified while keeping the setpoint values intact. This is the fundamental idea behind the path-centric tactile policies introduced in this section and other sections of this chapter. In this context, desired force or motion trajectories $\boldsymbol{f}_d(t), \boldsymbol{x}_d(t)$ are either directly defined as functions of phase (i.e., $\boldsymbol{f}_d(\phi), \boldsymbol{x}_d(\phi)$), or their recorded values (e.g., during teaching by demonstration stage) are learned[2] as functions of phase, using techniques such as Gaussian radial basis functions [386]. The same approach can be applied to the phase trajectory $\phi(t)$, either by directly defining it as a function of time according to the policy objective or by learning it during the demonstration stage. The phase trajectory can then be adjusted during the task, for example, via an online phase progress speed adaptation law as

$$\Omega = \sigma \Omega^{\dagger}, \tag{4.1}$$

where $\sigma \in \mathbb{R}$ is the phase velocity adaptation gain defined according to the policy objective, and Ω is the phase velocity defined as

$$\Omega = \dot{\phi}. \tag{4.2}$$

Furthermore, $\Omega^{\dagger}$ in (4.1) is referred to as the nominal (original) phase velocity, e.g., learned during the teaching by demonstration stage. In this section, various path-centric motion trajectory adaptation methods are introduced to avoid collisions, utilizing the adaptation gain σ_{coll}. For this purpose, different methods for determining σ_{coll} are presented.

Remark: It should be mentioned that the effectiveness of the proposed collision-preventing policies relies on the controller's ability to react effectively to the adaptation in the desired trajectories.

---

[1] Please note that in the literature, this variable may be denoted differently; for instance, as s in [384].

[2] Referred to as Imitation Learning in the literature [385].

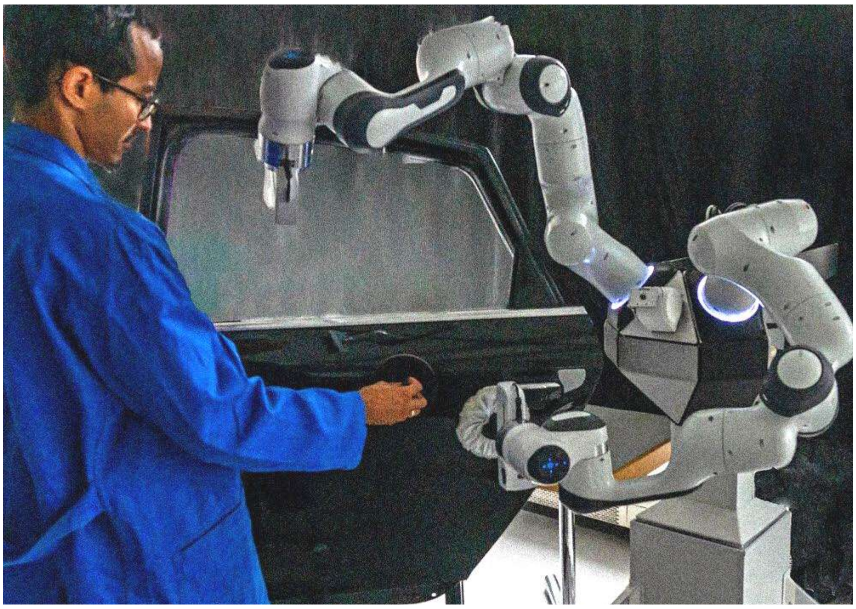

Figure 4.2: In human-robot collaboration, preventing unexpected collisions is vital, especially when humans make unpredictable movements.

4.1.2 Impulse Orb Approach

Consider a human-robot collaboration environment in which the robot needs to avoid collisions with a human, as illustrated in Figure 4.2. A typical approach to address this involves adapting the robot motion trajectory $\boldsymbol{x}_d(t)$. However, in a confined collaborative environment, adjusting the robot trajectory to prevent collisions with the human might inadvertently lead to collisions with the environment. In such scenarios, rather than modifying the geometric attributes of the trajectory, the emphasis can be placed on adjusting its timing. As explained in the preceding section, this can be achieved by encoding the desired motion using the phase variable ϕ, yielding the phase-encoded desired path $\boldsymbol{x}_d(\phi)$. Subsequently, by adapting the phase trajectory $\phi(t)$—for example, through the phase velocity adaptation law (4.1)—the timing characteristics of $\boldsymbol{x}_d(t)$ can be altered while keeping its geometric characteristics unchanged.

The implementation of adaptation law (4.1) involves a phase velocity adaptation gain σ_{coll}. When there is a potential for collisions with the human, the phase progress speed Ω is decreased. This can be accomplished by introducing a braking gain $\eta \in [0, 1]$, where the value of η can be fine-tuned to adjust the desired trajectory according to Table 4.1. The collision-preventing phase velocity adaptation gain σ_{coll} is then defined as

$$\sigma_{\text{coll}} = 1 - \eta. \tag{4.3}$$

In the following, several methods for determining the value of the braking gain η and, consequently, the adaptation gain σ_{coll} are proposed. Throughout these methods, the human pose, representing any specific point on a particular body part, is denoted as $\boldsymbol{x}_h \in \mathbb{R}^m$ and is utilized to determine the braking gain value.

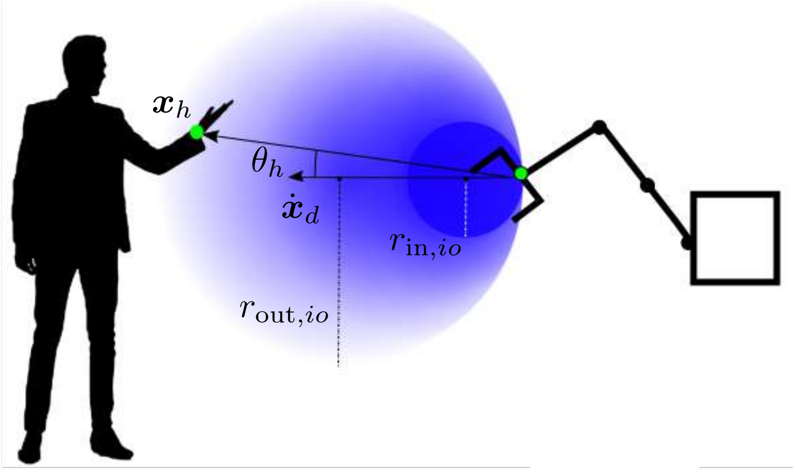

Figure 4.3: Visualization of an impulse orb.

Braking gain value	Corresponding desired behavior
$\eta = 1$	Full stoppage
$0 < \eta < 1$	Speed reduction
$\eta = 0$	No speed reduction

Table 4.1: The intended effects of the braking gain value on the phase progress speed.

The first approach, termed the *Impulse Orb* (IO) method, involves defining a geometric orb composed of two concentric virtual spheres. The virtual orb is attached to the robot end-effector and is oriented in the direction of the desired velocity $\dot{\boldsymbol{x}}_d(t)$. see Figure 4.3. By assessing the location of the human relative to this orb, the value of the braking gain can be determined. To achieve this, first, considering $\boldsymbol{x}_t, \boldsymbol{x}_{h,t} \in \mathbb{R}^{m_t}$ as the translational components of the robot end-effector and human pose vectors $\boldsymbol{x}, \boldsymbol{x}_h \in \mathbb{R}^m$, respectively, the relative position between them (i.e., ${}_{\text{ee}}\boldsymbol{p}_h \in \mathbb{R}^{m_t}$) can be derived as

$$ {}_{\text{ee}}\boldsymbol{p}_h = \boldsymbol{x}_{h,t} - \boldsymbol{x}_t. \tag{4.4}$$

The Impulse Orb braking gain value η_{io} can then be determined as a smooth function as

$$\eta_{io}=\begin{cases} 1 & \text{if } \frac{0.5}{r_{\text{in,r}}} \leq \frac{\cos(\theta_h)}{\|{}_{\text{ee}}\boldsymbol{p}_h\|}, \\ \frac{1}{2}\left(1-\cos\left(\pi\frac{\frac{0.5\cos(\theta_h)}{\|{}_{\text{ee}}\boldsymbol{p}_h\|}-\frac{1}{r_{\text{out},io}}}{\frac{1}{r_{\text{in},io}}-\frac{1}{r_{\text{out},io}}}\right)\right) & \text{if } \frac{0.5}{r_{\text{out},io}} \leq \frac{\cos(\theta_h)}{\|{}_{\text{ee}}\boldsymbol{p}_h\|} < \frac{0.5}{r_{\text{in},io}}, \\ 0 & \text{else,} \end{cases} \tag{4.5}$$

in which θ_h is the angle between the robot desired velocity $\dot{\boldsymbol{x}}_d(\phi)$ and the relative position ${}_{\text{ee}}\boldsymbol{p}_h$. Additionally, $r_{\text{in},io}, r_{\text{out},io} \in \mathbb{R}_{>0}$ are the radii of the inner and the outer virtual spheres respectively, where $r_{\text{out},io} \geq r_{\text{in},io}$; see Figure 4.3. To address the hypothesis that higher robot speed may lead to a higher probability of human collision, the dimensions of the orb

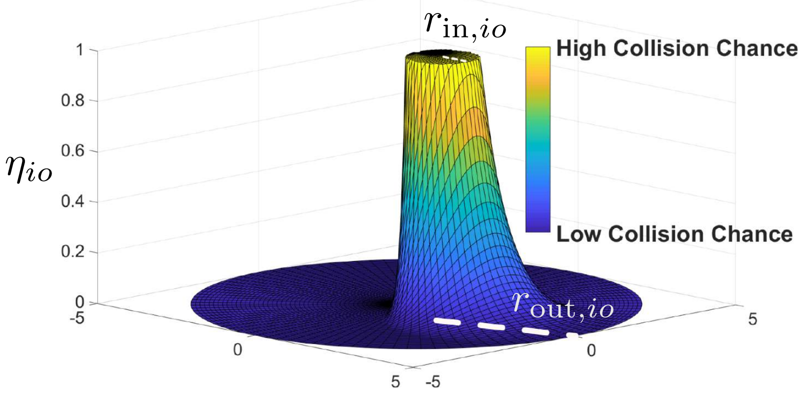

Figure 4.4: The variation of the braking gain η_{io} across a planar cross-section of an impulse orb with $r_{\mathrm{in},io} = 0.075$ m and $r_{\mathrm{out},io} = 0.225$ m.

are scaled based on the robot desired velocity, as follows:

$$r_{\mathrm{in},io} = \xi_{\mathrm{in},io} \|\dot{\boldsymbol{x}}_d\|, \tag{4.6}$$

$$r_{\mathrm{out},io} = \xi_{\mathrm{out},io} \|\dot{\boldsymbol{x}}_d\|, \tag{4.7}$$

where $\xi_{\mathrm{in},io}, \xi_{\mathrm{out},io} \in \mathbb{R}_{>0}$ are the user-defined inner and outer sphere radius lengths, respectively, for when $\|\dot{\boldsymbol{x}}_d\| = 1$ m/s. Subsequently, (4.5) can be rewritten[3] as

$$\eta_{io} = \begin{cases} 1 & \text{if } \frac{0.5}{\xi_{\mathrm{in},io}} \leq \frac{\dot{\boldsymbol{x}}_d^T \, {}_{\mathrm{ee}}\boldsymbol{p}_h}{{}_{\mathrm{ee}}\boldsymbol{p}_h^T \, {}_{\mathrm{ee}}\boldsymbol{p}_h}, \\ \frac{1}{2}\left(1 - \cos\left(\pi \frac{\frac{0.5\dot{\boldsymbol{x}}_d^T \, {}_{\mathrm{ee}}\boldsymbol{p}_h}{{}_{\mathrm{ee}}\boldsymbol{p}_h^T \, {}_{\mathrm{ee}}\boldsymbol{p}_h} - \frac{1}{\xi_{\mathrm{out},io}}}{\frac{1}{\xi_{\mathrm{in},io}} - \frac{1}{\xi_{\mathrm{out},io}}}\right)\right) & \text{if } \frac{0.5}{\xi_{\mathrm{out},io}} \leq \frac{\dot{\boldsymbol{x}}_d^T \, {}_{\mathrm{ee}}\boldsymbol{p}_h}{{}_{\mathrm{ee}}\boldsymbol{p}_h^T \, {}_{\mathrm{ee}}\boldsymbol{p}_h} < \frac{0.5}{\xi_{\mathrm{in},io}}, \\ 0 & \text{else.} \end{cases} \tag{4.8}$$

Figure 4.4 illustrates the values of η_{io} for a representative orb dimension.

The Impulse Orb approach adapts the desired trajectory based on the robot's direction of motion in relation to the human's location, considering the robot speed. This approach offers an advantage over similar standard methods in the literature, such as the *Reduced Speed Zone* (RSZ) approach [105], where the proximity of the human is considered without accounting for the robot direction of motion. Unlike the Impulse Orb approach, the Reduced Speed Zone approach may trigger unnecessary trajectory adaptations when the human is close but not in the robot path, making the Impulse Orb approach a more effective solution.

4.1.3 Prognosis Window Approach

In the second proposed method for adapting the phase velocity to prevent collisions, not only is the relative location of the current setpoint to the human considered, but also upcoming setpoints that have not yet been commanded to the controller are taken into account during a collision probability assessment stage. This approach is referred to as the *Prognosis Window* approach, where a designated portion of the encoded path is considered for collision

---

[3] It is considered that $\dot{\boldsymbol{x}}_d^T \ {}_{\mathrm{ee}}\boldsymbol{p}_h = \|\dot{\boldsymbol{x}}_d\| \ \|{}_{\mathrm{ee}}\boldsymbol{p}_h\| \ \cos(\theta_h)$.

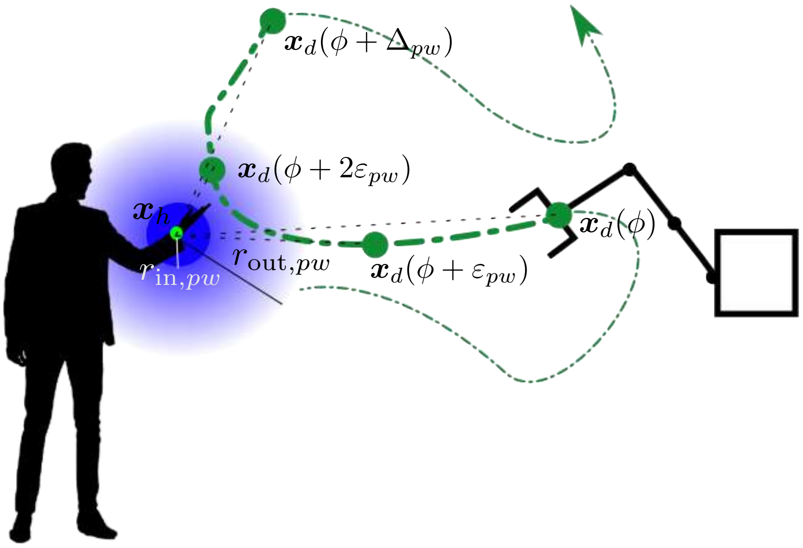

Figure 4.5: Visualization of a prognosis window along the encoded path.

probability assessment. Denoting the minimum and maximum values of the phase as 0 and 1, respectively, a window length $\Delta_{pw} \in [0,1]$ is chosen. Subsequently, with n_{pw} setpoints along the window, equally spaced from each other with the distance of

$$\varepsilon_{pw} = \frac{\Delta_{pw}}{n_{pw}}, \tag{4.9}$$

a number of n_{pw} weighted proximity values can be defined between these setpoints and the human pose as (see Figure 4.5)

$$\psi_{i,pw} = \frac{\xi_{i,pw}}{\|\boldsymbol{x}_d(\phi+i\varepsilon_{pw}) - \boldsymbol{x}_h\|}, \qquad i \in \{0,1,\dots,n_{pw}\}. \tag{4.10}$$

Here, $\xi_{i,pw}$ represents the priority weight of the proximity of the i-th setpoint within the window. If it is more crucial to avoid a collision at the beginning of the window, higher priority gains should be assigned to the setpoints with lower indices, and vice versa. Subsequently, an overall weighted proximity value can be defined as

$$\psi_{pw} = \sum_{i=0}^{n_{pw}} \psi_{i,pw}. \tag{4.11}$$

To evaluate the collision potential, two virtual spheres are centered at the human location, with radius lengths denoted as $r_{\text{in},pw}, r_{\text{out},pw} \in \mathbb{R}_{\geq 0}$, where $r_{\text{out},pw} \geq r_{\text{in},pw}$. Consequently, two braking boundaries are established as

$$\beta_{\text{in},pw} = \sum_{i=0}^{n_{pw}} \frac{\xi_{i,pw}}{r_{\text{in},pw}}, \tag{4.12}$$

$$\beta_{\text{out},pw} = \sum_{i=0}^{n_{pw}} \frac{\xi_{i,pw}}{r_{\text{out},pw}}. \tag{4.13}$$

Window location	Corresponding gain value
Within the inner sphere	$\eta_{pw} = 1$
Beyond the inner sphere but within the outer sphere	$0 < \eta_{pw} < 1$
Beyond the outer sphere	$\eta_{pw} = 0$

Table 4.2: Derivation of the braking gain value using the Prognosis Window approach.

Next, the relative location of the prognosis window with respect to the two spheres is considered to determine the braking gain value η_{pw}. This is done via a smooth function derived as

$$\eta_{pw} = \begin{cases} 1 & \text{if } \beta_{\text{in},pw} \leq \psi_{pw}, \\ \frac{1}{2}\left(1 + \cos\left(\pi \frac{\beta_{\text{in},pw} - \psi_{pw}}{\beta_{\text{in},pw} - \beta_{\text{out},pw}}\right)\right) & \text{if } \beta_{\text{out},pw} \leq \psi_{pw} < \beta_{\text{in},pw}, \\ 0 & \text{else.} \end{cases} \tag{4.14}$$

The rationale behind this derivation is illustrated in Table 4.2.

Fused Approach

The two proposed approaches, Impulse Orb and Prognosis Window, each possess distinct advantages. The Prognosis Window approach is better suited for static environments, where predicting collisions with upcoming setpoints is meaningful. On the other hand, the Impulse Orb approach is more fitting for dynamic scenarios that require a consistent re-evaluation of the proximity of the human to the end-effector. To harness the benefits of both, these two approaches can be integrated in a *Fused Approach.* Depending on the scenario, the priority of each approach can take precedence over the other. Considering $\xi_{io}, \xi_{pw} \in \mathbb{R}_{\geq 0}$ as the priority weights for the Impulse Orb and Prognosis Window approaches, respectively, the braking gain value for the Fused approach can be defined as

$$\eta_{fu} = \frac{\xi_{io}\eta_{io} + \xi_{pw}\eta_{pw}}{\xi_{io} + \xi_{pw}}, \tag{4.15}$$

in which η_{io} and η_{pw} are the braking gain values associated with the Impulse Orb and Prognosis Window approaches, respectively, defined in (4.8) and (4.14). Clearly, assigning zero priority to either approach negates its impact on the overall velocity adaptation.

Remark: Given that the phase speed adaptation gain ranges from 0 to 1, the proposed methods do not amplify the amplitude of the desired trajectory. Referring to (3.24), when using only an impedance controller (i.e., $\boldsymbol{f}_f = \boldsymbol{0}$), and for the same $\boldsymbol{f}_{\text{ext}}$, this approach leads to a reduction in the power's magnitude, $P_{T,i} = -\dot{\boldsymbol{x}}_d^T \boldsymbol{f}_{\text{ext}}$. Hence, if $P_{T,i}$ is positive (indicating passivity violation), the introduced collision-prevention methods diminish such passivity-violating power. On the other hand, if $P_{T,i}$ is negative (indicating no passivity violation), these methods do not violate passivity, as σ_{coll} is never negative.

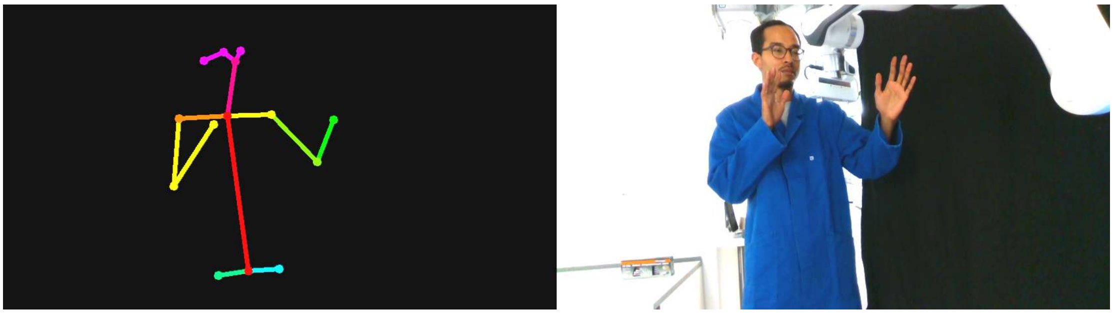

Figure 4.6: Estimated body configuration using the OpenPose software in the experiments.

4.1.4 Experiments

To validate the efficacy of the collision-preventing policies, a 7-DoF Franka Emika robot is utilized, tasked with moving in close proximity to a human without collision. Human location is determined through an Intel RealSense RGB-D Camera. Prior to the experiments, camera calibration is performed using AruCo markers to establish the relative pose of the camera frame to the robot base. The images are processed using the camera Python API [387] and the OpenCV3 software [347]. OpenPose library [388] is employed to analyze color images, calculating estimated human keypoints based on the BODY-25 model, as shown in Figure 4.6. The identified wrist locations serve as the human position for implementing the proposed approaches.

Experiment 1: Impulse Orb Approach

In the initial experiment, the robot desired trajectory follows a linear path spanning 1 m along the robot x-axis; see Figure 4.7. The desired velocity initiates from 0 m/s, reaching a constant maximum of 0.3 m/s within a 0.4 s duration. The human wrist is situated at a distance of 0.12 m from the desired path at 0.35 m along the x-axis; refer to Figure 4.7. The Impulse Orb is configured with $\xi_{\mathrm{in},io} = 0.15$ m and $\xi_{\mathrm{out},io} = 0.45$ m.

To assess the Impulse Orb approach's effectiveness, it is compared to the standard Reduced Speed Zone approach [105]. In the latter, a fixed-sized sphere with a radius of 0.3 m is defined around the robot end-effector. When the human is detected within this sphere, the desired speed is reduced to 1/3 of the original speed.

As depicted in Figure 4.8, during time stage ①, when the desired velocity increases, the orb size dynamically adjusts following (4.6) and (4.7). This adjustment is manifested in the reduction of $1/(2r_{\mathrm{in},io})$ and $1/(2r_{\mathrm{out},io})$. Conversely, the Reduced Speed Zone maintains a fixed size. Throughout this stage, the braking gain variable η remains at zero, resulting in the phase velocity adaptation gain σ remaining at 1.

As evident from the results, during stage ② of the experiments, the robot speed diminishes due to proximity to the human. Notably, the Impulse Orb approach exhibits less conservative behavior compared to the Reduced Speed Zone approach, where the duration of the entire movement is nearly twice that of the Impulse Orb approach. Finally, the velocity adaptation gains return to 1 at stage ③, where the robot is not close to the human wrist anymore.

Figure 4.7: Experiment 1 – Snapshots of the experiment with the sequential timing ⓘ-ⓘⓘ-ⓘⓘⓘ.

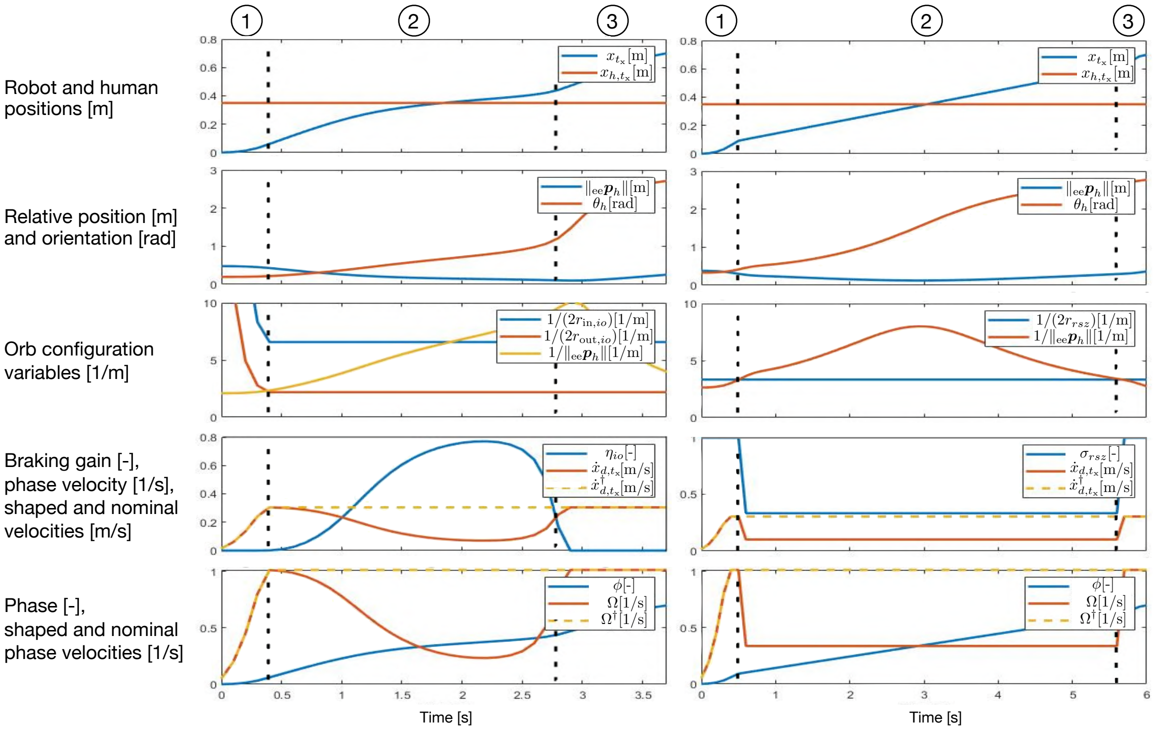

Figure 4.8: Experiment 1 – While collisions are avoided in both experiments, the Impulse Orb approach (left) exhibits less conservative behavior compared to the Reduced Speed Zone approach (right).

Experiment	Δ_{pw}	n_{pw}	$\xi_{0,pw}$	$\xi_{1,pw}$	$\xi_{2,pw}$	$\xi_{3,pw}$	$r_{\mathrm{in},pw}$ [m]	$r_{\mathrm{out},pw}$ [m]
2.a	0.045	3	4	3	2	1	0.05	0.15
2.b	0.045	3	1	2	3	4	0.05	0.15
2.c	0.45	3	4	3	2	1	0.05	0.15

Table 4.3: Derivation of the braking gain value using the Prognosis Window approach.

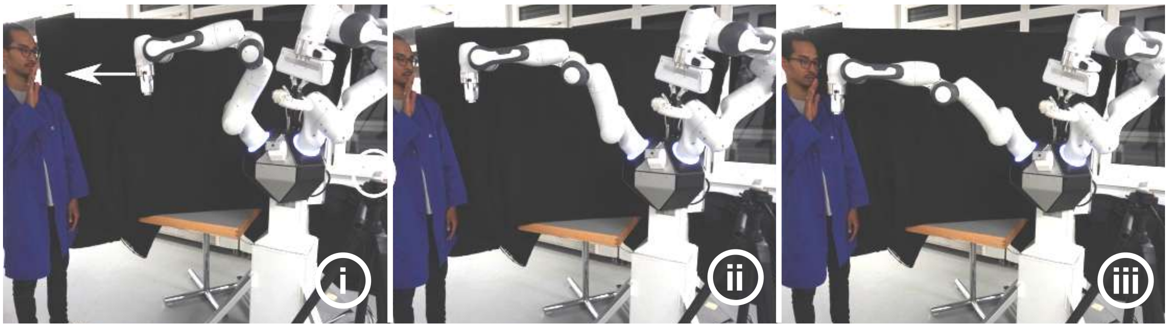

Figure 4.9: Experiment 2 – Snapshots of the experiment with the sequential timing ⓘ-ⓘⓘ-ⓘⓘⓘ.

Experiment 2: Prognosis Window Approach

In this experiment, the Prognosis Window approach is assessed for various values of the window length Δ_{pw} and proximity weights ξ_{pw}. Table 4.3 outlines three different sets of values employed in the experiment. For all three scenarios, the desired trajectory aligns with the robot x-axis and is encoded into the phase domain as

$$x_{d,t_\mathrm{x}} = 0.35\cos(2\pi\phi) - 0.35, \tag{4.16}$$

$$\dot{x}_{d,t_\mathrm{x}} = -0.7\pi\Omega^\dagger\sin(2\pi\phi), \tag{4.17}$$

with a nomminal phase velocity of $\Omega^\dagger = 0.1$. The human wrist is positioned along the desired path at $x_{h,t_\mathrm{x}} = 0.4$ m, as illustrated in Figure 4.9.

As depicted in Figure 4.10, during stage ① of the experiments, the window in Experiments 2.a and 2.b enters the outer sphere around the human later than in Experiment 2.c, where the window length is much longer. The extended window length in Experiment 2.c enables the approach to discern that as the robot approaches the human, the path configuration suggests that a collision is unlikely, prompting the braking gain variable to return to zero. This distinction is not observed in Experiments 2.a and 2.b, where the short window length inhibits such realization. Consequently, the robot halts in these two experiments during stage ②. Furthermore, the impact of the proximity weight distribution $\xi_{i,pw}$ on braking behavior is evident in the differences between Experiments 2.a and 2.b. In Experiment 2.b, the weights are distributed with more emphasis on the setpoints farther into the window. Consequently, collision prediction occurs earlier compared to Experiment 2.a.

Experiment 3: Fused Approach

To evaluate the Fused approach, the same desired trajectory derived in (4.16) and (4.17) is used. This time, both human wrists are in proximity to the robot motion. The right wrist is located as in the previous experiment, and the left wrist is positioned at 0.35 m on the x-axis and 0.05 m on the y-axis; see Figure 4.11. The collision-preventing policy consistently selects the closest wrist to the end-effector for the velocity adaptation law. Three experiments are performed with three distinct priority weights: $\xi_{io} = 1$, $\xi_{pw} = 0$ for experiment 3.a, $\xi_{io} = 0$, $\xi_{pw} = 1$ for Experiment 3.b, and $\xi_{io} = 0.5$, $\xi_{pw} = 0.5$ for Experiment 3.c.

As seen in Figure 4.12, the system exhibits a conservative reaction when only the Impulse Orb approach is being used. The robot approaches the edge of the encoded path, and because

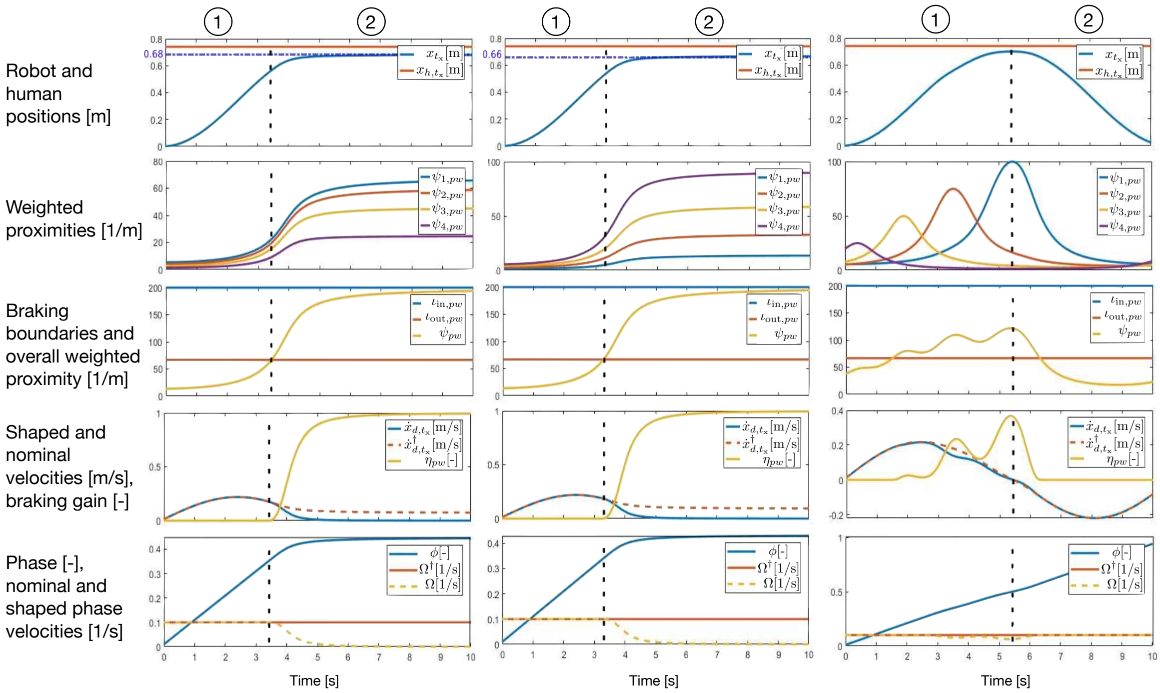

Figure 4.10: Experiment 2 – From left to right: Experiment 2.a and 2.b with short prognosis windows, and Experiment 2.c (rightmost) with a longer window.

it assumes that a collision is imminent, the braking gain value increases, leading the robot to come to a stop. On the other hand, when only the Prognosis Window is employed, and the size of windows is not well-tuned, the end-effector may undergo premature stoppage, even though the trajectory is not directed toward the human position but is only in the vicinity of the human. In this case, as well, the robot comes to a halt despite the absence of an imminent collision. The effectiveness of the overall behavior can be improved by fusing both approaches, as demonstrated in Experiment 3.c. In this case, the robot does not stop, and no collision occurs; see Figure 4.12.

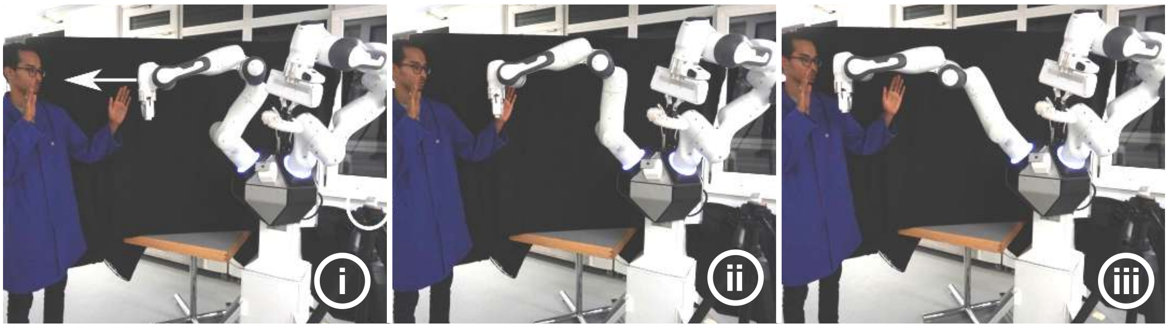

Figure 4.11: Experiment 3 – Snapshots of the experiment with the sequential timing (i)-(ii)-(iii).

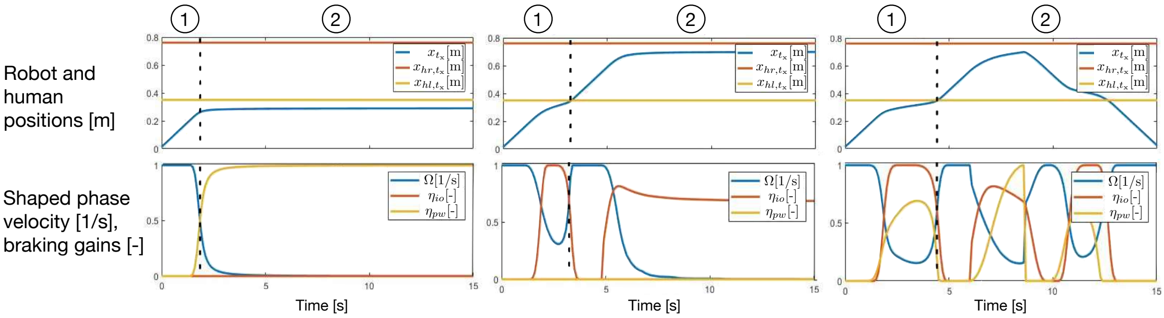

Figure 4.12: Experiment 3 – From left to right: Experiment 3.a using only the Impulse Orb approach, Experiment 3.b using only the Prognosis Window approach, and Experiment 3.c using the Fused approach.

4.2 Path-Constrained Adaptive Haptic Motion Guidance

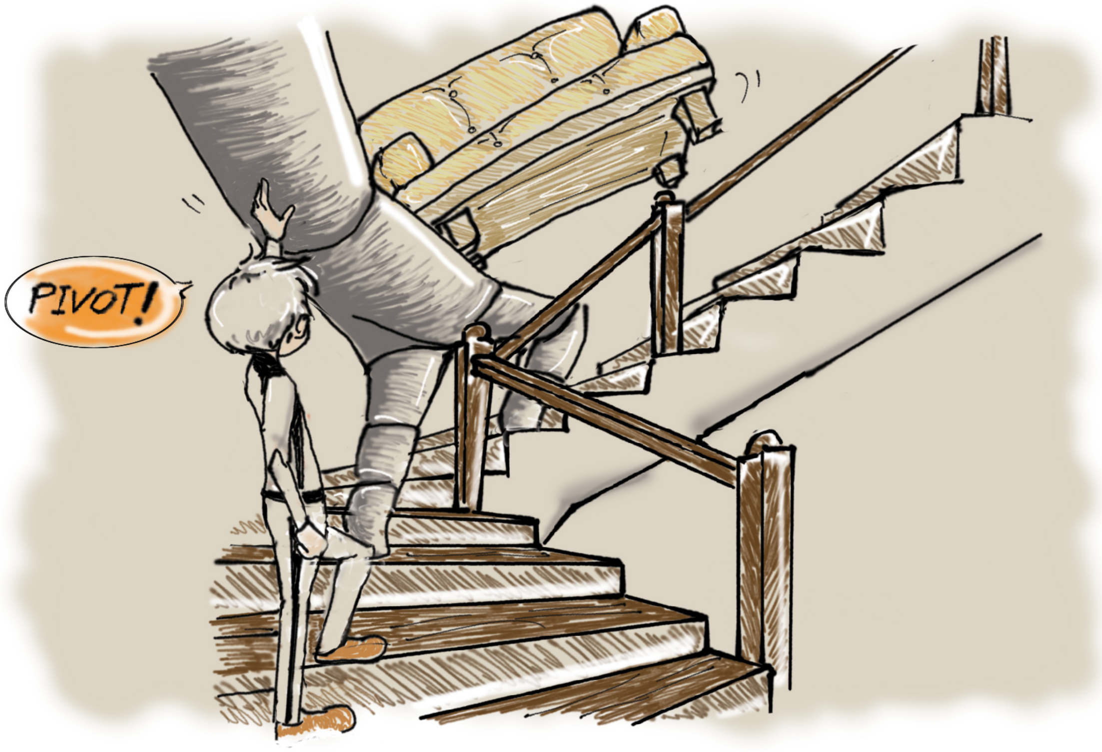

There are situations that demand the combined expertise of both humans and robots to execute a task effectively. For instance, when the robot's strength and accuracy need to be complemented by the profound decision-making capability of a human. A relevant scenario in this context is when human guidance becomes essential for the robot motion under strict geometrical constraints, such as adhering to a specific path. Figure 4.13 illustrates various instances of this collaboration. In this section, this challenge is addressed through three primary steps. Firstly, a phase-based motion guidance law is developed for a robot. Next, to improve human ergonomics and comfort, a configuration-dependent adaptation policy is introduced for the proposed guidance law. Finally, stability is ensured through the utilization of a virtual energy tank. Figure 4.14 presents the high-level architecture of the approach proposed in this section.

4.2.1 Human-Guided Phase-Based Motion Generator

Consider a rigid-body robot with the dynamics model (2.7). The robot holds an object (e.g., a tool) and is tasked with moving it along a constrained path, guided by human, utilizing a Cartesian impedance controller defined by (3.1); see Figure 4.15. For simplicity, the object dynamics are assumed to be incorporated in the mass, centrifugal, and Coriolis matrices in the robot dynamics model. The human guidance input is conveyed through the interaction wrench $\boldsymbol{f}_h \in \mathbb{R}^m$, applied by the human to the robot. Considering (3.13) and excluding the

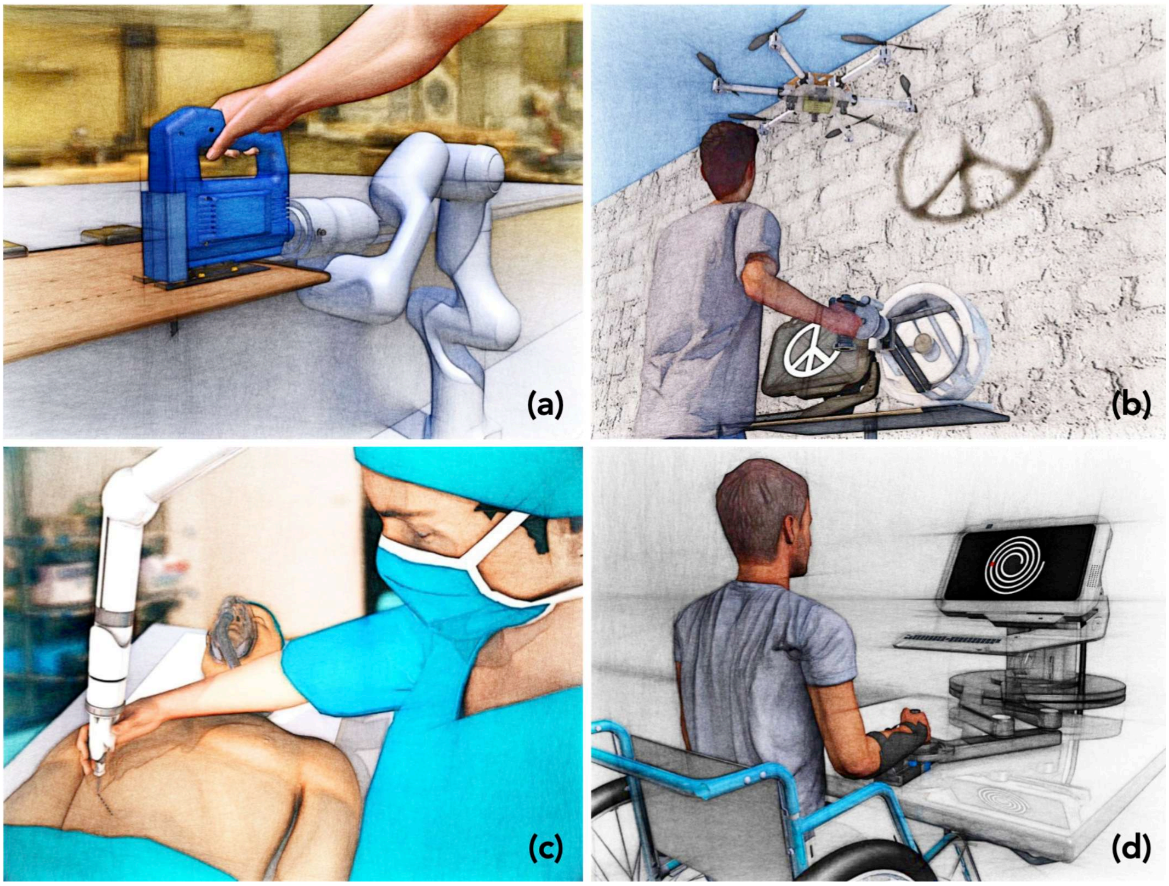

Figure 4.13: Examples of path-constrained haptic motion guidance scenarios – (a) cutting wood with a jigsaw machine (b) remote graffiti execution (c) accurate surgical incision execution (d) movement rehabilitation.

force control input, the closed-loop dynamics of this human-robot interaction setup become

$$\boldsymbol{M}_C(\boldsymbol{q})\ddot{\tilde{\boldsymbol{x}}} + \boldsymbol{C}_C(\boldsymbol{q}, \dot{\boldsymbol{q}})\dot{\tilde{\boldsymbol{x}}} + \boldsymbol{D}_C\dot{\tilde{\boldsymbol{x}}} + \boldsymbol{K}_C\tilde{\boldsymbol{x}} + \boldsymbol{f}_h = \boldsymbol{0}, \tag{4.18}$$

in which $\boldsymbol{f}_{\text{ext}}$ is replaced with $\boldsymbol{f}_h$.

In order to derive and implement the proposed motion guidance policy, the path is first encoded using phase, i.e., $\boldsymbol{x}_d(\phi)$, as elaborated in Section 2.1. The human-applied wrench $\boldsymbol{f}_h$ is then mapped into the phase domain, yielding the *steering force* variable $f_s \in \mathbb{R}$ derived as

$$f_s = \boldsymbol{f}_h^T \frac{d\boldsymbol{x}_d(\phi)}{d\phi}. \tag{4.19}$$

Next, the steering force is set as an input to a non-linear *phase-based admittance law* defined as

$$m_\phi\ddot{\phi} + d_\phi\dot{\phi} + c_\phi\dot{\phi}^2 = f_s, \tag{4.20}$$

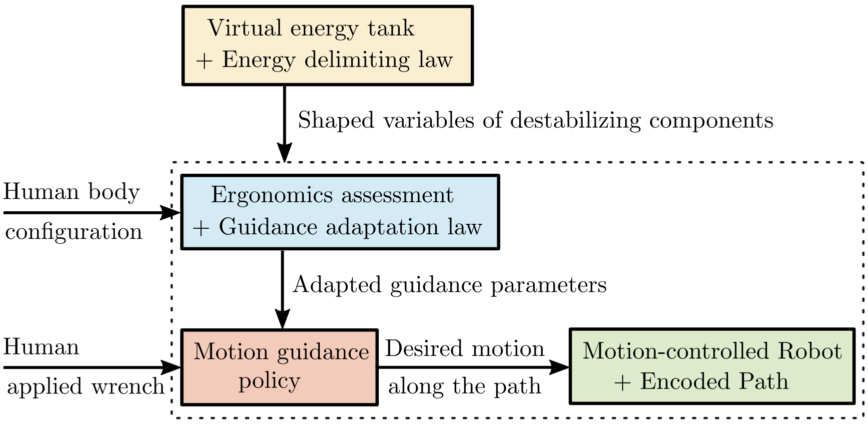

Figure 4.14: Approach structure – The concepts related to modeling and motion control (green) are presented in the previous sections, while the guidance law (red), guidance adaptation (blue), and stability (yellow) concepts are explained in this section.

where $m_\phi, d_\phi \in \mathbb{R}_{\geq 0}$ denote phase-based mass and damping coefficients, and $c_\phi \in \mathbb{R}$ represents the coefficient for the non-linear term $\dot{\phi}^2$. As shown in the following, the rationale for the nonlinear form of the phase-based admittance law is to provide an intuitive physical representation, simplifying parameter tuning.

The phase-based admittance (4.20) serves to transform the applied wrench $\boldsymbol{f}_h$ into the phase trajectory $\phi(t)$ yielding the intended motion $\boldsymbol{x}_d(\phi(t))$ along the predefined path. The phase-based parameters m_ϕ, d_ϕ, and c_ϕ govern the characteristics of this transformation, affecting the force required for a specific desired motion profile. Yet, adjusting them might lack intuitiveness, as (4.20) primarily addresses phase dynamics rather than direct motion aspects. To address this, auxiliary parameters $m_a, d_a \in \mathbb{R}^+$ are introduced. These parameters endow the wrench-to-motion mapping with the familiar properties of a mass-damper system. To achieve this, the phase-based admittance parameters are defined as

$$m_\phi = m_a \frac{d\boldsymbol{x}_d^T(\phi)}{d\phi} \frac{d\boldsymbol{x}_d(\phi)}{d\phi}, \tag{4.21}$$

$$d_\phi = d_a \frac{d\boldsymbol{x}_d^T(\phi)}{d\phi} \frac{d\boldsymbol{x}_d(\phi)}{d\phi}, \tag{4.22}$$

$$c_\phi = m_a \frac{d^2\boldsymbol{x}_d^T(\phi)}{d\phi^2} \frac{d\boldsymbol{x}_d(\phi)}{d\phi}. \tag{4.23}$$

As a result, the guidance policy (4.20) can be effectively tailored by adjusting the intuitive admittance mass and damping coefficients m_a and d_a with standard units [kg, kg m^2] and [Ns/m, Nms/rad], respectively. When the contact wrench aligns with the path tangent vector, the phase-based guidance law (4.20) transforms into

$$m_a \ddot{\boldsymbol{x}}_d + d_a \dot{\boldsymbol{x}}_d = \boldsymbol{f}_h. \tag{4.24}$$

The proposed phase progress control (4.19)–(4.24) empowers the human operator to determine the intended motion along the constrained path by exerting a wrench on the robot. Subsequently, the robot's controller follows the generated desired motion. By adjusting the

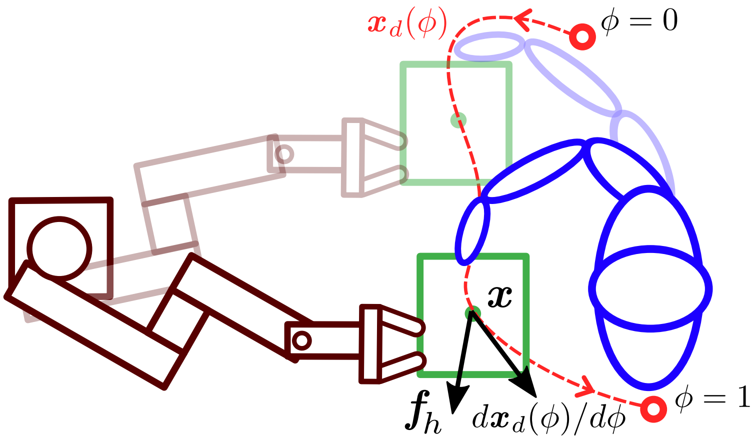

Figure 4.15: A human guides a robot (carrying an object) along a predefined path. The applied wrench $\boldsymbol{f}_h$ directs the desired motion through the encoded path $\boldsymbol{x}_d(\phi)$, from $\phi = 0$ to $\phi = 1$.

admittance mass and damping coefficients m_a and d_a, the responsiveness of this guidance law can be fine-tuned. Lower values of these coefficients result in faster motions for a given wrench, while higher values lead to slower motion. Depending on task requirements, admittance coefficients can be preset to suitable values or alternatively adapted dynamically according to the task situation. In the upcoming section, an exemplary adaptation policy is presented that takes into account the estimation of the human operator configuration-based guiding capability.

Derivation of the Admittance Phase-Based Parameters

The goal is to establish a mass-damper admittance property between the contact wrench $\boldsymbol{f}_h$ and the desired motion $\boldsymbol{x}_d(t)$ when $\boldsymbol{f}_h$ is aligned with the path tangent vector $d\boldsymbol{x}_d/d\phi$, yielding (4.24). Considering the chain rules

$$\dot{\boldsymbol{x}}_d = \dot{\phi}\frac{d\boldsymbol{x}_d}{d\phi}, \tag{4.25}$$

$$\ddot{\boldsymbol{x}}_d = \dot{\phi}^2\frac{d^2\boldsymbol{x}_d}{d\phi^2} + \ddot{\phi}\frac{d\boldsymbol{x}_d}{d\phi}, \tag{4.26}$$

the admittance law (4.24) becomes

$$m_a\ddot{\phi}\frac{d\boldsymbol{x}_d}{d\phi} + m_a\dot{\phi}^2\frac{d^2\boldsymbol{x}_d}{d\phi^2} + d_a\dot{\phi}\frac{d\boldsymbol{x}_d}{d\phi} = \boldsymbol{f}_h. \tag{4.27}$$

By multiplying the tangent vector $d\boldsymbol{x}_d(\phi)/d\phi$ to (4.27) it follows

$$\ddot{\phi}\underbrace{m_a\frac{d\boldsymbol{x}_d^T}{d\phi}\frac{d\boldsymbol{x}_d}{d\phi}}_{m_\phi} + \dot{\phi}^2\underbrace{m_a\frac{d^2\boldsymbol{x}_d^T}{d\phi^2}\frac{d\boldsymbol{x}_d}{d\phi}}_{c_\phi} + \dot{\phi}\underbrace{d_a\frac{d\boldsymbol{x}_d^T}{d\phi}\frac{d\boldsymbol{x}_d}{d\phi}}_{d_\phi} = \underbrace{\boldsymbol{f}_h^T\frac{d\boldsymbol{x}_d}{d\phi}}_{f_s}. \tag{4.28}$$

Stopping Policy in the Contact-Free Mode

The phase-based admittance law (4.20) adjusts the phase value ϕ, either increasing or decreasing it. To constrain ϕ within the range $[0,1]$ for iterative tasks (e.g., circular path traversal), the phase resets to 0 or 1 upon reaching the boundary. Conversely, for non-repetitive tasks (e.g., linear segment motion), one approach is to exponentially increase d_ϕ as ϕ approaches the borders or, alternatively, to saturate the phase value. Note that even when f_s is absent (e.g., during contact-free mode), the phase value may alter due to the virtual momentum $m_\phi\dot{\phi}$, which could be undesired when the human lacks contact and control over the motion. To counter this, the following stopping policy can be implemented by using a third-order polynomial to smoothly halt the phase evolution within a duration $t_s > 0$ as soon as $f_s = 0$.

$$\dot{\phi} = \begin{cases} a_3(t-t_0)^3 + a_2(t-t_0)^2 + a_1(t-t_0) + a_0 & \text{if } t \leq t_s, \\ 0 & \text{else.} \end{cases} \tag{4.29}$$

The incorporated parameters are defined as

$$a_0 = \dot{\phi}(t_0), \tag{4.30}$$

$$a_1 = \ddot{\phi}(t_0), \tag{4.31}$$

$$a_2 = -\frac{3\dot{\phi}(t_0) + 2\ddot{\phi}(t_0)t_s}{t_s^2}, \tag{4.32}$$

$$a_3 = \frac{2\dot{\phi}(t_0) + \ddot{\phi}(t_0)t_s}{t_s^3}. \tag{4.33}$$

Phase-Based Motion Generator vs. Dynamic Movement Primitives

As elucidated in Section 3.3, the Dynamic Movement Primitive (DMP) is a well-established system allowing for the encoding of a trajectory. Given (3.100), the DMP formulation also incorporates the phase variable. Therefore, it is worthwhile to compare DMPs with the proposed phase-based motion generator approach (4.19)–(4.20).

To facilitate this comparison without altering the derivation, the variable conventions used in the DMP formulation (3.100) and (3.102) are adjusted as follows:

$$\Omega := \frac{1}{\sqrt{m_a}}, \tag{4.34}$$

$$\boldsymbol{x}_{\mathrm{DMP}} := \boldsymbol{x}_d, \tag{4.35}$$

$$\alpha_z := \frac{d_a}{\sqrt{m_a}}, \tag{4.36}$$

$$\beta_z := \frac{k_a\sqrt{m_a}}{d_a}. \tag{4.37}$$

Thus, the DMP formulation (3.100) transforms into

$$m_a\ddot{\boldsymbol{x}}_d + d_a\dot{\boldsymbol{x}}_d = k_a(\boldsymbol{g}_z - \boldsymbol{x}_d) + \boldsymbol{f}_z(\phi). \tag{4.38}$$

By comparing (4.38) with (4.24), the primary distinction between a Dynamic Movement Primitive and the proposed human-guided motion generator becomes evident. Considering (4.38), in a DMP, the desired trajectory $\boldsymbol{x}_d(t)$ can be conceptualized as the outcome of the summation of two wrenches acting on a mass-damper system. These wrenches comprise a linear spring wrench with stiffness k_a, extended between the current setpoint $\boldsymbol{x}_d$ and a goal variable $\boldsymbol{g}_z$, as well as a phase-encoded wrench $\boldsymbol{f}_z(\phi)$. By adjusting the parameters m_a, d_a, and k_a in a coupled manner, the convergence speed to the goal $\boldsymbol{g}_z$ can be regulated. Traditionally, such parameter adaptations should also influence predetermined phase dynamics, for instance, as outlined in [383] via

$$\sqrt{m_a}\dot{\phi} = -\kappa_z \phi, \tag{4.39}$$

where $\kappa_z \in \mathbb{R}_{\geq 0}$ is a user-defined parameter. However, as seen in (4.24), in the proposed phase-based motion generation law, the applied wrench on the mass-damper system originates solely from the human-applied wrench $\boldsymbol{f}_h$. This grants full authority to the human to adjust the speed. It is important to note that while in DMPs, only the overall duration of the trajectory can be shaped and the dynamics remain unchanged, in the proposed motion guidance law, the progression speed along the path can be dynamically adjusted freely.

4.2.2 Configuration-Driven Motion Guidance Adaptation

The adaptation of guidance law parameters can follow various policies. Here, the proposed policy is founded on the assumption of continuous interaction between the human operator and the robot for guidance. Consequently, the operator must adhere to the resulting robot motion, which could lead to different body configurations and varying abilities to guide. For instance, certain configurations might make applying the guidance wrench more challenging, while in other configurations, moving along with the robot could become difficult. One method to evaluate the guiding capability is to estimate the necessary joint torques and motions for both the guiding wrench $\boldsymbol{f}_h$ and the resulting guided motion $\boldsymbol{x}_d(t)$. The required joint values depend on the joint-to-Cartesian space mapping, represented by the Jacobian matrix $\boldsymbol{J}_h(\boldsymbol{q}_h) \in \mathbb{R}^{m \times n_h}$, with $\boldsymbol{q}_h \in \mathbb{R}^{n_h}$ being the n_h-DoF human body joint angles. Thus, the evaluation of guidance can be achieved through the ongoing assessment of the effectiveness of the Jacobian matrix. A well-established approach for this purpose is the manipulability concept, initially introduced in [185, 186] for robot arms, and later in [189, 190] for the human body. The mapping $\boldsymbol{J}_h(\boldsymbol{q}_h)$ can be assessed via the so-called *manipulability ellipsoid* with a symmetric positive definite core matrix $\boldsymbol{\Lambda} \in \mathbb{R}^{m \times m}$ defined as

$$\boldsymbol{\Lambda}(\boldsymbol{q}_h) = \boldsymbol{J}_h(\boldsymbol{q}_h)\boldsymbol{\Upsilon}\boldsymbol{J}_h^T(\boldsymbol{q}_h). \tag{4.40}$$

Here, if $\boldsymbol{\Upsilon}$ is an n_h-dimensional identity matrix, (4.40) represents the core matrix of the velocity manipulability ellipsoid [186]. This ellipsoid determines the attainability of end-point velocities in various directions, achieved by selecting joint velocity vectors of unit norm. On the other hand, considering $\boldsymbol{M}_h(\boldsymbol{q}_h) \in \mathbb{R}^{n_h \times n_h}$ as the mass matrix of the body, and defining $\boldsymbol{\Upsilon} = \boldsymbol{M}_h^{-1}(\boldsymbol{q}_h)$, (4.40) characterizes the mobility end-point tensor [59]. This tensor governs the range of achievable end-point motions in different directions when unit-norm wrench vectors are applied to the end-point, while the body is at rest. This concept is similarly employed in other studies, such as in [368], which introduces the concept of the belted ellipsoid to represent inertial properties in the task space, and in [389], which distinguishes between inertial properties associated with individual tasks a robot is supposed to perform. Independent of the choice of $\boldsymbol{\Upsilon}$, the manipulability ellipsoid with a core matrix $\boldsymbol{\Lambda}(\boldsymbol{q})$ can be visualized in the Cartesian space by $\boldsymbol{x}_{\text{ell}} \in \mathbb{R}^m$ via

$$(\boldsymbol{x}_{\text{ell}} - \boldsymbol{x}_h)^T \boldsymbol{\Lambda}^{-1}(\boldsymbol{q}_h)(\boldsymbol{x}_{\text{ell}} - \boldsymbol{x}_h) = 1. \tag{4.41}$$

with $n_\Lambda \leq m$ principal radii along the eigenvectors $\boldsymbol{\nu}_i \in \mathbb{R}^m$ of the core matrix $\boldsymbol{\Lambda}(\boldsymbol{q}_h)$. Their lengths $r_i \in \mathbb{R}_{\geq 0}$ can be determined as

$$r_i = \sqrt{\lambda_i}, \tag{4.42}$$

with $\lambda_i \in \mathbb{R}_{\geq 0}$ being the eigenvalues of $\boldsymbol{\Lambda}(\boldsymbol{q}_h)$. The ellipsoid radii lengths represent the viability of end-point motions in the Cartesian space along their respective directions. A longer radius length r_i implies smaller joint motions are required to achieve the Cartesian motion along that radius. Orthogonal to this ellipsoid is the force manipulability ellipsoid, whose radii determine the feasibility of applying wrenches along their corresponding directions. When the path follows the longest radius of the force manipulability ellipsoid (i.e., the shortest radius of the manipulability ellipsoid (4.40)), smaller joint torque values are necessary to produce the same applied wrench magnitudes. Thus, to evaluate the situation at each phase ϕ, the path direction $d\boldsymbol{x}_d(\phi)/d\phi$ can be compared with the manipulability ellipsoid principal radii directions and lengths. To achieve this, the principal radii can be first projected onto the path direction $\boldsymbol{\nu}(\phi) \in \mathbb{R}^m$, resulting in the projected lengths $l_i \in \mathbb{R}$ via

$$l_i = |r_i \boldsymbol{\nu}_i^T \boldsymbol{\nu}(\phi)|, \tag{4.43}$$

where

$$\boldsymbol{\nu}(\phi) = \frac{d\boldsymbol{x}_d(\phi)/d\phi}{\|d\boldsymbol{x}_d(\phi)/d\phi\|}. \tag{4.44}$$

Considering $\boldsymbol{l}_\Lambda = [l_1, l_2, \ldots, l_{n_\Lambda}]$ being the vector containing the projection lengths, its norm l, denoted as the *projection norm*, is derived as

$$l = \sqrt{\sum_{i=1}^{n_\Lambda} l_i^2} = \sqrt{\sum_{i=1}^{n_\Lambda} (r_i \boldsymbol{\nu}_i^T \boldsymbol{\nu}(\phi))^2}, \tag{4.45}$$

which is always between the shortest and longest principal radii, as demonstrated below. Figure 4.16 depicts an illustrative manipulability ellipsoid with its principal radii, projection lengths, and the projection norm for a 12-DoF human arm model.

To incorporate l into the adaptation of admittance parameters, first, a range $[r_{\min}, r_{\max}]$ needs to be defined. Here, $r_{\min}, r_{\max} \in \mathbb{R}_{\geq 0}$ denote the assumed smallest and largest potential values of l, respectively, associated with $m_{a,\max}, m_{a,\min} \in \mathbb{R}_{\geq 0}$, representing the lowest and highest m_a values. For instance, given that the shortest radius of the manipulability ellipsoid becomes 0 during singularities, one possible choice for presetting $r_{\min}$ could be 0. Similarly, considering $\lambda_{\max}$ as the largest possible eigenvalue of the matrix $\boldsymbol{\Lambda}(\boldsymbol{q}_h)$, $r_{\max}$ may be set to $r_{\max} = \sqrt{\lambda_{\max}}$.

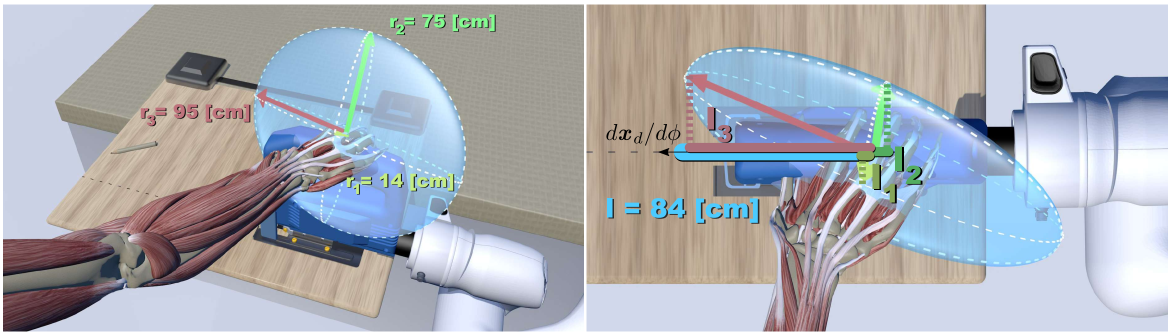

Figure 4.16: A co-manipulation scenario with the manipulability ellipsoid visualization (downscaled) for a right arm 12-DoF kinematics model, based on the VHP dataset [390] with the following joint values (in radian): sternoclavicular [-0.31, 0.33], acromioclavicular [0.47, 0.1, -0.02], glenohumeral [0.52, 0.37, -0.98], humeroulnar [0.17], radioulnar [1.86] and radiocarpal [-0.11, -0.25]. The right figure depicts the principal radii projected to the path direction, the associated projected lengths l_i, and the norm l.

The guidance law can be adjusted in a manner such that when l approaches $r_{\max}$, less interaction wrench from the human is needed to guide the motion. Conversely, when the projection norm l is nearer to $r_{\min}$, lower velocities result from the interaction wrench. One approach to achieve this is by establishing a linear relationship between the projection norm l and the admittance parameters. For instance, the admittance mass m_a can be tailored through

$$m_a = \begin{cases} m_{a,\max} & l \leq r_{\min}, \\ m_{a,\min} + (r_{\max} - l)\frac{\Delta m_a}{\Delta r} & r_{\min} < l < r_{\max}, \\ m_{a,\min} & r_{\max} \leq l, \end{cases} \tag{4.46}$$

with[4] $\Delta r = r_{\max} - r_{\min}$ and $\Delta m_a = m_{a,\max} - m_{a,\min}$. Hence, when l is large—suggesting weaker force capacity—m_a (and m_ϕ) will be lower, reducing the demand for steering force in (4.20). Conversely, when l is small—indicating limited motion feasibility along the path—m_a is set higher, resulting in slower desired motions. Please note that a similar approach could be employed to shape the admittance damping parameter d_a.

Ellipsoid Radii Projection Norm

Considering θ_i as the angle between the path direction $\boldsymbol{\nu}(\phi)$ and the ellipsoid principal axes $\boldsymbol{\nu}_i$, the projection length of each axis (4.43) becomes

$$l_i = r_i \cos(\theta_i), \tag{4.47}$$

and the projection norm l will be

$$l = \sqrt{\sum_{i=1}^{n_\Lambda} r_i^2 \cos^2(\theta_i)}. \tag{4.48}$$

---

[4] Note that the following is always assumed: $\Delta r = 0 \implies m_{a,\min} = m_{a,\max}$.

Given r_{min} and r_{max} as the minimum and maximum values of r_i, respectively, the following holds

$$\sqrt{\sum_{i=1}^{n_\Lambda} r_{\text{min}}^2 \cos^2(\theta_i)} \leq \sqrt{\sum_{i=1}^{n_\Lambda} r_i^2 \cos^2(\theta_i)} \leq \sqrt{\sum_{i=1}^{n_\Lambda} r_{\text{max}}^2 \cos^2(\theta_i)}. \tag{4.49}$$

As $\sqrt{\sum_{i=1}^{n_\Lambda} \cos^2(\theta_i)}$ is the norm of a unit vector defined in a coordinate system aligned with the ellipsoid principal axes, it follows

$$r_{\text{min}} \underbrace{\sqrt{\sum_{i=1}^{n_\Lambda} \cos^2(\theta_i)}}_{=1} \leq \underbrace{\sqrt{\sum_{i=1}^{n_\Lambda} r_i^2 \cos^2(\theta_i)}}_{l} \leq r_{\text{max}} \underbrace{\sqrt{\sum_{i=1}^{n_\Lambda} \cos^2(\theta_i)}}_{=1}, \tag{4.50}$$

resulting in

$$r_{\text{min}} \leq l \leq r_{\text{max}}. \tag{4.51}$$

4.2.3 Enhancing Robustness by Manipulability Pseudo-Ellipsoid

The manipulability ellipsoid, originally developed for articulated robotic arms [185], serves as a geometric representation of the potential configuration-dependent task-space motion or wrench properties. The length of each ellipsoid radius encodes how easy it is to either stabilize a wrench or move in the direction of the radius. To derive the ellipsoid radius length $r \in \mathbb{R}_{\geq 0}$ along the direction $\boldsymbol{\nu}$, consider the following condition [391]

$$\sum_{i|r_i \neq 0} \frac{(r\cos(\theta_i))^2}{r_i^2} = 1, \tag{4.52}$$

where θ_i is the angle between $\boldsymbol{\nu}$ and the ellipsoid principal vector $\boldsymbol{\nu}_i$, resulting in

$$\cos(\theta_i) = \boldsymbol{\nu}_i^T \boldsymbol{\nu}. \tag{4.53}$$

Employing (4.53) in (4.52) leads to

$$r^2 \sum_{i|r_i \neq 0} \frac{(\boldsymbol{\nu}_i^T \boldsymbol{\nu})^2}{r_i^2} = 1, \tag{4.54}$$

from which r can be achieved:

$$r = \frac{1}{\sqrt{\sum_{i|r_i \neq 0} \frac{(\boldsymbol{\nu}_i^T \boldsymbol{\nu})^2}{r_i^2}}}. \tag{4.55}$$

Note that in the case of singularity, when at least one eigenvalue is zero, if the associated eigenvector is not perpendicular to the vector $\boldsymbol{\nu}$, the radius length r also becomes zero.

For the proposed guidance adaptation policy (4.46), instead of the ellipsoid radius r, the projection norm l defined in (4.45) is utilized representing the relative configuration of the

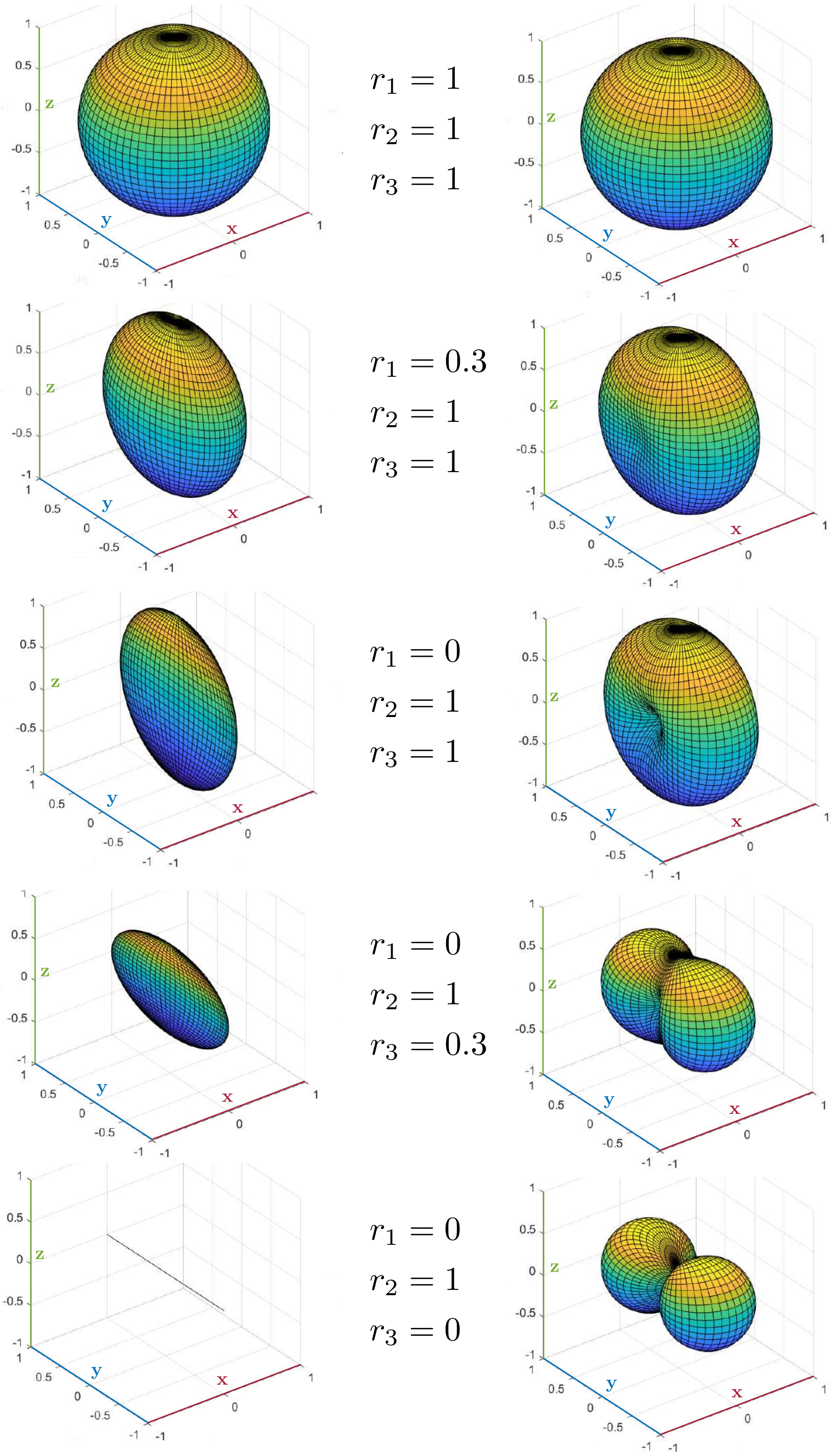

Figure 4.17: Ellipsoids on the left, and their corresponding pseudo-ellipsoids on the right. The principal radii with the lengths r_1, r_2 and r_3 are along the axes x, y and z, respectively.

manipulability ellipsoid with respect to the vector $\boldsymbol{\nu}$. By visualizing the associated norm l for all possible directions $\boldsymbol{\nu}$, a new geometric shape will be constructed, which has a smoother surface than the actual ellipsoid; see Figure 4.17. The projection norm l can be perceived as the radius of this so-called *manipulability pseudo-ellipsoid*. In line with the principles of manipulability analysis mentioned above, the ellipsoid radius r serves as a more precise evaluation metric compared to the pseudo-ellipsoid radius l. However, the computation of l, as shown in (4.45), is simpler and avoids issues of singularity (i.e., division by zero) encountered when deriving r as outlined in (4.55). Yet, the utilization of l instead of r presents a more notable advantage in terms of lower sensitivity to inaccuracies. This is particularly crucial in scenarios where a precise model of the articulated body under analysis is lacking or if the sensors used for determining the joint values $\boldsymbol{q}_h$ are either imprecise or, more importantly, prone to noise. While this may not pose a significant challenge for mechanical arms, it gains significance when evaluating human body limbs, primarily due to the absence of proprioceptive sensors for determining accurate body joint angles. To highlight the latter issue, a sensitivity analysis is conducted for both ellipsoid and pseudo-ellipsoid approaches, considering potential sensory inaccuracies in the configuration data.

Sensitivity Analysis

The configuration of the manipulability ellipsoid is contingent on the body joint angles $\boldsymbol{q}_h$. Consequently, any sensory inaccuracies in $\boldsymbol{q}_h$ can directly impact the estimated configuration of the ellipsoid, including the principal axes $\boldsymbol{\nu}_i$, radii lengths r_i, and ultimately the evaluation metrics r and l in (4.55) and (4.45), respectively. Considering (4.52) and (4.48), (4.55) and (4.45) can be reformulated as

$$r = \frac{1}{\sqrt{\Gamma_r}}, \qquad l = \sqrt{\Gamma_l}, \tag{4.56}$$

where

$$\Gamma_r = \sum_{i=1}^{n_\Lambda} \frac{\cos^2(\theta_i)}{r_i^2}, \qquad \Gamma_l = \sum_{i=1}^{n_\Lambda} r_i^2 \cos^2(\theta_i), \tag{4.57}$$

yielding

$$\frac{\partial r}{\partial \Gamma_r} = -\frac{1}{2(\sqrt{\Gamma_r})^3} = -\frac{r^3}{2}, \tag{4.58}$$

$$\frac{\partial l}{\partial \Gamma_l} = \frac{1}{2\sqrt{\Gamma_l}} = \frac{1}{2l}. \tag{4.59}$$

On the other hand, considering (4.57), the following can be observed.

$$\frac{\partial \Gamma_r}{\partial r_i} = -\frac{2\cos^2(\theta_i)}{r_i^3}, \tag{4.60}$$

$$\frac{\partial \Gamma_r}{\partial \theta_i} = -\frac{2\cos\theta_i \sin\theta_i}{r_i^2} = -\frac{\sin(2\theta_i)}{r_i^2} \tag{4.61}$$

$$\frac{\partial \Gamma_l}{\partial r_i} = 2r_i \cos^2(\theta_i) \tag{4.62}$$

$$\frac{\partial \Gamma_l}{\partial \theta_i} = -2r_i^2 \cos(\theta_i)\sin(\theta_i) = -r_i^2 \sin(2\theta_i). \tag{4.63}$$

As a result the sensitivity of r and l with respect to r_i and θ_i becomes

$$\frac{\partial r}{\partial r_i} = \frac{\partial r}{\partial \Gamma_r}\frac{\partial \Gamma_r}{\partial r_i} = \frac{r^3\cos^2(\theta_i)}{r_i^3}, \tag{4.64}$$

$$\frac{\partial l}{\partial r_i} = \frac{\partial l}{\partial \Gamma_l}\frac{\partial \Gamma_l}{\partial r_i} = \frac{r_i\cos^2(\theta_i)}{l}, \tag{4.65}$$

$$\frac{\partial r}{\partial \theta_i} = \frac{\partial r}{\partial \Gamma_r}\frac{\partial \Gamma_r}{\partial \theta_i} = \frac{r^3\sin(2\theta_i)}{2r_i^2}, \tag{4.66}$$

$$\frac{\partial l}{\partial \theta_i} = \frac{\partial l}{\partial \Gamma_l}\frac{\partial \Gamma_l}{\partial \theta_i} = -\frac{r_i^2\sin(2\theta_i)}{2l}. \tag{4.67}$$

According to (4.64) and (4.66), when a principal radius length r_i approaches zero but the ellipsoid radius r does not (i.e., $\boldsymbol{\nu}$ aligns with another long principal radius and $\theta_i \approx \frac{\pi}{2}$), the terms $\cos(\theta_i)$ and $\sin(2\theta_i)$ may have small values. However, $\partial r/\partial r_i$ and $\partial r/\partial \theta_i$ become large due to the higher power of r_i in the denominators. This leads to a situation where r becomes highly sensitive to potential changes in $\boldsymbol{q}$, which can result in variations of r_i and $\boldsymbol{\nu}_i$. On the other hand, considering (4.65) and (4.67), although it is possible for l to approach zero while r_i does not (e.g., when $\boldsymbol{\nu}$ aligns with another short principal radius and $\theta_i \approx \frac{\pi}{2}$), the small numerator terms $\cos(\theta_i)$ and $\sin(2\theta_i)$ will have either higher or equal powers compared to the small l in the denominators. Consequently, l would not be as sensitive as r to small changes in the estimated body configuration $\boldsymbol{q}_h$. Increased sensitivity implies that variations in the estimated ellipsoid configuration due to sensory uncertainties (e.g., noise) may lead to abrupt changes in the assessment metric. Hence, while still employing the manipulability ellipsoid concept, the projection norm l is used instead of the ellipsoid radius r to reduce the sensitivity of the manipulability assessment to sensory data.

4.2.4 Stabilization

For stability, the passivity analysis approach presented in Section 2.3 is employed here. Moreover, it is assumed that the robot is equipped with the Cartesian impedance controller (3.1) to follow the desired motion generated by the human-applied wrenches. For that, first, the storage function $S_\phi \in \mathbb{R}_{\geq 0}$ is proposed for the phase-based guidance law (4.20), and is derived as

$$S_\phi = \frac{1}{2} m_\phi \dot{\phi}^2. \tag{4.68}$$

Given S_i defined in (3.14) for the robot equipped with an impedance controller, and considering the storage function $S_h \in \mathbb{R}_{\geq 0}$, representing a limited energy of the guiding human such that

$$\dot{S}_h \leq -\dot{\boldsymbol{x}}^T \boldsymbol{f}_h, \tag{4.69}$$

the proposed overall storage function $S_{\text{sys}} \in \mathbb{R}_{\geq}0$ becomes

$$S_{\text{sys}} = S_i + S_\phi + S_h = \frac{1}{2}\dot{\tilde{\boldsymbol{x}}}^T \boldsymbol{M}_C(\boldsymbol{q})\dot{\tilde{\boldsymbol{x}}} + \frac{1}{2}\tilde{\boldsymbol{x}}^T \boldsymbol{K}_C \tilde{\boldsymbol{x}} + \frac{1}{2} m_\phi \dot{\phi}^2 + S_h. \tag{4.70}$$

To investigate passivity, the time evolution of S_{sys} is derived as in the following.

$$\dot{S}_{\text{sys}} = \dot{\tilde{\boldsymbol{x}}}^T \boldsymbol{M}_C(\boldsymbol{q})\ddot{\tilde{\boldsymbol{x}}} + \frac{1}{2}\dot{\tilde{\boldsymbol{x}}}^T \dot{\boldsymbol{M}}_C(\boldsymbol{q})\dot{\tilde{\boldsymbol{x}}} + \dot{\tilde{\boldsymbol{x}}}^T \boldsymbol{K}_C \tilde{\boldsymbol{x}} + m_\phi \ddot{\phi}\dot{\phi} + \frac{1}{2}\dot{m}_\phi \dot{\phi}^2 + \dot{S}_h \tag{4.71}$$

$$\begin{aligned} =& \dot{\tilde{\boldsymbol{x}}}^T \underbrace{\left(-\boldsymbol{C}_C(\boldsymbol{q},\dot{\boldsymbol{q}})\dot{\tilde{\boldsymbol{x}}} - \boldsymbol{D}_C\dot{\tilde{\boldsymbol{x}}} - \boldsymbol{K}_C\tilde{\boldsymbol{x}} - \boldsymbol{f}_h\right)}_{\boldsymbol{M}_C(\boldsymbol{q})\ddot{\tilde{\boldsymbol{x}}}} + \frac{1}{2}\dot{\tilde{\boldsymbol{x}}}^T \dot{\boldsymbol{M}}_C(\boldsymbol{q})\dot{\tilde{\boldsymbol{x}}} + \dot{\tilde{\boldsymbol{x}}}^T \boldsymbol{K}_C \tilde{\boldsymbol{x}} \\ &+ \underbrace{\left(f_s - d_\phi \dot{\phi} - c_\phi \dot{\phi}^2\right)}_{m_\phi \ddot{\phi}} \dot{\phi} + \frac{1}{2}\dot{m}_\phi \dot{\phi}^2 + \dot{S}_h \end{aligned} \tag{4.72}$$

$$\begin{aligned} =& \frac{1}{2}\dot{\tilde{\boldsymbol{x}}}^T \left(\dot{\boldsymbol{M}}_C(\boldsymbol{q}) - 2\boldsymbol{C}_C(\boldsymbol{q},\dot{\boldsymbol{q}})\right)\dot{\tilde{\boldsymbol{x}}} - \dot{\tilde{\boldsymbol{x}}}^T \boldsymbol{D}_C \dot{\tilde{\boldsymbol{x}}} - \dot{\tilde{\boldsymbol{x}}}^T \boldsymbol{f}_h + f_s\dot{\phi} - d_\phi\dot{\phi}^2 - c_\phi\dot{\phi}^3 \\ &+ \frac{1}{2}\dot{m}_\phi \dot{\phi}^2 + \dot{S}_h \end{aligned} \tag{4.73}$$

$$= -\dot{\tilde{\boldsymbol{x}}}^T \boldsymbol{D}_C \dot{\tilde{\boldsymbol{x}}} + \dot{\boldsymbol{x}}^T \boldsymbol{f}_h - \underbrace{\dot{\boldsymbol{x}}_d^T}_{\dot{\phi}\ d\boldsymbol{x}_d^T(\phi)/d\phi} \boldsymbol{f}_h + f_s\dot{\phi} - d_\phi\dot{\phi}^2 \underbrace{- c_\phi\dot{\phi}^3 + \frac{1}{2}\dot{m}_\phi\dot{\phi}^2}_{\frac{1}{2}\dot{m}_a \dot{\boldsymbol{x}}_d^T \dot{\boldsymbol{x}}_d} + \dot{S}_h \tag{4.74}$$

$$= -\dot{\tilde{\boldsymbol{x}}}^T \boldsymbol{D}_C \dot{\tilde{\boldsymbol{x}}} + \dot{\boldsymbol{x}}^T \boldsymbol{f}_h - \dot{\phi} \underbrace{\frac{d\boldsymbol{x}_d^T(\phi)}{d\phi}\boldsymbol{f}_h}_{f_s} + f_s\dot{\phi} - d_\phi\dot{\phi}^2 - \frac{1}{2}\dot{m}_a \dot{\boldsymbol{x}}_d^T \dot{\boldsymbol{x}}_d + \dot{S}_h \tag{4.75}$$

$$= -\dot{\tilde{\boldsymbol{x}}}^T \boldsymbol{D}_C \dot{\tilde{\boldsymbol{x}}} + \dot{\boldsymbol{x}}^T \boldsymbol{f}_h - d_\phi\dot{\phi}^2 + \frac{1}{2}\dot{m}_a \dot{\boldsymbol{x}}_d^T \dot{\boldsymbol{x}}_d + \dot{S}_h. \tag{4.76}$$

In (4.74), the time derivative of the phase-based admittance mass in (4.21) is used derived as

$$\dot{m}_\phi = \dot{m}_a \frac{d\boldsymbol{x}_d^T}{d\phi}\frac{d\boldsymbol{x}_d}{d\phi} + 2m_a\dot{\phi}\frac{d^2\boldsymbol{x}_d^T}{d\phi^2}\frac{d\boldsymbol{x}_d}{d\phi}, \tag{4.77}$$

which, considering (4.23), results in

$$\begin{aligned} \dot{m}_\phi\dot{\phi}^2 - 2c_\phi\dot{\phi}^3 =& \dot{m}_a \frac{d\boldsymbol{x}_d^T}{d\phi}\frac{d\boldsymbol{x}_d}{d\phi}\dot{\phi}^2 + \cancel{2m_a\dot{\phi}^3\frac{d^2\boldsymbol{x}_d^T}{d\phi^2}\frac{d\boldsymbol{x}_d}{d\phi}} \\ &- \cancel{2m_a\frac{d^2\boldsymbol{x}_d^T}{d\phi^2}\frac{d\boldsymbol{x}_d}{d\phi}\dot{\phi}^3} \\ =& \dot{m}_a \dot{\boldsymbol{x}}_d^T \dot{\boldsymbol{x}}_d, \end{aligned} \tag{4.78}$$

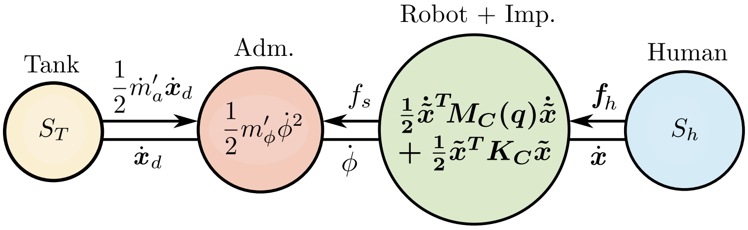

Figure 4.18: Port-based representation of the overall system. The phase-based admittance mass m'_ϕ is associated with the modified admittance mass m'_a after tank augmentation.

Given the non-negativity of $\dot{\tilde{\boldsymbol{x}}}^T\boldsymbol{D}_C\dot{\tilde{\boldsymbol{x}}}$ and $d_\phi\dot{\phi}^2$, and considering (4.69), it can be deduced from (4.76) that

$$\dot{S}_{\text{sys}} \leq \underbrace{\frac{1}{2}\dot{m}_a\dot{\boldsymbol{x}}_d^T\dot{\boldsymbol{x}}_d}_{P_T}. \tag{4.79}$$

As no assumption can be made for the sign of P_T in (4.79), a virtual energy tank with the storage function $S_T \in \mathbb{R}_{\geq 0}$ can be augmented with the controllable variable $\dot{m}_a$ such that $\dot{S}_T = -P_T$,. The admittance mass m_a is dynamically adjusted by the tank to m'_a in a manner (as illustrated below) ensuring that the magnitude of its variation rate is always limited to $\mu \in \mathbb{R}_{\geq 0}$ such that

$$|\dot{m}'_a| \leq \mu. \tag{4.80}$$

Finally, the variation rate limiter $\mu \in \mathbb{R}_{\geq 0}$ is consistently determined as a smooth function of the tank energy level as in the following.

$$\mu = \begin{cases} (m_{a,\max} - m_{a,\min}) & \text{if } S_T^\Delta \leq S_T, \\ \frac{1}{2}\left(m_{a,\max} - m_{a,\min}\right)\left(1 - \cos\left(\pi\frac{S_T - S_T^{\text{low}}}{S_T^\Delta}\right)\right) & \text{if } S_T^{\text{low}} \leq S_T < S_T^\Delta, \\ 0 & \text{else.} \end{cases} \tag{4.81}$$

Here, $S_T^{\text{low}}, S_T^\Delta \in \mathbb{R}_{\geq 0}$ are the tank lower limit and the corresponding threshold, respectively, as described in Section 2.3. Figure 4.18 depicts the port-based representation of the overall system.

Remark: Note that in the context of valve-based virtual energy tanks introduced in Section 2.3, it can be assumed that

$$\gamma_T = \frac{\mu}{(m_{a,\max} - m_{a,\min})}, \tag{4.82}$$

with $\gamma_T = 0$ for when $m_{a,\max} = m_{a,\min}$.

Admittance Variation Rate Limiter

Here, it is demonstrated how the variable μ effectively constrains the variation rate of the admittance mass m_a in practice. Consider $m_a(t)$ as the admittance mass determined by (4.46)

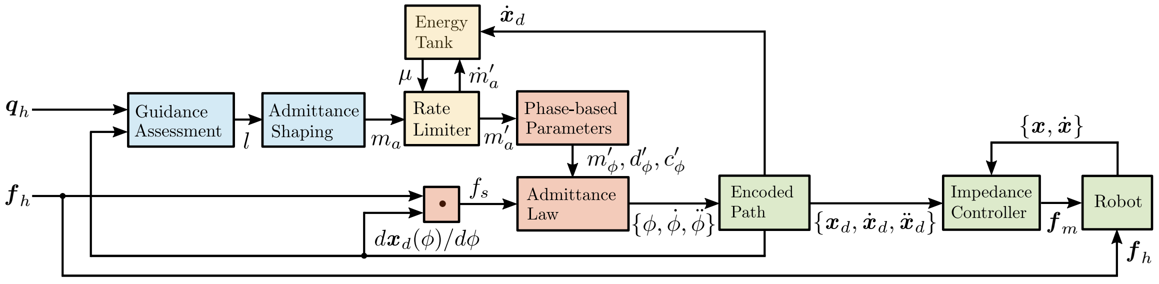

Figure 4.19: Proposed control architecture in detail – The block colors are in accordance with the approach structure depicted in Figure 4.14.

at time t, and $m'_a(t - \Delta t)$ as its tank-modified value in the previous time-step. Accordingly, $\dot{m}_a(t)$ can be approximated by

$$\dot{m}_a(t) = \frac{m_a(t) - m'_a(t - dt)}{dt}. \tag{4.83}$$

The admittance variation rate can then be limited by μ if $m'_a(t)$ is modified via

$$m'_a = \begin{cases} m_a(t) & \text{if } |\dot{m}_a(t)| \leq \mu, \\ m'_a(t - dt) + \mu \frac{m_a(t) - m'_a(t - dt)}{|\dot{m}_a(t)|} & \text{else.} \end{cases} \tag{4.84}$$

Consequently, the modified admittance mass variation rate is

$$\dot{m}'_a(t) = \frac{m'_a(t) - m'_a(t - dt)}{dt}, \tag{4.85}$$

which according to (4.84) becomes

$$\dot{m}'_a(t) = \begin{cases} \dot{m}_a(t) & \text{if } |\dot{m}_a(t)| \leq \mu, \\ \mu \underbrace{\frac{m_a(t) - m'_a(t - dt)}{dt|\dot{m}_a(t)|}}_{\pm 1} & \text{else.} \end{cases} \tag{4.86}$$

As a result, the modified admittance variation rate is always limited by μ, i.e.,

$$|\dot{m}'_a| \leq \mu. \tag{4.87}$$

Figure 4.19 depicts the overall control architecture of the proposed adaptive haptic motion guidance policy.

4.2.5 Experiments

Several experiments were conducted in this section to evaluate different aspects of the proposed approach, employing a 7-DoF Franka Emika robot. In Experiment 1 (see Figure 4.20), the guiding wrench $\boldsymbol{f}_h$ is generated by the gravity of an unmodeled load attached to the end-effector. In Experiments 2 and 3 (see Figure 4.24 and Figure 4.27), the guiding wrench

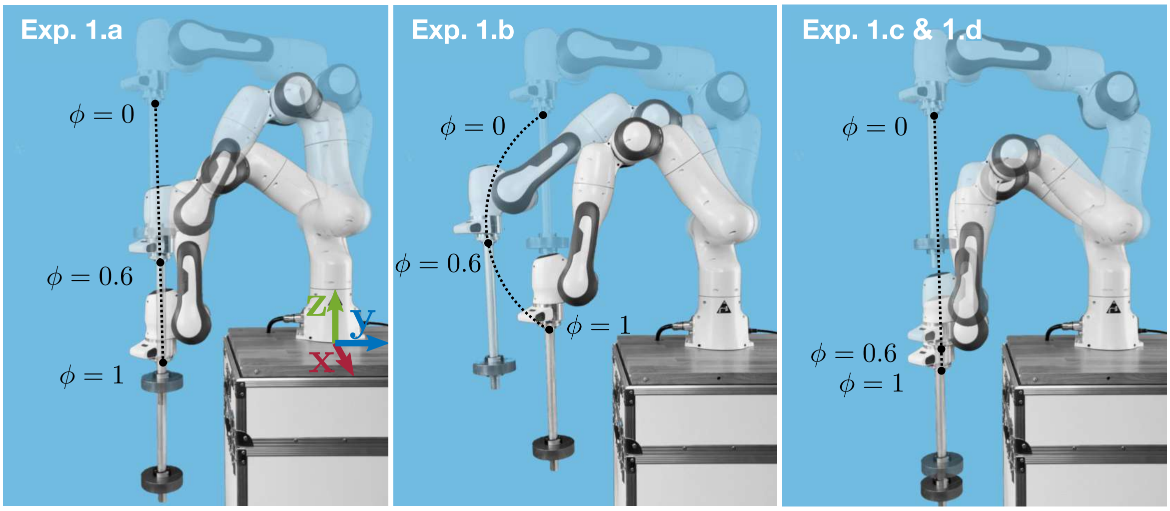

Figure 4.20: Experiment 1 – The attached weight propels the phase ϕ toward 1, causing the robot setpoint to move along the encoded path. To demonstrate the impact of phase distribution on the trajectory, in Experiment 1.a and Experiment 1.b, the phase is uniformly spread across the path, whereas in Experiment 1.c and Experiment 1.d, an exponential phase distribution is chosen.

is generated by a human operator. The wrench $\boldsymbol{f}_h$ measured by the robot is used to generate the desired trajectory according to (4.19)–(4.20). The robot is equipped with a Cartesian impedance controller (3.1) to follow the generated trajectory. Throughout the first three experiment sets, the controller stiffness $\boldsymbol{K}_C$ takes the form of a diagonal matrix with elements $\{1000, 1000, 1000, 50, 50, 50\}$ [N/m, Nm/rad]. The damping matrix $\boldsymbol{D}_C$ is configured for critical damping [381] in all experiments.

To measure the human body configuration to shape the guidance behavior in Experiments 2, 3, and 5, a setup similar to Section 4.1 is used. An Intel RealSense D435 RGB-D camera with OpenCV3 software [347] is utilized to detect human keypoints. Color images are processed by the OpenPose library [388] to estimate human keypoints based on the BODY-25 model. The keypoint locations are deprojected using the aligned depth image; see Figure 4.22 for an example of the model superposition over an RGB image. The keypoint positions are then fed to a simplified kinematics model of the human arm depicted in Figure 4.23, to estimate the joint angles $\boldsymbol{q}_h$ and the Jacobian matrix $\boldsymbol{J}_h(\boldsymbol{q}_h)$. As the BODY-25 model considers only three keypoints for each arm (wrist, elbow, and shoulder), the arm keypoint locations are used to identify the values of only three joints associated with arm abduction/adduction, arm flexion/extension, and elbow flexion/extension, depicted as joint 1, 2, and 4, respectively, in Figure 4.23. Due to this technical limitation, only three joints of the right arm kinematics are considered to build the body Jacobian matrix $\boldsymbol{J}_h(\boldsymbol{q}_h)$.

Experiment 1: Force-Driven Phase Evolution Control

This set of experiments evaluates the performance of the proposed human-guided motion generator. To maintain a consistent applied force on the robot, a 2.6 kg weight is attached to the robot end-effector, as depicted in Figure 4.20. In all experiments, the constrained

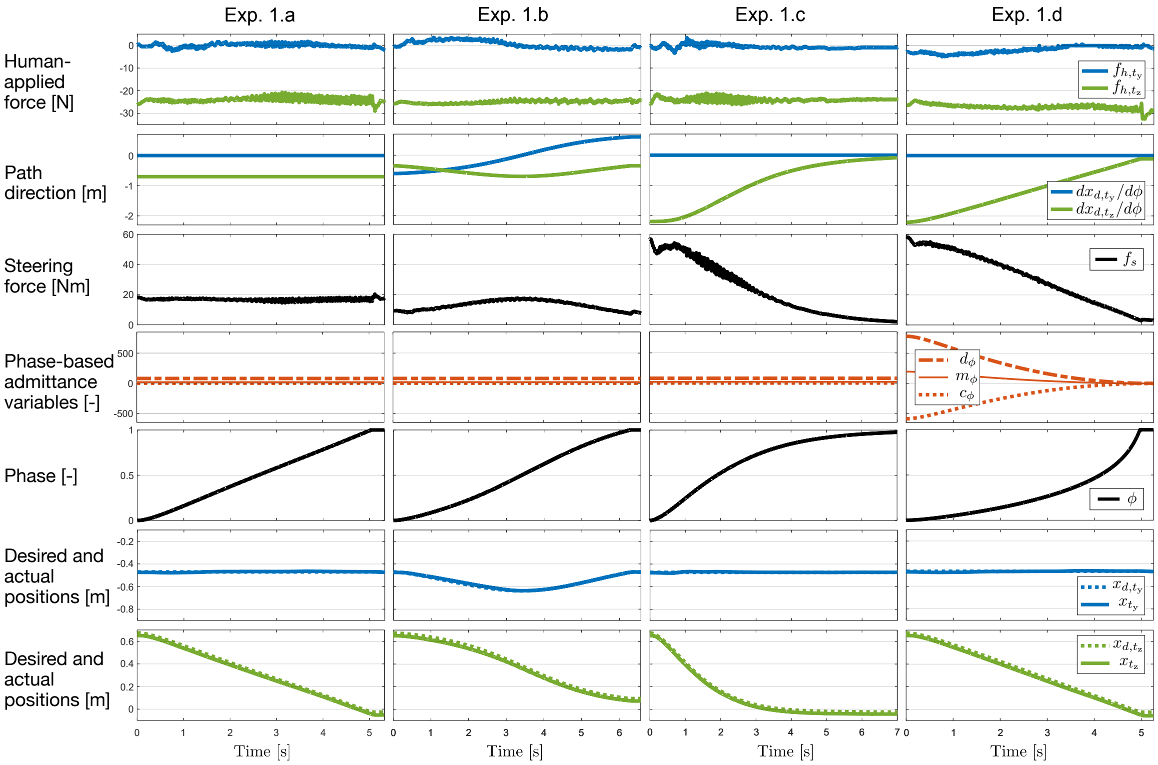

Figure 4.21: Experiment 1 – The attached weight applies a relatively constant force along the z-direction, which, in accordance with the phase-based admittance law, shapes the phase trajectory. The resultant desired motions in Experiment 1.a and Experiment 1.d exhibit similarities due to the closely matched generalized admittance parameters m_a and d_a.

path is defined in 3-dimensional Cartesian space ($m = 3$) with a length of 0.7 m. The path is vertical in Experiment 1.a, Experiment 1.c, and Experiment 1.d, and a circular arc in Experiment 1.b. The admittance parameters for Experiment 1.a, Experiment 1.b, and Experiment 1.c are empirically configured to produce appropriate motion under the influence of the attached weight gravity such that

$$m_\phi = 20, \quad d_\phi = 80, \quad c_\phi = 0. \tag{4.88}$$

They are shaped according to (4.21)–(4.23) in Experiment 1.d. Finally, the phase value is saturated at 1. This ensures that when the setpoint reaches the endpoint of the path, the phase no longer increases.

Experiment 1.a: In this experiment, the path is uniformly encoded by phase as

$$\boldsymbol{x}_d(\phi) = \boldsymbol{x}_{d,0} + [0, 0, -0.7\phi]^T. \tag{4.89}$$

In (4.89), $\boldsymbol{x}_{d,0} \in \mathbb{R}^3$ defines the initial pose. As a result, the path direction vector $d\boldsymbol{x}_d(\phi)/d\phi$ for the encoded path (4.89) remains constant according to

$$d\boldsymbol{x}_d(\phi)/d\phi = \Big[0, 0, -0.7\Big]^T. \tag{4.90}$$

Thus, considering an approximate constant wrench $\boldsymbol{f}_h$ being applied to the robot, a constant steering force f_s guides the phase toward 1 according to (4.20). As can be observed in Figure 4.21, the setpoint $\boldsymbol{x}_d$ proceeds throughout the desired path by the phase progress, and the robot impedance controller moves the robot accordingly.

Experiment 1.b: The path in this experiment is set to a 0.7 m long arc equivalent to one-third of a full circle; see Figure 4.20. It is again uniformly encoded according to

$$\boldsymbol{x}_d(\phi) = \boldsymbol{x}_{d,0} + 0.7\frac{3}{2\pi}\begin{bmatrix} 0 \\ \sin(\frac{\pi}{6}) - \sin(\frac{2\pi\phi}{3} + \frac{\pi}{6}) \\ \cos(\frac{2\pi\phi}{3} + \frac{\pi}{6}) - \cos(\frac{\pi}{6}) \end{bmatrix}, \tag{4.91}$$

with the direction vector

$$\frac{d\boldsymbol{x}_d(\phi)}{d\phi} = -0.7\Big[0, \cos\left(\frac{2\pi\phi}{3} + \frac{\pi}{6}\right), \sin\left(\frac{2\pi\phi}{3} + \frac{\pi}{6}\right)\Big]^T. \tag{4.92}$$

Hence, while the path direction vector maintains a constant magnitude, it does not consistently align with the applied wrench $\boldsymbol{f}_h$. Consequently, the steering force f_s fluctuates along the path, as depicted in Figure 4.21. As a result, the evolution of the phase differs from the previous experiment. Specifically, at the midpoint of the path (i.e., for $\phi = 0.5$, due to the uniform encoding of the path), when the path direction vector aligns with gravity, f_s reaches its maximum value, thereby accelerating the progression of the phase.

Experiment 1.c: The manner in which the phase-based admittance law (4.20) generates the intended motion relies on the distribution of the variable phase throughout the encoded path, or in other words, how the path is encoded. To illustrate this, in contrast to the preceding scenarios, the path in this case—although akin to Experiment 1.a in its exclusive alignment along the z-axis—is not uniformly encoded (refer to Figure 4.20).

$$\boldsymbol{x}_d(\phi) = \boldsymbol{x}_{d,0} + \Big[0, 0, -0.7\frac{1 - e^{-3\phi}}{1 - e^{-3}}\Big]^T. \tag{4.93}$$

As a result, the path direction vector becomes

$$d\boldsymbol{x}_d(\phi)/d\phi = \frac{-2.1}{1 - e^{-3}}\Big[0, 0, e^{-3\phi}\Big]^T, \tag{4.94}$$

which has no constant norm anymore. At the path outset ($\phi = 0$), the path direction vector norm is about 22× that at the path end ($\phi = 1$). This leads to higher initial values of f_s, resulting in pronounced accelerations in both ϕ and $\boldsymbol{x}_d(t)$ compared to Experiment 1.a, as shown in Figure 4.21. As the phase approaches 1, the steering force diminishes, significantly slowing down the phase progression.

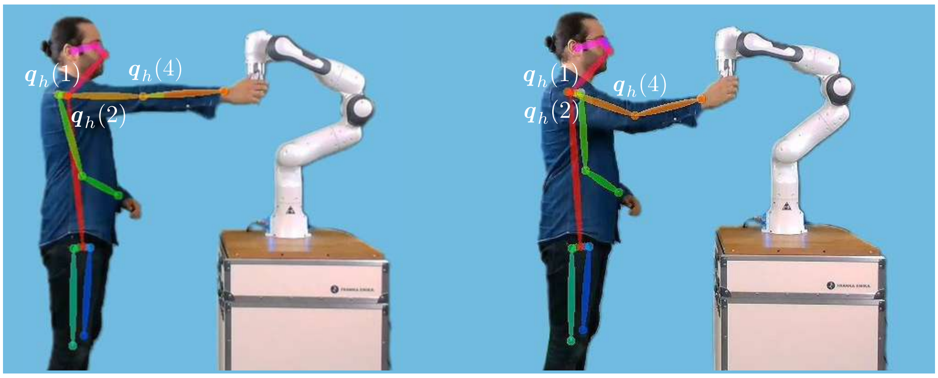

Figure 4.22: Body configuration at the start (left) and end (right) of Experiment 2.b. Joint angles are estimated using the positions of the detected body keypoints.

Experiment 1.d: As mentioned earlier, utilizing the conventions (4.21), (4.22), and (4.23), the phase-based parameters m_ϕ, d_ϕ, and c_ϕ can be expressed as functions of physically intuitive variables m_a and d_a. This experiment aims to analyze the effect of such a transformation on the approach behavior. Here, the same encoded path as in Experiment 1.c is used. The admittance mass and damping variables are set to $m_a = 40$ kg and damping $d_a = 160$ Ns/m, respectively. As shown in Figure 4.21, the phase-based parameters evolve along the path due to changes in the path direction vector $d\boldsymbol{x}_d(\phi)/d\phi$ in (4.94). At the path outset, $d\boldsymbol{x}_d(\phi)/d\phi$ has greater magnitude, leading to larger phase-based parameters. However, as ϕ approaches 1, the vector magnitude decreases, causing reductions in m_ϕ, d_ϕ, and c_ϕ.

These admittance parameters are shaped such that the phase progress $\phi(t)$ yields a desired motion $\boldsymbol{x}_d(t)$ akin to motion resulting from applied wrench $\boldsymbol{f}_h$ on a 40 kg mass with viscous friction coefficient 160 Ns/m. In other words, by utilizing generalized admittance parameters m_a and d_a and adjusting phase-based parameters accordingly, desired motion generation (4.20) becomes independent of phase distribution policy. Figure 4.21 illustrates that generated desired motions in Experiment 1.a and Experiment 1.d are nearly identical despite differing desired path encodings. This similarity arises because the phase-based parameters in Experiment 1.a are comparable to those obtainable by using the path direction vector (4.90), along with generalized parameters $m_a = 40$ and $d_a = 160$ in (4.21)–(4.23) as follows:

$$m_\phi = 19.6, \quad d_\phi = 78.4, \quad c_\phi = 0. \tag{4.95}$$

These values are almost equivalent to the ones in (4.88).

Experiment 2: Human-Aware Motion Guidance Adaptation

This set of experiments aims to explore the behavior of the guidance law with the incorporation of parameter adaptation algorithm (4.46). Here, a human operator is supposed to guide the robot through a 0.1 m predefined uniformly encoded path by applying wrenches on the robot end-effector; see Figure 4.24. As previously mentioned, the human body configuration is determined by detecting and locating the keypoints (shoulder, elbow, and wrist) using the OpenPose software and a RealSense RGB-D camera, as shown in Figure 4.22. Using the

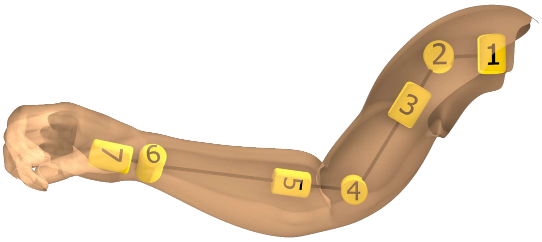

Figure 4.23: Arm kinematic structure introduced in [392]. In the experiments, only the 1st, 2nd, and 4th joints were used to calculate the Jacobian matrix.

detected keypoint positions along with the 7-DoF kinematics model of the human arm from [392], three joint angles $\boldsymbol{q}_h(1)$, $\boldsymbol{q}_h(2)$, and $\boldsymbol{q}_h(4)$ are identified; see Figure 4.23. These angles are used to calculate the Jacobian matrix $\boldsymbol{J}_h(\boldsymbol{q}_h)$. Consequently, the manipulability ellipsoid can be continuously recognized, and the metric l is determined by projecting the principal radii of the ellipsoid onto the desired path.

Across all experiments, the minimum and maximum values for the principal radii lengths are defined as $r_{\min} = 0$ and $r_{\max} = 0.7$ m, respectively. The admittance mass m_a is shaped based on (4.46), using minimum and maximum values of $m_{a,\min} = 1$ kg and $m_{a,\max} = 80$ kg, respectively. Finally, the damping coefficient d_a is consistently set to half of m_a throughout all experiments.

Experiment 2.a: In the first experiment, the operator's arm initial configuration is approximately $\boldsymbol{q}_h \approx [75, 45, 97]^T$ degrees. This configuration leads to the manipulability ellipsoid illustrated in Figure 4.24. Projecting the principal radii of this ellipsoid onto the encoded path—a straight line to the operator's left side—yields $l \approx 0.26$ m, corresponding to an admittance mass of approximately $m_a \approx 50$ kg. The operator guides the robot by applying the wrench $\boldsymbol{f}_h$, resulting in the generation of the steering force f_s, visible in Figure 4.25.

Experiment 2.b: In this experiment, the human operator's arm starts in an extended position near a singularity, resulting in an extremely elongated manipulability ellipsoid, depicted in Figure 4.24. The constrained path aligns as a straight line following the human arm, requiring the operator to pull the robot toward themselves. At $\phi = 0$, projecting the ellipsoid radii onto the encoded path yields a minimal metric value $l \approx 0.04$ m. This metric corresponds to a high admittance mass of around $m_a \approx 76$ kg. As elucidated before, such an arm configuration results in low joint torques for the necessary guiding wrench. Conversely, a relatively high joint velocity may be necessary for swift movement along the path. Thus, a high admittance mass is preferable in this scenario. As illustrated in Figure 4.25, achieving the desired motion along the path requires notably elevated steering forces. Despite these considerable forces, completing the 0.1 m path takes the longest duration, approximately $t \approx 1.8$ s.

Experiment 2.c: Though the human arm configuration resembles the previous case, the constrained path in this experiment closely follows the ellipsoid longer radius; see Figure 4.24. Consequently, the initial projection norm $l \approx 0.67$ m is in close proximity to $r_{\max}$. This

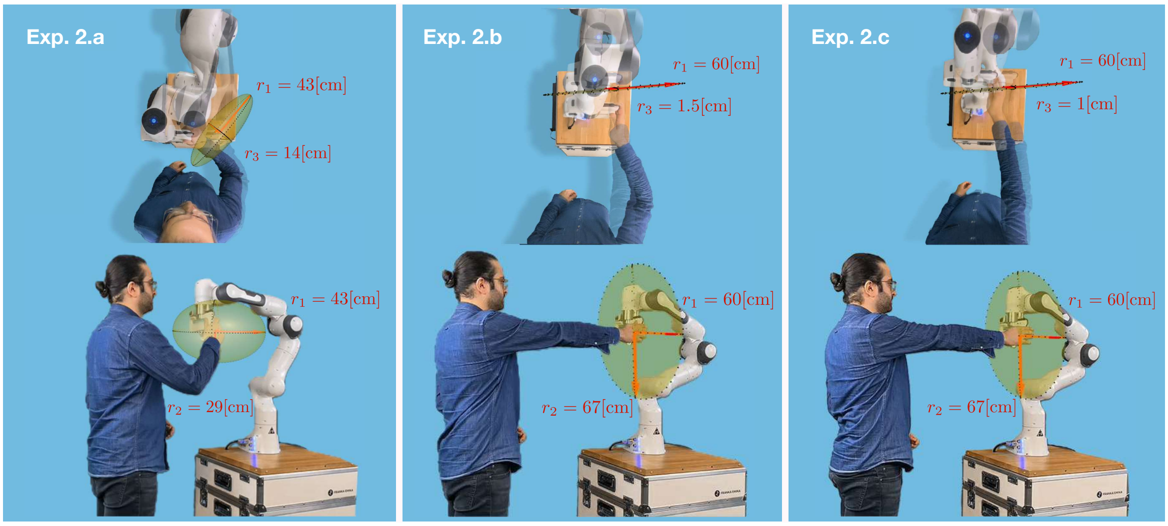

Figure 4.24: Experiment 2 – Lower figures display initial configurations, while upper figures depict motion along the 0.1 m paths. Manipulability ellipsoids and their principal radii are shown for operator arm initial configurations. To enhance detail, ellipsoids are presented at half their actual size.

proximity results in a relatively low admittance mass of $m_a \approx 4$ kg. While the configuration is similar to the previous case, the altered guidance direction may require significant joint torques to achieve the same magnitude as the guiding wrench. Hence, the reduced admittance mass in this experiment serves to diminish the necessary magnitude of the guiding wrench. Unlike in Experiment 2.a, as evident in Figure 4.25, the joint motions required for Cartesian motion are comparatively minor. Thus, even the swift Cartesian motion ($\phi = 1$ at $t = 0.55$ s) does not result in high joint velocities. Therefore, for this scenario, the comparatively light admittance mass, designed to minimize configuration-related large joint torques and velocities during guidance, effectively aligns with the adaptation objective.

Here, it is valuable to compare the effect of using the manipulability pseudo-ellipsoid approach instead of the conventional ellipsoid. In other words, how would the control approach have worked if, instead of the manipulability pseudo-ellipsoid radius along the path (i.e., the projection norm l), the actual ellipsoid radius r was used? To answer this question, the evolution of the operator arm configuration and, thus the manipulability ellipsoid should be examined first. Figure 4.26 illustrates the variation of the arm joint angles $\Delta \boldsymbol{q}_h$, the ellipsoid principal radii lengths Δr_i, and the angles between the desired path direction and the principal radii $\Delta\theta_i$ during the guidance. As the maximum variation of the body joints is less than 3 degrees, the ellipsoid configuration does not significantly change. In fact, the maximum change in the principal radii lengths is less than 0.005 m, and in the angles between the principal radii and the path is 2.5 degrees, as shown in Figure 4.26. However, at $t = 0.35$ s and $t = 0.53$ s, the ellipsoid radius along the path, i.e., r, experiences abrupt changes.

Figure 4.26 demonstrates that if, instead of l in the admittance adaptation law (4.46), the radius length r was used, the admittance mass $m_{a,r}$ would have had instantaneous variations from 47 kg to 13 kg and from 26 kg to 56 kg at the aforementioned time instants. For the same steering force f_s, by suddenly changing the mass m_a, the desired acceleration would

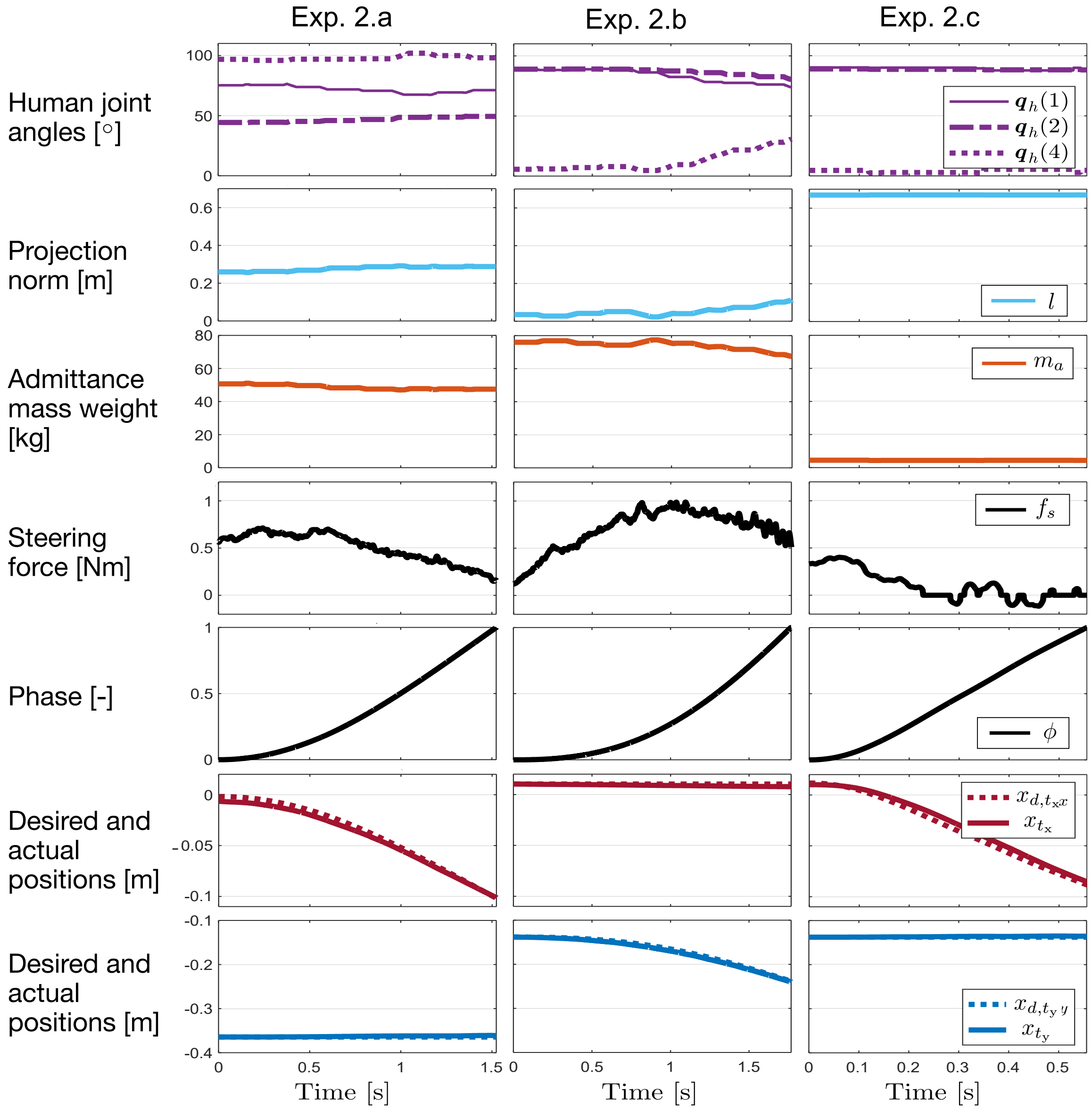

Figure 4.25: Experiment 2 – The mass m_a adjusts continuously based on the norm l. The average force magnitudes applied in the path direction are -5 N, -7 N, and -1 N for Experiment 2.a, Experiment 2.b, and Experiment 2.c, respectively.

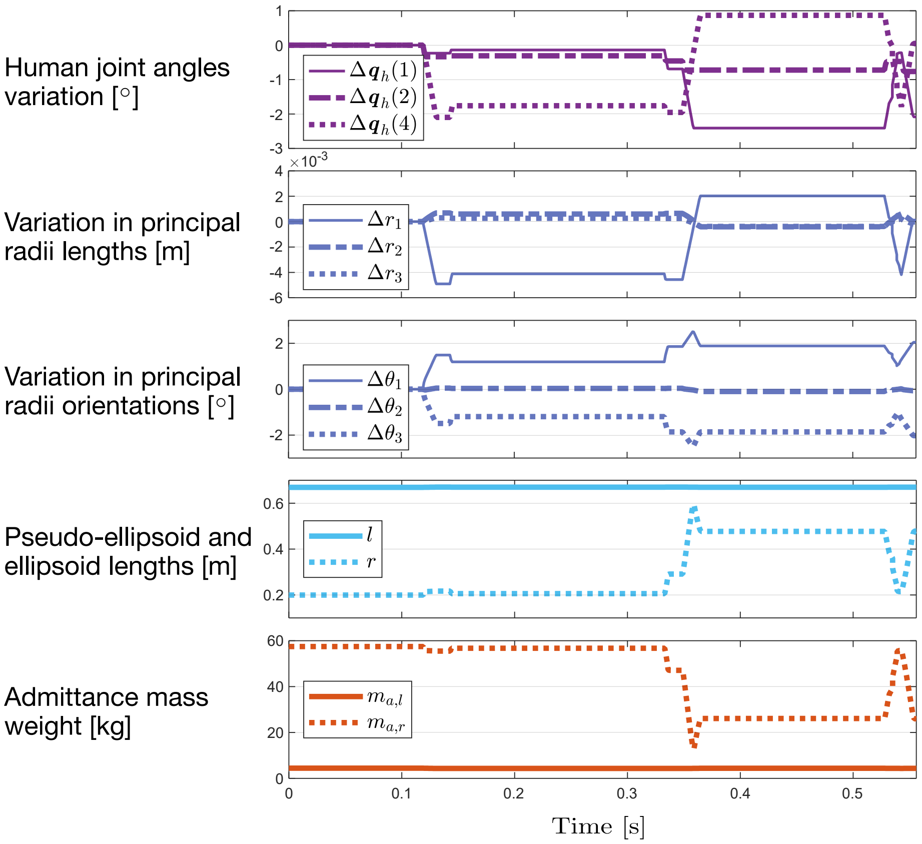

Figure 4.26: Experiment 2.c – The ellipsoid radius r along the path and the associated admittance mass $m_{a,r}$ show abrupt changes, potentially diminishing the control performance.

instantly change accordingly. With a proper motion controller, this would result in abrupt changes in the robot motion during the interaction, which could be harmful to the human. Additionally, the maximum admittance variation rate $\dot{m}_{a,r}$ associated with the ellipsoid radius r is 200 times larger than the same value $\dot{m}_{a,l}$ associated with the pseudo-ellipsoid radius l. Hence, the tank energy level would have experienced fluctuations with 200 times larger magnitudes if r was used as the assessment metric. Note that such abrupt variations in metric r exist even though the rate of changes in the signal $\boldsymbol{q}_h$ is limited to π rad/s, as shown in Figure 4.26. This phenomenon indicates that at certain human body configurations, even a slight variation in the sensory data could drastically change the control behavior when using the conventional manipulability ellipsoid.

Experiment 3: The Impact of Tank Energy in a Pendulum Collision Scenario

Previous experiments demonstrated how applying a wrench to the robot can guide the set-point along a constrained path and how the guidance response varies with different m_a values. Moreover, the adaptability of m_a was shown according to the human body configuration for a desired guidance behavior. Subsequent experiments reveal potential issues with shaping m_a, leading to undesired energy generation that violates passivity. A solution involving a virtual

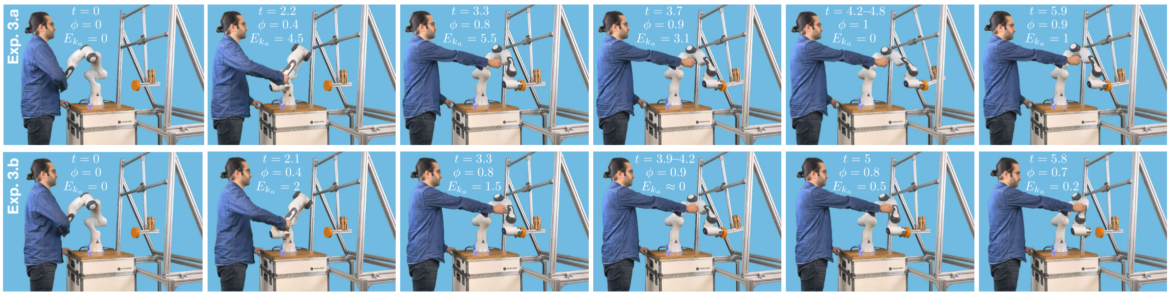

Figure 4.27: Experiment 3 – The operator guides the robot through the path, and the robot collides with a pendulum. The generated high virtual kinetic energy in Experiment 3.a pushes the pendulum to the maximum until $\phi = 1$. In contrast, the augmented virtual tank in Experiment 3.b prevents the virtual kinetic energy from growing, and as a result, the impact force is able to stop the desired motion. Time t and energy E_{k_a} are indicated in seconds and joules, respectively.

energy tank is applied to curb this by constraining the rate of admittance mass change, $\dot{m}_a$, ensuring it remains below the permissible μ as defined in (4.86). In this scenario, the operator guides the robot along a uniformly encoded path with changing arm configuration; see Figure 4.27. The guidance adaptation policy mirrors the earlier experiment. The minimum and maximum manipulability ellipsoid radii are set to $r_{\min} = 0.05$ m and $r_{\max} = 0.5$ cm, with corresponding admittance mass $m_{a,\min} = 10$ kg and $m_{a,\max} = 100$ kg, respectively. Damping coefficient is $d_a = m_a/4$. As the operator configuration alters, l decreases, and m_a increases. At $\phi = 0.8$ along the path, a collision occurs with a pendulum bearing a 5 kg weight, depicted in Figure 4.27. Two experiments are presented: one with high initial tank energy, insignificantly affecting performance, and another with low initial energy, limiting mass variation. Both cases utilize an energy threshold $E_\Delta = 1$ J. The post-tank admittance mass is denoted as m'_a, accompanied by its virtual kinetic energy E_{k_a} defined as

$$E_{k_a} = \frac{1}{2} m'_a \dot{\boldsymbol{x}}_d^T \dot{\boldsymbol{x}}_d. \tag{4.96}$$

The impact of the initial energy level in the tank on the virtual kinetic energy E_{k_a} and, consequently, the behavior after collision in each experiment are illustrated in the following experiments; see Figure 4.27.

Experiment 3.a: As depicted in Figure 4.28, the initial three seconds showcase the human operator exerting the interaction wrench $\boldsymbol{f}_h$ on the robot. This action produces the steering force f_s, propelling the robot along the path. The projection norm l and, consequently, the admittance mass m_a vary due to changes in the operator's arm configuration. Despite the high initial energy in the tank ($S_T(t = 0) = 18$ J), the energy level diminishes as m_a increases. However, since the tank energy never reaches the S_T^Δ threshold, the tank output μ remains constant. Thus, the admittance mass can freely adjust using (4.46). These admittance parameters, m_a and d_a, influence the phase-based parameters in the guidance law (4.20), ultimately giving rise to the desired motion $\boldsymbol{x}_d(\phi)$, as shown in Figure 4.26.

Around $t \approx 3$ s, the operator withdraws their hand, and at approximately $t \approx 3.3$ s, the robot collides with the pendulum. The impact force abruptly opposes the steering force,

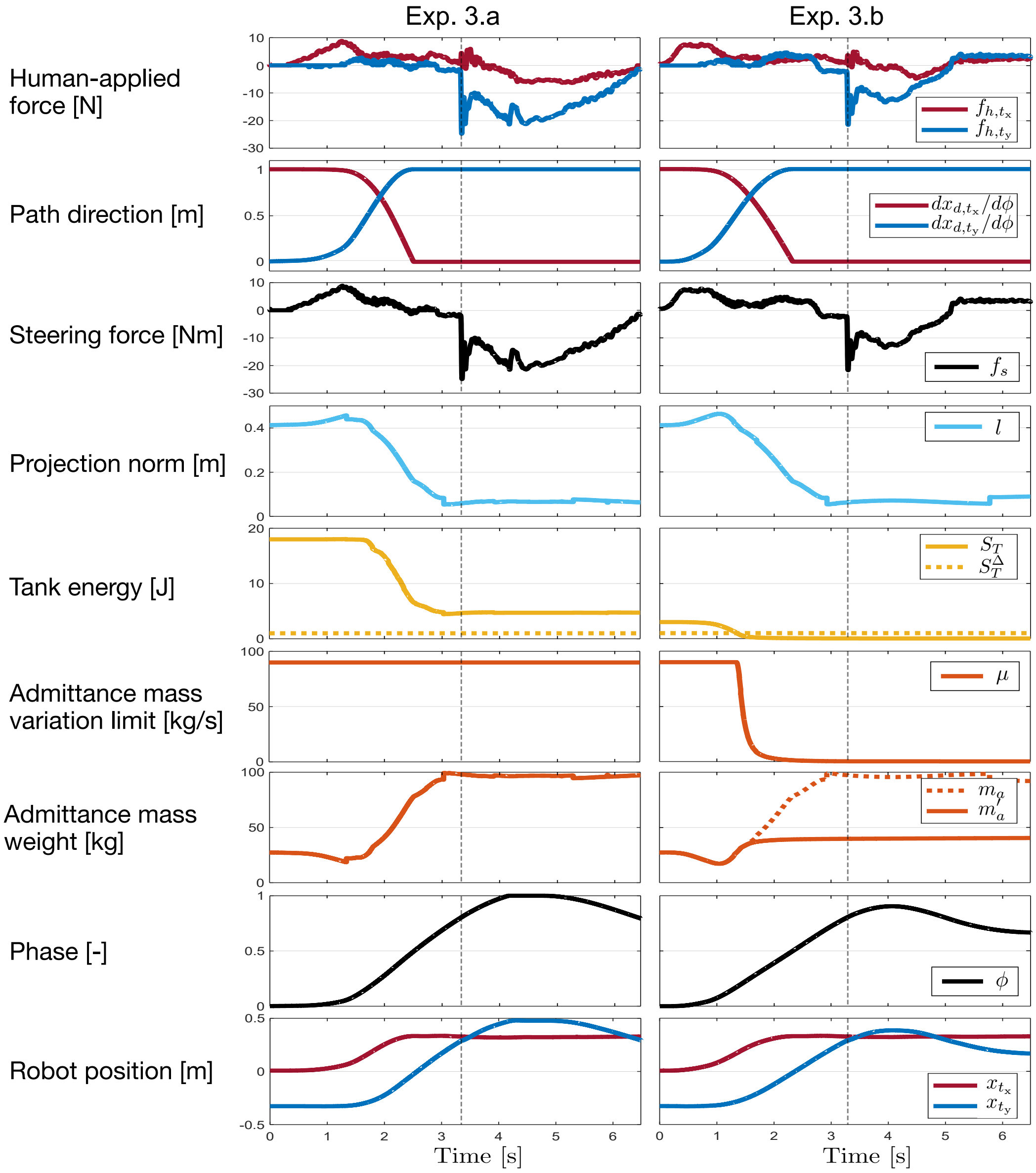

Figure 4.28: Experiment 3 – Unlike Experiment 3.a, low initial energy of tank in Experiment 3.b prevents the admittance mass from increasing. Consequently, m'_a remains below m_a. The dashed vertical lines mark the collision time.

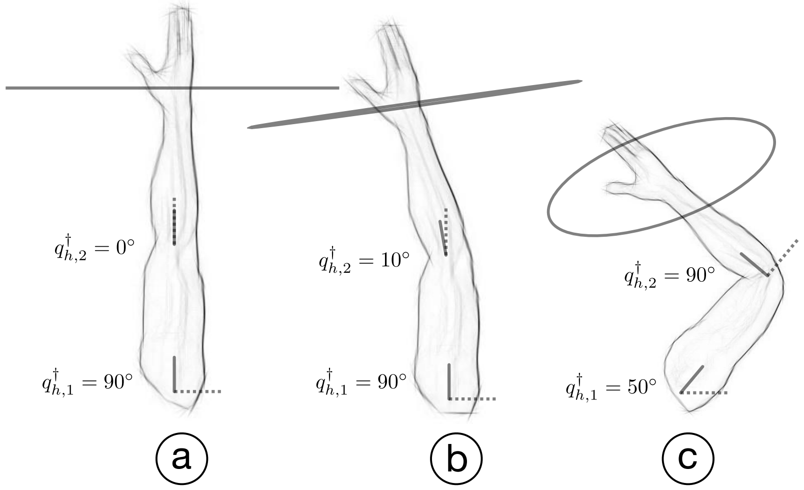

Figure 4.29: Experiment 4 – A simulated 2-DoF human arm kinematics model in three different configurations with their associated manipulability ellipses.

countering the phase progression. By this moment, the low projection norm l caused by the extended arm configuration leads to m_a reaching its peak value. Consequently, a substantial virtual momentum arises, generating high virtual kinetic energy ($E_{k_a} = 5.5$ J). Therefore, during the collision, the opposing force f_s is insufficient to halt phase advancement. As the phase hits 1, the desired trajectory halts, and due to the pendulum tilting, gravitational force strengthens, driving the phase in reverse. Subsequently, the robot traces the desired trajectory back toward the operator.

Experiment 3.b: The initial energy within the virtual tank for this experiment is set at 3 J. Consequently, the rise in admittance mass m_a gradually consumes the tank energy until it reaches the lower threshold S_T^{Δ}. At this juncture, the tank output μ decreases to zero, and the ability to shape m_a ceases. This leads to a distinctive outcome compared to the previous experiment, where the virtual kinetic energy remains steady at $E_{k_a} = 1.5$ J. Subsequently, the robot post-impact behavior differs. The impact force from the pendulum, while weaker than in Experiment 3.a, proves sufficient to arrest and reverse the robot motion prior to completing the path, specifically at $\phi = 0.9$. The findings clearly illustrate that the drained tank energy during the rise of admittance mass in Experiment 3.a amplified the virtual kinetic energy of the motion generator. This energy was then expended to fully elevate the pendulum post-impact. On the other hand, the constrained tank energy in Experiment 3.b limited the generated virtual kinetic energy, which was insufficient to raise the pendulum entirely.

Experiment 4: Sensitivity Evaluation of Manipulability Analysis for a Simulated Arm

To better understand the impact of errors in joint angle estimation on the assessment metrics r and l, an example of a 2-DoF planar arm is examined here with each link measuring 0.3 m in length, as depicted in Figure 4.29. For each configuration, there is an ideal manipulability ellipse determined by the actual joint positions $q^{\dagger}_{h,1}$ and $q^{\dagger}_{h,2}$. Depending on the vector $\boldsymbol{\nu}$, the

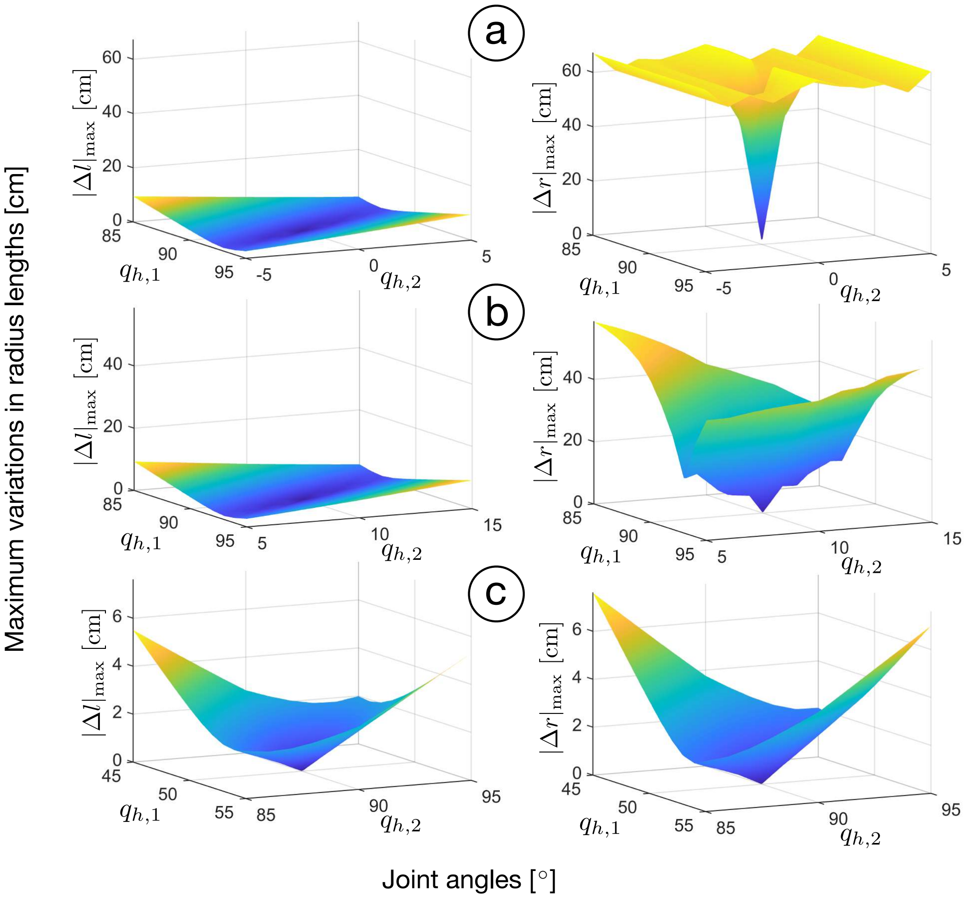

Figure 4.30: Experiment 4 – Maximum deviation of the estimated values associated with the manipulability pseudo-ellipsoid l (left) and the conventional ellipsoid r (right) due to changes in joint angle values $q_{h,1}$ and $q_{h,2}$ corresponding to different body configurations depicted in Figure 4.29.

ideal metrics $r^\dagger$ and $l^\dagger$ can be calculated using (4.55) and (4.45), respectively, considering the principal radii lengths and directions of the ideal ellipse. If the sensed human configuration $\boldsymbol{q}_h$ deviates from the actual one $\boldsymbol{q}_h^\dagger$, the estimated ellipse, and consequently the estimated metrics r and l, will differ from the ideal values with the following errors

$$\Delta r = r^\dagger - r, \qquad \Delta l = l^\dagger - l. \tag{4.97}$$

Considering all possible directions $\boldsymbol{\nu}$ and consequently all potential values for Δr and Δl, Figure 4.30 illustrates the maximum absolute errors (i.e., $|\Delta r|_{\max}$ and $|\Delta l|_{\max}$) for all combinations of sensed joint angles $q_{h,1}$ and $q_{h,2}$ within a range of ± 5 degrees from the actual joint angles $q_{h,1}^\dagger$ and $q_{h,2}^\dagger$. It is evident that when the arm is close to a singularity, even a slight estimation imprecision in one joint angle can lead to significant errors in r. Conversely, this is not the case for l, and consequently, even in the presence of considerable noise in the joint angle estimation during manipulability evaluation, the assessment metric l would not undergo significant changes. This becomes particularly crucial when the manipulability

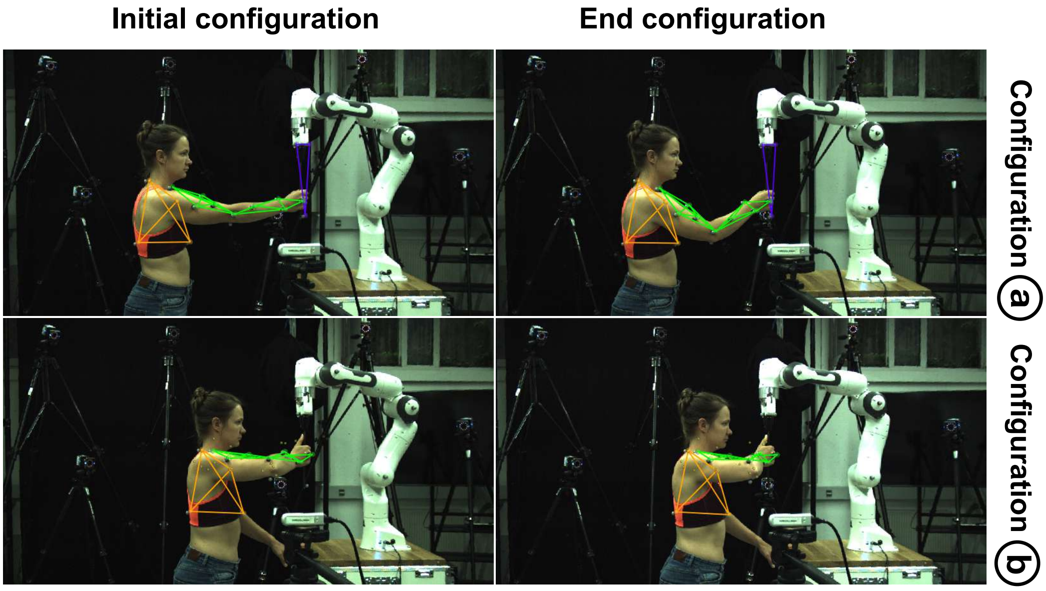

Figure 4.31: Experiment 5 – The subject moves along the direction index 6 depicted in Figure 4.32. The 16 Vicon cameras track the attached markers, and the body joint angles are continuously measured based on the Vicon built-in upper limb human model.

assessment metric is employed to execute an action, such as adjusting the control parameters of a collaborative robot. Sudden and drastic changes in this metric could lead to undesirable behavior or inconvenience. It should be mentioned that much like the radius r, the metric l is derived from the manipulability ellipsoid. However, it serves as a less stringent (and therefore more robust) tool for assessing manipulability, making it more suitable in the presence of noisy body pose estimation.

Experiment 5: Manipulability Ellipsoid vs. Pseudo-Ellipsoid

As previously discussed, manipulability analysis enables the assessment of the feasibility of end-point motions in various directions based on the required joint motion. In this context, an experiment is devised to evaluate the effectiveness of the manipulability pseudo-ellipsoid in comparison to the conventional ellipsoid approach. Three participants are instructed to move their hand along seven distinct horizontal Cartesian directions, starting from two different initial arm configurations, as depicted in Figure 4.31. The participants are identified as Subject 1, a male with a height of 1.76 m, Subject 2, a female with a height of 1.63 m, and Subject 3, a male with a height of 1.89 m. To determine the anticipated body Cartesian motions, the participants are instructed to hold and move in sync with a robot end-effector following the specified directions; see Figure 4.31. The Cartesian paths consisted of short straight lines measuring 10 m in length, directed toward the hours 3 to 9 on an imaginary horizontal clock face positioned in front of the participants; see Figure 4.32. Prior to each motion, the metrics r and l are computed using (4.55) and (4.45), respectively, based on the direction $\boldsymbol{\nu}$ and the body configuration $\boldsymbol{q}_h$ recorded by the RealSense camera. These metrics signify the requisite instantaneous joint motions for the corresponding Cartesian motions.

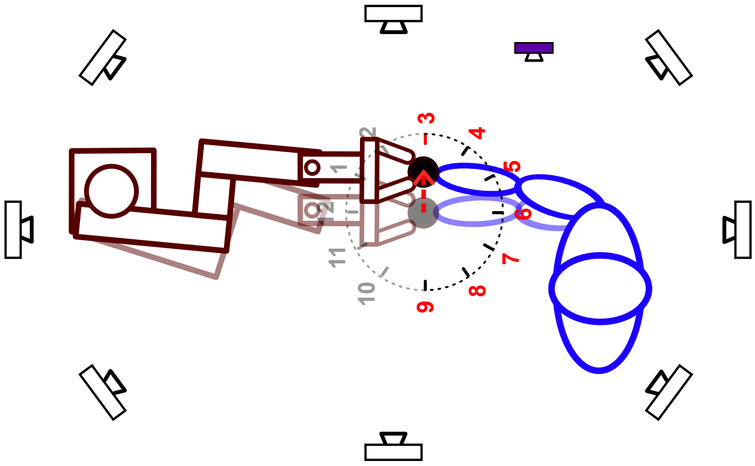

Figure 4.32: Experiment 5 – Subjects are asked to have instantaneous short motions along seven directions according to an imaginary horizontal clock face.

To assess their accuracy, the actual resulting body joint motions needed to be determined as the ground truth. To achieve this, a Vicon® motion capture system equipped with 16 infrared cameras and one HD camera is utilized to record the motion of the right upper limb at 200 Hz during the experiment. Markers are strategically placed on bony landmarks in accordance with Vicon recommendations for upper limb tracking; see Figure 4.31. The Vicon Nexus software is employed to compute joint angles using a predefined model template of upper limbs.

Given the length r of the manipulability ellipsoid radius along the direction $\boldsymbol{\nu}$, the joint velocity norm $\|\dot{\boldsymbol{q}}_{h,\boldsymbol{\nu}}\|$ associated with the Cartesian velocity $\dot{\boldsymbol{x}}_{h,\boldsymbol{\nu}}$ along $\boldsymbol{\nu}$ can be estimated via[5]

$$\|\dot{\boldsymbol{q}}_{h,\boldsymbol{\nu}}\| = \frac{\|\dot{\boldsymbol{x}}_{h,\boldsymbol{\nu}}\|}{r}. \tag{4.98}$$

Given that the motion duration along the 0.1 m lines was 1 s, it can be assumed that $\|\dot{\boldsymbol{x}}_{h,\boldsymbol{\nu}}\| \approx 0.1$ m/s. Utilizing (4.98), the significance of the motion in the body joints can be estimated according to both the manipulability ellipsoid radius r and the manipulability pseudo-ellipsoid radius l as

$$\delta_r = \frac{0.1}{r}, \qquad \delta_l = \frac{0.1}{l}. \tag{4.99}$$

The estimated values δ_r and δ_l are then compared with the observed joint motions $\|\Delta\boldsymbol{q}_h\|$ recorded by the Vicon system for the three body joints used to derive r and l. As shown in Figure 4.33, the joint motion estimation δ_l obtained through the manipulability pseudo-ellipsoid closely aligns with the actual values when compared to the estimated values δ_r derived from the conventional method. Specifically, during configuration ⓐ, the mean absolute errors between δ_l and $\|\Delta\boldsymbol{q}_h\|$ are 14, 7, and 17 degrees for subjects 1, 2, and 3, respectively. In configuration ⓑ, the mean absolute errors are 3, 5, and 3 degrees for the

---

[5] For a unit-norm joint velocity, the Cartesian velocity's norm along $\boldsymbol{\nu}$ is r.

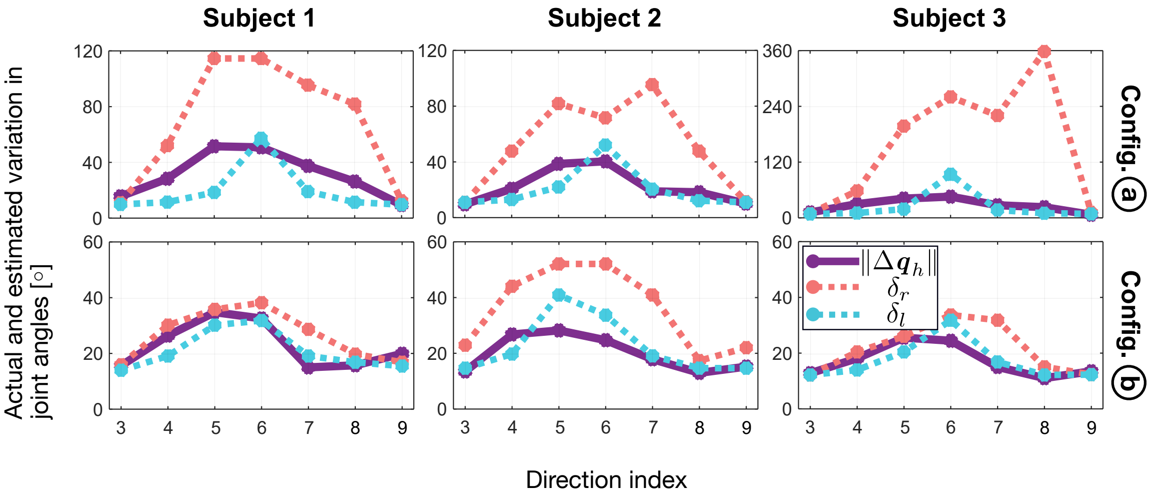

Figure 4.33: Experiment 5 – Estimated and actual values of body joints motions for seven Cartesian motions depicted in Figure 4.32. The manipulability pseudo-ellipsoid estimation δ_l resulted in being closer to the actual values compared to the standard method.

same subjects. In contrast, the mean absolute errors between δ_r and $\|\Delta \boldsymbol{q}_h\|$ during configuration ⓐ are 39, 30, and 134 degrees, and during configuration ⓑ are 4, 16, and 5 degrees for subjects 1, 2, and 3, respectively. The disparity between δ_l and δ_r is much more pronounced in configuration ⓐ, where the arm is in close proximity to a singularity, resulting in a much narrower manipulability ellipsoid compared to configuration ⓑ. As previously mentioned, one potential explanation for the relatively subpar performance of the conventional manipulability ellipsoid method may be its sensitivity to the measurement of body configuration. The Vicon motion capture system boasts significantly higher measurement accuracy compared to the markerless single-camera vision system utilized for manipulability assessment. Hence, especially when sensitivity is heightened, the outcomes could diverge considerably from one another.

Another contributing factor to the significant disparity between δ_r and $\|\Delta \boldsymbol{q}_h\|$ may be the overly simplified model employed to construct the Jacobian matrix. As previously described, only three joints are taken into consideration in the human arm kinematics model, with the assumption that the other joints remained fixed during the motions, as depicted in Figure 4.23. Consequently, the subjects are instructed to focus solely on manipulating the specified three joints during the experiments. However, based on the results from the Vicon system, they inadvertently engage other joints to a small extent. The average values of $\|\Delta \boldsymbol{q}_h\|$ across all seven directions, when only the primary three joints are considered, are 31, 22, and 27 degrees during configuration ⓐ, and 23, 20, and 17 degrees during configuration ⓑ, for subjects 1, 2, and 3, respectively, as shown in Figure 4.33. Yet, when six joints (i.e., joint 2 to joint 7, as indicated in Figure 4.23) are taken into account, the average values of $\|\Delta \boldsymbol{q}_h\|$ shifted to 45, 28, and 32 degrees in configuration ⓐ, and 28, 22, and 20 degrees in configuration ⓑ, for subjects 1, 2, and 3, respectively. The inclusion of these additional joints may have compensated for the need for substantial motions in the primary three joints, which are estimated by the simplified 3-DoF model. Therefore, it is possible that

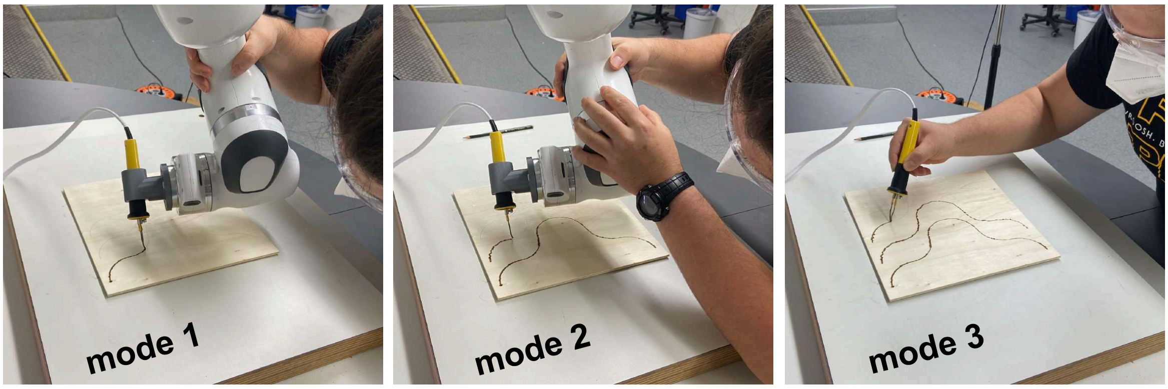

Figure 4.34: Pyrography on a wood plate with three different modes; the operator is supposed to create a consistent line along the drawn paths.

if the additional joints were kept stationary or a more sophisticated kinematics model was utilized, the estimations might have been more accurate. However, due to the constraints of the vision system, which only permits the measurement of three joint values, the simplified model was the only feasible option for the assessment. Interestingly, even with this limitation, the estimated values δ_l are, on average, closer to the actual values $\|\Delta \boldsymbol{q}_h\|$ that included all six joints, compared to the estimated values δ_r. In summary, for the manipulability assessment objective, considering both sensory errors and model inaccuracies, the approach relying on the manipulability pseudo-ellipsoid yields more dependable estimations compared to the conventional method.

4.2.6 User Study in Pyrography

To assess the effectiveness of the proposed haptic motion guidance in a real-world human-robot interaction scenario, a user study with approval from the Ethics Commission of the Technical University of Munich (review number 744/21 S-SR) is designed for a pyrography (wood burning) task. In this task, a heated metal tip is moved on a wooden surface to create a line mark; see Figure 4.34. The thickness of the line is controlled by adjusting metal pressure and movement speed, demanding both precision (staying on the line) and robustness (coping with wood surface or metal temperature changes). The objective is to achieve a consistent mark along a predefined line; see Figure 4.34. A disturbance is introduced by reducing metal temperature midway, potentially causing line inconsistency if the burner speed is not adjusted. Figure 4.35 depicts the result of a robot autonomously moving the wood burner at constant speed on various wood types; a fainter mark on the latter half underlines the need to address the disturbance. As advanced sensors may be absent, human involvement is crucial to visually assess the quality and adapt the burner pace.

Twenty volunteers were tasked with creating a uniform line along drawn paths on 20 wood plates using three modes (see Figure 4.34):

- **Mode 1:** The robot holds the wood burner, and the human operator guides the motion via the proposed guidance law (i.e., the phase-based motion generator + impedance control + gravity compensation).

Figure 4.35: Automated pyrography with an impedance-controlled robot along a predefined path at a constant speed. The wood burner temperature intentionally drops by a quarter in the middle, resulting in a fainter marked line thereafter.

- **Mode 2:** The robot holds the wood burner, and the human operator guides the motion by freely moving the robot (i.e., only gravity compensation).
- **Mode 3:** The human operator holds the wood burner in hand, without a robot.

In mode 1, the desired path is uniformly encoded, and the stiffness of the impedance controller orthogonal to the plate surface is set to zero. This enables the operator to easily lift the robot end-effector, removing the wood burner from the plate (see Figure 4.34). Notably, any parameter adaptation is excluded from the guidance law. Instead, after a few preliminary trials, the parameters m_a and d_a are fixed based on each user's preference. In mode 2, for enhanced comfort, the rotational stiffness is set high. This allows the operator to move the wood burner solely in a linear manner, without the need to adjust the orientation of the tip. Safety-wise, the human is instructed to keep their hand away from both the wood burner tip and the wood surface. Importantly, the intention behind this user study is not to compare the proposed guidance algorithm with related literature works. Rather, the focus is on gaining firsthand insights into the proposed approach, particularly in comparison to scenarios without robot involvement.

A total of 20 participants took part, including an equal split of 10 males and 10 females, with ages ranging from 22 to 61 and an average of 31.3 years. Initially, each participant's table height was adjusted, and they were given a few minutes to acquaint themselves with pyrography. Subsequently, the experiment and questionnaire (depicted in Figure 4.37) were explained. Additionally, they had a brief period before each mode to practice and, especially in mode 1, set their personalized, comfortable admittance parameters. The order of modes was randomized for each user to prevent potential questionnaire response bias. In the questionnaire, participants were first queried about their experience in physical interaction with robots, yielding an average response of 2.45 on a scale of 1 (none) to 5 (very experienced). They were also asked about their prior involvement in crafts or pyrography-related activities, resulting in an average response of 2.9. Following this, participants engaged in the task using one of the three modes and promptly provided responses to mode-specific questions using a Likert scale (ranging from strongly disagree to strongly agree, as depicted in Figure 4.37):

- <u>Comfort</u>: I felt comfortable during the task.

Figure 4.36: Pyrography user study results; twenty participants utilized three distinct modes to produce uniform lines on twenty wooden plates. The lines on the left, center, and right of each plate correspond to mode 1, mode 2, and mode 3, respectively.

- Freedom: My body posture was unconstrained, and I was free to change it during the task.
- Control: I had complete control over the task performance.
- Ease: It was easy to fulfill the task requirement of staying on the path.
- Safety: I felt safe during the task.

Finally, on a scale of 1 to 5 with 1 being the worst and 5 being the best evaluation score, the participants replied to the two following questions:

- Efficacy: How would you rate your ability to deliver a good result with the approach (given your current training level)?
- Overall: What is your overall evaluation of the approach?

Figure 4.36 illustrates the resulting wood plate shapes, while Figure 4.38 presents the questionnaire outcomes. Mode 1 garnered the highest scores across most questions. On average, participants found mode 1 notably easier and more effective in achieving the desired outcome. Specifically, among participants with handicraft expertise below 3, the *comfort* question had an average response of 4.7 for mode 1, compared to 3.4 and 2.7 for mode 3 and mode 2, respectively. This subgroup also considered mode 3 the least safe, with an average rating of 3.9. Intriguingly, participants with handicraft expertise above 3 still awarded the highest average score for the *efficacy* question to mode 1 (4.4), followed by mode 3 (4.1) and mode 2 (3). Regarding the *freedom* question, mode 3 garnered the highest overall average response. An interesting observation emerged from participants with a robot interaction experience level of 1 or 2, who assigned a 4.8 average score for the *control* question to mode 1, compared to 3.6 for mode 2 and 3.9 for mode 3. This suggests that, relative to the overall ratings, they had a more favorable experience when the robot was engaged. Notably, their mean response for the question regarding overall experience was 4.9 for mode 1. Lastly, time was another factor under consideration. Mode 1 proved to be the fastest for 14 participants, whereas mode 3 was the fastest for only 4 participants. Conversely, mode 3 was the slowest for 10 participants, followed by mode 2 for 7 participants.

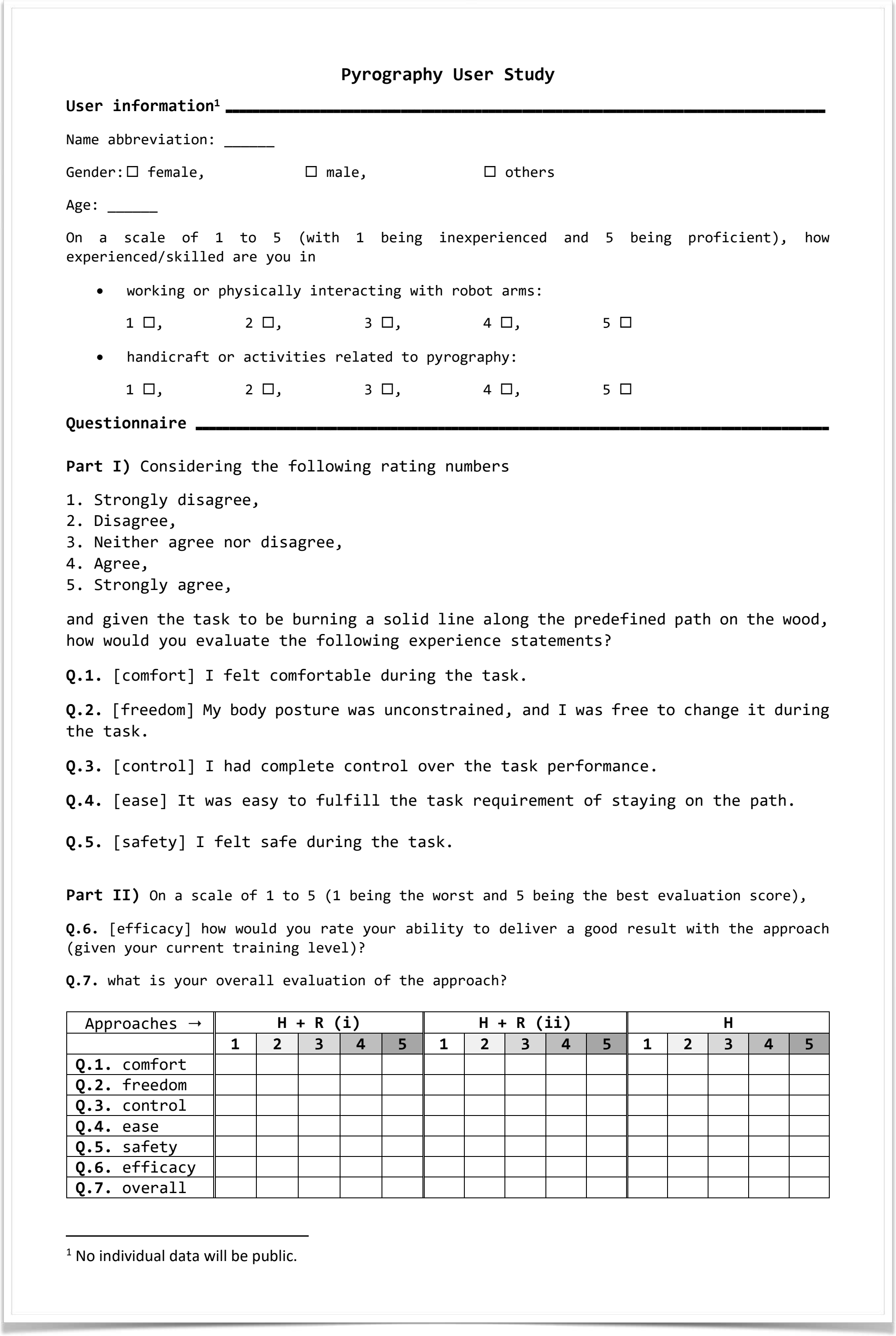

Pyrography User Study

User information[1]

Name abbreviation: ______

Gender: ☐ female, ☐ male, ☐ others

Age: ______

On a scale of 1 to 5 (with 1 being inexperienced and 5 being proficient), how experienced/skilled are you in

- working or physically interacting with robot arms:

  1 ☐, 2 ☐, 3 ☐, 4 ☐, 5 ☐
- handicraft or activities related to pyrography:

  1 ☐, 2 ☐, 3 ☐, 4 ☐, 5 ☐

Questionnaire

Part I) Considering the following rating numbers

1. Strongly disagree,
2. Disagree,
3. Neither agree nor disagree,
4. Agree,
5. Strongly agree,

and given the task to be burning a solid line along the predefined path on the wood, how would you evaluate the following experience statements?

Q.1. [comfort] I felt comfortable during the task.

Q.2. [freedom] My body posture was unconstrained, and I was free to change it during the task.

Q.3. [control] I had complete control over the task performance.

Q.4. [ease] It was easy to fulfill the task requirement of staying on the path.

Q.5. [safety] I felt safe during the task.

Part II) On a scale of 1 to 5 (1 being the worst and 5 being the best evaluation score),

Q.6. [efficacy] how would you rate your ability to deliver a good result with the approach (given your current training level)?

Q.7. what is your overall evaluation of the approach?

Approaches →	**H + R (i)**					**H + R (ii)**					**H**				
	1	**2**	**3**	**4**	**5**	**1**	**2**	**3**	**4**	**5**	**1**	**2**	**3**	**4**	**5**
Q.1. comfort															
Q.2. freedom															
Q.3. control															
Q.4. ease															
Q.5. safety															
Q.6. efficacy															
Q.7. overall															

---

[1] No individual data will be public.

Figure 4.37: The questionnaire employed in the pyrography user study.

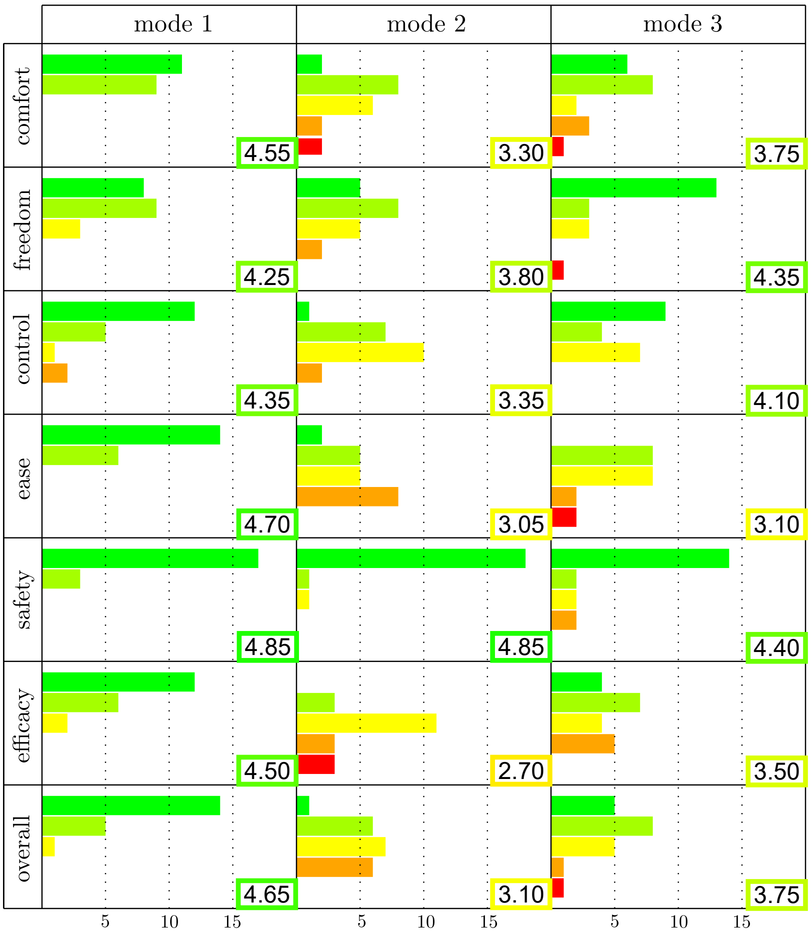

Figure 4.38: Pyrography questionnaire results; in each box, bars of varying colors (from green to red, top to bottom) represent votes for each question and mode. They encode responses from *strongly agree* to *strongly disagree* for the initial five questions and scores 5 to 1 for the last two questions. Bar lengths correspond to the number of votes, and the average vote is displayed in the bottom-right corner of each box.

4.3 Support-Adaptive Robot-Aided Movement Rehabilitation

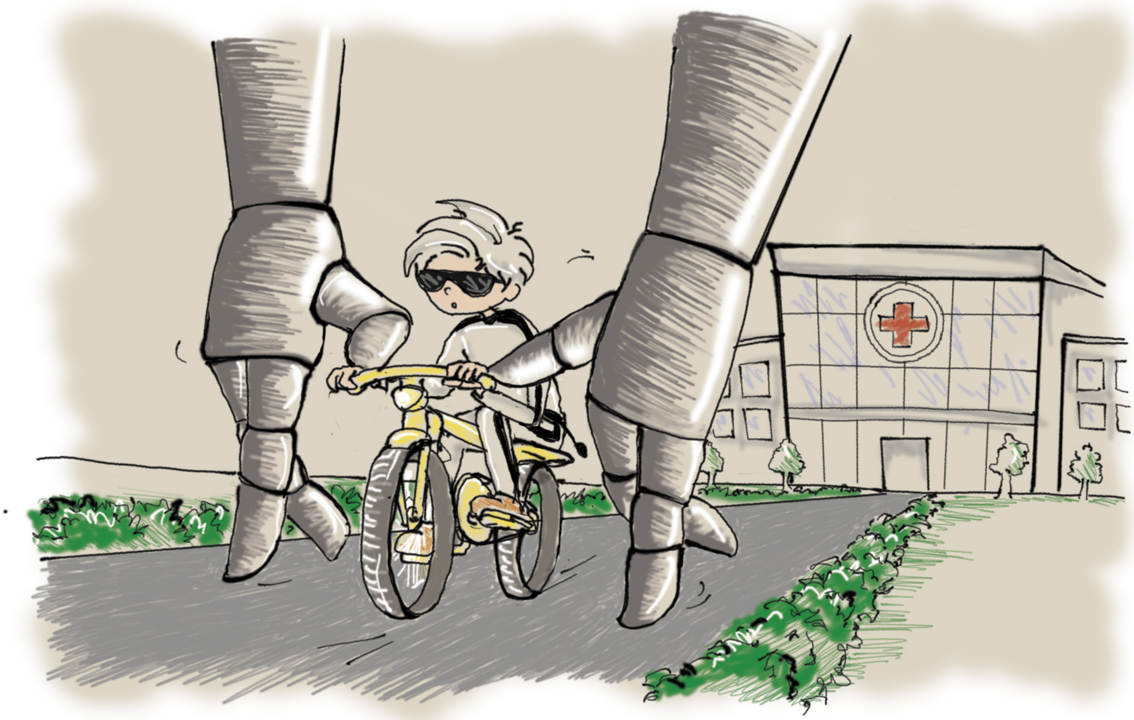

Repetitive motion plays a pivotal role in movement rehabilitation, a factor that can be effectively facilitated by robots. However, for enhanced therapy effectiveness, active patient participation in the movement is equally crucial. Recognizing this, a new class of robot control, known as *Assist-As-Needed* (AAN) control, has emerged in rehabilitation robotics. Its primary objective is to adjust the level of robot support provided to the patient, maintaining a challenge point that may motivate the patient to actively engage in the motion. This policy, however, is effective only if the patient is not impeded (e.g., by the robot) when intending to move in the appropriate direction. While reducing robot support can enhance this, it may not be sufficient, as the physical characteristics of the robot (e.g., inertia) can still impede the patient's voluntary movements. Thus, the rehabilitation robot should possess a permissiveness feature when necessary.

This section aims to address all three aforementioned aspects: repetitive movement along a therapeutic path, adjusting robot support and regulating robot permissiveness along the path. Similar to the other sections of this chapter, the concept of phase-encoded paths and adjusting the phase trajectory is employed here. The proposed approach offers two distinctive benefits in practice. First, since it is derived on the trajectory level (i.e., decoupled from the controller), it is applicable to any rehabilitation robot with diverse motion controllers. Second, the approach can provide a controllable degree of permissiveness to robots that, due to their physical characteristics, are not inherently capable of offering it. Consequently, it can render a greater number of robots suitable for rehabilitation, even those with lower costs.

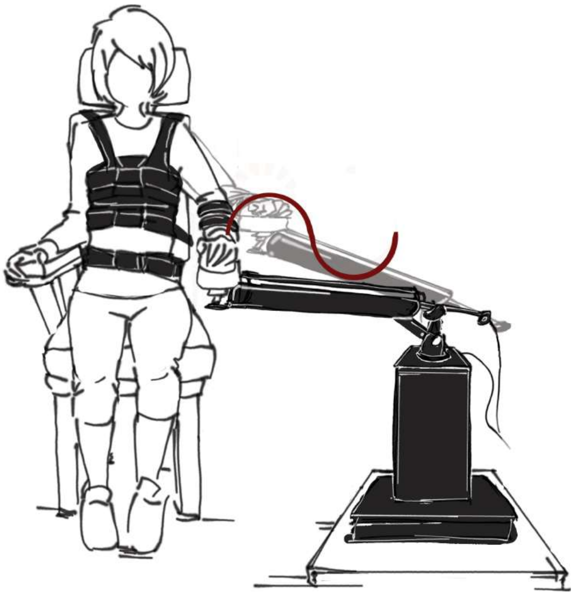

Figure 4.39: A rehabilitation robot moving the patient's limb along a therapeutic path.

The proposed approach addresses the dual aspects of support and permissiveness in a complementary manner. It establishes a relationship where a higher level of support along a therapeutic path corresponds to a lower level of permissiveness and vice versa. Consequently, manipulating a single value—phase speed—enables the delivery of the intended level of support/permissiveness. This modulation is tailored to the patient's physical impact on the movement. The following sections introduce a metric to monitor the patient's influence on the motion. Subsequently, a phase-modulation policy is presented, followed by an iterative learning method that determines the appropriate support/permissiveness level. Finally, the proposed policies are compared with the energy-based modeling paradigm.

4.3.1 Patient Physical Effect Metric

Consider a robot affixed to the patient's limb, equipped with a controller to trace a desired trajectory along a therapeutic path defined in an m-dimensional Cartesian space; refer to Figure 4.39. Unless the patient precisely follows the desired trajectory, their unmodelled presence introduces disturbances to the motion-following task. Instead of having the controller reject such disturbances to adjust the support/permissiveness level, the objective is to grant the patient flexibility in their movement along the path. Depending on the control performance and the robot's physical characteristics, one consequence of the patient's presence may be a deviation of the robot from the setpoint. For the same controlled robot, a more pronounced deviation indicates that the patient is exerting greater effort to diverge from the desired trajectory, whether intentionally or unintentionally. Thus, an observation metric can be derived based on this deviation.

The goal is to adjust the support/permissiveness level exclusively along the therapeutic path. Therefore, the observation metric should align with this objective. To achieve this, the path can be encoded using the phase variable $\phi \in [0,1]$, as outlined in Section 4.1.

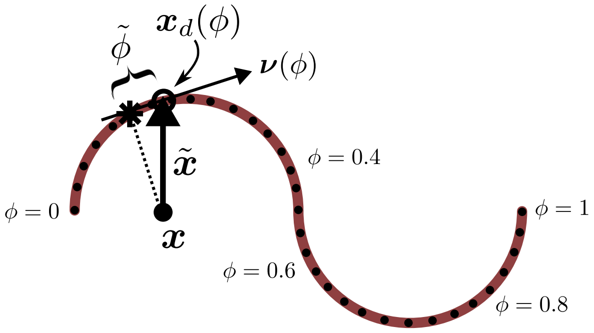

Figure 4.40: Projection of the Cartesian error $\tilde{\boldsymbol{x}}$ onto the phase-encoded path.

Subsequently, the phase-based tracking error $\tilde{\phi} \in \mathbb{R}$ can be approximated by projecting the Cartesian error $\tilde{\boldsymbol{x}} = \boldsymbol{x}_d - \boldsymbol{x}$ onto the path tangent unit vector $\boldsymbol{\nu}(\phi)$ derived in (4.44) as follows (see Figure 4.40):

$$\tilde{\phi} \approx \frac{\tilde{\boldsymbol{x}}^T \boldsymbol{\nu}(\phi)}{l_d}. \tag{4.100}$$

Here, $l_d \in \mathbb{R}_{>0}$ is the length of the desired path, determined by

$$l_d = \int_0^1 \boldsymbol{x}_d(\phi) d\phi. \tag{4.101}$$

Ultimately, the significance of the deviation of the robot from the setpoint along the path can be ascertained through $\tilde{\phi}$, for instance, by defining[6] the *phase-based deviation metric* E as

$$E = \frac{1}{2} k_\phi \tilde{\phi}^2, \tag{4.102}$$

with $k_\phi \in \mathbb{R}_{>0}$ being a user-defined parameter. The non-zero values of E may stem from two distinct patient behaviors: either resistance to the motion or an attempt to move faster than the desired trajectory. These cases can be differentiated by comparing the direction of the patient-applied wrench $\boldsymbol{f}_h \in \mathbb{R}^m$ with respect to the path direction. This is achieved by projecting the interaction wrench onto the desired path as

$$f_\phi = \boldsymbol{f}_h^T \boldsymbol{\nu}(\phi), \tag{4.103}$$

and considering the sign of f_ϕ. Combining (4.102) and (4.103), the path-centric patient's physical effect metric $\hat{E} \in \mathbb{R}$ can be derived as

$$\hat{E} = \operatorname{sgn}(f_\phi) E. \tag{4.104}$$

A relatively larger $\hat{E}$ indicates that the patient is (intentionally/unintentionally) trying to deviate from the setpoint. Its sign indicates whether the intended movement is in the forward or backward direction relative to the desired motion. In the following, it is shown how adapting the desired trajectory based on $\hat{E}$ can result in support/permissiveness adaptation of the robot.

---

[6] Note that other definitions could be used for the phase-based deviation metric, e.g., by taking into account the velocity error as in (4.112).

4.3.2 Reactive Phase Modulation for Support Regulation

As mentioned above, the proposed approach adjusts the robot's level of support or permissiveness through the modulation of the desired trajectory. To ensure this adaptive behavior is exclusive to the therapeutic path, the trajectory modulation is carried out in phase space. This is achieved through the adjustment of the phase progression speed, maintaining the robot setpoint consistently on the desired path. Suppose there exists a nominal phase trajectory $\phi^\dagger(t)$, with the phase velocity $\Omega^\dagger(t) = \dot{\phi}^\dagger(t)$, associated with the initially assigned therapist's nominal desired trajectory $\boldsymbol{x}_d^\dagger(t)$. During therapy, the phase trajectory $\phi(t)$, determining the desired Cartesian trajectory $\boldsymbol{x}_d(t)$, can be shaped by adjusting the nominal phase velocity via

$$\phi(t) = \int_0^t \sigma_{\mathrm{aan}} \Omega^\dagger(\varepsilon)\; d\varepsilon. \tag{4.105}$$

Here, $\sigma_{\mathrm{aan}} \in \mathbb{R}$ represents the Assist-As-Needed velocity adaptation gain used to adjust the nominal phase velocity. As demonstrated in the following, its value can be dynamically determined based on the patient's input $\hat{E}$ to consistently provide the desired level of support along the path.

When the magnitude of $\hat{E}$ (i.e., E) is low, associated with negligible physical effect of the patient, σ_{aan} can be set to 1, indicating no velocity adaptation. However, when $\hat{E}$ is positive and large, indicating the patient's attempt to move faster, σ_{aan} can take on larger values to align with the patient's motion intention. In contrast, when $\hat{E}$ is negative and large, signifying resistance from the patient, σ_{aan} can be reduced to zero. Finally, when $\hat{E}$ takes even larger negative values, indicating the patient's attempt to move backward, σ_{aan} can assume negative values, resulting in a backward desired trajectory. Thus, the phase velocity is adjusted according to the thresholds defined for $\hat{E}$. Consequently, a *cascading-shaped map* between $\hat{E}$ and σ_{aan} could be constructed as a smooth function (depicted in Figure 4.41) derived as

$$\sigma_{\mathrm{aan}}(\hat{E}) = \begin{cases} -\sigma_{N,\max} & \text{if} \quad \hat{E} < -E_{N4}, \\ -\sigma_{N,\max} + \frac{\sigma_{N,\max}}{2}\left(1 - \cos\left(\frac{E_{N4}+\hat{E}}{E_{N4}-E_{N3}}\pi\right)\right) & \text{if} \quad -E_{N4} \leq \hat{E} < -E_{N3}, \\ 0 & \text{if} \quad -E_{N3} \leq \hat{E} < -E_{N2}, \\ \frac{1}{2}\left(1 - \cos\left(\frac{E_{N2}+\hat{E}}{E_{N2}-E_{N1}}\pi\right)\right) & \text{if} \quad -E_{N2} \leq \hat{E} < -E_{N1}, \\ 1 & \text{if} \quad -E_{N1} \leq \hat{E} < E_{P1}, \\ 1 + \frac{\sigma_{P,\max}-1}{2}\left(1 - \cos\left(\frac{\hat{E}-E_{P1}}{E_{P2}-E_{P1}}\pi\right)\right) & \text{if} \quad E_{P1} \leq \hat{E} < E_{P2}, \\ \sigma_{P,\max} & \text{if} \quad E_{P2} \leq \hat{E}. \end{cases} \tag{4.106}$$

Here, $\sigma_{P,\max} \geq 1$ and $\sigma_{N,\max} \geq 0$ represent the maximum magnitudes of the velocity adaptation gain for forward and backward motions, respectively. Moreover, $E_j \geq 0$ with $j = P1, P2, N1, N2, N3, N4$ represent the velocity adaptation thresholds from which the smooth transitions between different values of σ_{aan} begin.

The cascading-shaped map determines the reactive behavior of the robot in response to variations in the patient's physical effect $\hat{E}$. If the patient remains close to the desired trajectory without significant deviation, resulting in small values for $\tilde{\phi}(t)$ and thus $\hat{E}$, no

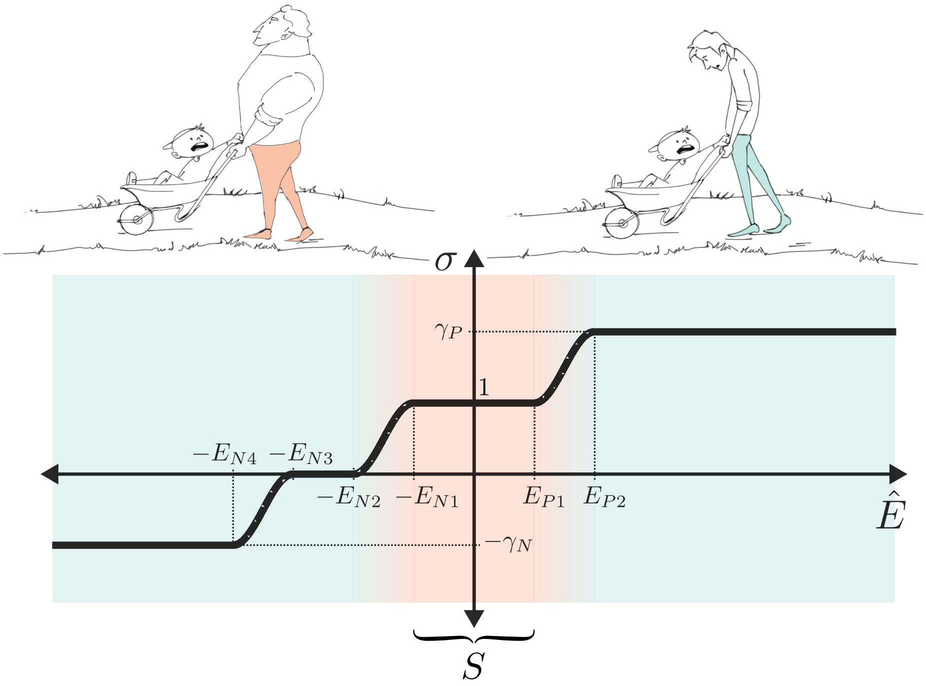

Figure 4.41: Cascading-shaped map – The red area indicates minimal velocity adaptation, signifying full support, while in the blue area, the nominal velocity is adjusted based on the patient's input. A larger red region implies a more supportive robot behavior.

velocity modulation would occur (i.e., $\sigma_{\text{aan}} \approx 1$). When the patient actively or passively resists the motion, $\hat{E}$ becomes negative. If the resistance is strong enough to exceed the threshold $-E_{N1}$, σ_{aan} will decrease, allowing the patient to slow down, stop or even reverse the motion. Finally, if the patient tries to move faster than the nominal trajectory, $\hat{E}$ becomes positive. In this case, when $\hat{E}$ surpasses the limit E_{P1}, σ_{aan} increases, enabling the patient to move faster. Therefore, the configuration of the thresholds E_j directly influences the robot's supportive/permissive behavior. A larger region with $\sigma_{\text{aan}} \approx 1$ (the red area in Figure 4.41) indicates greater support from the robot, while a larger area with $\sigma_{\text{aan}} \neq 1$ (the blue area in Figure 4.41) signifies more ease for the patient to modify the phase trajectory, corresponding to a more permissive behavior of the robot.

4.3.3 Progressive Phase-Based Assist-As-Needed Control

As elaborated before, when $\hat{E}$ falls between E_{P1} and $-E_{N1}$, σ_{aan} remains 1, and thus there is no velocity adaptation. In other words, when $-E_{N1} \leq \hat{E} < E_{P1}$, there is no permissiveness, and depending on the performance of the employed controller, the robot provides the support to keep the human on the nominal trajectory $\boldsymbol{x}_d^{\dagger}(t)$. Accordingly, considering Figure 4.41, the variable $S \in \mathbb{R}_{\geq 0}$ can be defined to represent the extent of the no-adaptation region and, equivalently, the support level according to

$$S = E_{N1} + E_{P1}. \tag{4.107}$$

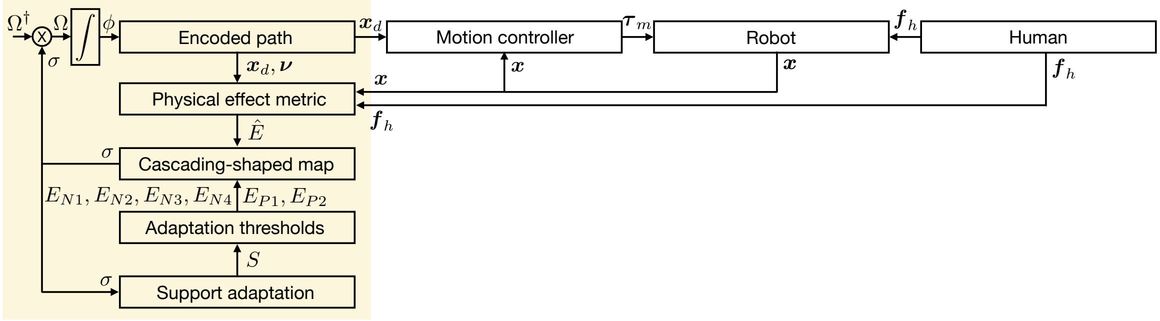

Figure 4.42: Overall control architecture – The proposed support-adaptive approach (highlighted) can be modularly integrated with any motion-controlled robot.

The larger S is, the less reactive and permissive, and equivalently, the more supportive the robot becomes. Hence, the configuration of the cascading-shaped map (4.106) can be dynamically adjusted based on the desired support level by defining adaptation thresholds $E_\circ$ (where $\circ \in \{P1, P2, N1, N2, N3, N4\}$) to maintain a constant linear relationship with S such that

$$E_\circ = \epsilon_\circ S, \tag{4.108}$$

where $\epsilon_\circ > 0$ represents constant scaling values predetermined prior to therapy.

A common strategy to encourage patient engagement in therapeutic movements, thereby improving recovery outcomes, involves progressively decreasing support when the patient demonstrates competence and increasing it when the patient faces difficulties in performing movements independently. This method is known in the literature as the Assist-As-Needed (AAN) control policy. Similarly, an iterative learning approach is proposed here to adjust the support level S with each therapeutic motion cycle. Considering that a patient's body configuration may vary along the therapeutic path, their capability to execute movements and the requisite support level might need adjustments within a single motion cycle. Consequently, both the learning parameters and the support level can be defined as functions of phase ϕ. Considering $S_j(\phi)$ as the phase-based support profile for iteration j, the adaptation law for iteration $j+1$ can be derived as

$$S_{j+1}(\phi) = S_j(\phi) + \kappa_l(\phi)(1 - \bar{\sigma}_j(\phi)) - \kappa_f(\phi). \tag{4.109}$$

Here, $\kappa_l(\phi), \kappa_f(\phi) \geq 0$ are the learning and forgetting factors, where usually $\kappa_l >> \kappa_f$. Moreover, $\bar{\sigma}_j(\phi)$ is the average of the σ_{aan} values at each phase[7] during iteration j.

The adaptation policy (4.109) iteratively determines the appropriate level of support that the robot should provide to the patient. The idea is to adjust the support level based on the value of $\hat{E}$ during an iteration. If $\hat{E}$ falls below $-E_{N1}$, indicating the patient's resistance to the motion or their inability to move, the support is increased in the subsequent iteration. Conversely, when the opposite occurs, the support is decreased with the aim of keeping the patient at the challenge point. These adjustments can be monitored by observing the value

---

[7] A phase value can be traversed more than once due to a non-positive σ_{aan}.

of σ_{aan} during the iterations. Upon establishing the value of S, the adaptation thresholds $E_\circ$ are set in accordance with (4.108) with $\epsilon_\circ$ predetermined at the therapy's outset. By employing the iterative adaptation law (4.109), the support level of the robot is adjusted to provide the patient with only the minimum amount required. This may increase the patient's motivation to participate more actively in rehabilitation. Figure 4.42 depicts the overall architecture.

4.3.4 Energy-Based Support Modeling for an Impedance-Controlled Robot

It is demonstrated in Section 3.1 that when the robot is equipped with an impedance controller (3.1), an energy storage function $S_i \in \mathbb{R}_{\geq 0}$ can be assigned to the controlled robot system, defined as

$$S_i = \frac{1}{2}\dot{\tilde{\boldsymbol{x}}}^T \boldsymbol{M}_C(\boldsymbol{q})\dot{\tilde{\boldsymbol{x}}} + \frac{1}{2}\tilde{\boldsymbol{x}}^T \boldsymbol{K}_C \tilde{\boldsymbol{x}}. \tag{4.110}$$

Considering its time evolution derived[8] in (3.18), it can be observed that the changes in the energy level S_i have a direct relationship with the physical power $P_h = \dot{\boldsymbol{x}}^T \boldsymbol{f}_h$ exchanged between the patient and the robot according to

$$\dot{S}_i = \underbrace{\dot{\boldsymbol{x}}^T \boldsymbol{f}_h}_{P_h} \underbrace{-\dot{\boldsymbol{x}}_d^T \boldsymbol{f}_h}_{P_d} - \underbrace{\dot{\tilde{\boldsymbol{x}}}^T \boldsymbol{D}_C \dot{\tilde{\boldsymbol{x}}}}_{P_{\text{diss}}}. \tag{4.111}$$

Here, P_d represents the power associated with the desired trajectory in contact with the patient, and P_{diss} denotes the dissipation power corresponding to the controller damping effect. Considering (4.110) and (4.111), it can be observed that as S_i increases, it becomes more likely for P_h to take on large negative values. A negative P_h indicates motion opposing the wrench applied by the human to the robot, corresponding to the supportive behavior of the robot. Therefore, to adapt the support level, one way could be to adjust the maximum level that S_i could reach. Referring to (4.111), one way to achieve this is by manipulating the power P_d, specifically by adjusting the desired velocity $\dot{\boldsymbol{x}}_d$; see Figure 4.43.

To exclusively apply the aforementioned observations along the therapeutic path, the energy function S_i can be derived in a path-centric manner by expressing the relevant variables in the phase domain. This yields the phase-based energy function $S_{i,\phi} \in \mathbb{R}_{\geq 0}$, derived as

$$S_{i,\phi} = \frac{1}{2} m_{C,\phi} \dot{\tilde{\phi}}^2 + \frac{1}{2} k_{C,\phi} \tilde{\phi}^2. \tag{4.112}$$

Here, $m_{C,\phi} \in \mathbb{R}_{>0}$ and $k_{C,\phi} \in \mathbb{R}_{\geq 0}$ represent the robot mass matrix and the controller stiffness matrix, respectively, as approximated in the phase domain. Their values can be determined through the following derivations.

$$\begin{aligned}
& m_{C,\phi}\ \dot{\tilde{\phi}} = \dot{\tilde{\boldsymbol{x}}}^T \boldsymbol{M}_C^T(\boldsymbol{q})\ \boldsymbol{\nu}(\phi), \\
\Longrightarrow\ & m_{C,\phi} \left(\frac{\dot{\tilde{\boldsymbol{x}}}^T \boldsymbol{\nu}(\phi)}{l_d} + \frac{\tilde{\boldsymbol{x}}^T \dot{\boldsymbol{\nu}}(\phi)}{l_d} \right) \approx \dot{\tilde{\boldsymbol{x}}}^T \boldsymbol{M}_C^T(\boldsymbol{q})\ \boldsymbol{\nu}(\phi), \\
\Longrightarrow\ & m_{C,\phi} \approx l_d\ \frac{\dot{\tilde{\boldsymbol{x}}}^T \boldsymbol{M}_C^T(\boldsymbol{q}) \boldsymbol{\nu}(\phi)}{\dot{\tilde{\boldsymbol{x}}}^T \boldsymbol{\nu}(\phi) + \tilde{\boldsymbol{x}}^T \dot{\boldsymbol{\nu}}(\phi)},
\end{aligned} \tag{4.113}$$

---

[8] Note that the force control output $\boldsymbol{f}_f$ is excluded here, and the notation $\boldsymbol{f}_{\text{ext}}$ is replaced with $\boldsymbol{f}_h$.

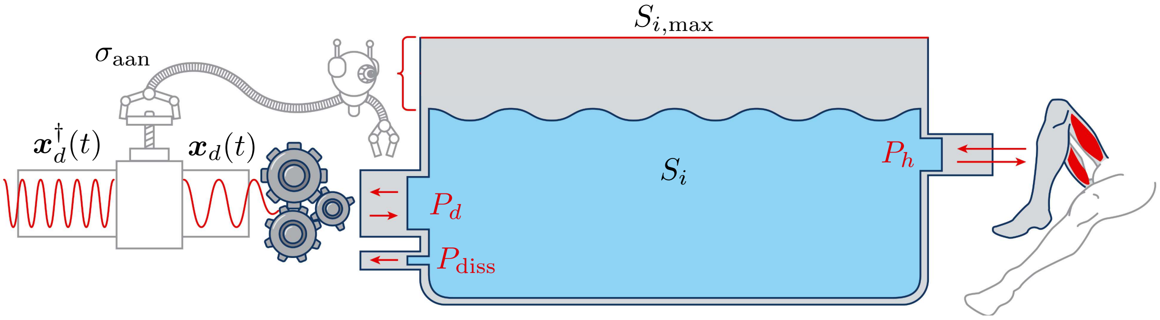

Figure 4.43: By adapting the speed of the desired trajectory using the adaptation gain σ_{aan}, the input power P_d can be controlled to maintain the energy level S_i below a maximum threshold, $S_{i,\max}$. This regulation ensures control over the maximum magnitudes of the transferred power P_h exchanged with the patient.

and

$$
\begin{aligned}
k_{C,\phi}\ \tilde{\phi} &= \tilde{\boldsymbol{x}}^T \boldsymbol{K}_C^T\ \boldsymbol{\nu}(\phi), \\
\Longrightarrow k_{C,\phi}\ \frac{\tilde{\boldsymbol{x}}^T \boldsymbol{\nu}(\phi)}{l_d} &\approx \tilde{\boldsymbol{x}}^T \boldsymbol{K}_C^T\ \boldsymbol{\nu}(\phi), \\
\Longrightarrow k_{C,\phi} &\approx l_d\ \frac{\tilde{\boldsymbol{x}}^T \boldsymbol{K}_C^T\ \boldsymbol{\nu}(\phi)}{\tilde{\boldsymbol{x}}^T \boldsymbol{\nu}(\phi)}.
\end{aligned}
\tag{4.114}
$$

Note that for a diagonal matrix $\boldsymbol{K}_C$ with elements k_C, (4.114) simplifies to

$$
k_\phi \approx l_d\ k_C. \tag{4.115}
$$

The phase-based energy function (4.112) is linked to the physical power exchanged along the path between the robot and the patient. The magnitude of an upper limit for $S_{i,\phi}$ can serve as an indicator of the robot support along the path. It is interesting to observe that if the controller stiffness is sufficiently high, making the effect of $\boldsymbol{K}_C$ more significant than that of $\boldsymbol{M}_C(\boldsymbol{q})$, the first term of (4.112) can be neglected, and $S_{i,\phi}$ reduces to the proposed phase-based deviation metric E defined in (4.102).

Remark: It is crucial to emphasize that such energy-based modeling plays a pivotal role in analyzing system stability. Within the passivity analysis paradigm, if the storage function S_i can be demonstrated to be bounded, it ensures the overall stability of the system [269]. As discussed earlier, the modulation of the desired trajectory in the proposed approach consistently leads to a reduction in S_i (and similarly $S_{i,\phi}$ and E), thereby confirming that the proposed method does not compromise system stability.

4.3.5 Pre-Clinical Experiments

Four sets of experiments are conducted to evaluate the proposed velocity adaptation approach. The first and second sets are carried out using a 7-DoF Franka Emika robot (see Figure 4.44 and Figure 4.46), while the third and fourth sets utilize a simulation and a prototype of a lower-limb rehabilitation robot (see Figure 4.48 and Figure 4.51), respectively.

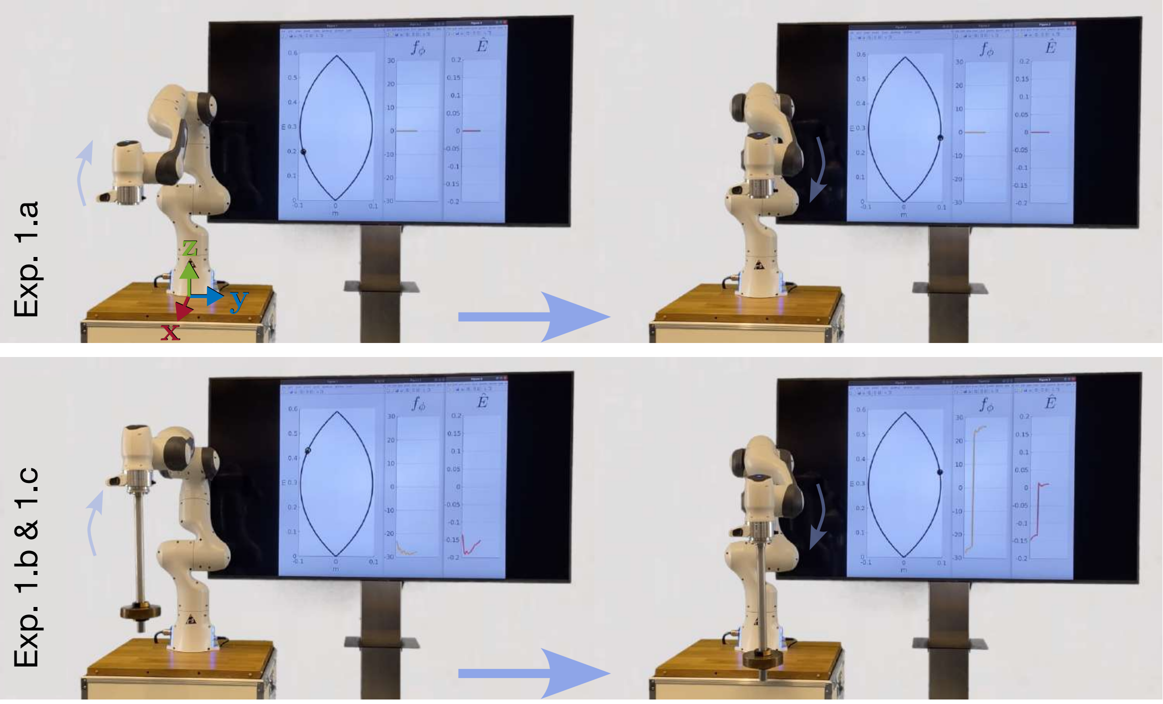

Figure 4.44: Experiment 1 – The attached weight applies a consistent wrench to the robot, simulating an imaginary patient limb.

Experiment 1: Evolution of the Phase-Based Variables

The first set of experiments illustrates the evolution of the introduced variables along the path. A Franka Emika robot is used, equipped with an impedance controller featuring a diagonal stiffness matrix with elements $\{1000, 1000, 1000, 50, 50, 50\}$ [N/m, Nm/rad]. Additionally, the damping matrix is selected to achieve critical damping [381].

The desired path is an almond-shaped curve comprised of two circular arcs, each spanning 1/5 of a circle with a 2.5 m radius (Figure 4.44). The phase variable is monotonically distributed along the path, and the nominal phase velocity $\Omega^\dagger$ is consistently set to 0.1 Hz. Three experiments are conducted. In the first one, no external wrench is applied to the robot. In the second and third experiments, a weight of 2.6 kg is attached to generate an approximately constant external wrench. While the first two experiments are designed to illustrate the behavior of the proposed physical effect metrics, the third experiment utilizes the phase modulation policy derived in (4.106). The results are shown in Figure 4.45.

Experiment 1.a: As shown in Figure 4.45, the phase value increases from 0 to 1 with a constant velocity in 10 seconds. The small tracking error results in a non-zero phase error $\tilde{\phi}$ and thus deviation metric E. Yet, considering (4.103), as the applied wrench $\boldsymbol{f}_h$ (equivalent to $\boldsymbol{f}_{\text{ext}}$ in Figure 4.45) is zero, f_ϕ and consequently $\hat{E}$ remain zero during the experiment.

Experiment 1.b: In the second experiment, the attached weight leads to a larger tracking error, resulting in a more substantial phase error and deviation metric. Since $\boldsymbol{f}_h$ is no longer

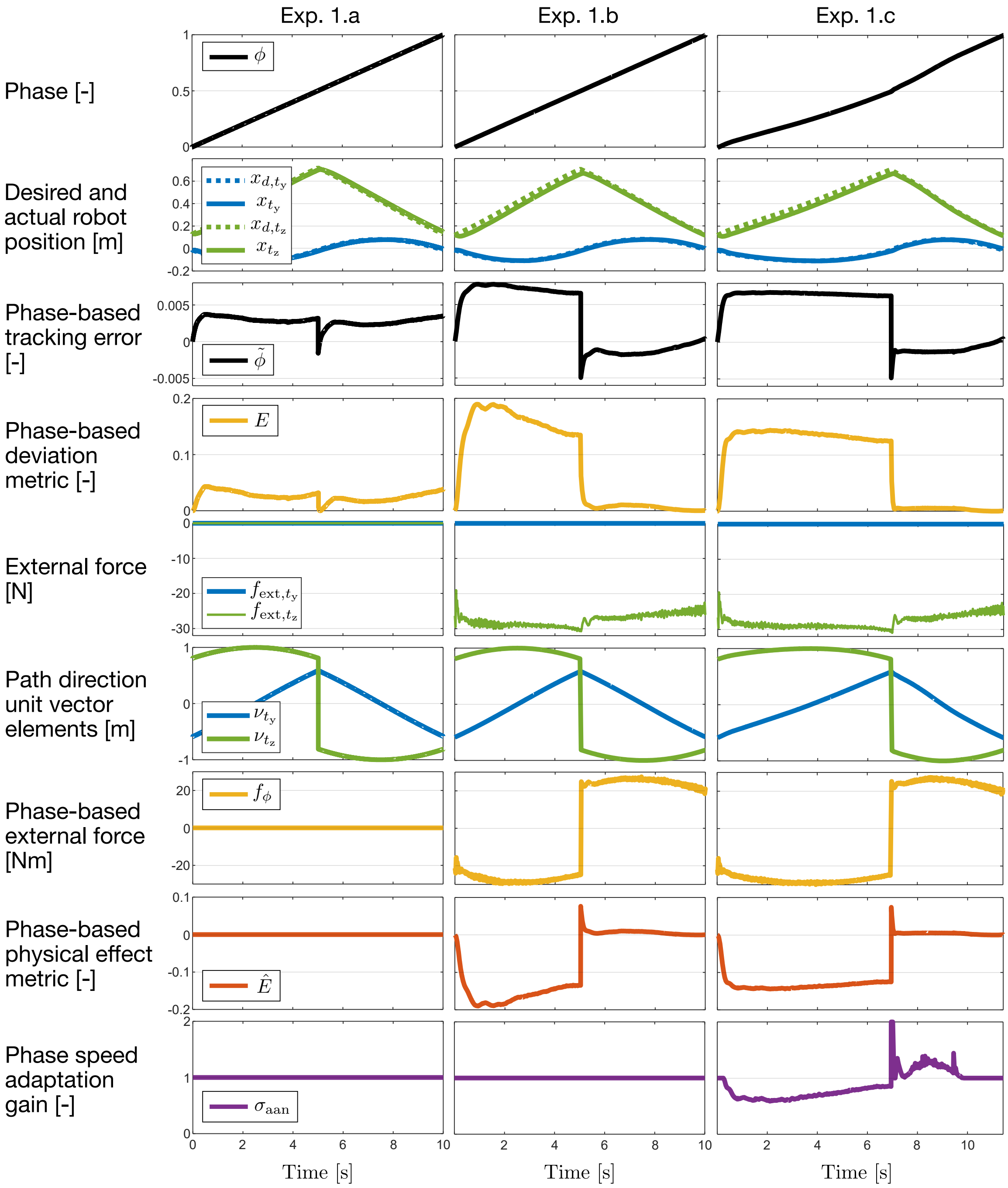

Figure 4.45: Experiment 1 – The physical effect metric $\hat{E}$ quantifies the impact of the attached weight on the motion.

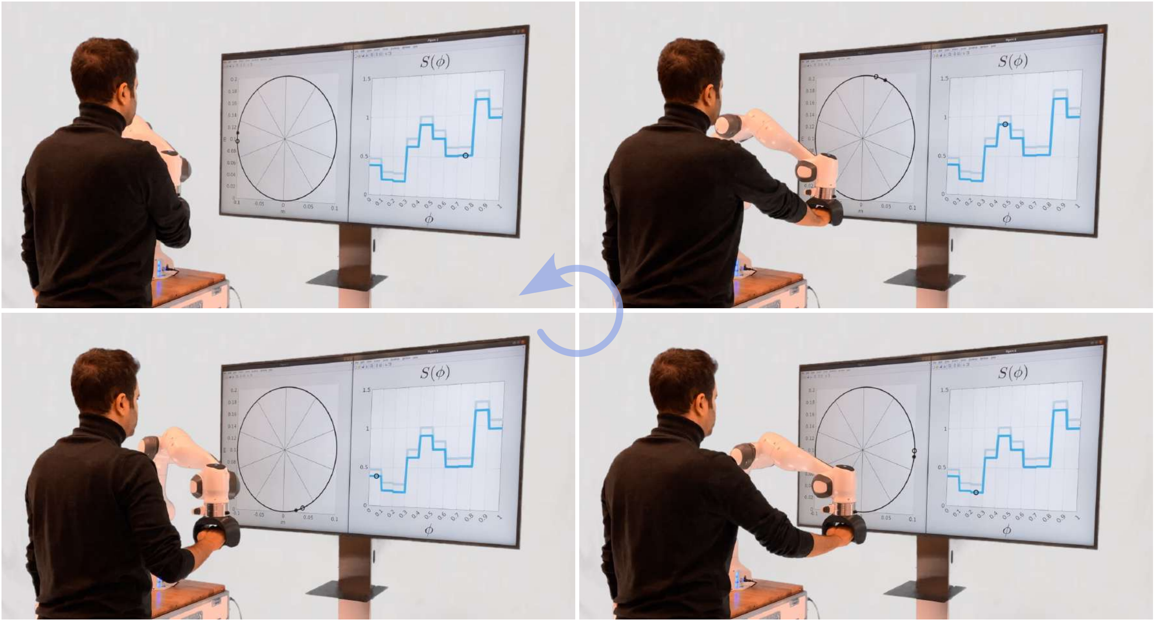

Figure 4.46: Experiment 2 – The desired path and the iteratively adapted support profile are visualized. The markers indicate the actual phase value. The faded lines depict the support profile from the previous iteration.

zero, f_ϕ and $\hat{E}$ attain non-zero values. During the first half of the path (i.e., when $\phi < 0.5$), the attached weight gravity is against the desired motion. This situation is realized via the large negative values of the effect metric $\hat{E}$. However, in the second half of the path (i.e., when $\phi > 0.5$), the weight gravity pushes the robot in the desired velocity direction. As shown in Figure 4.45, $\hat{E}$ has a positive value in this period.

Experiment 1.c: In this experiment, the phase modulation policy (4.106) is employed with the adaptation thresholds $E_{P1} = 0.004$, $E_{P2} = 0.008$, $E_{N1} = 0.1$, $E_{N2} = 0.2$, $E_{N3} = 0.3$, and $E_{N4} = 0.4$. Moreover, the maximum adaptation gains are set to $\sigma_{P,\max} = 2$ and $\sigma_{N,\max} = 1$. As depicted in Figure 3.4, when $\phi < 0.5$, $\hat{E}$ falls between $-E_{N1}$ and $-E_{N2}$. Thus, considering (4.106), the phase velocity adaptation gain[9] becomes $0 < \sigma < 1$. As a result, the phase velocity decreases according to (4.105). This can be observed in Figure 3.4, where it takes around 2 seconds longer for the setpoint to reach the middle of the path compared to the previous two experiments. In contrast, as the value of σ gets larger than 1 in the second half of the path, the phase velocity increases. Thus, the desired trajectory is continuously modified according to the contribution of the attached weight to the motion.

Experiment 2: Assist-As-Needed Control

In this experiment, the iterative support adaptation policy is evaluated in the presence of a human operator using the same robot and controller as in the previous experiment. The path is a horizontal circle with a radius of 0.2 m (Figure 4.46). The support variable S is defined as

---

[9] In the experimental section, for brevity, σ_{aan} is denoted as σ.

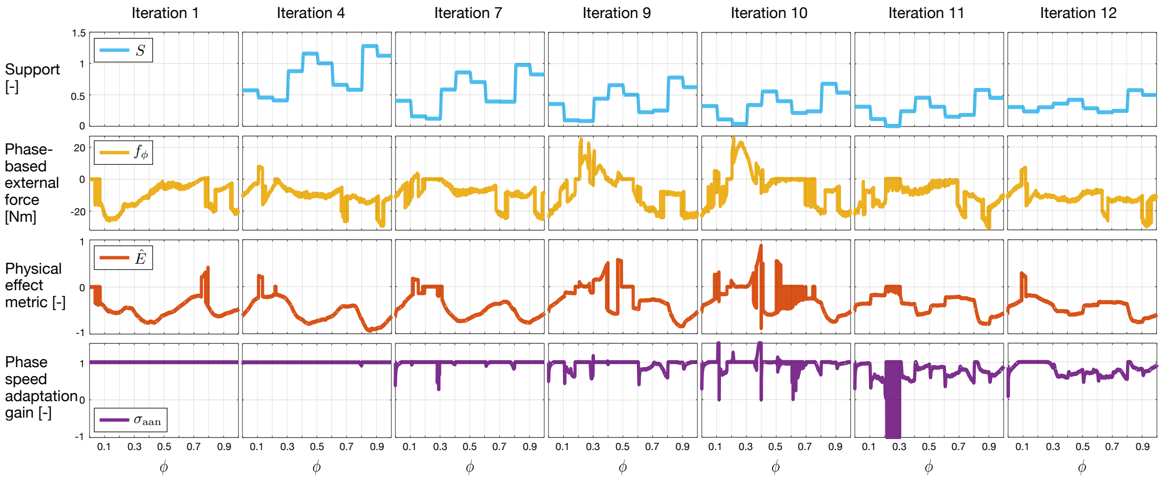

Figure 4.47: Experiment 2 – The phase-based support profile $S(\phi)$ iteratively adapts according to the human operator's performance in the motion.

a function of phase. The path is divided into ten regions with individual support values, and $S(\phi)$ is defined by smoothly connecting those values. For achieving the threshold parameters for each iteration, (4.108) is used with $\epsilon_{P1} = 1$, $\epsilon_{P2} = 2$, $\epsilon_{N1} = 1$, $\epsilon_{N2} = 2$, $\epsilon_{N3} = 3$, and $\epsilon_{N4} = 4$. The maximum adaptation gains are $\sigma_{P,\max} = 1.5$ and $\sigma_{N,\max} = 1$. Finally, the learning and forgetting factors are chosen to be $\kappa_l = 0.5$ and $\kappa_f = 0.1$, respectively. As κ_f is comparatively large, a minimum value of 0.01 is defined for S.

A novel approach is used to identify the required initial support value. The phase modulation is deactivated during the first three iterations, and the operator is asked to remain passive. Prior to iteration 4, the support is set to be slightly more than the average value of $-\hat{E}$, for each region. As shown in Figure 4.47, in the middle and end of the path in iteration 4, higher required support was estimated due to a more perceived resistance at those regions during the initial stage.

As of iteration 4, the support value of each region at each iteration is determined as a function of the previous iteration support as well as the average value of σ at that region according to (4.109). Until iteration 7, as σ remains close to 1, the estimated support value is decreased due to the forgetting factor. At this stage, let us focus mainly on the second and third regions (i.e., where $0.1 < \phi < 0.3$). In iteration 9, the support is very low for these regions. Therefore, as the human operator is still passive, the velocity drops during the second region (i.e., $\sigma < 1$). Subsequently, the operator gets involved by pushing the robot ($f_\phi >> 0$), resulting in keeping $\hat{E}$ close to zero. Consequently, σ remains at 1 almost all over the third region. That leads to an even lower support level in iteration 10. Eventually, S for the third region reaches its minimum value in iteration 11. The operator is then asked not to participate in the motion to mimic the muscle fatigue phenomenon. At that point, as f_ϕ constantly switches between 0 and negative values, σ switches between -1 and $+1$, and the robot slowly carries the human arm to the fourth region. As a result, $\bar{\sigma}$ gets a small value for the third region in iteration 11, and thus $S(\phi)$ is increased for iteration 12. In practice, it feels as if the robot has noticed that the operator cannot contribute to the motion anymore and thus increases the support.

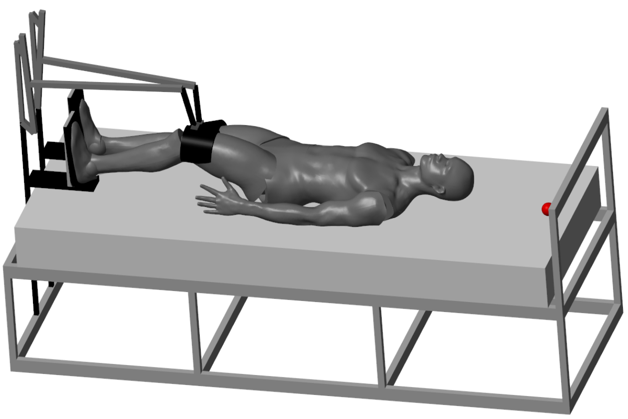

Figure 4.48: Experiment 3 – Visual representation of the lower-limb rehabilitation robot and the patient simulated in MATLAB Simscape.

Experiment 3 – Simulated Lower-Limb Rehabilitation

A lower-limb rehabilitation robot is simulated for this experiment using MATLAB Simscape software, as depicted in Figure 4.48. A human model is designed to anthropomorphically resemble a human, and limb weights are chosen according to [393]. Joint impedance control is implemented on the hip joint with a stiffness of 300 Nm/rad and damping of 20 Nm/rad. A Cartesian impedance controller is used for the robot with a diagonal stiffness matrix having elements of 150 and 4000 N/m in the horizontal and vertical axes, respectively, as shown in Figure 4.48. The damping matrix is adjusted to achieve critical damping [381]. The test scenario was designed as follows: the human is in a horizontal configuration, and their motion trajectory is intentionally slower (sinusoidal with a frequency of 0.6 Hz) than the robot desired trajectory (sinusoidal with a frequency of 1 Hz). This motion discrepancy results in an increase in E. Three scenarios with three sets of values for the velocity adaptation thresholds are considered, as illustrated in Figure 4.49.

The results of this simulation experiment, as shown in Figure 4.48, demonstrate how the desired trajectory adapts according to the error imposed by the human motion. Considering Figure 4.49, when the adaptation threshold is set high (indicating high support), no velocity modification is observed. On the other hand, when the threshold is set low (indicating high permissiveness), the resulting motion aligns with the human's desired trajectory.

Experiment 4 – Correlation of Support Level and Muscle Activity

In this set of experiments, the actual robot prototype used in the previous simulation is employed. The system is torque-controlled and comprises three joints, including one passive and two active joints, as depicted in Figure 4.51. An impedance control is implemented with parameters similar to the simulation. To quantitatively assess the human participation level in the motion, muscle activity of the rectus femoris is measured via EMG sensors during hip flexion. The signals are post-processed by applying a bandpass filter (50 - 600 Hz, 4th order Butterworth), rectifying the signal, applying a lowpass filter (2 Hz cutoff, 4th order Butterworth), and normalizing to the peak value during the session.

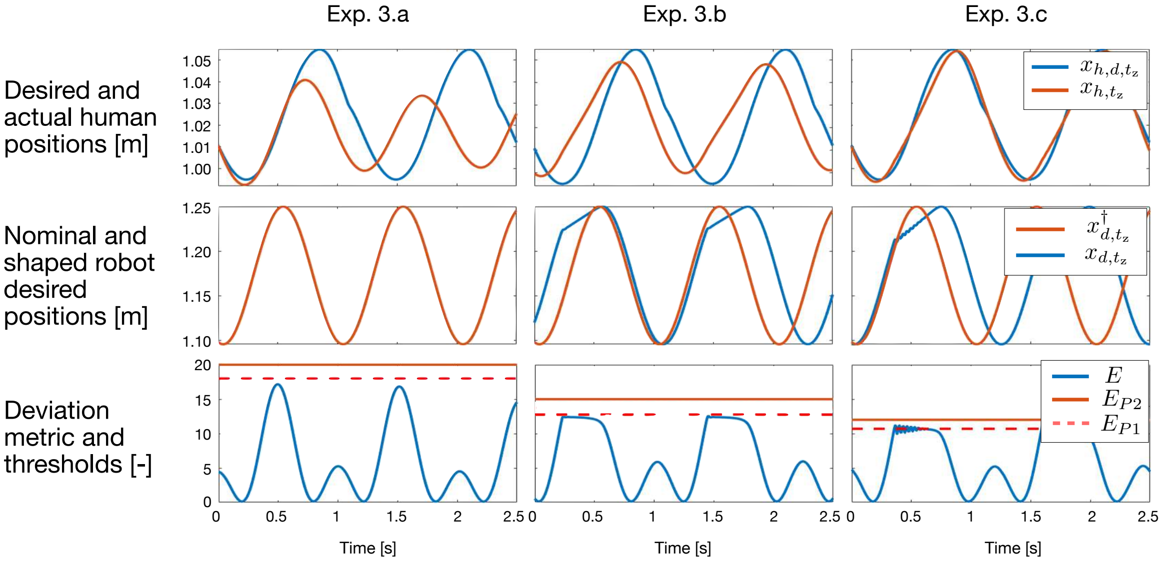

Figure 4.49: Experiment 3 – As the adaptation thresholds E_{P1} and E_{P2} decrease, the robot behavior becomes more permissive.

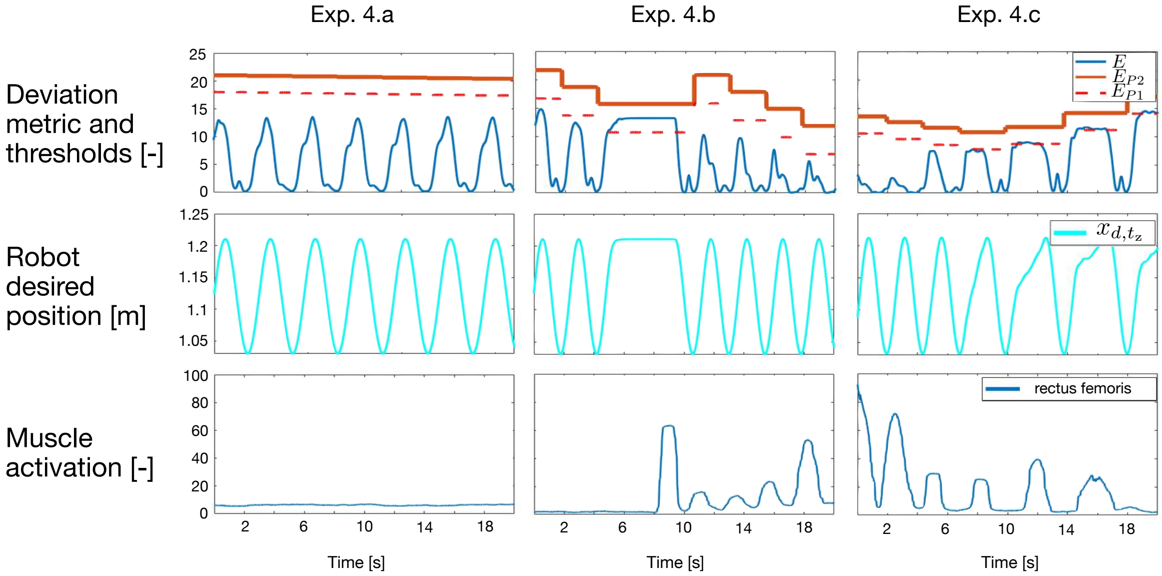

Figure 4.50: Experiment 4 – The involvement of the human in the motion can be validated by observing the EMG signal of the rectus femoris muscle.

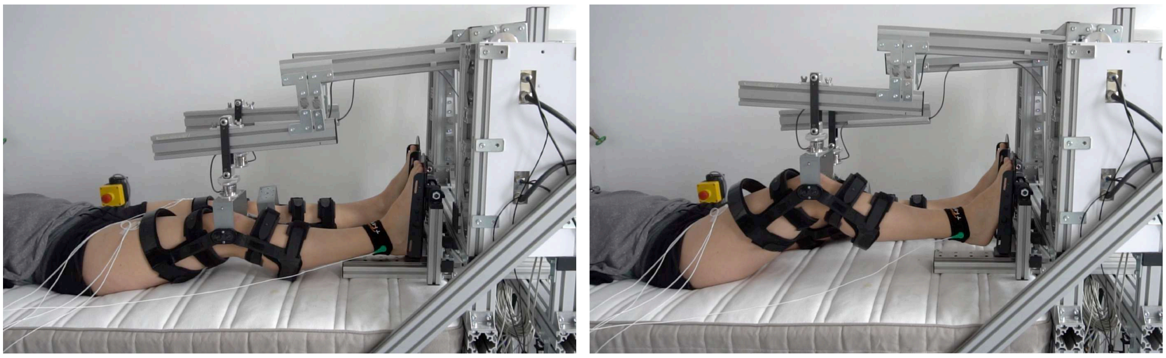

Figure 4.51: Experiment 4 – Initial configuration (left) and final configuration (right) of the leg during a half-cycle of the iterative motion.

Figure 4.50 illustrates the experiment procedure. Three experiments are conducted with $\sigma_{P,\max} = \sigma_{N,\max} = 1$. The cascading-shaped map is configured such that $E_{P1} = E_{N1}$ and $E_{P2} = E_{N2} = E_{N3} = E_{N4}$. The initial values of the threshold E_{P2} are set to 23 for Experiment 3.a, 22 for Experiment 3.b, and 21 for Experiment 3.c. The support level is constant throughout the path and is iteratively adjusted at each iteration according to (4.109). The learning and forgetting factors are set to 0 and 0.1 for Experiment 3.a, 2 and 3 for Experiment 3.b, and 3 and 1 for Experiment 3.c, respectively.

As depicted in Figure 4.51, in Experiment 4.a, the value of E consistently remains well below E_{P1}, keeping the adaptation gain σ constantly at 1. However, in Experiment 4.b, σ drops to zero, resulting in a stationary setpoint between times 5 s and 10 s. Nevertheless, as soon as the rectus femoris is activated to initiate hip flexion, the desired motion resumes. This correlation between human participation in the motion and the decrease in the support level is more noticeable in Experiment 4.c.

4.3.6 Certified Lower-Limb Rehabilitation Therapy

The proposed Assist-As-Needed control (AAN) approach has been successfully certified for clinical use and subsequently commercialized [360, 394] through the lower-limb rehabilitation robot, VEMOTION, manufactured by Reactive Robotics GmbH in Munich, Germany. This innovative support-adaptive rehabilitation system is currently being actively utilized in clinical settings worldwide, with clinicians and physiotherapists offering highly positive feedback [359].

The VEMOTION system (depicted in Figure 4.53) comprises a hospital bed with a harness/seat support system and two torque-controlled arms designed to move the patient's legs in a stepping-like motion. The bed allows tilting, providing a maximum patient inclination angle of 70 degrees. Each foot is strapped to a footplate, capable of passive sliding along the y-axis and rotation about the z'-axis (Figure 4.53). The z'-axis, perpendicular to the x-y plane, aligns with the patient's sagittal plane but not the ankle. The end effectors attach to the patient's thighs and execute an arc trajectory in the sagittal plane around the hip joint center, inducing a stepping-like motion in the patient's legs. The system moves one leg at a time, holding the other in full extension (stance phase). Clinicians can set therapy parameters, including hip range of motion (ROM) and step frequency.

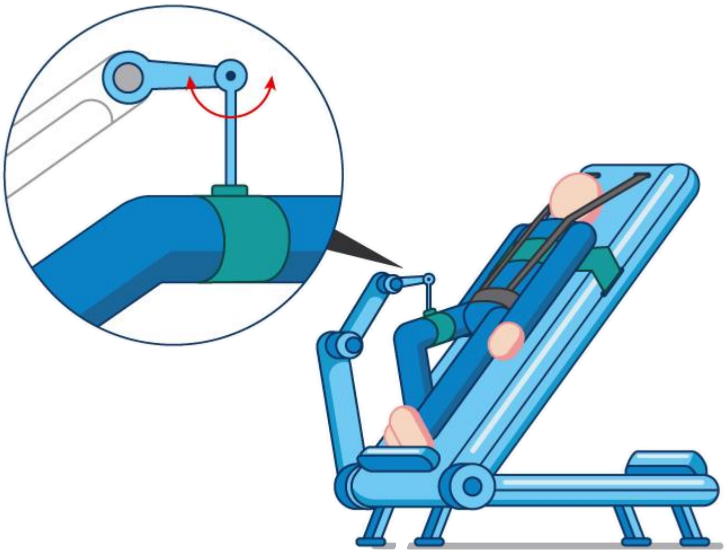

Figure 4.52: Schematic representation of the VEMOTION system, featuring only one arm; the last joint of the arm is passive to prevent closed-chain kinematic constraints.

The kinematic structure of the arms is illustrated in Figure 4.52. The last joint, being passive, contributes to the motion control derivation through its position. The Assist-As-Needed (AAN) policy is flexible, allowing therapists to enable or disable it during therapy sessions. When inactive, the robot impedance control provides full support to the patient throughout the motion cycle. The AAN policy encompasses an initial calibration stage, as introduced in Experiment 2. During this stage, the patient is instructed to relax fully, and the necessary data is collected from three complete left and right leg cycles. Subsequently, the learned support is delivered to the patient through the phase speed adaptation policy introduced in this section. In instances where the patient struggles to maintain motion and the learned support proves insufficient, a time-based auto-support strategy is activated. This strategy exponentially increases the assistance level to facilitate continuous motion. Throughout the therapy session, the therapist retains control over the support level, with the option to assign or adjust it directly through the robot's intuitive interface; see Figure 4.53.

Several clinical studies have recently commenced to investigate the effectiveness of the proposed support-adaptive (AAN) policy in the VEMOTION system. In a recent pilot study [348], an improvement was observed in patients undergoing the AAN policy. However, it was not entirely certain if the improvement was solely attributable to using the AAN mode. In this dissertation, detailed in Section 5.3, a series of clinical studies are conducted on both healthy subjects and ICU patients. The results, illustrated in Figure 5.20, clearly demonstrate an increase in the subjects' engagement when the support level is decreased, as measured by two distinct metrics. For further insights into the clinical outcomes of the CE-certified support-adaptive policy proposed here, please refer to Section 5.3.

Figure 4.53: Various components of the lower-limb movement rehabilitation robot VEMOTION, featuring the proposed innovative Assist-As-Needed policy.


Fuel

5 Energy: An Intrinsic Tool for Control, Planning, and Monitoring

Irrespective of the abstraction level employed for modeling physical interactions, one constant factor prevails: every interaction involves an exchange of energy. Energy serves as the catalyst for the occurrence of all phenomena in our surroundings. This metric, devoid of specific coordinates, enables the creation of a unified model for multi-domain systems.

The two key elements utilized in this dissertation for planning and controlling tactile manipulation, namely force, and motion, provide direct access to the energy domain. The interaction wrench and twist can yield the transferred power, representing the rate of exchanged energy through the port connecting the robot to its surrounding physical world. This interaction port repeatedly served as the starting point for constructing the control and policy blocks within the dissertation, forming a network through which energy flow across components can be monitored or estimated. A significant advantage of adopting such an energy-based modeling approach is the ability to explore stability through passivity analysis. Following this, an energy-based component, i.e., a virtual energy tank, can stabilize an unstable control or policy block. In this context and through such a perspective, this dissertation introduced a more robust representation of energy tanks. Referred to as valve-based energy tanks, they enable the regulation of energy flow through their connection ports. In the initial stage of this chapter, these innovative energy tanks are employed to integrate energy as an intrinsic tool, offering an additional degree of freedom to shape the physical behavior of the robot.

The ability to control a system's behavior always raises the question of defining the desired behavior. When there is control over the energy flow within a system, the initial step involves estimating the energy budget for that system. Similar to other estimation methods, this can be achieved either by utilizing the system model and making predictions accordingly, by observing an expert exhibiting optimal behavior and learning from it, or by initiating from a random guess and refining the optimal budget through trial and error. In the second stage, this chapter delves into these methods for reference energy assignment.

Throughout this dissertation, the primary goal has been to establish an architecture wherein the control and policy blocks can be designed and positioned up to the interaction port with the external world. However, what about the world beyond this port? In this context, the universal metric—energy—can serve as a valuable tool to comprehend the events occurring on the other side. The evolution of energy flow through the interaction port can provide information that allows for (even partial) perception of the status or characteristics of the entity with which the robot is interacting. In the concluding stage of this chapter, this concept is applied within the realm of rehabilitation, ultimately resulting in a practical patient monitoring approach suitable for clinical settings.

5.1 Extended Virtual Energy Tanks for Energy-Aware Control

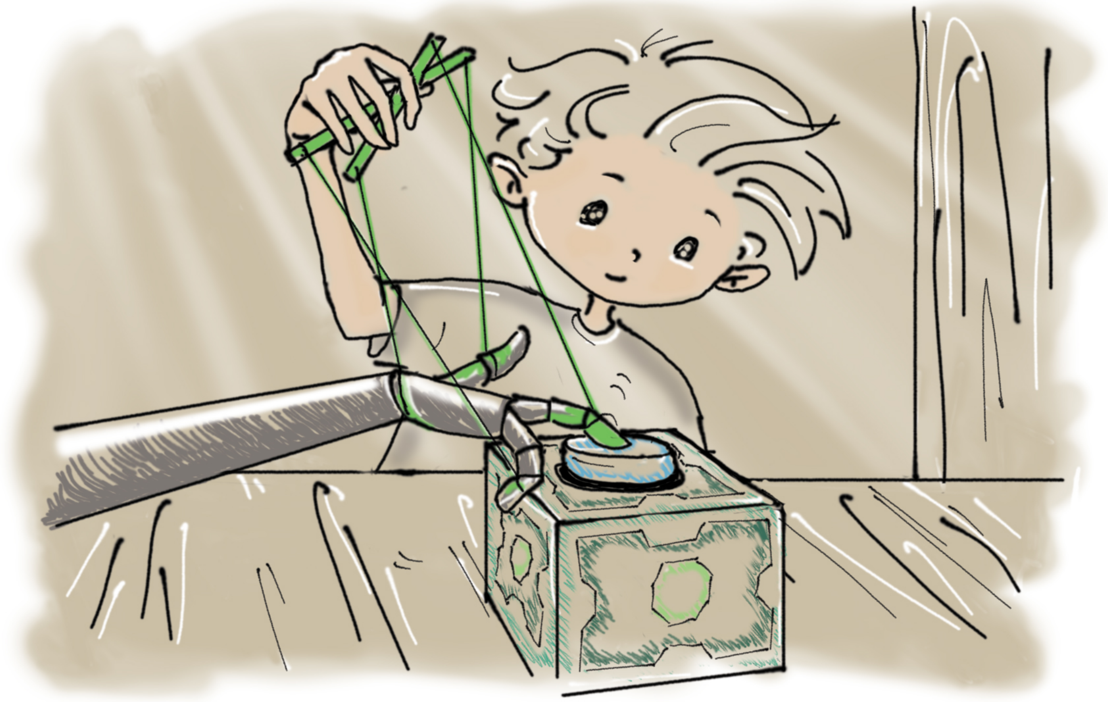

A virtual energy tank can ensure stability by supplying a limited amount of energy to a potentially passivity-violating action. In this context, the concept of a *valve* is introduced in Section 2.3, allowing the shaping of energy flow to/from the tank. This not only prevents abrupt and undesirable behaviors associated with depleted tanks but also enables the independent consideration of different tank conditions, such as lower and upper energy limits. The objective here is to illustrate how this extension can address even more intricate energy-based criteria. Specifically, the focus is on showcasing how valves can regulate the energy flow in various parts of the system architecture, aligning it with task objectives. In other words, this section demonstrates how a *Valve-Based Virtual Energy Tank* can be utilized not only to ensure system passivity but also to achieve additional energy-aware control objectives.

5.1.1 Multi-Port Energy Tanks

Considering $S_T \in \mathbb{R}_{\geq 0}$ as the tank energy and $P_T \in \mathbb{R}$ as the potentially passivity-violating power that the tank should provide, (2.93) represents the tank energy dynamics derived as

$$\dot{S}_T = -\gamma_T P_T, \tag{5.1}$$

where $\gamma_T \in [0, 1]$ denotes the overall valve gain, addressing multiple energy-based conditions by incorporating associated valve gains according to

$$\gamma_T = \prod_{i \in \Gamma_T} \gamma_i, \qquad \Gamma_T = [\mathrm{low}, \mathrm{up}, \mathrm{diss}, p_i, p, \ldots]. \tag{5.2}$$

The valve conditions enumerated in (5.2) have two additional conditions compared to the original formulation (2.92) in the initial derivation of tanks in Section 2.3. These two conditions are associated with the tank's power limits and are presented here for tanks with multiple ports.

System stability can be compromised by the presence of multiple passivity-violating actions with their respective powers. In such cases, one approach is to attach multiple tanks, each for an associated port, enabling individual regulation of the powers. This methodology is implemented in the unified force-impedance control (UFIC) framework, as demonstrated in Section 3.1. An alternative approach involves attaching a single tank with one port for the integration of all passivity-violating powers, allowing for the regulation of the overall energy flow to the system; see Figure 5.1. This approach is employed in the extended UFIC, as discussed in Section 3.2. To leverage the benefits of both approaches, a third method is introduced here, involving the attachment of one tank to control the overall energy flow, coupled with multiple ports to control each power independently. This is achieved using the innovative concept of valves.

For a tank with multiple ports, each port i possesses its individual valve gain $\gamma_{T,i}$. In this context, the tank gains associated with the lower and upper energy limits $\gamma_{\mathrm{low},i}$ and $\gamma_{\mathrm{up},i}$, as well as the dissipation enforcing gain $\gamma_{\mathrm{diss},i}$, remain the same as introduced in (2.94), (2.95) and (2.96), respectively, in Section 2.3. Additionally, another valve gain can be derived for each port's individual power limits. This is particularly relevant when the actions associated with each port exhibit different characteristics. For example, if a port is responsible for a sensitive action where a substantial amount of exchanged power could be hazardous, a conservative power limit can be defined for that specific port. Considering $P_T^{\mathrm{up},i} \in \mathbb{R}_{\geq 0}$ and $P_T^{\mathrm{low},i} \in \mathbb{R}_{\leq 0}$ as the lower and upper power limits for the i-th port of the tank, the valve gain associated with the individual power limits can be determined as

$$\gamma_{p_i,i} = \begin{cases} \frac{P_T^{\mathrm{up}_i}}{P_{T,i}} & \text{if } \; P_T^{\mathrm{up}_i} < P_{T,i}, \\ \frac{P_T^{\mathrm{low}_i}}{P_{T,i}} & \text{if } \; P_{T,i} < P_T^{\mathrm{low}_i}, \\ 1 & \text{else}, \end{cases} \tag{5.3}$$

where $P_{T,i} \in \mathbb{R}$ represents the power intended to be transferred through the i-th port of the tank. By implementing the valve gain (5.3), the transferred power is always between the designated power limits. Note that by setting $P_T^{\mathrm{low},i} = 0$, the individual power limit valve, as indicated in (5.3), exhibits the behavior of the dissipation enforcing valve γ_{diss} defined in (2.96) for the i-th port.

5.1.2 Energy Flow Regulation for Multi-Priority Control Actions

As explained earlier, the advantage of using a multi-port tank—as opposed to several conventional uni-port tanks for each passivity-violating power—is to facilitate the supervision and regulation of the overall energy flow. One scenario where this benefit is pertinent is when there is a conservative limitation on the overall tank energy. In such cases, managing the energy distribution to individual ports becomes crucial. With such limitations, the rate of overall exchanged energy flow (i.e., the overall power) can be constrained. Considering

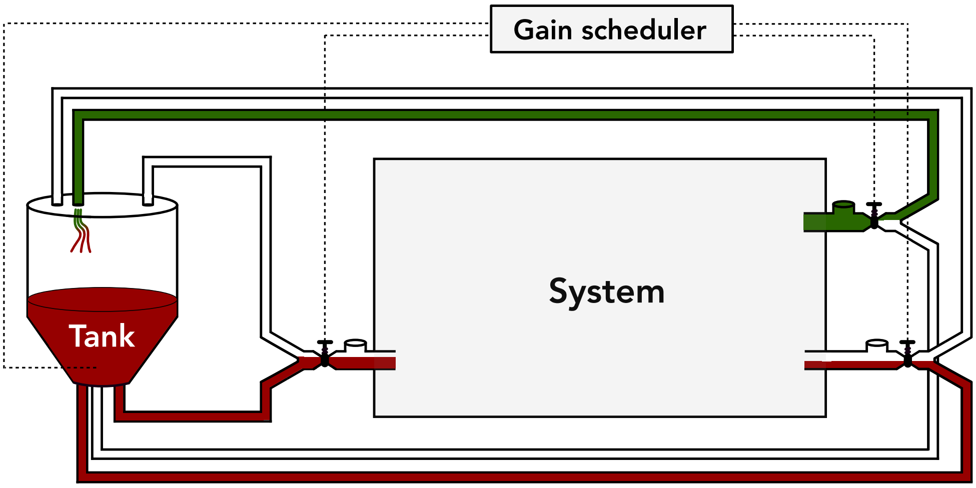

Figure 5.1: A multi-port valve-based virtual energy tank whose port powers are shaped by controlling valve gains. Red color corresponds to a passivity-violating power (i.e., $P_{T,i} > 0$), and green color is associated with dissipative power (i.e., $P_{T,i} < 0$).

$P_T^{\text{low}} \in \mathbb{R}_{\leq 0}$ and $P_T^{\text{up}} \in \mathbb{R}_{\geq 0}$ as the lower and upper overall power limits, respectively, for a tank with n_T ports, the valve gain for the i-th port can be derived according to one of the following three methodologies.

Equality-Based Gain Scaling (EGS): If all the ports are considered equally for constraining their respective exchanged powers, their valve gains become

$$\gamma_{p,i} = \begin{cases} \frac{P_T^{\text{up}}}{\sum_{i=1}^{n_T} P_{T,i}} & \text{if} \quad P_T^{\text{up}} < \sum_{i=1}^{n_T} P_{T,i}, \\ \frac{P_T^{\text{low}}}{\sum_{i=1}^{n_T} P_{T,i}} & \text{if} \quad \sum_{i=1}^{n_T} P_{T,i} < P_T^{\text{low}}, \\ 1 & \text{else.} \end{cases} \tag{5.4}$$

Weight-Based Gain Scaling (WGS): In contrast to the previous case, the gain value for each port can be assigned based on the port priority. This is relevant when certain passivity-violating actions play a more crucial role in achieving the task control objective. Considering $\xi_{T,i} \in \mathbb{R}_{\geq 0}$ as the weight for the i-th port, the valve gain becomes

$$\gamma_{p,i} = \begin{cases} \frac{\xi_{T,i} P_T^{\text{up}}}{\sum_{i=1}^{n_T} \xi_{T,i} P_{T,i}} & \text{if} \quad P_T^{\text{up}} < \sum_{i=1}^{n_T} P_{T,i}, \\ \frac{\xi_{T,i} P_T^{\text{low}}}{\sum_{i=1}^{n_T} \xi_{T,i} P_{T,i}} & \text{if} \quad \sum_{i=1}^{n_T} P_{T,i} < P_T^{\text{low}}, \\ 1 & \text{else.} \end{cases} \tag{5.5}$$

Sequential Gain Assignment (SGA): Instead of constraining all the port powers, as in the previous two approaches, only the ports with lower priorities can be constrained according

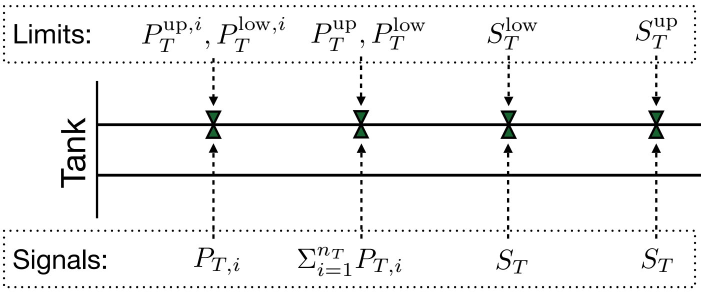

Figure 5.2: Valve gain scheduling order (from left to right) to avoid the over-conservativeness of a virtual tank.

to

$$\gamma_{p,i} = \begin{cases} 0 & \text{if } \; P_T^{\mathrm{up}} < \sum_{j \in \Xi_i} P_{T,j} + P_{T,i}, \\ 0 & \text{if } \; \sum_{j \in \Xi_i} P_{T,j} + P_{T,i} < P_T^{\mathrm{low}}, \\ 1 & \text{else,} \end{cases} \tag{5.6}$$

where

$$\Xi_i = \{1 \leq j \leq n_T | \xi_j \geq \xi_i\}. \tag{5.7}$$

According to (5.6), power is permitted to be transferred through a port only if the overall power limit would not be violated when the intended power is exchanged through the port as well as the higher-priority ports.

Gain Scheduling Order

Each valve gain used in (5.2) can influence the exchanged power through the tank ports. If, during the derivation of each valve condition, the effect of other valves is not considered, this could lead to an over-conservative behavior of the tank. For example, limiting port powers via (5.3) can already delimit the overall power exchange, obviating the need for the associated gain derivation laws (5.4)–(5.6) and thus allowing γ_p to remain at 1. Therefore, ordering the sequence of applying valve gain conditions (i.e., gain scheduling sequence) is crucial. To address this, Figure 5.2 proposes a gain scheduling order that prevents the over-conservativeness of the tank behavior.

5.1.3 Experiments

To demonstrate the effectiveness of the proposed valve gain scheduling policies in practice and illustrate how they impact the physical behavior of a system, two experiments are designed using a DLR LWR III robot equipped with a UFIC law (3.12). In the first experiment, only the Cartesian impedance controller is used, i.e., the force controller is deactivated. In the second experiment, both controllers are active. The control parameters are shown in Table 5.1.

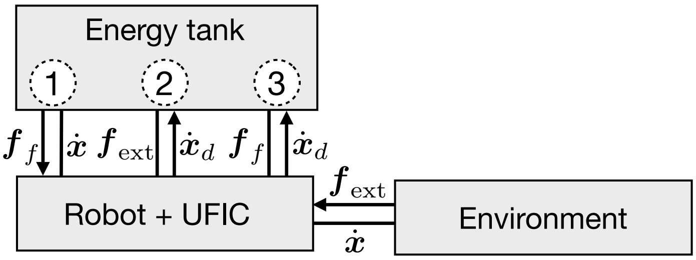

Figure 5.3: Port-based model of a rigid-body robot equipped with the unified force-impedance control, utilizing a multi-port tank, and in contact with a passive environment.

	f_{d,t_z} [N]	$\boldsymbol{K}_C$ [N/m, N.m/rad]	$\boldsymbol{K}_{f,p}$	$\boldsymbol{K}_{f,i}$ [1/s]	$\boldsymbol{K}_{f,d}$ [s]
Exp. 1	—	$\text{diag}([1000, 1500, 1500, 150, 150, 150])$	—	—	—
Exp. 2	10	$\text{diag}([1000, 1500, 0, 150, 150, 150])$	$\boldsymbol{I}_6$	$\boldsymbol{0}_{6\times 6}$	$2.5\boldsymbol{I}_6$

Table 5.1: Control parameters employed in the experiments – The Cartesian damping is continually adjusted to achieve critical damping [381].

As demonstrated in Section 3.1, the stability of this system can be investigated by assigning the storage function S_i defined in (3.14) derived as

$$S_i = \frac{1}{2}\dot{\tilde{\boldsymbol{x}}}^T \boldsymbol{M}_C(\boldsymbol{q})\dot{\tilde{\boldsymbol{x}}} + \frac{1}{2}\tilde{\boldsymbol{x}}^T \boldsymbol{K}_C \tilde{\boldsymbol{x}}. \tag{5.8}$$

where $\tilde{\boldsymbol{x}} \in \mathbb{R}^6$ represents the tracking error, and $\boldsymbol{K}_C, \boldsymbol{M}_C \in \mathbb{R}^{6\times 6}$ denote the stiffness and mass matrices in a 6-dimensional Cartesian space. As shown in (3.18), the following can be seen for the time evolution of the storage function.

$$\dot{S}_i \leq \dot{\boldsymbol{x}}^T \boldsymbol{f}_{\text{ext}} + \dot{\boldsymbol{x}}^T \boldsymbol{f}_f - \dot{\boldsymbol{x}}_d^T(\boldsymbol{f}_f + \boldsymbol{f}_{\text{ext}}). \tag{5.9}$$

Considering a passive environment satisfying (3.21), the overall system is shown to remain passive by augmenting two energy tanks for the powers $\dot{\boldsymbol{x}}^T \boldsymbol{f}_f$ and $-\dot{\boldsymbol{x}}_d^T(\boldsymbol{f}_f + \boldsymbol{f}_{\text{ext}})$. In this section, instead of using two individual tanks, a single multi-port tank is considered with three ports for the following powers (see Figure 5.3).

$$P_{T,1} = \dot{\boldsymbol{x}}^T \boldsymbol{f}_f, \tag{5.10}$$

$$P_{T,2} = \dot{\boldsymbol{x}}_d^T \boldsymbol{f}_{\text{ext}}, \tag{5.11}$$

$$P_{T,3} = \dot{\boldsymbol{x}}_d^T \boldsymbol{f}_f. \tag{5.12}$$

Obviously, in Experiment 1, as no force control is active, only the second port remains active. Moreover, in Experiment 2, as force control space is reciprocal to the desired motion, $P_{T,3}$ remains zero, and thus only the first and second ports are active. The tank parameters for each experiment are shown in Table 5.2. As evident, the power lower limits are always set to 0, indicating dissipation enforcing valves (2.96).

	$P_T^{\text{up},1}$	$P_T^{\text{low},1}$	$P_T^{\text{up},2}$	$P_T^{\text{low},2}$	P_T^{up}	P_T^{low}	$\xi_{T,1}$	$\xi_{T,2}$	S_T^{low}	S_T^{Δ}	S_T^{up}
Exp. 1	—	—	(5.14)	0	(5.14)	0	—	—	90	0.5	120
Exp. 2	2	0	2	0	1	0	15	1	5	0.5	20

Table 5.2: Tank parameters used in the experiments – Since only one port is active in the first experiment, the individual and overall power limits remain identical. Moreover, the power upper limit is consistently modified according to (5.14).

Experiment 1: Limiting Power for Enhanced Behavior

In the first experiment, the force controller is deactivated, and only the Cartesian impedance control is active to highlight the impact of setting a power limit on a single port of the tank. To showcase a practical application of valve-based tanks, a common challenging scenario is considered: the robot is tracking a desired trajectory, and its end-effector encounters an environmental constraint, preventing it from following the trajectory. This results in an accumulation of energy in the storage function S_i as defined in (5.8). When the constraint on the end-effector is suddenly removed, this accumulated energy may lead to a high acceleration, posing a potential risk to the robot and its environment. To mitigate this issue, an upper limit for S_i can be defined based on a maximum allowance of tracking error. Designating $\tilde{\boldsymbol{x}}_{\text{max}}, \dot{\tilde{\boldsymbol{x}}}_{\text{max}} \in \mathbb{R}^6_{\geq 0}$ as the maximum allowed magnitudes of position and velocity errors, respectively, the maximum limit for S_i can be chosen as

$$S_{i,\text{max}} = \frac{1}{2}\tilde{\boldsymbol{x}}_{\text{max}}^T \boldsymbol{K}_C \tilde{\boldsymbol{x}}_{\text{max}} + \frac{1}{2}\dot{\tilde{\boldsymbol{x}}}_{\text{max}}^T \boldsymbol{M}_C(\boldsymbol{q}) \dot{\tilde{\boldsymbol{x}}}_{\text{max}}. \tag{5.13}$$

Note that the energy limit $S_{i,\text{max}} \in \mathbb{R}_{\geq 0}$ is not a constant value and can change due to alterations in the robot mass matrix $\boldsymbol{M}_C(\boldsymbol{q})$ caused by the changes in the configuration $\boldsymbol{q}$. However, due to the boundedness of the mass matrix and by selecting bounded $\boldsymbol{K}_C$, $\tilde{\boldsymbol{x}}_{\text{max}}$, and $\dot{\tilde{\boldsymbol{x}}}_{\text{max}}$, the energy limit $S_{i,\text{max}}$ is also bounded. To adhere to this energy limit, a power upper limit can be defined as a smooth function of the energy level S_i and the energy limit variables $S_{i,\text{max}}$ and $S_{i,\Delta}$ such that

$$P_T^{\text{up}} = \begin{cases} P_T^{\text{up}^\dagger} & \text{if } \; S_i \leq S_{i,\text{max}} - S_{i,\Delta}, \\ \frac{1}{2} P_T^{\text{up}^\dagger} \left(1 - \cos\left(\frac{S_{i,\text{max}} - S_i}{S_{i,\Delta}} \pi\right)\right) & \text{if } \; S_{i,\text{max}} - S_{i,\Delta} \leq S_i < S_{i,\text{max}}, \\ 0 & \text{else,} \end{cases} \tag{5.14}$$

in which $P_T^{\text{up}^\dagger} \in \mathbb{R}_{>0}$ is a randomly chosen maximum allowance for the power limit. Additionally, $S_{i,\Delta}$ is a threshold below $S_{i,\text{max}}$, from which the power flow starts to decrease and is defined as

$$S_{i,\Delta} = \frac{1}{2}\tilde{\boldsymbol{x}}_{\Delta}^T \boldsymbol{K}_C \tilde{\boldsymbol{x}}_{\Delta} + \frac{1}{2}\dot{\tilde{\boldsymbol{x}}}_{\Delta}^T \boldsymbol{M}_C(\boldsymbol{q}) \dot{\tilde{\boldsymbol{x}}}_{\Delta}. \tag{5.15}$$

Here $\boldsymbol{0} < \tilde{\boldsymbol{x}}_{\Delta} < \tilde{\boldsymbol{x}}_{\text{max}}$ and $\boldsymbol{0} < \dot{\tilde{\boldsymbol{x}}}_{\Delta} < \dot{\tilde{\boldsymbol{x}}}_{\text{max}}$ are the user-defined position and velocity error thresholds, respectively. Setting (5.14) as the port's power limit and applying (5.3) to shape the valve gain $\gamma_{p_i,2}$, the magnitude of the port's controllable variable, i.e., the desired

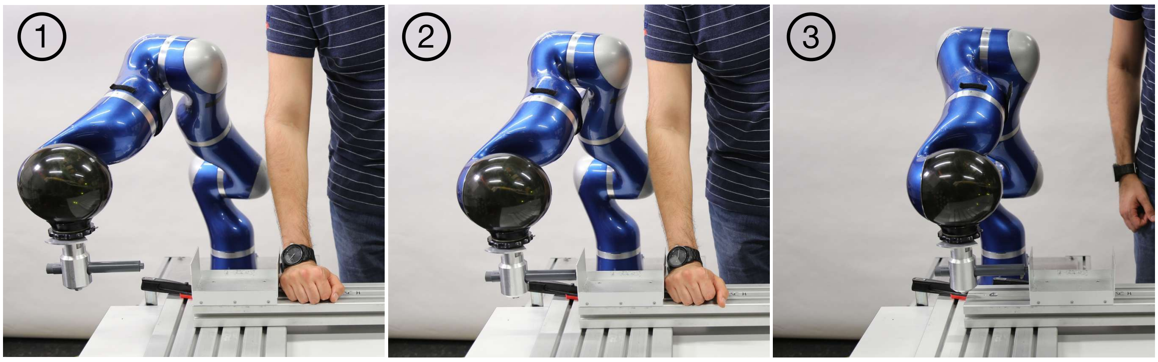

Figure 5.4: Experiment 1 – The robot encounters an obstruction with the environment and is subsequently released.

velocity $\dot{\boldsymbol{x}}_d$, and consequently the power flow $P_{T,2}$ in (5.11) start to decrease as soon as the accumulated energy has exceeded the threshold, i.e., when $S_i \geq S_{i,\max} - S_{i,\Delta}$.

The experiment is structured for two scenarios, each with distinct values for $\tilde{\boldsymbol{x}}_{\max}$ and, consequently, for the limit $S_{i,\max}$. Each experiment comprises three stages (see Figure 5.4). In stage ①, the robot tracks the trajectory in a contact-free mode. It encounters an obstruction with the environment in stage ② and is subsequently released in stage ③.

As depicted in Figure 5.5, with a high absolute error limit $\tilde{\boldsymbol{x}}_{\max} = [0.05, 0.05, 0.05, 0, 0, 0]^T$ [m, rad], the system accumulates a significant amount of energy during stage ② until the tank power $P_{T,2}$ is constrained by P_T^{up}, leading to a reduction in $\gamma_{p_i,2}$. Upon releasing the robot in stage ③, the accumulated energy results in a substantial jump in the actual motion of the robot. However, as depicted in Figure 5.6, by opting for a more conservative value of the maximum error magnitude $\tilde{\boldsymbol{x}}_{\max} = [0.005, 0.005, 0.005, 0, 0, 0]^T$ [m, rad], the accumulated energy is reduced, and the robot does not exhibit a jump in stage ③.

Experiment 2: Valve-Based Tanks for Multi-Priority Control Actions

For this experiment, the UFIC framework is fully activated, incorporating both force and impedance control laws. As previously explained, only the first two ports in Figure 5.3 with the associated powers $P_{T,1}$ and $P_{T,2}$, defined in (5.10) and (5.12), respectively, are active, as $P_{T,3}$ is always zero. The experiment scenario is depicted in Figure 5.7. The robot is moving a wagon that carries a weight. Simultaneously, it regulates the interaction force with the operator's hand in stage ①. The operator elevates their hand during stage ②, causing the robot to move upward due to the force control effect[1]. Considering (5.10), this action drains energy from the tank. At the same time, considering (5.11), the external force due to the moving wagon, which opposes the desired velocity, also drains energy. Therefore, at stage ②, the tank energy decreases through two ports simultaneously. When the robot reestablishes contact in stage ③, the interaction force is again regulated, and the associated power approaches zero. For the distribution of energy among the two ports, the three gain scaling approaches introduced in this section are employed in three separate experiments.

---

[1] Please note that the force control shaping function (3.9) is deactivated in this experiment.

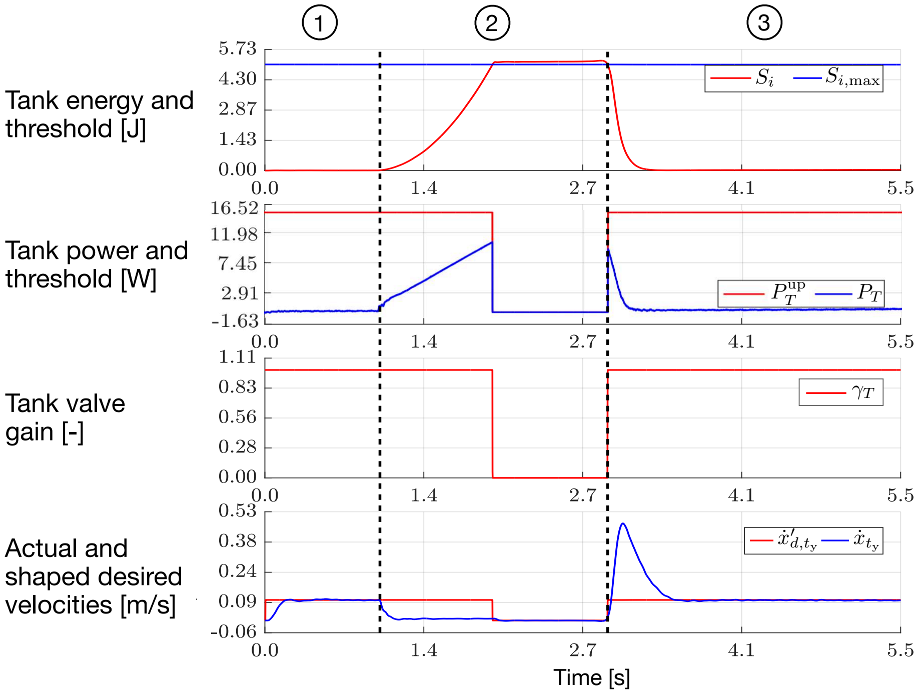

Figure 5.5: Experiment 1 – The large limit $\tilde{\boldsymbol{x}}_{\max} = [0.05, 0.05, 0.05, 0, 0, 0]^T$ [m, rad] leads to a relatively substantial accumulation of energy in the system, resulting in a jump in $\dot{x}_{t_y}$ at ③.

EGS approach: In the first scenario, the valve gain values are determined via (5.4). As depicted in Figure 5.8, the gains are assigned equally when the power limit is violated during stage ②.

WGS approach: In the second scenario, the port priorities are assigned according to Table 5.2. The valve gains are then continuously adjusted based on (5.5). The force control action has a much higher priority than the impedance control one. Hence, the gains are assigned such that the force controller can obtain a higher power from the tank compared to the impedance control when the power flow approaches its limit, as shown in Figure 5.9.

SGA approach: The approach utilized for gain assignment here is based on (5.6). As evident from Figure 5.10, during stage ②, the force controller receives the entire power from the tank. Since there is no remaining power for the impedance controller, the desired velocity $\dot{\boldsymbol{x}}'_d$ reduces to $\mathbf{0}$. As a result, the wagon nearly stops, and the robot moves vertically to regulate the force.

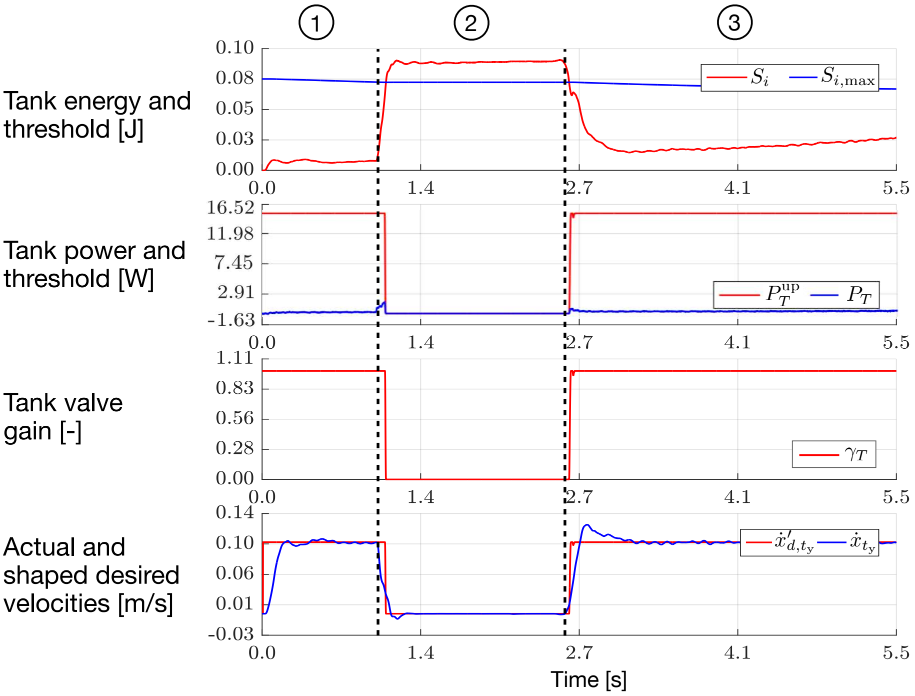

Figure 5.6: Experiment 1 – The more conservative error limit $\tilde{\boldsymbol{x}}_{\max} = [0.005, 0.005, 0.005, 0, 0, 0]^T$ [m, rad] prevents a significant accumulation of energy in the system. Consequently, the robot does not experience a high acceleration when the environmental constraint is released.

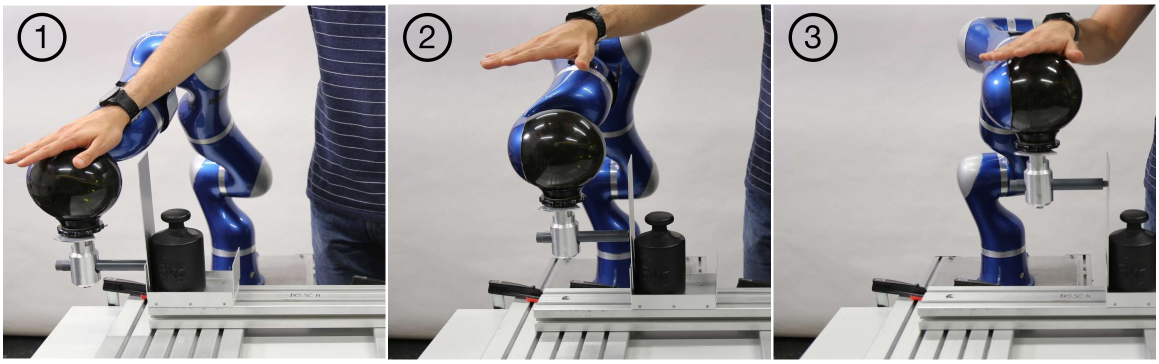

Figure 5.7: Experiment 2 – The robot is simultaneously moving the wagon and attempting to regulate a force perpendicular to the desired trajectory.

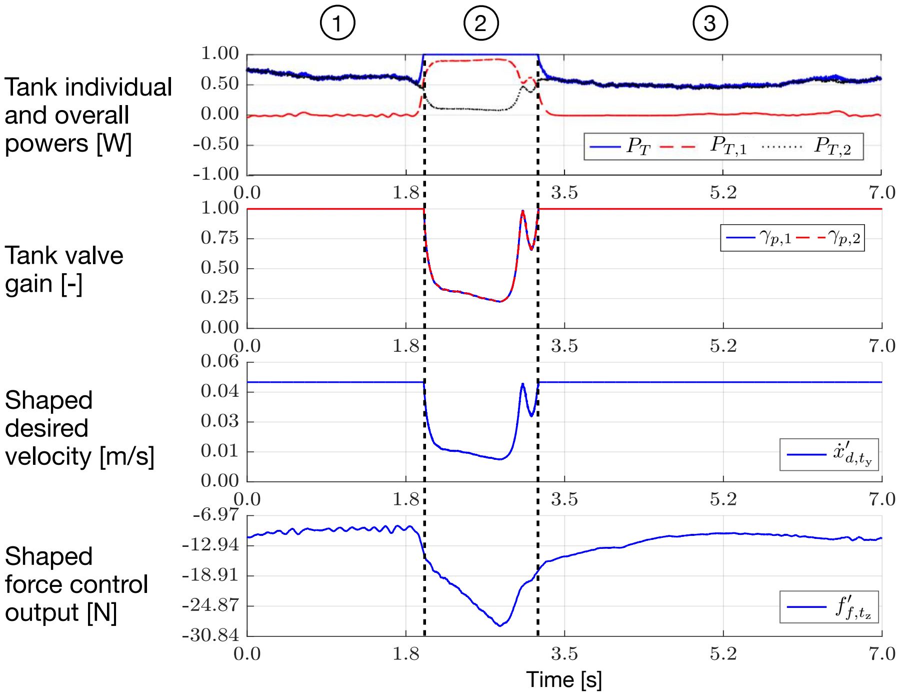

Figure 5.8: Experiment 2 – Multi-priority actions using the EGS approach; the valve gains $\gamma_{p,1}$ and $\gamma_{p,2}$ are adjusted equally.

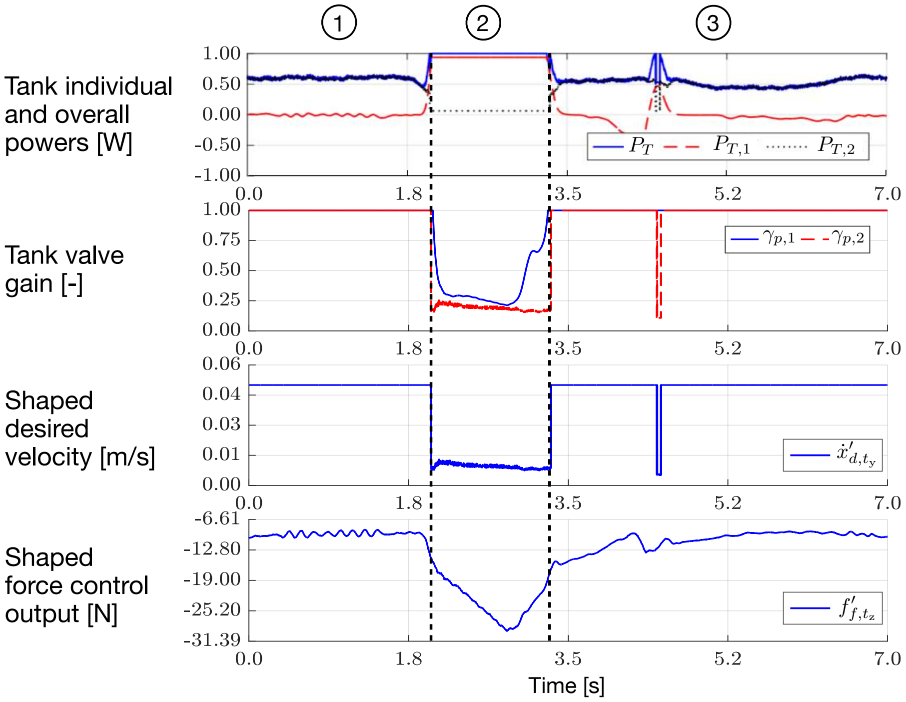

Figure 5.9: Experiment 2 – Multi-priority actions using the WGS approach; the valve gain $\gamma_{p,1}$ is always greater than or equal to $\gamma_{p,2}$ due to the higher priority of the power $P_{T,1}$ compared to $P_{T,2}$.

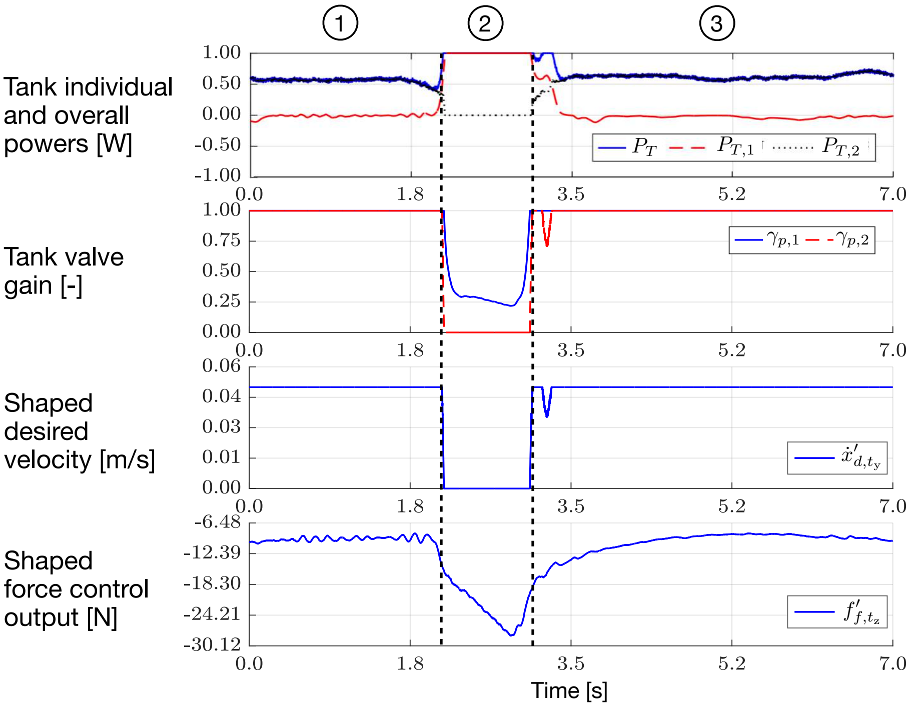

Figure 5.10: Experiment 2 – Multi-priority actions using the SGA approach; the valve gain $\gamma_{p,2}$ reduces to zero to allow the first port to receive all the limited power.

5.2 Energy-Based Reference Behavior in Tactile Manipulation

The allocation of energy for a control action can significantly influence the physical behavior of the system. This phenomenon is underscored throughout various experiments in this dissertation. Examples include the pendulum collision experiment discussed in Section 4.2, the energy-based support adaptation in the context of rehabilitation in Section 4.3, and the power constraint experiments detailed in Section 5.1. With control over the energy flow, a natural and consequential inquiry emerges: what should be the designated energy budget for each control action, and what rate of energy usage (i.e., power) is desired? In Section 5.1, it is illustrated that valve-based virtual energy tanks empower the regulation of energy flow based on specified energy and power limits. This section shifts its focus to the derivation methods for these reference energy-based limits, encompassing model-based methodologies, learning by demonstration approaches, as well as iterative learning methods.

5.2.1 Reference Energy

When employing an energy tank, determining the optimal amount of energy allocated for a control action is crucial. From a stability standpoint, as long as the tank energy is limited, the overall system remains passive. However, this energy is intended to be consumed for a passivity-violating action, leading to a momentary divergence from the desired system state, as elaborated in Section 2.3. Therefore, it is essential to ascertain the appropriate energy provision from the tank. The influence of the tank energy level on the physical behavior of the system is studied in Section 4.2, Experiment 3. It is demonstrated how a higher initial energy in the augmented tank can result in higher magnitudes of post-impact wrenches when the robot collides with a pendulum. In contrast, when the initial energy of the tank is low, the robot is not able to fully elevate the pendulum, due to its lower virtual momentum.

One approach to determining the optimal energy level for a tank is to demonstrate the optimal behavior and subsequently learn the associated energy. In the literature, this method is referred to as Learning by Demonstration (LbD). In Section 3.3, this method is employed to determine the reference energy $S_d \in \mathbb{R}_{\geq 0}$ of the augmented tank for an impedance-controlled robot in contact with the environment when using a Dynamic Movement Primitive. Another approach is to estimate the reference energy, considering the nature of the passivity-violating action and the model of the involved systems. Here, as an example of such model-based reference energy estimation methods, the virtual tank designed for impedance control in the UFIC framework presented in Section 3.1 is taken into account (Figure 5.11).

Model-Based Energy Budget Estimation for the Impedance Control Tank in UFIC

Considering (3.24) the potentially passivity-violating power corresponding to the impedance controller in the unified force-impedance control frameowrk (UFIC) is $P_{T,i} = -\dot{\boldsymbol{x}}_d^T(\boldsymbol{f}_f + \boldsymbol{f}_{\text{ext}})$, where $\dot{\boldsymbol{x}}_d \in \mathbb{R}^m$ is the desired twist and $\boldsymbol{f}_f, \boldsymbol{f}_{\text{ext}} \in \mathbb{R}^m$ are the force control output and the interaction wrenches, respectively, all in an m-dimensional Cartesian space. Assume that the robot is in contact with the environment, and the desired motion is in such a way that a friction wrench $\boldsymbol{f}_{\text{fri,env}} \in \mathbb{R}^m$ is generated opposite to the motion direction, according to

$$\boldsymbol{f}_{\text{fri,env}} = -\boldsymbol{d}_{v,\text{env}} \circ \dot{\boldsymbol{x}} - \underbrace{[d_{c_t,\text{env}} \mathbf{1}_{1\times m_t}, d_{c_r,\text{env}} \mathbf{1}_{1\times m_r}]^T}_{\boldsymbol{d}_{c,\text{env}}} \circ \operatorname{sgn}(\dot{\boldsymbol{x}}), \tag{5.16}$$

where $\dot{\boldsymbol{x}} \in \mathbb{R}^m$ is the twist vector and $\boldsymbol{d}_{v,\text{env}}, \boldsymbol{d}_{c,\text{env}} \in \mathbb{R}^m$ are the viscous and Coulomb friction coefficient vectors of the interacting environment, respectively. The Coulomb friction can be related to the environment surface normal vector $\boldsymbol{f}_N \in \mathbb{R}^m$ as

$$\begin{bmatrix} d_{c_t,\text{env}} \\ d_{c_r,\text{env}} \end{bmatrix} = \underbrace{\begin{bmatrix} \mu_{tt,\text{env}} & \mu_{tr,\text{env}} \\ \mu_{rt,\text{env}} & \mu_{rr,\text{env}} \end{bmatrix}}_{\boldsymbol{\mu}_{\text{env}}} \begin{bmatrix} \|\boldsymbol{f}_{t,N}\| \\ \|\boldsymbol{f}_{r,N}\| \end{bmatrix}, \tag{5.17}$$

where $\boldsymbol{f}_{t,N} \in \mathbb{R}^{m_t}$ and $\boldsymbol{f}_{r,N} \in \mathbb{R}^{m_r}$ are the translational and rotational components[2] of $\boldsymbol{f}_N$, and $\boldsymbol{\mu}_{\text{env}} \in \mathbb{R}^{2\times 2}$ is the environment friction coefficient matrix.

Assuming accurate force control perpendicular to the surface, it can be inferred that $\boldsymbol{f}_N \approx -\boldsymbol{f}_d$. Moreover, by approximating $\dot{\boldsymbol{x}} \approx \dot{\boldsymbol{x}}_d$, the estimated reference energy budget for the impedance control tank during movements on a frictional surface is

$$S_{d,i} = \int_0^T \left(|\dot{\boldsymbol{x}}_d(\varepsilon)|^T \boldsymbol{d}_{c,\text{env}}(\boldsymbol{f}_d(\varepsilon)) + \dot{\boldsymbol{x}}_d^T(\varepsilon) \left(\boldsymbol{d}_{v,\text{env}} \circ \dot{\boldsymbol{x}}_d(\varepsilon) \right) \right) d\varepsilon, \tag{5.18}$$

where $T \in \mathbb{R}_{\geq 0}$ is the task duration.

---

[2] $m_t + m_r = m$.

Figure 5.11: A tank provides the required power $-\dot{\boldsymbol{x}}_d^T \boldsymbol{f}_{\text{ext}}$ to control motion on a frictional surface.

5.2.2 Reference Power

When allocating an energy budget for a control action, it is crucial to determine how this energy should be used throughout the task. Without considering this aspect, the entire energy might be consumed at the beginning of the task, leaving insufficient energy for later stages when it is actually required. In Section 4.1, it is demonstrated how a valve-based energy tank can address this issue by imposing power limits on the energy flow. These power limits constrain the rate of exchanged energy. However, the significance of such constraints may vary throughout the task. To address this, an approach can be to define the power limit as a function of the task progress. This can be achieved using the concept of phase $\phi \in \mathbb{R}$ introduced in Chapter 4. Similar to the reference force and motion trajectories, the reference power limit can also be defined as a function of phase, with $\phi = 0$ and $\phi = 1$ associated with the beginning and the end of the task, respectively.

Among numerous phase-encoding approaches, here, the phase-based power profile, e.g., for the power upper limit P_T^{up} in (5.3), can be derived as

$$\forall \phi \in \Phi_i,\ P_T^{\text{up}}(\phi) = \begin{cases} \frac{p_i + p_{i-1}}{2} + \frac{p_i - p_{i-1}}{2} \sin(\pi \frac{\phi - \phi_i}{2\phi_\Delta}) & \text{if} \quad \phi < \phi_i + \phi_\Delta, \\ \frac{p_i + p_{i-1}}{2} + \frac{p_i - p_{i+1}}{2} \sin(\pi \frac{\phi_{i+1} - \phi}{2\phi_\Delta}) & \text{if} \quad \phi_{i+1} - \phi_\Delta < \phi, \\ p_i & \text{else} \end{cases} \tag{5.19}$$

Here, the phase value ϕ is divided into several segments Φ_i with the beginning and end phase values of ϕ_i, ϕ_{i+1}, such that $\phi_i \leq \phi \leq \phi_{i+1}$. The magnitude of the reference power at segment Φ_i is denoted as $p_i \in \mathbb{R}_{\geq 0}$. Additionally, at the borders of each segment, a smooth transition threshold is defined with a unified length of ϕ_Δ such that

$$\forall i, 2\phi_\Delta \leq \phi_{i+1} - \phi_i \tag{5.20}$$

Figure 5.12 depicts the visual representation of the proposed phase-based power profile. By assigning the value of p_i at all segments, the reference power profile is constructed. To determine these values, an iterative learning method is proposed in the following.

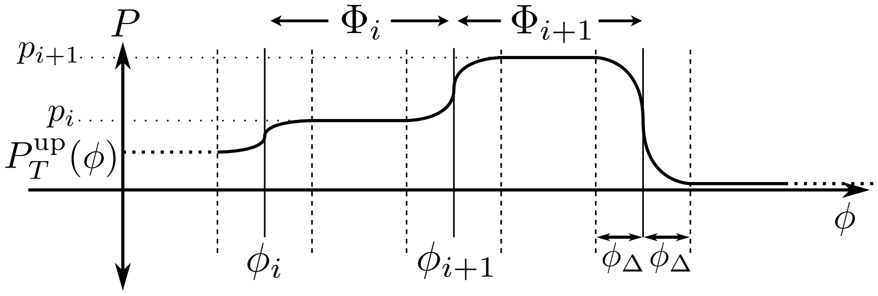

Figure 5.12: Phase-based reference profile for the power upper limit.

5.2.3 Iterative Learning of Power Trajectory

When devising a phase-encoding method for the reference power, the challenge lies in determining the associated parameters. As discussed earlier, one approach involves the Learning by Demonstration method, where the power trajectory needed for optimal task execution is recorded and learned through methods like function fitting. However, this approach has a drawback: if task conditions change in subsequent iterations, the initially learned reference profile may no longer be suitable. This issue becomes particularly pronounced in tasks involving physical interaction with the environment, where replicating exact signals may be challenging, especially with even slight changes in the environment. Therefore, an Iterative Learning method is proposed here, allowing for the adaptation of the power profile (5.19) over iterations, ensuring the reference profile remains suitable even with changing conditions.

Like any adaptive method, a metric needs to be defined to guide the adaptation. In this case, the metric is rooted in the fundamental principle of the involved tanks, i.e., the valve gains. As shown in (5.3), $\gamma_p = 1$ corresponds to a scenario where the demanded passivity-violating power is within acceptable limits. This observation may suggest well-tuned limits. Conversely, it could also imply that the limits are set too loosely. Since this power is utilized for a passivity-violating control action, setting the limits too loosely is not ideal. Consequently, the logic is structured such that when γ_p is 1 in one iteration, the limits become more conservative in the next iteration. Conversely, if γ_p is less than 1 in an iteration, the power limits are set loosely for the next iteration. This logic ensures that the reference power limit prevents an excessive amount of passivity-violating power while avoiding overly restrictive constraints. The adaptation policy, as a function of phase, allows the power value for each segment to be independently adjusted in (5.19). Specifically, considering $p_{i,j}$ as the power value for segment Φ_i in iteration j, its value for iteration $j+1$ is determined as:

$$p_{i,j+1} = p_{i,j} - \kappa_l + \bar{\gamma}_{p,i,j}(\kappa_l + \kappa_f). \tag{5.21}$$

Here, $\bar{\gamma}_{p,i,j} \in [0,1]$ represents the average value of the valve gain γ_p at segment Φ_i for iteration j. The parameters $\kappa_l, \kappa_f \in \mathbb{R}_{\geq 0}$ are user-defined learning and forgetting factors, respectively, typically with $\kappa_l >> \kappa_f$.

5.2.4 Experiments

To showcase the impact of reference energy-based behaviors on the physical performance of a system and demonstrate how these behaviors can be learned to enhance overall performance,

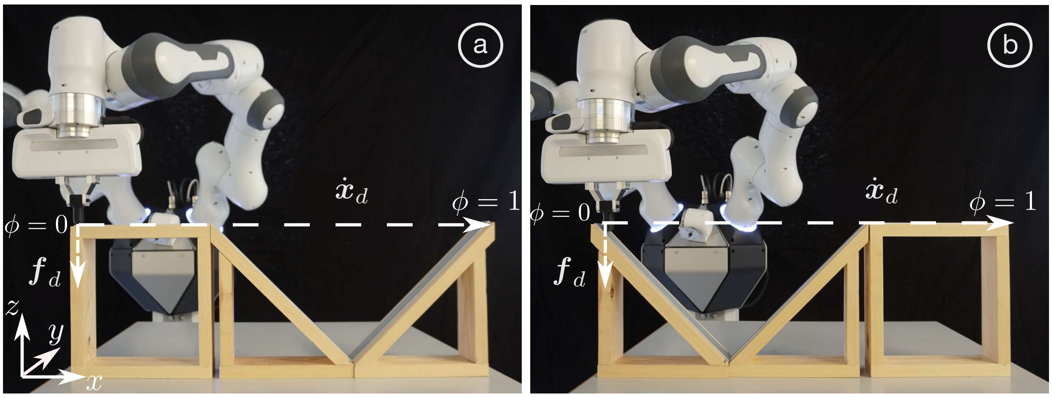

Figure 5.13: Experiment scenarios – Setup ⓐ is utilized for all experiments, while setup ⓑ is employed exclusively in the final experiment.

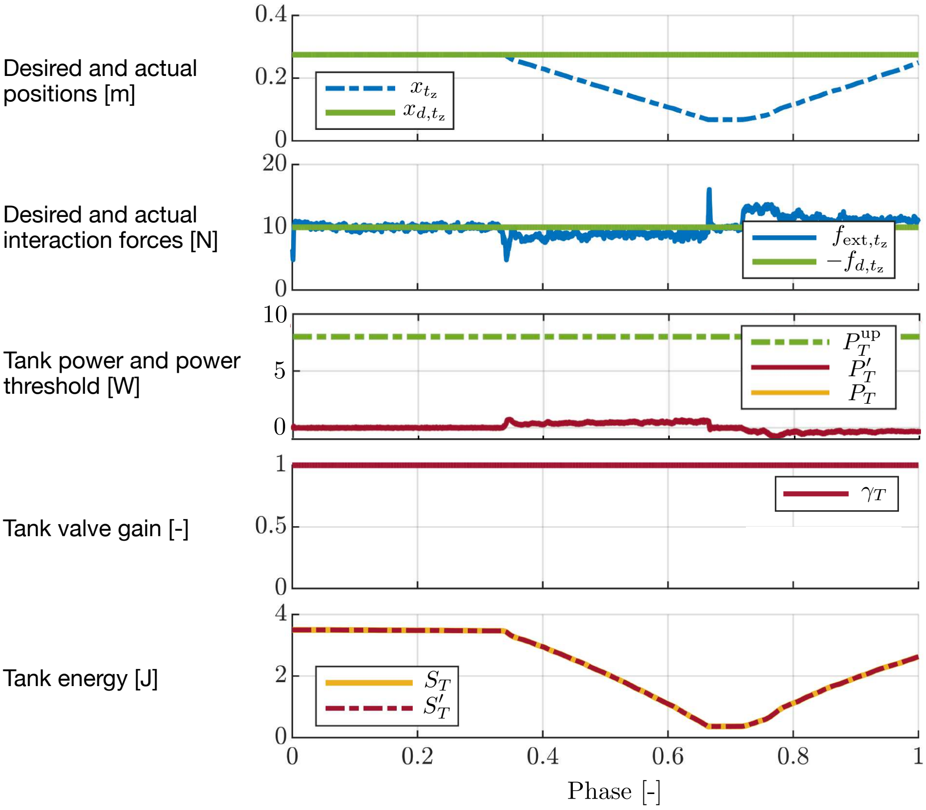

Figure 5.14: Experiment 1 – The tank power limit P_T^{up} is set generously to ensure the tank valve gain γ_1 is always at 1. Phase values 0 and 1 are associated with the start point ($x_{d,t_x} = 0$ [m]), and end point ($x_{d,t_x} = 0.63$ [m]), respectively.

a series of experiments have been conducted. A Franka Emika robot equipped with a unified force-impedance control (3.25) is employed, featuring its two energy tanks. The robot is commanded to move horizontally along a 0.63 m path at a constant speed of 0.03 cm/s while simultaneously applying a 10 N vertical force to the surface, as depicted in Figure 5.13. The control law utilizes a diagonal stiffness matrix with elements $\{1000, 1000, 35, 100, 100, 100\}$ [N/m, Nm/rad], and the damping matrix is shaped for critical damping [381]. Force control gains are set to zero for all directions except for the desired force direction (i.e., y-direction in Figure 5.13), where proportional, integrator and derivative gains are set to 0.2, 1, and 0, respectively. The surface for interaction features three different slopes, and the end-effector is a 3D-printed (PLA) cylindrical object with a small, low-friction surface. The primary focus of the experiments lies in exploring the force control energy tank and assessing how its reference power limit can influence physical interaction behavior.

Experiment 1: Baseline Scenario

The first experiment illustrates the system behavior when employing a loose reference power limit. Considering Figure 5.14, when the robot encounters the downhill slope, due to the comparatively lower stiffness in the z-direction, force control takes precedence over impedance control, causing the robot to move downward. This action corresponds to a positive power $P_T = \dot{\boldsymbol{x}}^T \boldsymbol{f}_f$, where $\dot{\boldsymbol{x}}, \boldsymbol{f}_f \in \mathbb{R}^6$ denote the end-effector twist and the force control output, respectively. This positive power is drawn from the energy tank, leading to a decrease in tank energy $S_T \in \mathbb{R}_{\geq 0}$ as $\dot{S}_T = -P_T$. Conversely, as the robot ascends the uphill slope, the power P_T becomes negative, resulting in the replenishment of the energy tank. Throughout this experiment, no tank limit is violated, and as a consequence, the valve gain γ_T remains consistently at 1.

Experiment 2: Power Constraints for Increased Robustness to Disturbances

In the second experiment, the entire surface is lowered by 0.12 m before commencing the task. Consequently, the robot does not make contact with the surface from the outset. Due to the force control dominance over impedance control in the z-direction, force control moves the robot downward until it makes contact with the surface again. This behavior results in a positive power P_T, significantly larger than in the previous experiment due to the faster robot speed in the absence of contact. Two scenarios are considered with distinct power limits: one loose, as in the previous experiment, and the other conservative. Examining Figure 5.15, in scenario ①, the impact force rapidly increases up to 70 N, which could be perceived as a hazardous behavior. This behavior is mitigated in scenario ②, thanks to the conservative power limit of 0.175 W. As a result, the impact force increases only up to 20 N. The interaction force is later regulated in both scenarios. However, this experiment vividly demonstrates that by adjusting only the reference power limit, the physical behavior of the robot can undergo drastic changes.

Experiment 3: Phase-Based Reference Power Profile

In this experiment, instead of setting a constant value for the reference power, the phase-based trajectory encoding method (5.19) is employed with three phase segments. The power amplitudes are configured as $p_1 = 0.1$ W for the even surface, $p_2 = 0.42$ W for the downhill slope, and $p_3 = 0.1$ W for the uphill slope. The threshold length ϕ_Δ is set to 0.002. Figure 5.16 illustrates the experiment results for scenario ①, where a constant power limit of $P_T = 0.175$ W is used, and scenario ②, where the proposed three-segment power limit is employed. As evident from the results, while the force regulation quality is similar for the even surface, the performance on the uphill and downhill slopes is significantly improved in scenario ②. This emphasizes that appropriately designing a reference profile enhances system performance.

Experiment 4: Iterative Learning of Reference Power

This experiment investigates the effectiveness of the iterative learning method (5.21). Here, four phase segments with equal lengths are considered. The learning and forgetting factors are set to $\kappa_l = 0.1$ and $\kappa_f = 0.01$, respectively. Ten iterations are conducted, and the results are depicted in Figure 5.17. It can be observed that by the 10th iteration, the valve gain γ_T approaches 1. This indicates that initially, the power limits are too conservative, and over iterations, thanks to the learning factor, they adapted to provide enough power for the force regulation task. The force error is thus much smaller at iteration 10 compared to the first iteration. To assess the impact of an increased number of phase segments, the same experiment is repeated, this time with forty phase segments. As shown in Figure 5.17, the overall behavior is improved. Specifically, for the 10th iteration with four segments, the force standard deviation and overall energy consumption are 2.5 N and 1.8 J, respectively. These values improve to 2.1 N and 1.3 J when 40 segments are considered. The primary reason for this improvement is that a higher number of segments allows for better adaptation to characteristic differences along the path.

Experiment 5: Power Trajectory Adaptation in Changing Environments

In the final experiment, conducted to verify the robustness of the approach to changes in task conditions, the setup is suddenly altered after the learned reference trajectory in the previous experiment, as illustrated in Figure 5.13. The learning process remains active. Figure 5.18 demonstrates how the reference power profile is re-adapted after such a substantial disturbance, once again improving the force control performance. In fact, during the first iteration, the robot accelerates after $\phi = 0.33$, resulting in an impact force with a magnitude of 40 N. This does not happen when the trajectory is adapted to the environment after ten iterations.

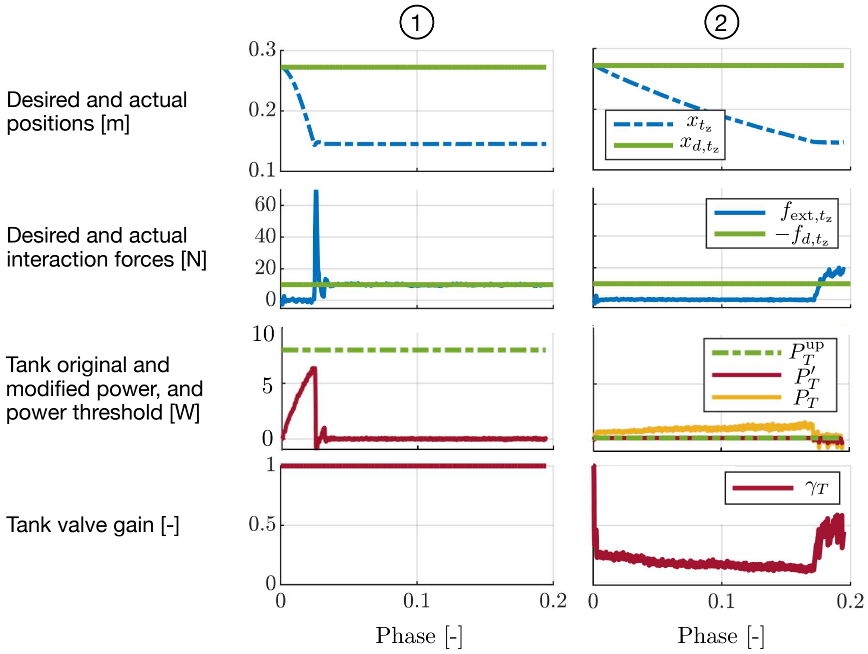

Figure 5.15: Experiment 2 – The more conservative power limit P_T^{up} in scenario ② alters the power flow P_T to P_T' through the valve gain γ_T according to (5.3).

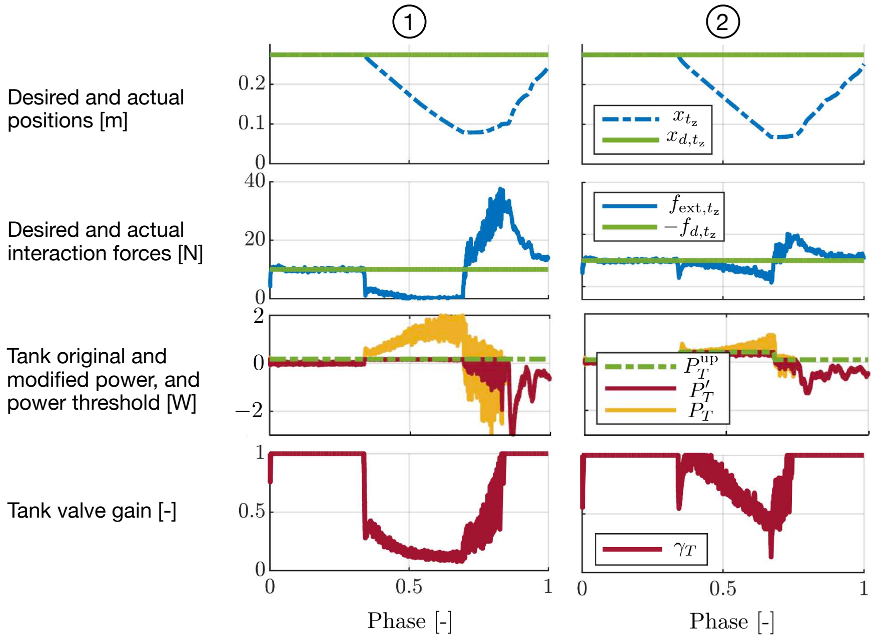

Figure 5.16: Experiment 3 – The power limit consists of three phase segments in scenario ②.

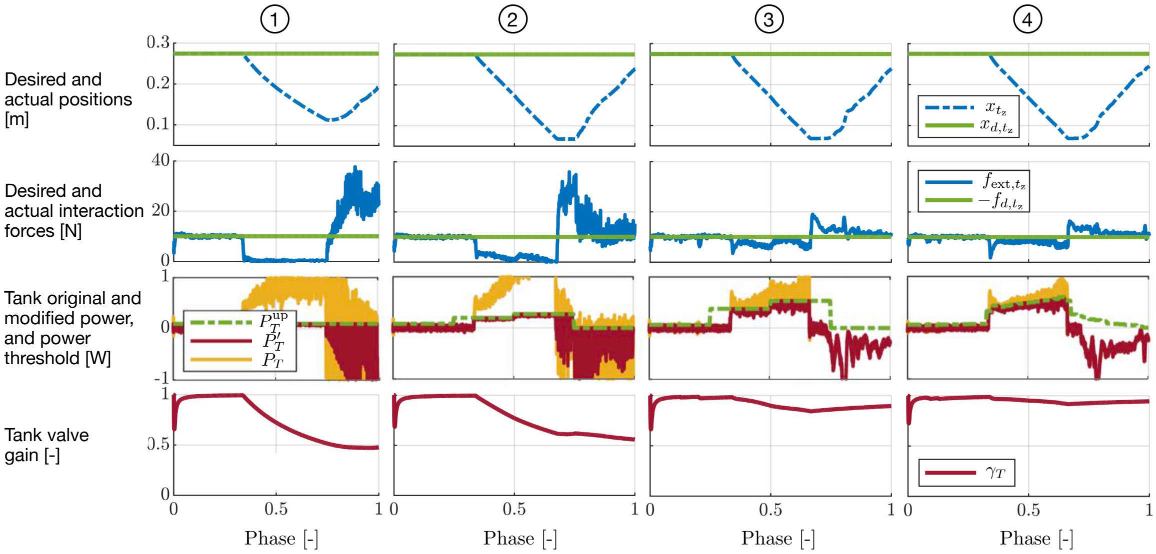

Figure 5.17: Experiment 4 – Performance comparison for a reference power profile with four phase segments at iteration 1 (①), iteration 2 (②), and iteration 10 (③), as well as a power profile with forty segments at iteration 10 (④). The standard deviation in the force error is 8.8 N, 7 N, 2.5 N, and 2.1 N for ①, ②, ③, and ④, respectively.

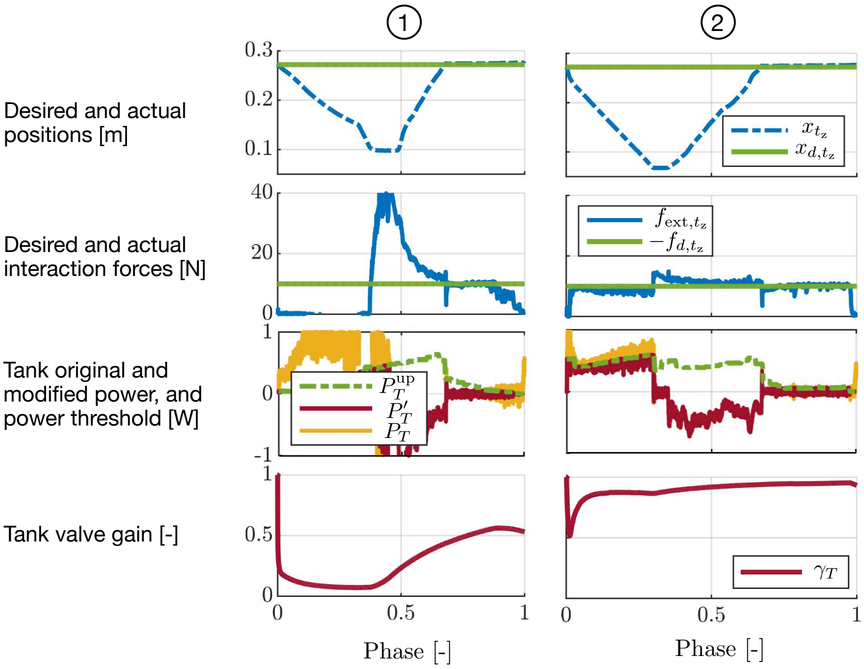

Figure 5.18: Experiment 5 – Force regulation performance after environment disturbance, given 1 (①) and 10 (②) learning iterations.

5.3 Energy-Based Performance Monitoring in Rehabilitation

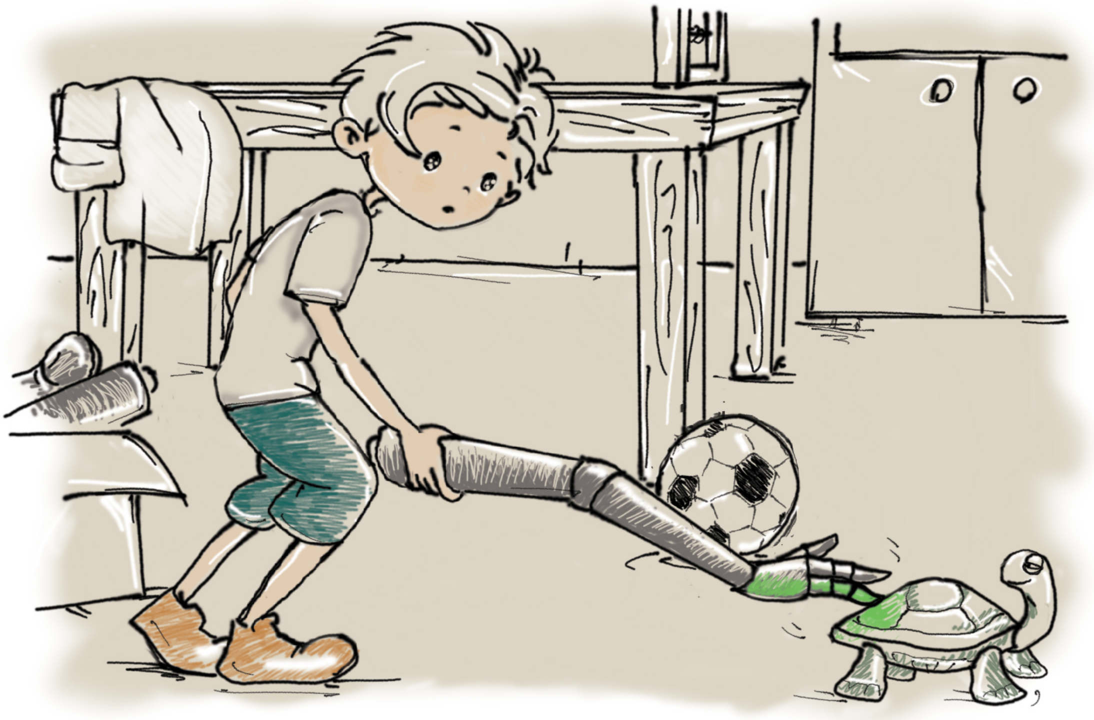

At each stage of this dissertation, it is demonstrated how energy can be systematically employed as an intrinsic tool for shaping control performance. This is achieved by incorporating an energy-based model of the system architecture, accounting for the relevant control variables and parameters. Yet, what if access to such detailed information is unavailable? Applying the proposed energy-based control algorithms might not be feasible, but energy can still serve as a potent tool for understanding the unmodelled system. Consider a patient's body undergoing therapy, for instance, with a rehabilitation robot. To assess the progress of recovery, it is essential to gauge the patient's active participation in the rehabilitation task. Communication with the patient offers only qualitative insights, while external sensing devices, like Electromyography, often entail complex setups and may not be practical in clinical settings. Additionally, motion and interaction wrench signals from standard robot sensors alone might not be suitable for this purpose, as changing the controller compliance over therapy iterations renders the motion and force signals confounding. This is where the coordinate-free metric of energy proves invaluable. This section employs the concept of energy to develop a performance monitoring technique that identifies the patient's active participation in motion and, consequently, the stage of recovery.

5.3.1 Patient Participation Assessment via Work Metric

The fundamental concept driving the proposed energy-based patient monitoring approach is that in the absence of active patient participation during rehabilitation (indicating no involvement in the motion), the robot is responsible for executing a specific amount of physical work to move the patient's body. This baseline work can be quantified through the analysis of the robot motion and interaction wrench signals. Consequently, any active engagement from the patient in subsequent motion cycles can be discerned by monitoring the performed work and assessing it against the established baseline.

Human limb movement is controlled by muscle activation. In the case of a robot attached to the limb via n_r points and considering $\boldsymbol{\tau}_m \in \mathbb{R}^{n_h}$ as the joint torque of the n_h-degrees-of-freedom human limb associated with muscle activation, the limb's motion can be described by the following dynamics equation [367] derived as

$$\boldsymbol{M}_h(\boldsymbol{q}_h)\ddot{\boldsymbol{q}}_h + \boldsymbol{C}_h(\boldsymbol{q}_h, \dot{\boldsymbol{q}}_h)\dot{\boldsymbol{q}}_h + \boldsymbol{g}_h(\boldsymbol{q}_h) + \boldsymbol{d}_h(\dot{\boldsymbol{q}}_h) + \boldsymbol{k}_h(\boldsymbol{q}_h) = \boldsymbol{\tau}_m + \sum_{i=1}^{n_r} \boldsymbol{J}_{h,i}^T(\boldsymbol{q}_h)\boldsymbol{f}_{h,\text{ext},i}. \tag{5.22}$$

Here, $\boldsymbol{q}_h \in \mathbb{R}^{n_h}$ represents the limb's joint angles, $\boldsymbol{M}_h(\boldsymbol{q}_h), \boldsymbol{C}_h(\boldsymbol{q}_h, \dot{\boldsymbol{q}}_h) \in \mathbb{R}^{n_h \times n_h}$ are the mass and the centrifugal and Coriolis matrices, respectively, and $\boldsymbol{g}_h(\boldsymbol{q}_h),\ \boldsymbol{d}_h(\dot{\boldsymbol{q}}_h),\ \boldsymbol{k}_h(\dot{\boldsymbol{q}}_h) \in \mathbb{R}^{n_h}$ denote the torque vectors associated with the limb's gravity, the energy dissipation, and the elasticity of the musculo-tendon units. Moreover, $\boldsymbol{f}_{h,\text{ext},i} \in \mathbb{R}^m$ denotes the interaction wrench defined in an m-dimensional Cartesian space, acting on the i-th point of contact with the limb. Finally, $\boldsymbol{J}_{h,i}(\boldsymbol{q}_h) \in \mathbb{R}^{m \times n_h}$ is the Jacobian matrix corresponding to the i-th contact point, such that

$$\dot{\boldsymbol{x}}_i = \boldsymbol{J}_{h,i}(\boldsymbol{q}_h)\dot{\boldsymbol{q}}_h, \tag{5.23}$$

where $\dot{\boldsymbol{x}}_i \in \mathbb{R}^m$ denotes the twist vector at the i-th contact point.

For the musculoskeletal system (5.22), three forms of energy can be associated, namely kinetic energy $T_h(\boldsymbol{q}_h, \dot{\boldsymbol{q}}_h) \in \mathbb{R}_{\geq 0}$, gravitational energy $U_{g,h}(\boldsymbol{q}_h) \in \mathbb{R}_{\geq 0}$, and elastic energy $U_{j,h}(\boldsymbol{q}_h) \in \mathbb{R}_{\geq 0}$, with the following relations.

$$T_h(\boldsymbol{q}_h, \dot{\boldsymbol{q}}_h) = \frac{1}{2}\dot{\boldsymbol{q}}_h^T \boldsymbol{M}_h(\boldsymbol{q}_h)\dot{\boldsymbol{q}}_h, \tag{5.24}$$

$$\boldsymbol{g}_h(\boldsymbol{q}_h) = \frac{\partial U_{g,h}(\boldsymbol{q}_h)}{\partial \boldsymbol{q}_h}, \tag{5.25}$$

$$\boldsymbol{k}_h(\boldsymbol{q}_h) = \frac{\partial U_{j,h}(\boldsymbol{q}_h)}{\partial \boldsymbol{q}_h}. \tag{5.26}$$

Accordingly, the overall energy for the limb can be defined as

$$S_{h,l} = T_h + U_{g,h} + U_{j,h}. \tag{5.27}$$

Considering (5.22), the time derivative of the limb energy $S_{h,l}$ can be expressed as

$$\dot{S}_{h,l} = P_{h,m} + P_{h,\text{ext}} - P_{h,\text{diss}}, \tag{5.28}$$

where

$$P_{h,m} = \dot{\boldsymbol{q}}_h^T \boldsymbol{\tau}_m, \tag{5.29}$$

$$P_{h,\text{ext}} = \sum_{i=1}^{n_r} P_{h,\text{ext},i} = \sum_{i=1}^{n_r} \dot{\boldsymbol{x}}_i^T \boldsymbol{f}_{h,\text{ext},i}, \tag{5.30}$$

$$P_{h,\text{diss}} = \dot{\boldsymbol{q}}_h^T \boldsymbol{d}_h(\dot{\boldsymbol{q}}_h) \geq 0. \tag{5.31}$$

According to (5.28), the variations in the energy $S_{h,l}$ result from the summation of the human input power $P_{h,m}$ associated with muscle activation and the external power $P_{h,\text{ext}}$ from the contact points with the robot, subtracted by the dissipated power $P_{h,\text{diss}}$. During a motion cycle from time t_start to t_end, the work performed associated with each of these sources can be derived as

$$W_m = \int_{t_\text{start}}^{t_\text{end}} P_{h,m}\, dt, \tag{5.32}$$

$$W_{h,\text{ext}} = \int_{t_\text{start}}^{t_\text{end}} P_{h,\text{ext}}\, dt = -\sum_{i=1}^{n_r} \int_{t_\text{start}}^{t_\text{end}} \dot{\boldsymbol{x}}_i^T \boldsymbol{f}_{\text{ext},i}\, dt, \tag{5.33}$$

$$E_{h,\text{diss}} = \int_{t_\text{start}}^{t_\text{end}} P_{h,\text{diss}}\, dt, \tag{5.34}$$

where $\boldsymbol{f}_{\text{ext},i} \in \mathbb{R}^m$ denotes the external wrench sensed by the robot at the i-th point of contact with the human limb such that $\boldsymbol{f}_{\text{ext},i} = -\boldsymbol{f}_{h,\text{ext},i}$. Accordingly, the work equation corresponding to (5.28) becomes

$$S_{h,l,\text{end}} - S_{h,l,\text{start}} + E_{h,\text{diss}} = W_m + W_{h,\text{ext}}, \tag{5.35}$$

where $S_{h,l,\text{start}}, S_{h,l,\text{end}} \in \mathbb{R}_{\geq 0}$ denote the limb energy levels at the beginning and the end of the motion cycle.

For a repetitive rehabilitation motion, considering (5.24)–(5.27), the values of $S_{h,l,\text{start}}$ and $S_{h,l,\text{end}}$ remain the same where the initial and final limb configurations and velocities (i.e., $\boldsymbol{q}_h, \dot{\boldsymbol{q}}_h$) are kept the same for all iterations[3]. Moreover, when the limb's mass is large enough, the magnitudes of the kinetic and potential energy are significantly larger than the changes in dissipated energy $E_{h,\text{diss}}$ between steps; thus, the changes in $E_{h,\text{diss}}$ can be considered negligible, and the left side of (5.35) can be assumed constant across iterations. Therefore, it can be deduced that any increase/decrease in $W_{h,\text{ext}}$ (i.e., work performed by the robot) for two consecutive cycles is associated with a decrease/increase in W_m (i.e., work performed by the human). In other words, by monitoring the changes in the work performed by the robot according to (5.33), the human's active participation in the motion, i.e., the evolution of W_m, can be indirectly evaluated. As mentioned before, this analysis is the core idea behind the proposed metric. By defining $W_{h,\text{ext}}^{\dagger}$ as the work performed by the interactive robot when the human limb is entirely passive (i.e., for $W_m = 0$), the active participation of the human in the movement can be monitored by iteratively comparing $W_{h,\text{ext}}$ with $W_{h,\text{ext}}^{\dagger}$. This is done by defining the work metric $W_{m,\text{rob}} \in \mathbb{R}$ as

$$W_{m,\text{rob}} = W_{h,\text{ext}}^{\dagger} - W_{h,\text{ext}}. \tag{5.36}$$

Note that no extra sensors, besides the standard force and motion sensors of the robot, are required to obtain $W_{m,\text{rob}}$.

---

[3] Please note that the effect of musculo-tendon elasticity variation over iterations, which would result in different values of $U_{j,h}$ even for the same configuration $\boldsymbol{q}_h$, is neglected here.

5.3.2 EMG-Based Verification Metric

In order to verify the effectiveness of the proposed energy-based performance monitoring metric, it is essential to compare it with a validation metric that takes into account more sensory information to be closer to the ground truth. Therefore, here, a secondary metric based on the biological aspects of patient participation in a motion is derived.

Muscles convert chemical energy (i.e., ATP) into mechanical work in the form of force generated by the muscle contractile element (CE). This is also referred to as the *active force* of the muscle, while the *passive force* results from passive stretching of the muscle viscoelastic elements [395]. In (5.22), $\boldsymbol{\tau}_m$ represents the torque generated by the active muscle force, whereas the torque vector $\boldsymbol{k}_h(\boldsymbol{q}_h)$ is associated with the energy stored due to passive stretching of the muscle viscoelastic elements. The total muscle force is the sum of the active force generated by the contractile unit and the passive force provided by the elastic elements in parallel with the contractile unit [396]. By definition, the work performed by a muscle m must be calculated from the active force, $f_{ma} \in \mathbb{R}$. While there is no way to directly measure this force or the resulting work, it has been well established that EMG activity is correlated with f_{ma} under certain conditions [397, 398], wherein

$$f_{ma} = a_m \; f_{ma,\max} \; f_{mf}(\bar{l}_{mf}, \dot{\bar{l}}_{mf}). \tag{5.37}$$

Here, $a_m \in [0, 1]$ is muscle activation, $f_{ma,\max} \in \mathbb{R}_{>0}$ is the maximum active muscle force, while $\bar{l}_{mf} \in \mathbb{R}_{>0}$ and $\dot{\bar{l}}_{mf} \in \mathbb{R}$ are normalized muscle fiber length and change rate, respectively. Model $f_{mf}(\cdot)$ in (5.37) contains shape parameters for the force-length and the force-velocity curves of skeletal muscle. The detailed equation can be found in [396]. The muscle activation a_m can be estimated directly from Electromyography (EMG) measurement $\hat{a}_m$ according to

$$a_m = \kappa_m \hat{a}_m + \hat{a}_{m,0}, \tag{5.38}$$

where $\kappa_m \in \mathbb{R}_{>0}$ is a constant scaling factor and $\hat{a}_{m,0} \in \mathbb{R}$ is the quiescent EMG baseline. These parameters are unique to each subject, muscle, and sensor placement. By the further assumption that the tendon is rigid, it can be deduced that $\bar{l}_{mf}$ is a function of limb joint angles $\boldsymbol{q}_h$, and $\dot{\bar{l}}_{mf}$ is a function of joint angles and velocities $\boldsymbol{q}_h, \dot{\boldsymbol{q}}_h$, making it possible to estimate f_{ma} from EMG and kinematic data, given parameters κ_m, $\hat{a}_{m,0}$, and $f_{ma,\max}$. Finally, considering the sets of agonist muscles M_{ag} and antagonist muscles M_{ant} involved in a given motion, the work performed by the patient muscles (m) can be estimated according to

$$W_{m,\text{emg}} = \sum_{m \in M_{\text{ag}}} \int_{t_{\text{start}}}^{t_{\text{end}}} f_{ma} \dot{l}_m dt - \sum_{m \in M_{\text{ant}}} \int_{t_{\text{start}}}^{t_{\text{end}}} f_{ma} \dot{l}_m dt. \tag{5.39}$$

Here, $\dot{l}_m \in \mathbb{R}$ is the rate of change of muscle length, which, as elaborated above, can also be assumed to be a function of joint angles and velocities $\boldsymbol{q}_h, \dot{\boldsymbol{q}}_h$. Please refer to [399] for more details.

5.3.3 Clinical Results

In order to compare the proposed energy-based robot-measured metric with the EMG-measured verification metric, the VEMOTION robot introduced in Section 4.3 is utilized.

The experiments were conducted on both healthy and patient subjects. Twelve healthy subjects participated, including seven males and five females, with an average age of 31 ± 4 years, height of 1.74 ± 0.11 m, and weight of 73 ± 13 kg. Additional data were collected from two ICU patients at the Schön Klinik Bad Aibling Harthausen (SKBA) undergoing VEMOTION-based mobilization as part of their hospital care. Patient 1, a 79-year-old female (1.71 m, 77 kg), experienced polytrauma following a traffic accident, suffering from muscle weakness, delirium, dysphagia, and respiratory insufficiency. Patient 2, an 81-year-old male (1.70 m, 93 kg), had a critical illness-polyneuropathy/-myopathy following a prolonged ICU stay due to complications from Covid-19. He was dealing with muscle weakness, dysphagia, and respiratory insufficiency. In addition to VEMOTION therapy, both patients received standard care, including a combination of physiotherapy, occupational therapy, swallowing therapy, neuropsychology, and breathing therapy. The healthy subject experiments were conducted with the approval of the Ethics Commission of the Technical University of Munich (review number 2022-623-S-KH). Similarly, for the patient experiments, the experimental protocol was reviewed by the Ludwig Maximilians University of Munich (LMU) Ethics Committee under review number 18-645.

Experimental Protocols

During the experiments, healthy subjects were instructed to lie on the VEMOTION bed. Subsequently, their thighs and feet were secured to the robot end effectors and foot plates, respectively, with the seat support adjusted according to their body size, following the manufacturer's guidelines. Surface electromyography (sEMG) sensors with integrated accelerometers (Mini Wave Infinity, Cometa Srl, Milan, Italy) were affixed to the subjects' skin to measure muscle activity from the left and right m. iliopsoas (IP) at 2 kHz, as per [400]. Additionally, a third sEMG sensor was placed on the VEMOTION control console and manually tapped at the beginning and end of each protocol stage for easier post-processing and temporal alignment of sEMG and VEMOTION data. The initialization protocol recommended by the manufacturer was followed, and the therapy settings were configured as follows: bed tilt angle 50°, hip flexion/extension range of motion (ROM) from 0° to 25°, and a step frequency of 30 per minute. Each data collection session commenced with a calibration phase, during which the subject was instructed to fully relax, the VEMOTION was set to full (100%) support, and data were collected from three complete left and right steps. Following this, the AAN setting (introduced in Section 4.3) was initialized. Subjects were instructed to actively participate for approximately 30 seconds, simulate fatigue (i.e., decrease active participation) for about 30 seconds, and finally return to full active participation for another 30 seconds. The same procedure was followed using the standard therapy setting.

The protocol for the patient experiments mirrored that of the healthy subjects. The therapist determined the robotic end effector range of motion (ROM) based on the patient's hip ROM. Robot-supported leg movement commenced with full support, and the patient's bed was horizontal. The therapist gradually adjusted the bed angle to the highest setting the patient could tolerate on that day, guided by the therapist's professional judgment. The final settings were as follows: bed tilting angle 30° (patient 1), 25° (patient 2), hip flexion/extension range of motion between 0° and 25° (both patients) and step frequency 20 per minute (both patients). Four active trials were conducted for each patient, two using the full support setting and two utilizing the AAN setting. The order of the trials alternated, starting with full support. In each trial, patients were instructed to actively engage in the movement as much as possible. Instructions were kept consistent across therapy types. After approximately one minute (corresponding to approximately 8 to 16 steps per leg), patients were allowed to relax. For AAN trials, the full support setting was reinstated. Patients were granted about a 3-minute break between each active trial. Once all trials were completed, the bed angle was reverted to the horizontal position, concluding the therapy session.

Metrics Derivation

The performance participation metrics were calculated exclusively for the flexion motion. Therefore, for each cycle, the joint velocities at t_{start} and t_{end} are zero. Additionally, due to kinematic constraints, the leg configuration, and thus $S_{h,l,\text{start}}$ and $S_{h,l,\text{end}}$ in (5.35), can be assumed to remain constant at these times across iterations. Finally, given the assumption of only one connection point between the robot and the leg (i.e., $n_r = 1$), (5.33) can be modified according to

$$W_{h,\text{ext},f} = -\int_{t_{\text{start},f}}^{t_{\text{end},f}} \dot{\boldsymbol{x}}^T \boldsymbol{f}_{\text{ext}} \, dt, \tag{5.40}$$

where $t_{\text{start},f}$ and $t_{\text{end},f}$ represent the start and end time stamps for each flexion motion, respectively. Finally, the energy-based robot-measured patient performance estimation metric used in the experiments is derived as

$$\hat{W}_{m,\text{rob}} = W^{\dagger}_{h,\text{ext},f} - W_{h,\text{ext},f}, \tag{5.41}$$

where $W^{\dagger}_{h,\text{ext},f}$ is the work performed by the robot on the patient at the calibration stage.

In the EMG-based metric, the initial step involves muscle selection. Due to the kinematic constraint at the foot in the VEMOTION system, hip and knee joint flexion (or extension) are inherently coupled, limiting the effectiveness of bi-articular muscles such as m. rectus femoris (RF) and m. biceps femoris (BF) during VEMOTION therapy. Notably, the activation patterns of these muscles are observed to be highly inconsistent between subjects during VEMOTION therapy, even among healthy subjects [348]. Considering this evidence and preliminary experiments, it is assumed that the stepping motion primarily involves hip flexion- and extension-specific single-joint muscles. Surface EMG measurement of hip extensors, such as m. gluteus maximus is not feasible with the VEMOTION setup. Consequently, the focus here was to estimate hip flexion work by measuring EMG from an accessible hip flexion-specific muscle group, namely the m. iliopsoas (IP) [400]. For practical purposes, this also requires the assumption of minimal co-activation of antagonist muscles during hip flexion. A preliminary evaluation of the m. iliacus and the m. psoas muscles using a state-of-the-art musculoskeletal model [401] indicates that $\bar{l}_{mf,IP} \in [0.83, 1.0]$ and $\dot{\bar{l}}_{mf,IP} \in [-0.026, 0]$ for the lumped IP, during the hip flexion motion cycle. As mentioned before, a rigid tendon is assumed here, allowing $\bar{l}_{mf,IP}$ and $\dot{\bar{l}}_{mf,IP}$ to be directly estimated from the hip flexion angle $q_{h,1}(t)$. Further, in the experiments, $\hat{a}_m$ in (5.38) is estimated directly from the root mean square (RMS) of the m. iliopsoas sEMG measurement. At this stage, the values of parameters κ_m, $\hat{a}_{m,0}$, and $f_{ma,\max}$ were unknown for a given muscle and sensor setup. However, given that the flexion motion is primarily driven by the m. iliopsoas, i.e., a single muscle group, the correlation between $\hat{W}_{m,\text{rob}}$ and $\hat{W}_{m\text{emg}}$ is minimally affected by the

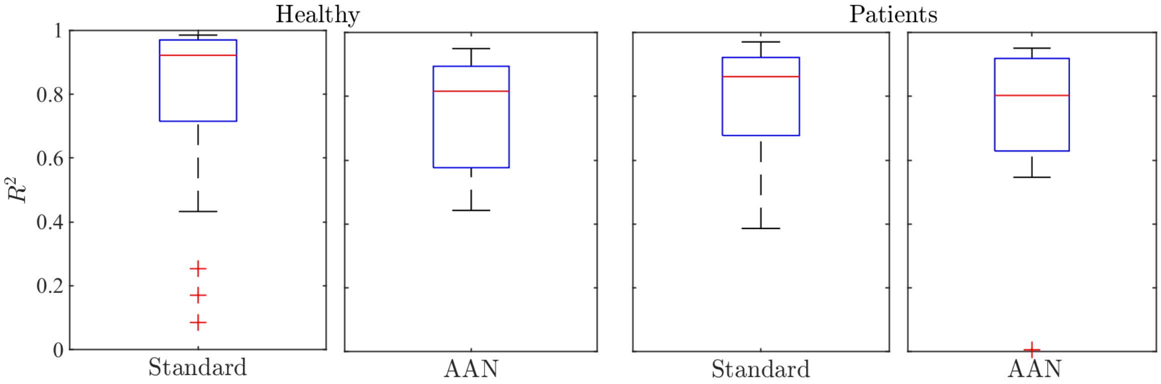

Figure 5.19: Distribution statistics depicting the correlation between $\hat{W}^*m,\mathrm{emg}$ and $\hat{W}m,\mathrm{rob}$ are calculated for each subject, side, and trial individually. Outliers are visually marked with red crosses for clarity.

choice of parameters[4]. Thus, in the first step, an intermediate version of the EMG-based metric—namely the pseudo-metric—is calculated according to (5.37) and (5.39), as

$$\hat{W}^*_{m,\mathrm{emg}} = \int_{t_{\mathrm{start}},f}^{t_{\mathrm{end}},f} \hat{a}_m \ \Gamma_{m,IP} \ dt, \tag{5.42}$$

with

$$\Gamma_{m,IP} = f(\bar{l}_{mf,IP}, \dot{\bar{l}}_{mf,IP}) \dot{l}_{m,IP}. \tag{5.43}$$

Note that (5.42) is equivalent to arbitrarily assuming that $\kappa_m = 1$, $\hat{a}_{m,0} = 0$, and $f_{ma,\max} = 1$. Here, the standard shape parameters reported in [396] are used. In the second step, $\kappa_m f_{ma,\max}$ and $\hat{a}_{m,0} f_{ma,\max}$ for each subject and leg side are estimated by assuming $\hat{W}_{m,\mathrm{rob}} = \hat{W}_{m,\mathrm{emg}}$. For this, by substituting (5.37) and (5.38) into (5.39), the EMG-based metric can be reformulated as

$$\hat{W}_{m,\mathrm{emg}} = \kappa_m \ f_{ma,\max} \hat{W}^*_{m,\mathrm{emg}} \ + \ \hat{a}_{m,0} \ f_{ma,\max} \int_{t_{\mathrm{start}},f}^{t_{\mathrm{end}},f} \Gamma_{m,IP} \ dt. \tag{5.44}$$

Using the data set (i.e., all steps) from each subject and side separately, linear regression is then used to estimate $\kappa_m f_{ma,\max}$ and $\hat{a}_{m,0} f_{ma,\max}$, corresponding to that muscle and sensor setup. Finally, $\hat{W}_{m,\mathrm{emg}}$ is calculated for each subject (healthy or patient), side, therapy type, and step.

Results

The goal of these experiments has been to validate the new energy-based robot-measured metric by demonstrating its strong correlation with the EMG-based metric. For this purpose, the energy-based metric $\hat{W}_{m,\mathrm{rob}}$ is computed according to (5.41) for each subject (healthy

---

[4] Note that this only holds for a given muscle and sensor setup. A more precise estimate of κ_m, $\hat{a}_{m,0}$, and $f_{ma,\max}$ is required for inter-subject comparison.

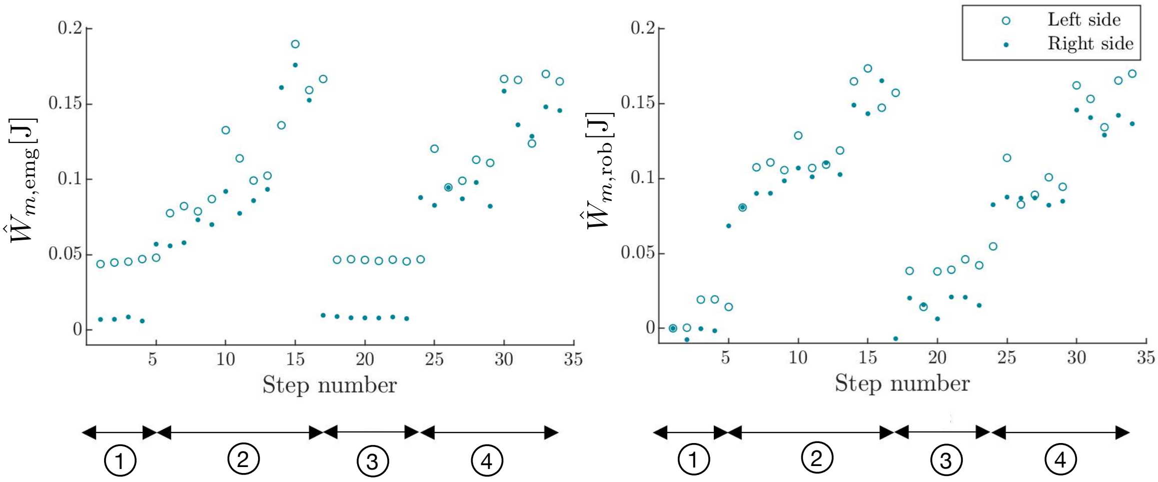

Figure 5.20: Measured metrics $\hat{W}_{m,\mathrm{rob}}$ and $\hat{W}_{m,\mathrm{emg}}$ from one healthy subject performing the AAN trial are shown. In the calibration stage ① and stage ③, the subject was instructed to be passive and let the robot move their leg. In stages ② and ④, the subject was instructed to actively participate in the motion.

or patient), side, and therapy type. Simultaneously, the EMG-based metrics $\hat{W}^{*}_{m,\mathrm{emg}}$ and $\hat{W}_{m,\mathrm{emg}}$ are determined following (5.42) and (5.44). Subsequently, the coefficient of determination R^2 is calculated between $\hat{W}_{m,\mathrm{rob}}$ and $\hat{W}^{*}_{m,\mathrm{emg}}$ for each subject and side individually. The range of R^2 values varies from 0.43 to 0.99 (excluding outliers) for standard therapy and from 0.44 to 0.95 for the AAN therapy, both with a P-value of $p < 0.01$. Similar trends are observed in the patient data, with R^2 ranging from 0.39 to 0.97 for standard therapy and from 0.55 to 0.95 (excluding outliers) for the AAN therapy ($p < 0.05$); refer to Figure 5.19.

When the data from $\hat{W}_{m,\mathrm{rob}}$ and $\hat{W}_{m,\mathrm{emg}}$ are combined for all twelve healthy subjects, R^2 is determined to be 0.93 for the standard therapy case (excluding data from the three outlier trials seen in Figure 5.19) and 0.86 for the AAN therapy case ($p < 0.001$). In the case of combined patient data, R^2 is 0.77 for the standard therapy data and 0.92 for the AAN therapy data ($p < 0.001$, excluding data from the outlier trial seen in Figure 5.19); refer to Figure 5.21. For further verification, the two metrics are illustrated for a representative example of a healthy subject AAN trial in Figure 5.20. During the stages when the subject was instructed to be passive, the work performed by the subject, estimated by both $\hat{W}_{m,\mathrm{rob}}$ and $\hat{W}_{m,\mathrm{emg}}$, is very low. During the stages when the subject was instructed to participate actively, the work, as estimated with each independent metric, increases with each step. Similar results are found for all subjects.

5.3.4 Validation of the Support-Adaptive Rehabilitation Therapy

As detailed earlier, the clinical results demonstrate a strong correlation between the proposed robot-measured energy-based metrics and the EMG-based metrics. However, another significant outcome emerges from the results. The clinical experiments are conducted using both the pure impedance control with a cyclic trajectory and the Assist-As-Needed (AAN) policy, as proposed in Section 4.3. This innovative support-adaptive rehabilitation therapy

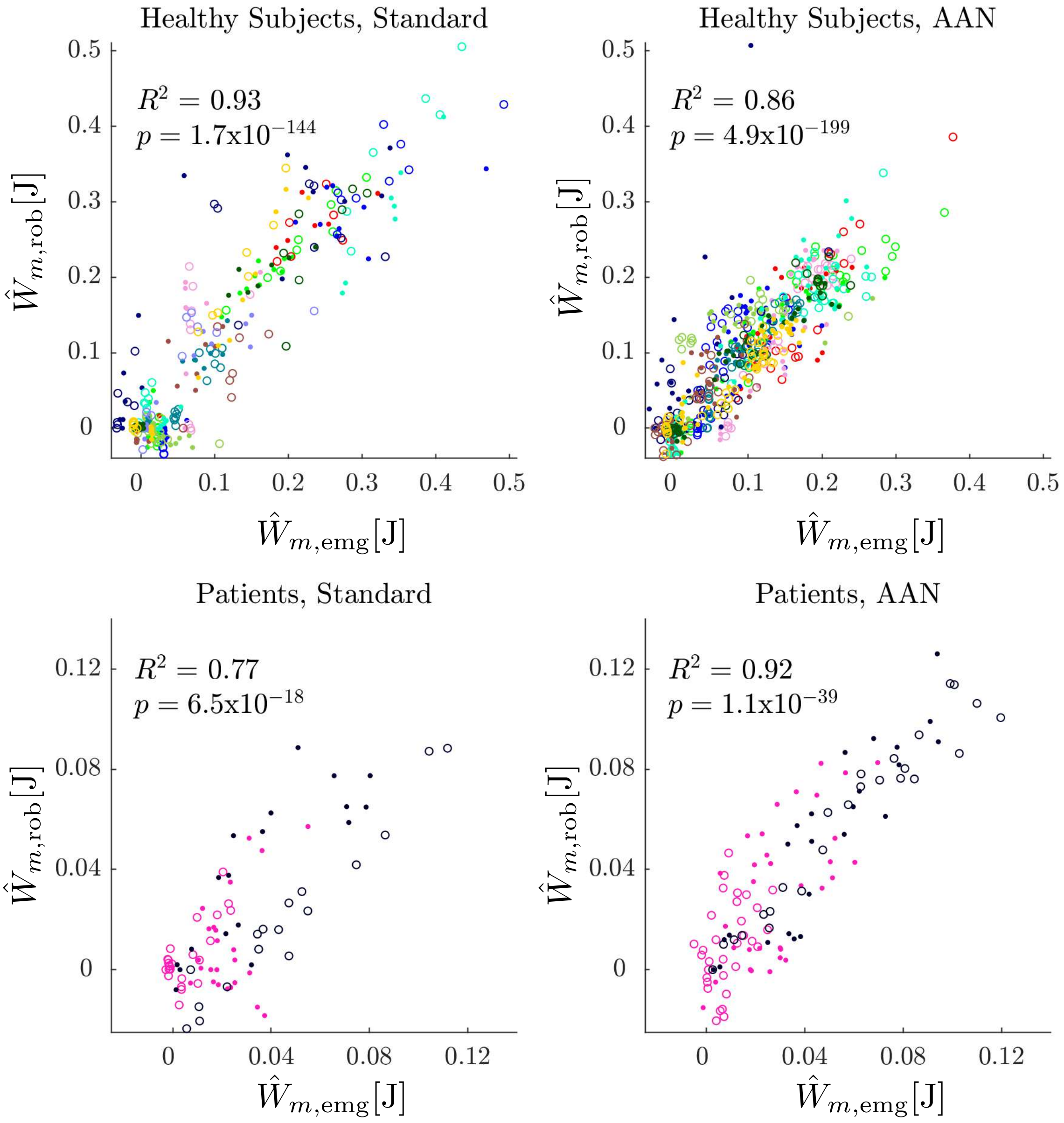

Figure 5.21: Comparison between $\hat{W}_{m,\text{emg}}$ and $\hat{W}_{m,\text{rob}}$ for all steps of all healthy subjects and patients using the standard therapy and the AAN therapy settings. A distinct color uniquely represents each subject. The right leg data is depicted with closed circles, while the left leg data is represented with open circles.

is fully integrated into the VEMOTION system, and the conducted experiments represent among the very first clinical studies on this therapy. Referring to Figure 5.20, it is evident that as the robot's support level decreases, the subject's engagement in the therapy increases. This phenomenon is observable using both robot-based and EMG-based metrics. As discussed in Section 4.3, a patient's active participation in the rehabilitation motion can enhance the recovery process. Thus, employing such support-adaptive methods can improve therapy outcomes. Currently, larger clinical studies are in progress as a continuation of this dissertation to further validate the long-term effectiveness of the proposed AAN policy.

6 Conclusion

This dissertation focuses on the challenge of constructing a modular planning and control framework for manipulation and physical interaction. The approach taken involves the development of symbiotic force-motion controllers and policies grounded and interconnected in the fabric of the energy-based paradigm. The interplay between force, motion, and energy serves as the construction principle of elementary modules that, when interconnected, show the remarkable ability to even solve extremely challenging problems. The primary goal in formulating the proposed framework has been to derive and employ a minimal set of such fundamental building blocks, fostering the creation of intuitive and robust solutions with enhanced generalizability and extendability. This claim is supported by extensive experimental and translational results.

At the core of the proposed framework is a control law built upon the generalization of the Unified Force-Impedance Control (UFIC), addressing the common limitations inherent in conventional methods for the simultaneous control of force and motion. By eliminating the need for a precise environment or task model, this fundamental building module adeptly facilitates diverse real-world applications when deploying tailored force-motion policies, as demonstrated in various industrial scenarios, including polishing and filing of unmodelled objects. Furthermore, the dissertation demonstrates the extension of UFIC to address more intricate objectives, including multi-manual object manipulation, where a modular single-arm control framework is developed, enabling the seamless addition or removal of arms on the fly—a feature lacking in conventional approaches. Finally, for scenarios where the developed force-motion policies cannot be directly commanded to the controller (e.g. when employing an impedance controller accepting only motion commands), a novel class of Dynamic Movement Primitives (DMP), namely Admittance-Coupled DMPs, is introduced, enabling the integration of force and motion trajectories into a motion policy. Unlike similar methods, the employed coupling term has a clear physical interpretation, facilitating enhanced stability analysis and fine-tuning.

The systematic methodology used to construct the proposed architecture is grounded in the port-Hamiltonian framework, which elegantly accommodates the application of passivity-based modeling and control approaches. In this paradigm, the overall system can be conceptualized as the interconnection of energy capsules through ports. Utilizing such energy-based modeling not only enables an intuitive stabilization process through passivity analysis and virtual tank augmentation methods but also fosters several advancements in classical energy-aware manipulation control. In this context, the dissertation expands upon the traditional notion of virtual energy tanks by introducing the concept of valves. Valve-Based Energy Tanks allow for the regulation of energy flow. This feature not only mitigates the typical abrupt impact when the tanks are empty but also enables the pursuit of additional energy-based objectives, such as prioritizing actions while concurrently executing the primary task. Furthermore, with the goal of facilitating robust physical interactions with unknown environments, the dissertation introduces innovative approaches centered around the concept of reference energy budget, ranging from model-based estimation techniques to iterative learning control and imitation learning methods. The energy-aware control framework provides an intuitive and straightforward means to monitor the performance of tactile manipulation tasks from the perspective of energy evolution. Illustrated through the exemplary medical application in rehabilitation, this capability eliminates the necessity for sophisticated sensors, which may not always be readily deployable in settings such as Intensive Care Units.

Built upon the core control block and following the port-based construction methodology, the dissertation further expands the framework by developing policies that address more intricate scenarios involving human-in-the-loop interactions. To achieve this, the policies are equipped with ports through which human input can be conveyed. Additionally, to address complex scenarios involving geometric constraints, the framework is minimally extended by incorporating new elements, such as phase, which reduces the planning space. These steps led to the development of several novel phase-based reactive policies capable of addressing challenges such as collision avoidance with human's intended body parts in confined spaces. In another class of systems, a modular path-constrained haptic motion guidance policy is developed, featuring online adaptation capabilities to address objectives such as ergonomics. In this context, the concept of a Manipulability Pseudo-Ellipsoid is introduced as a robust ergonomics assessment method specifically designed for systems like the human body. Among the various human-centered algorithms developed in this dissertation, a particularly impactful contribution lies in the application of robot-aided movement rehabilitation. In this regard, an innovative support-adaptive policy is developed, capable of adjusting and learning the appropriate level of robot assistance along the therapeutic path while also enhancing the permissive characteristic of the robot. This, in turn, may promote the patient's active participation and, consequently, enhance the recovery process. This patented approach has been commercialized and successfully integrated into a lower-limb rehabilitation robot, now extensively utilized in clinics worldwide. Its effectiveness has been corroborated through numerous clinical studies and surveys, including one conducted as part of this dissertation. The notable success of this approach, highlighting the scalability of the proposed framework, has been recognized with multiple national and international awards, including the prestigious 2021 euRobotics Technology Transfer Award for the best research-based commercialized technology in Europe.

In essence, this dissertation systematically constructs a framework based on fundamental concepts of physics, encompassing force, motion, and energy. The resulting advancements in passivity-based planning and control not only enhance the stability and robustness of the proposed solutions but also enable the energy-based shaping of physical interactions in accordance with the manipulation objectives. The developed robust controllers are not constrained by typical limitations, rendering them suitable for real-world applications where unforeseen disturbances are inevitable. The array of proposed policy modules adeptly tackles diverse, complex scenarios involving both human and geometric constraints in an intuitive manner, requiring a minimal number of involved variables. The development of each framework component brought about theoretical contributions that led to novel practical applications in tactile manipulation. These applications feature increased modularity and robustness, making them suitable for real-world settings. The developed components underwent individual verification through extensive experiments, clinical and user studies, demonstrations, and commercialized setups within the scope of numerous national and international research projects. The dissertation introduces theoretical concepts, including the generalized UFIC and the support-adaptive rehabilitation policy, which have successfully translated into practical industrial setups, showcasing the real-life effectiveness of the proposed framework.

Despite the numerous impacts, the utilized construction approach could be further employed to expand the proposed framework readily, addressing objectives not directly tackled in the dissertation. The construction methodology is grounded in physics concepts, providing high scalability of solutions, and at the same time, it adopts a minimalist approach, enabling intuitive adjustments for new objectives without necessitating an in-depth understanding of the field. This physics-based minimalism significantly enhances generalizability by reducing the search space, particularly when employing data-driven approaches. This feature is crucial, as the generation of real-world tactile manipulation data involves executing actual physical actions, thereby rendering the data generation process exceptionally costly compared to other data types.

Future Work

The proposed constructive approach can ultimately serve as a foundation for data-driven methods, enabling a generative framework capable of automatically generalizing to diverse manipulation objectives. This can be accomplished both for developing and tuning the framework components or for determining optimized sequences, e.g., behavior trees, of differently-tuned frameworks. These explorations will serve as the primary next step.

From a stability standpoint, the passivity of all proposed solutions was verified, ensuring that the system would not indefinitely diverge from and would eventually converge to the equilibrium state. What was not addressed, however, was the rate of convergence. In future work, stability will be considered beyond simply proving passivity, with an emphasis on achieving faster convergence to the desired equilibrium states.

A substantial part of future work will focus on deploying and translating the proposed concepts (excluding those already undergone) into real-life setups. In this regard, the multi-manual object manipulation control framework will be implemented on an artificial hand, with each finger representing an individual arm. Additionally, vision-based grasping policies will be developed as a pre-stage of the object manipulation task. In another aspect, the path-constrained haptic motion guidance will be implemented on relevant setups, such as assistive surgical robots, with the aim of leveraging the strength and accuracy of robots under the supervision of the human operator.

Finally, as extensive clinical studies are currently in progress to analyze the long-term effects of the proposed innovative support-adaptive robot-aided rehabilitation therapy, further refinement is planned. This involves incorporating physiological aspects such as biomechanics and human neural motor control, with a specific focus on concepts like stereotypical human motions, submovements, and abnormal synergies [402–404]. These concepts can also serve as a foundational idea for developing efficient policies, such as motion generators, within the proposed framework.

The unified force-impedance control (Section 3.1) enables robust performance in manipulation tasks involving physical interactions, overcoming classical stability-related limitations.

The direction-dependent compliance adaptation law (Section 3.2) allows for the dynamic addition/removal of robots on the fly, enabling scalable, multi-manual object manipulation.

The phase-based haptic motion generator (Section 4.2) facilitates the fusion of robot precision and strength with human supervision for movements within geometric constraints.

The robot's capacity to iteratively adjust its support and permissiveness features (Section 4.3) can enhance rehabilitation therapy, while its energy-based performance monitoring metric (Section 5.3) can increase accessibility.

Bibliography

[1] David Arranz, Stefano Bianchini, Valentina Di Girolamo, and Julien Ravet. “Trends in the use of AI in science: a bibliometric analysis”. *European Commission*, 2023.

[2] Nestor Maslej, Loredana Fattorini, Erik Brynjolfsson, John Etchemendy, Katrina Ligett, Terah Lyons, James Manyika, Helen Ngo, Juan Carlos Niebles, Vanessa Parli, Yoav Shoham, Russell Wald, Jack Clark, and Raymond Perrault. “The AI index 2023 annual report”. *Institute for Human-Centered AI, Stanford University*, 2023.

[3] International Federation of Robotics. “World robotics report 2023”. —, 2023.

[4] World Economic Forum. “The future of jobs report 2018”. —, 2018.

[5] Bergur Thormundsson. “Global robotics revenue 2016-2028, by category”. *Statistica*, 2023.

[6] Bergur Thormundsson. “Artificial intelligence (AI) market size/revenue comparisons 2018-2030”. *Statistica*, 2023.

[7] World Economic Forum and Frontiers Science News. “Top 10 emerging technologies of 2023”. —, 2023.

[8] Group of 20. “G20 New Delhi leaders’ declaration”. —, 2023.

[9] Group of 7. “G7 leaders’ statement on the Hiroshima AI process”. —, 2023.

[10] Robert Riener, Luca Rabezzana, and Yves Dominic Zimmermann. “Do robots outperform humans in human-centered domains?”. *Frontiers in Robotics and AI*, 2023.

[11] Aafke Eppinga. “Work productivity is stagnating; do we expect too much from new technologies?”. *Innovation Origins*, 2023.

[12] Klaas de Vries. “Global productivity brief 2023”. *The Conference Board, Inc.*, 2023.

[13] Charles Atkins, Olivia White, Asutosh Padhi, Kweilin Ellingrud, Anu Madgavkar, and Michael Neary. “Rekindling US productivity for a new era”. *McKinsey Global Institute*, 2023.

[14] Jonathan Haskel and Christopher Martin. “Do skill shortages reduce productivity? theory and evidence from the United Kingdom”. *The Economic Journal*, 103(417):386–394, 1993.

[15] Korn Ferry. “Future of work, the global talent crunch”. —, 2018.

[16] European Commission. “Employment and social developments in Europe; addressing labour shortages and skills gaps in the EU - annual review”. *Publications Office of the European Union*, 2023.

[17] Blake Moret. “Can automation pull us through the global labour shortage?”. *World Economic Forum*, 2023.

[18] Neville Hogan. “Impedance control: An approach to manipulation”. *ASME Journal of Dynamic Systems, Measurement, and Control*, 107:1–24, 1985.

[19] J Kenneth Salisbury. “Active stiffness control of a manipulator in cartesian coordinates”. *IEEE Conference on Decision and Control Including the Symposium on Adaptive Processes*, pages 95–100, 1980.

[20] Daniel E Whitney. “Force feedback control of manipulator fine motions”. *ASME Journal of Dynamic Systems, Measurement, and Control*, 1977.

[21] Ewald Lutscher, Emmanuel C Dean-León, and Gordon Cheng. “Hierarchical force and positioning task specification for indirect force controlled robots”. *IEEE Transactions on Robotics*, 2017.

[22] Steven Eppinger and Warrenp Seering. “Understanding bandwidth limitations in robot force control”. *IEEE International Conference on Robotics and Automation*, 4:904–909, 1987.

[23] Ganwen Zeng and Ahmad Hemami. “An overview of robot force control”. *Robotica*, 15(05):473–482, 1997.

[24] Luigi Villani and Joris De Schutter. “Force control”. *Springer Handbook of Robotics*, pages 161–185, 2016.

[25] Richard Volpe and Pradeep Khosla. “The equivalence of second-order impedance control and proportional gain explicit force control”. *The International Journal of Robotics Research*, 14(6):574–589, 1995.

[26] Justin Won, Stefano Stramigioli, and Neville Hogan. “Comment on the equivalence of second-order impedance control and proportional gain explicit force control”. *The International Journal of Robotics Research*, 16(6):873–875, 1997.

[27] Daniel E Whitney. “Historical perspective and state of the art in robot force control”. *The International Journal of Robotics Research*, 6(1):3–14, 1987.

[28] Marc H Raibert and John J Craig. “Hybrid position/force control of manipulators”. *Journal of Dynamic Systems, Measurement, and Control*, 1981.

[29] Oussama Khatib and Joel Burdick. “Motion and force control of robot manipulators”. *IEEE International Conference on Robotics and Automation*, 3:1381–1386, 1986.

[30] Oussama Khatib. “A unified approach for motion and force control of robot manipulators: The operational space formulation”. *IEEE Journal on Robotics and Automation*, 3(1):43–53, 1987.

[31] Tsuneo Yoshikawa. “Dynamic hybrid position/force control of robot manipulators–description of hand constraints and calculation of joint driving force”. *IEEE Journal on Robotics and Automation*, 3(5):386–392, 1987.

[32] Chae H An and John M Hollerbach. “Dynamic stability issues in force control of manipulators”. *American Control Conference*, pages 821–827, 1987.

[33] William D Fisher and M Shahid Mujtaba. “Hybrid position/force control: A correct formulation”. *The International Journal of Robotics Research*, 11(4):299–311, 1992.

[34] Robert J Anderson and Mark W Spong. “Hybrid impedance control of robotic manipulators”. *IEEE Journal on Robotics and Automation*, 4(5):549–556, 1988.

[35] Karen Bodie, Maximilian Brunner, Michael Pantic, Stefan Walser, Patrick Pfändler, Ueli Angst, Roland Siegwart, and Juan Nieto. “Active interaction force control for contact-based inspection with a fully actuated aerial vehicle”. *IEEE Transactions on Robotics*, 37(3):709–722, 2020.

[36] Maximilian Brunner, Livio Giacomini, Roland Siegwart, and Marco Tognon. “Energy tank-based policies for robust aerial physical interaction with moving objects”. *IEEE International Conference on Robotics and Automation*, pages 2054–2060, 2022.

[37] Chun-Yi Su, Tin-Pui Leung, and Qi-Jie Zhou. “Force/motion control of constrained robots using sliding mode”. *IEEE Transactions on Automatic Control*, 37(5):668–672, 1992.

[38] Gerd Hirzinger. “Direct digital robot control using a force-torque sensor”. *IFAC Proceedings Volumes*, 16(1):243–255, 1983.

[39] Joris De Schutter and Hendrik Van Brussel. “Compliant robot motion II. A control approach based on external control loops”. *The International Journal of Robotics Research*, 7(4):18–33, 1988.

[40] Fernando Almeida, António Lopes, and Paulo Abreu. “Force-impedance control: a new control strategy of robotic manipulators”. *Recent Advances in Mechatronics*, 1:126–137, 1999.

[41] António Lopes and Fernando Almeida. “A force–impedance controlled industrial robot using an active robotic auxiliary device”. *Robotics and Computer-Integrated Manufacturing*, 24(3):299–309, 2008.

[42] Alexander Dietrich and Neville Hogan. “Control of physical interaction”. *Encyclopedia of Robotics*, pages 1–7, 2022.

[43] Oussama Khatib. “The operational space formulation in the analysis, design, and control of robot manipulators”. *International Symposium of Robotics Research*, pages 7–11, 1985.

[44] Matthew T Mason. “Compliance and force control for computer controlled manipulators”. *IEEE Transactions on Systems, Man, and Cybernetics*, 11(6):418–432, 1981.

[45] Joseph Duffy. “The fallacy of modern hybrid control theory that is based on orthogonal complements of twist and wrench spaces”. *Journal of Robotic Systems*, 7(2):139–144, 1990.

[46] Richard P Paul. “Problems and research issues associated with the hybrid control of force and displacement”. *Workshop on Space Telerobotics*, 3, 1987.

[47] Siciliano Chiaverini, Bruno Siciliano, and Luigi Villani. “A stable force/position controller for robot manipulators”. *IEEE Conference on Decision and Control*, pages 1869–1874, 1992.

[48] Stefano Chiaverini and Lorenzo Sciavicco. “The parallel approach to force/position control of robotic manipulators”. *IEEE Transactions on Robotics and Automation*, 9(4):361–373, 1993.

[49] Stefano Chiaverini, Bruno Siciliano, and Luigi Villani. “Force and position tracking: Parallel control with stiffness adaptation”. *IEEE Control Systems Magazine*, 18(1):27–33, 1998.

[50] Bruno Siciliano. “Parallel force/position control of robot manipulators”. *Springer Robotics Research*, pages 78–89, 1996.

[51] Joris De Schutter, Herman Bruyninckx, Wen-Hong Zhu, and Mark W Spong. “Force control: A bird’s eye view”. *Control Problems in Robotics and Automation*, pages 1–17, 1998.

[52] Harry West and Haruhiko Asada. “A method for the design of hybrid position/force controllers for manipulators constrained by contact with the environment”. *IEEE International Conference on Robotics and Automation*, 2:251–259, 1985.

[53] Mehrzad Namvar and Farhad Aghili. “Adaptive force-motion control of coordinated robots interacting with geometrically unknown environments”. *IEEE Transactions on Robotics*, 21(4):678–694, 2005.

[54] Zoe Doulgeri and Yiannis Karayiannidis. “Force position control for a robot finger with a soft tip and kinematic uncertainties”. *Robotics and Autonomous Systems*, 55(4):328–336, 2007.

[55] Yiannis Karayiannidis and Zoe Doulgeri. “Adaptive control of robot contact tasks with on-line learning of planar surfaces”. *Automatica*, 45(10):2374–2382, 2009.

[56] Yinjie Lin, Zheng Chen, and Bin Yao. “Unified motion/force/impedance control for manipulators in unknown contact environments based on robust model-reaching approach”. *IEEE/ASME Transactions on Mechatronics*, 26(4):1905–1913, 2021.

[57] Jamie Hathaway, Alireza Rastegarpanah, and Rustam Stolkin. “Learning robotic milling strategies based on passive variable operational space interaction control”. *IEEE Transactions on Automation Science and Engineering*, 2023.

[58] Michael Dyck, Arne Sachtler, Julian Klodmann, and Alin Albu-Schäffer. “Impedance control on arbitrary surfaces for ultrasound scanning using discrete differential geometry”. *IEEE Robotics and Automation Letters*, 7(3):7738–7746, 2022.

[59] Neville Hogan. “Impedance control of industrial robots”. *Robotics and Computer-Integrated Manufacturing*, 1(1):97–113, 1984.

[60] Ryuta Ozawa and Kenji Tahara. “Grasp and dexterous manipulation of multi-fingered robotic hands: a review from a control view point”. *Advanced Robotics*, 31(19-20):1030–1050, 2017.

[61] Stanleya Schneider and Robert H Cannon. “Object impedance control for cooperative manipulation: Theory and experimental results”. *International Conference on Robotics and Automation*, pages 1076–1083, 1989.

[62] Fabrizio Caccavale, Pasquale Chiacchio, Alessandro Marino, and Luigi Villani. “Six-dof impedance control of dual-arm cooperative manipulators”. *IEEE/ASME Transactions On Mechatronics*, 13(5):576–586, 2008.

[63] Hamid Sadeghian, Fanny Ficuciello, Luigi Villani, and Mehdi Keshmiri. “Global impedance control of dual-arm manipulation for safe interaction”. *International Federation of Automatic Control*, 45(22):767–772, 2012.

[64] Jianfeng Gao, You Zhou, and Tamim Asfour. “Projected force-admittance control for compliant bimanual tasks”. *IEEE International Conference on Humanoid Robots*, pages 1–9, 2018.

[65] RC Bonitz and Tien C Hsia. “Internal force-based impedance control for cooperating manipulators”. *IEEE Transactions on Robotics and Automation*, 12(1):78–89, 1996.

[66] Suguru Arimoto, Fumio Miyazaki, and Sadao Kawamura. “Cooperative motion control of multiple robot arms or fingers”. *IEEE International Conference on Robotics and Automation*, 4:1407–1412, 1987.

[67] Jinoh Lee, Pyung Hun Chang, and Rodrigo S Jamisola. “Relative impedance control for dual-arm robots performing asymmetric bimanual tasks”. *IEEE Transactions on Industrial Electronics*, 61(7):3786–3796, 2013.

[68] Thomas Wimbock, Christian Ott, and Gerd Hirzinger. “Impedance behaviors for two-handed manipulation: Design and experiments”. *International Conference on Robotics and Automation*, pages 4182–4189, 2007.

[69] Christian Ott, Máximo A Roa, Florian Schmidt, Werner Friedl, Johannes Englsberger, Robert Burger, Alexander Werner, Alexander Dietrich, Daniel Leidner, Bernd Henze, Oliver Eiberger, Alexander Beyer, Berthold Bäuml, Christoph Borst, and Alin Albu-Schäffer. “Mechanisms and design of DLR humanoid robots”. *Humanoid Robotics: A Reference*, pages 1–26, 2016.

[70] Fuhai Zhang, Jiadi Qu, He Liu, and Yili Fu. “A pose/force symmetric coordination method for a redundant dual-arm robot”. *Assembly Automation*, 2018.

[71] Zhenyu Lu, Panfeng Huang, and Zhengxiong Liu. "Relative impedance-based internal force control for bimanual robot teleoperation with varying time delay". *IEEE Transactions on Industrial Electronics*, 67(1):778–789, 2019.

[72] Darong Huang, Hong Zhan, and Chenguang Yang. "Impedance model-based optimal regulation on force and position of bimanual robots to hold an object". *Complexity*, 2020.

[73] Christian Smith, Yiannis Karayiannidis, Lazaros Nalpantidis, Xavi Gratal, Peng Qi, Dimos V Dimarogonas, and Danica Kragic. "Dual arm manipulation—a survey". *Robotics and Autonomous systems*, 60(10):1340–1353, 2012.

[74] Tsuneo Yoshikawa and Kiyoshi Nagai. "Manipulating and grasping forces in manipulation by multifingered robot hands". *IEEE Transactions on Robotics and Automation*, 7(1):67–77, 1991.

[75] Ian D Walker, Robert A Freeman, and Steven I Marcus. "Analysis of motion and internal loading of objects grasped by multiple cooperating manipulators". *The International Journal of Robotics Research*, 10(4):396–409, 1991.

[76] Sebastian Erhart and Sandra Hirche. "Internal force analysis and load distribution for cooperative multi-robot manipulation". *IEEE Transactions on Robotics*, 31(5):1238–1243, 2015.

[77] Robert G Bonitz and Tien C Hsia. "Robust dual-arm manipulation of rigid objects via palm grasping-theory and experiments". *IEEE International Conference on Robotics and Automation*, 4:3047–3054, 1996.

[78] Joseph M Romano, Kaijen Hsiao, Günter Niemeyer, Sachin Chitta, and Katherine J Kuchenbecker. "Human-inspired robotic grasp control with tactile sensing". *IEEE Transactions on Robotics*, 27(6):1067–1079, 2011.

[79] Seiichi Teshigawara, Takahiro Tsutsumi, Satoru Shimizu, Yosuke Suzuki, Aiguo Ming, Masatoshi Ishikawa, and Makoto Shimojo. "Highly sensitive sensor for detection of initial slip and its application in a multi-fingered robot hand". *IEEE International Conference on Robotics and Automation*, pages 1097–1102, 2011.

[80] Mohsen Kaboli, Kunpeng Yao, and Gordon Cheng. "Tactile-based manipulation of deformable objects with dynamic center of mass". *IEEE-RAS International Conference on Humanoid Robots*, pages 752–757, 2016.

[81] Tsuneo Yoshikawa. "Multifingered robot hands: Control for grasping and manipulation". *Annual Reviews in Control*, 34(2):199–208, 2010.

[82] Ping Hsu. "Coordinated control of multiple manipulator systems". *IEEE Transactions on Robotics and Automation*, 9(4):400–410, 1993.

[83] Tsuneo Yoshikawa. "Control algorithm for grasping and manipulation by multifingered robot hands using virtual truss model representation of internal force". *IEEE International Conference on Robotics and Automation*, 1:369–376, 2000.

[84] Tsuneo Yoshikawa. “Virtual truss model for characterization of internal forces for multiple finger grasps”. *IEEE Transactions on Robotics and Automation*, 15(5):941–947, 1999.

[85] Oussama Khatib, Kazu Yokoi, K Chang, Diego Ruspini, Robert Holmberg, and Arancha Casal. “Coordination and decentralized cooperation of multiple mobile manipulators”. *Journal of Robotic Systems*, 13(11):755–764, 1996.

[86] David Williams and Oussama Khatib. “The virtual linkage: A model for internal forces in multi-grasp manipulation”. *IEEE International Conference on Robotics and Automation*, pages 1025–1030, 1993.

[87] Ning Xi, Tzyh-Jong Tarn, and Antal K Bejczy. “Intelligent planning and control for multirobot coordination: An event-based approach”. *IEEE Transactions on Robotics and Automation*, 12(3):439–452, 1996.

[88] Dong Sun and James K Mills. “Manipulating rigid payloads with multiple robots using compliant grippers”. *IEEE/ASME Transactions on Mechatronics*, 7(1):23–34, 2002.

[89] Tetsuyou Watanabe, Kensuke Harada, Zhongwei Jiang, and Tsuneo Yoshikawa. “Object manipulation under hybrid active/passive closure”. *IEEE International Conference on Robotics and Automation*, pages 1013–1020, 2005.

[90] Daniel Kruse, John T Wen, and Richard J Radke. “A sensor-based dual-arm telerobotic system”. *IEEE Transactions on Automation Science and Engineering*, 12(1):4–18, 2014.

[91] Torsten Kröger. “Literature survey: Trajectory generation in and control of robotic systems”. *Springer*, 2010.

[92] Luigi Villani and Joris De Schutter. “Force control”. *Springer Handbook of Robotics*, pages 195–220, 2016.

[93] Christian Ott, Ranjan Mukherjee, and Yoshihiko Nakamura. “Unified impedance and admittance control”. *IEEE International Conference on Robotics and Automation*, pages 554–561, 2010.

[94] Christian Ott, Ranjan Mukherjee, and Yoshihiko Nakamura. “A hybrid system framework for unified impedance and admittance control”. *Journal of Intelligent and Robotic Systems*, 78:359–375, 2015.

[95] Francesco Cavenago, Lorenzo Voli, and Mauro Massari. “Adaptive hybrid system framework for unified impedance and admittance control”. *Journal of Intelligent & Robotic Systems*, 91:569–581, 2018.

[96] Auke Jan Ijspeert, Jun Nakanishi, and Stefan Schaal. “Movement imitation with nonlinear dynamical systems in humanoid robots”. *IEEE International Conference on Robotics and Automation*, 2:1398–1403, 2002.

[97] Matteo Saveriano, Fares J Abu-Dakka, Aljaž Kramberger, and Luka Peternel. “Dynamic movement primitives in robotics: A tutorial survey”. *The International Journal of Robotics Research*, 2021.

[98] Peter Pastor, Ludovic Righetti, Mrinal Kalakrishnan, and Stefan Schaal. “Online movement adaptation based on previous sensor experiences”. *IEEE/RSJ International Conference on Intelligent Robots and Systems*, pages 365–371, 2011.

[99] Peter Pastor, Mrinal Kalakrishnan, Ludovic Righetti, and Stefan Schaal. “Towards associative skill memories”. *IEEE International Conference on Humanoid Robots*, pages 309–315, 2012.

[100] You Zhou, Martin Do, and Tamim Asfour. “Learning and force adaptation for interactive actions”. *IEEE International Conference on Humanoid Robots*, pages 1129–1134, 2016.

[101] Emre Ugur and Hakan Girgin. “Compliant parametric dynamic movement primitives”. *Robotica*, 38(3):457–474, 2020.

[102] Andrej Gams, Bojan Nemec, Auke Jan Ijspeert, and Aleš Ude. “Coupling movement primitives: Interaction with the environment and bimanual tasks”. *IEEE Transactions on Robotics*, 30(4):816–830, 2014.

[103] Liang Han, Peng Kang, Yongting Chen, Wenfu Xu, and Bing Li. “Trajectory optimization and force control with modified dynamic movement primitives under curved surface constraints”. *IEEE International Conference on Robotics and Biomimetics*, pages 1065–1070, 2019.

[104] ISO. “ISO 10218 robots and robotic devices – safety requirements for industrial robots”. *International Organization for Standardization*, 2011.

[105] ISO. “ISO/TS 15066 robots and robotic devices – collaborative robots”. *International Organization for Standardization*, 2016.

[106] Roni-Jussi Halme, Minna Lanz, Joni Kämäräinen, Roel Pieters, Jyrki Latokartano, and Antti Hietanen. “Review of vision-based safety systems for human-robot collaboration”. *Procedia CIRP*, 72(1):111–116, 2018.

[107] Andrea Maria Zanchettin, Paolo Rocco, Simone Chiappa, and Roberto Rossi. “Towards an optimal avoidance strategy for collaborative robots”. *Robotics and Computer-Integrated Manufacturing*, 59:47–55, 2019.

[108] Sean Murray, Will Floyd-Jones, Ying Qi, Daniel J Sorin, and George Konidaris. “Robot motion planning on a chip”. *Robotics: Science and Systems*, 2016.

[109] Oussama Khatib. “Real-time obstacle avoidance for manipulators and mobile robots”. *IEEE International Conference on Robotics and Automation*, 2:500–505, 1985.

[110] Oussama Khatib. “Real-time obstacle avoidance for manipulators and mobile robots”. *The International Journal of Robotics Research*, 5(1):90–98, 1986.

[111] Fabrizio Flacco, Torsten Kroeger, Alessandro De Luca, and Oussama Khatib. “A depth space approach for evaluating distance to objects”. *Journal of Intelligent and Robotic Systems*, 80(1):7–22, 2015.

[112] Bakir Lacevic, Paolo Rocco, and Andrea Maria Zanchettin. “Safety assessment and control of robotic manipulators using danger field”. *IEEE Transactions on Robotics*, 29(5):1257–1270, 2013.

[113] Dong Hai Phuong Nguyen, Matej Hoffmann, Alessandro Roncone, Ugo Pattacini, and Giorgio Metta. “Compact real-time avoidance on a humanoid robot for human-robot interaction”. *ACM/IEEE International Conference on Human-Robot Interaction*, pages 416–424, 2018.

[114] Federico Vicentini, Nicola Pedrocchi, Matteo Giussani, and Lorenzo Molinari Tosatti. “Dynamic safety in collaborative robot workspaces through a network of devices fulfilling functional safety requirements”. *International Symposium on Robotics*, pages 1–7, 2014.

[115] Christoph Byner, Björn Matthias, and Hao Ding. “Dynamic speed and separation monitoring for collaborative robot applications–concepts and performance”. *Robotics and Computer-Integrated Manufacturing*, 58:239–252, 2019.

[116] Matteo Parigi Polverini, Andrea Maria Zanchettin, and Paolo Rocco. “A computationally efficient safety assessment for collaborative robotics applications”. *Robotics and Computer-Integrated Manufacturing*, 46:25–37, 2017.

[117] Bakir Lacevic and Paolo Rocco. “Kinetostatic danger field-a novel safety assessment for human-robot interaction”. *IEEE/RSJ International Conference on Intelligent Robots and Systems*, pages 2169–2174, 2010.

[118] Matteo Ragaglia, Andrea Maria Zanchettin, and Paolo Rocco. “Trajectory generation algorithm for safe human-robot collaboration based on multiple depth sensor measurements”. *Mechatronics*, 55:267–281, 2018.

[119] Lei Wu, Redwan Alqasemi, and Rajiv Dubey. “Development of smartphone-based human-robot interfaces for individuals with disabilities”. *IEEE Robotics and Automation Letters*, 5(4):5835–5841, 2020.

[120] Kateryna Zinchenko, Chien-Yu Wu, and Kai-Tai Song. “A study on speech recognition control for a surgical robot”. *IEEE Transactions on Industrial Informatics*, 13(2):607–615, 2016.

[121] Meenakshi Gupta, Swagat Kumar, Laxmidhar Behera, and Venkatesh K Subramanian. “A novel vision-based tracking algorithm for a human-following mobile robot”. *IEEE Transactions on Systems, Man, and Cybernetics: Systems*, 47(7):1415–1427, 2016.

[122] Nikolaos Korovesis, Dionisis Kandris, Grigorios Koulouras, and Alex Alexandridis. “Robot motion control via an EEG-based brain-computer interface by using neural networks and alpha brainwaves”. *Electronics*, 8(12):1387, 2019.

[123] Laura Marchal-Crespo, Jan Furumasu, and David J Reinkensmeyer. “A robotic wheelchair trainer: design overview and a feasibility study”. *Journal of Neuroengineering and Rehabilitation*, 7(1):1–12, 2010.

[124] Gao Huang, Jiameng Fan, Weimin Zhang, Tony Xiao, Fei Meng, Marco Ceccarelli, and Qiang Huang. “A master-slave control system for lower limb rehabilitation robot with pedal-actuated exoskeleton”. *IEEE International Conference on Real-time Computing and Robotics*, pages 533–538, 2016.

[125] Jianhong Cui, Sabri Tosunoglu, Rodney Roberts, Carl Moore, and Daniel W Repperger. “A review of teleoperation system control”. *Florida Conference on Recent Advances in Robotics*, pages 1–12, 2003.

[126] Jaeheung Park and Oussama Khatib. “A haptic teleoperation approach based on contact force control”. *The International Journal of Robotics Research*, 25(5-6):575–591, 2006.

[127] Xiao Chen, Lars Johannsmeier, Hamid Sadeghian, Erfan Shahriari, Martin Danneberg, Anselm Nicklas, Fan Wu, Gerhard Fettweis, and Sami Haddadin. “‘On the communication channel in bilateral teleoperation: An experimental study for ethernet, wifi, lte and 5g”. *IEEE/RSJ International Conference on Intelligent Robots and Systems*, pages 7712–7719, 2022.

[128] Peter F Hokayem and Mark W Spong. “Bilateral teleoperation: An historical survey”. *Automatica*, 42(12):2035–2057, 2006.

[129] Yi-Hung Hsieh, Yi-Che Huang, Kuu-Young Young, Chun-Hsu Ko, and Sunil K Agrawal. “Motion guidance for a passive robot walking helper via user’s applied hand forces”. *IEEE Transactions on Human-machine Systems*, 46(6):869–881, 2016.

[130] Xavier Lamy, Frédéric Colledani, Franck Geffard, Yvan Measson, and Guillaume Morel. “Achieving efficient and stable comanipulation through adaptation to changes in human arm impedance”. *IEEE International Conference on Robotics and Automation*, pages 265–271, 2009.

[131] Sami Haddadin, Holger Urbanek, Sven Parusel, Darius Burschka, Jürgen Roßmann, Alin Albu-Schäffer, and Gerd Hirzinger. “Real-time reactive motion generation based on variable attractor dynamics and shaped velocities”. *IEEE/RSJ International Conference on Intelligent Robots and Systems*, pages 3109–3116, 2010.

[132] Sami Haddadin. “Verfahren und vorrichtung zum festlegen eines bewegungsablaufs für einen roboter”. *German Patent, DE102016004841B4*, 2018.

[133] Xiaoyu Wu, Zhijun Li, Zhen Kan, and Hongbo Gao. “Reference trajectory reshaping optimization and control of robotic exoskeletons for human-robot co-manipulation”. *IEEE Transactions on Cybernetics*, 2019.

[134] Zhijun Li, Bo Huang, Zhifeng Ye, Mingdi Deng, and Chenguang Yang. “Physical human-robot interaction of a robotic exoskeleton by admittance control”. *IEEE Transactions on Industrial Electronics*, 65(12):9614–9624, 2018.

[135] Sarra Jlassi, Sami Tliba, and Yacine Chitour. “An online trajectory generator-based impedance control for co-manipulation tasks”. *IEEE Haptics Symposium*, pages 391–396, 2014.

[136] Homayoun Seraji. “Adaptive admittance control: An approach to explicit force control in compliant motion”. *IEEE International Conference on Robotics and Automation*, pages 2705–2712, 1994.

[137] Arvid QL Keemink, Herman van der Kooij, and Arno HA Stienen. “Admittance control for physical human-robot interaction”. *The International Journal of Robotics Research*, 37(11):1421–1444, 2018.

[138] Daniel Reyes-Uquillas and Tesheng Hsiao. “Safe and intuitive manual guidance of a robot manipulator using adaptive admittance control towards robot agility”. *Robotics and Computer-Integrated Manufacturing*, 70:102127, 2021.

[139] Kevin Haninger, Marcel Radke, Axel Vick, and Jörg Krüger. “Towards high-payload admittance control for manual guidance with environmental contact”. *IEEE Robotics and Automation Letters*, 7(2):4275–4282, 2022.

[140] Davide Bazzi, Giorgio Priora, Andrea Maria Zanchettin, and Paolo Rocco. “RRT* and goal-driven variable admittance control for obstacle avoidance in manual guidance applications”. *IEEE Robotics and Automation Letters*, 7(2):1920–1927, 2022.

[141] Eleonora Mariotti, Emanuele Magrini, and Alessandro De Luca. “Admittance control for human-robot interaction using an industrial robot equipped with a F/T sensor”. *IEEE International Conference on Robotics and Automation*, pages 6130–6136, 2019.

[142] Martín Mujica, Martín Crespo, Mourad Benoussaad, Sergio Junco, and Jean-Yves Fourquet. “Robust variable admittance control for human-robot co-manipulation of objects with unknown load”. *Robotics and Computer-Integrated Manufacturing*, 79:102408, 2023.

[143] Louis B Rosenberg. “The use of virtual fixtures as perceptual overlays to enhance operator performance in remote environments.”. *Center for Design Research, Stanford University*, 1992.

[144] Louis B Rosenberg. “Virtual fixtures: Perceptual tools for telerobotic manipulation”. *IEEE Virtual Reality Annual International Symposium*, pages 76–82, 1993.

[145] Vincent Francoise, Anis Sahbani, and Guillaume Morel. “A comanipulation device for orthopedic surgery that generates geometrical constraints with real-time registration on moving bones”. *IEEE International Conference on Robotics and Biomimetics*, pages 38–43, 2011.

[146] Brian C Becker, Robert A MacLachlan, Louis A Lobes, Gregory D Hager, and Cameron N Riviere. “Vision-based control of a handheld surgical micromanipulator with virtual fixtures”. *IEEE Transactions on Robotics*, 29(3):674–683, 2013.

[147] Panadda Marayong, Ming Li, Allison M Okamura, and Gregory D Hager. “Spatial motion constraints: Theory and demonstrations for robot guidance using virtual fixtures”. *IEEE International Conference on Robotics and Automation*, 2:1954–1959, 2003.

[148] Jonathan Cacace, Riccardo Caccavale, Alberto Finzi, and Vincenzo Lippiello. “Variable admittance control based on virtual fixtures for human-robot co-manipulation”. *IEEE International Conference on Systems, Man and Cybernetics*, pages 1569–1574, 2019.

[149] Cristóvao Sousa, Rui Cortesao, and Pedro Queirós. “Compliant comanipulation control for medical robotics”. *IEEE Conference on Human System Interactions*, pages 265–271, 2009.

[150] Vincent Duchaine and Clement M Gosselin. “General model of human-robot cooperation using a novel velocity based variable impedance control”. *Second Joint EuroHaptics Conference and Symposium on Haptic Interfaces for Virtual Environment and Teleoperator Systems*, pages 446–451, 2007.

[151] Susana Sánchez Restrepo, Gennaro Raiola, Joris Guerry, Evelyn D’Elia, Xavier Lamy, and Daniel Sidobre. “Toward an intuitive and iterative 6D virtual guide programming framework for assisted human-robot comanipulation”. *Robotica*, 38(10):1778–1806, 2020.

[152] Gennaro Raiola, Xavier Lamy, and Freek Stulp. “Co-manipulation with multiple probabilistic virtual guides”. *IEEE/RSJ International Conference on Intelligent Robots and Systems*, pages 7–13, 2015.

[153] Dimitrios Papageorgiou, Fotios Dimeas, Theodora Kastritsi, and Zoe Doulgeri. “Kinesthetic guidance utilizing DMP synchronization and assistive virtual fixtures for progressive automation”. *Robotica*, 38(10):1824–1841, 2020.

[154] Davide Bazzi, Filippo Roveda, Andrea Maria Zanchettin, and Paolo Rocco. “A unified approach for virtual fixtures and goal-driven variable admittance control in manual guidance applications”. *IEEE Robotics and Automation Letters*, 6(4):6378–6385, 2021.

[155] Luc D Joly and Claude Andriot. “Imposing motion constraints to a force reflecting telerobot through real-time simulation of a virtual mechanism”. *IEEE International Conference on Robotics and Automation*, 1:357–362, 1995.

[156] Zachary Pezzementi, Allison M Okamura, and Gregory D Hager. “Dynamic guidance with pseudo admittance virtual fixtures”. *IEEE International Conference on Robotics and Automation*, pages 1761–1767, 2007.

[157] Theodora Kastritsi and Zoe Doulgeri. “A passive admittance controller to enforce remote center of motion and tool spatial constraints with application in hands-on surgical procedures”. *Robotics and Autonomous Systems*, 152:104073, 2022.

[158] Alireza Madani, Pouya P Niaz, Berk Guler, Yusuf Aydin, and Cagatay Basdogan. “Robot-assisted drilling on curved surfaces with haptic guidance under adaptive admittance control”. *IEEE/RSJ International Conference on Intelligent Robots and Systems*, pages 3723–3730, 2022.

[159] Wojciech Jastrzebowski. “Outline of ergonomics, i.e. science of work, based on the truths taken from the natural science”. *Centralny Instytut Ochrony Pracy, 1997*, 1857.

[160] Hywel Murrel. “The term ergonomics”. *American Psychologist*, 13(10):602, 1958.

[161] Robert Bridger. “Introduction to ergonomics”. *Crc Press*, 2008.

[162] ISO. “ISO 11228-2, ergonomics — manual handling — part 2: Pushing and pulling”. *International Organization for Standardization, Geneva, Switzerland*, 2007.

[163] Lynn McAtamney and Nigel Corlett. “Rapid upper limb assessment (RULA)”. *Handbook of Human Factors and Ergonomics Methods*, pages 86–96, 2004.

[164] Thomas R Waters, Vern Putz-Anderson, and Arun Garg. “Applications manual for the revised NIOSH lifting equation”. *Centers for Disease Control and Prevention*, 1994.

[165] Sue Hignett and Lynn McAtamney. “Rapid entire body assessment (REBA)””. *Applied Ergonomics*, 31(2):201–205, 2000.

[166] Steven J Moore and Arun Garg. “The strain index: a proposed method to analyze jobs for risk of distal upper extremity disorders”. *American Industrial Hygiene Association Journal*, 56(5):443–458, 1995.

[167] Kosmas Alexopoulos, Dimitris Mavrikios, and George Chryssolouris. “Ergotoolkit: an ergonomic analysis tool in a virtual manufacturing environment”. *International Journal of Computer Integrated Manufacturing*, 26(5):440–452, 2013.

[168] Ingram A Murray and Garth R Johnson. “A study of the external forces and moments at the shoulder and elbow while performing every day tasks”. *Clinical Biomechanics*, 19(6):586–594, 2004.

[169] Arne Aaras, Marvin Dainoff, Ola Ro, and Magne Thoresen. “Can a more neutral position of the forearm when operating a computer mouse reduce the pain level for visual display unit operators? a prospective epidemiological intervention study: part II”. *International Journal of Human-Computer Interaction*, 13(1):13–40, 2001.

[170] Yong-Ku Kong, Dae-Min Kim, Kyung-Sun Lee, and Myung-Chul Jung. “Comparison of comfort, discomfort, and continuum ratings of force levels and hand regions during gripping exertions”. *Applied Ergonomics*, 43(2):283–289, 2012.

[171] Luca Gualtieri, Erwin Rauch, and Renato Vidoni. “Emerging research fields in safety and ergonomics in industrial collaborative robotics: A systematic literature review”. *Robotics and Computer-Integrated Manufacturing*, 67:101998, 2020.

[172] Lefteris Benos, Avital Bechar, and Dionysis Bochtis. “Safety and ergonomics in human-robot interactive agricultural operations”. *Biosystems Engineering*, 200:55–72, 2020.

[173] George Michalos, Jason Spiliotopoulos, Sotiris Makris, and George Chryssolouris. "A method for planning human robot shared tasks". *CIRP Journal of Manufacturing Science and Technology*, 22:76–90, 2018.

[174] Sotiris Makris, Panagiota Tsarouchi, Aleksandros-Stereos Matthaiakis, Athanasios Athanasatos, Xenofon Chatzigeorgiou, Michael Stefos, Konstantinos Giavridis, and Sotiris Aivaliotis. "Dual arm robot in cooperation with humans for flexible assembly". *CIRP Annals*, 66(1):13–16, 2017.

[175] Gilbert Tang and Phil Webb. "The design and evaluation of an ergonomic contactless gesture control system for industrial robots". *Journal of Robotics*, 2018, 2018.

[176] Baptiste Busch, Guilherme Maeda, Yoan Mollard, Marie Demangeat, and Manuel Lopes. "Postural optimization for an ergonomic human-robot interaction". *IEEE/RSJ International Conference on Intelligent Robots and Systems*, pages 2778–2785, 2017.

[177] Linda van der Spaa, Michael Gienger, Tamas Bates, and Jens Kober. "Predicting and optimizing ergonomics in physical human-robot cooperation tasks". *IEEE International Conference on Robotics and Automation*, pages 1799–1805, 2020.

[178] Margaret Pearce, Bilge Mutlu, Julie Shah, and Robert Radwin. "Optimizing makespan and ergonomics in integrating collaborative robots into manufacturing processes". *IEEE Transactions on Automation Science and Engineering*, 15(4):1772–1784, 2018.

[179] Robert W Proctor and Trisha Van Zandt. "Human factors in simple and complex systems". *CRC press*, 2018.

[180] Luka Peternel, Nikos Tsagarakis, and Arash Ajoudani. "Towards multi-modal intention interfaces for human-robot co-manipulation". *IEEE/RSJ International Conference on Intelligent Robots and Systems*, pages 2663–2669, 2016.

[181] Luka Peternel, Cheng Fang, Nikos Tsagarakis, and Arash Ajoudani. "A selective muscle fatigue management approach to ergonomic human-robot co-manipulation". *Robotics and Computer-Integrated Manufacturing*, 58:69–79, 2019.

[182] Wansoo Kim, Jinoh Lee, Luka Peternel, Nikos Tsagarakis, and Arash Ajoudani. "Anticipatory robot assistance for the prevention of human static joint overloading in human-robot collaboration". *IEEE Robotics and Automation Letters*, 3(1):68–75, 2017.

[183] Wansoo Kim, Marta Lorenzini, Pietro Balatti, Phuong DH Nguyen, Ugo Pattacini, Vadim Tikhanoff, Luka Peternel, Claudio Fantacci, Lorenzo Natale, Giorgio Metta, et al. "Adaptable workstations for human-robot collaboration: A reconfigurable framework for improving worker ergonomics and productivity". *IEEE Robotics and Automation Magazine*, 26(3):14–26, 2019.

[184] Antonio Gonzales Marin, Mohammad S Shourijeh, Pavel E Galibarov, Michael Damsgaard, Lars Fritzsch, and Freek Stulp. "Optimizing contextual ergonomics models in human-robot interaction". *IEEE/RSJ International Conference on Intelligent Robots and Systems*, pages 1–9, 2018.

[185] Hideo Hanafusa, Tsuneo Yoshikawa, and Yoshihiko Nakamura. "Analysis and control of articulated robot arms with redundancy". *International Federation of Automatic Control*, 14(2):1927–1932, 1981.

[186] Tsuneo Yoshikawa. "Manipulability of robotic mechanisms". *The International Journal of Robotics Research*, 4(2):3–9, 1985.

[187] Sukhan Lee. "Dual redundant arm configuration optimization with task-oriented dual arm manipulability". *IEEE Transactions on Robotics and Automation*, 5(1):78–97, 1989.

[188] J-P Merlet. "Jacobian, manipulability, condition number and accuracy of parallel robots". *The Journal of Mechanical Design*, 128(1):199–206, 2005.

[189] J Lenarčič, A Umek, and S Savić. "Considerations on human arm workspace and manipulability". *Advances in Robot Kinematics*, pages 161–170, 1991.

[190] Y Tanaka, Naoki Yamada, Ichiro Masamori, and Toshio Tsuji. "Manipulability analysis of lower extremities based on human joint-torque characteristics". *Transactions of the Society of Instrument and Control Engineers*, pages 261–266, 2004.

[191] Yoshiyuki Tanaka, Naoki Yamada, Kazuo Nishikawa, Ichiro Masamori, and Toshio Tsuji. "Manipulability analysis of human arm movements during the operation of a variable-impedance controlled robot". *IEEE/RSJ International Conference on Intelligent Robots and Systems*, pages 1893–1898, 2005.

[192] Yoshiyuki Tanaka, Kazuo Nishikawa, Naoki Yamada, and Toshio Tsuji. "Analysis of operational comfort in manual tasks using human force manipulability measure". *IEEE Transactions on Haptics*, 8(1):8–19, 2014.

[193] Panagiotis K Artemiadis, Pantelis T Katsiaris, Minas V Liarokapis, and Kostas J Kyriakopoulos. "On the effect of human arm manipulability in 3D force tasks: Towards force-controlled exoskeletons". *IEEE International Conference on Robotics and Automation*, pages 3784–3789, 2011.

[194] Luka Peternel, Nikos Tsagarakis, and Arash Ajoudani. "A human-robot co-manipulation approach based on human sensorimotor information". *IEEE Transactions on Neural Systems and Rehabilitation Engineering*, 25(7):811–822, 2017.

[195] Sugeeth Gopinathan, Pouya Mohammadi, and Jochen J Steil. "Improved human-robot interaction: a manipulability based approach". *Workshop on Ergonomic Physical Human-Robot Collaboration*, 2018.

[196] Tadej Petrič and Jan Babič. "Augmentation of human arm motor control by isotropic force manipulability". *IEEE/RSJ International Conference on Intelligent Robots and Systems*, pages 696–701, 2016.

[197] Jan Babič, Tadej Petrič, Luka Peternel, and Jun Morimoto. "Power-augmentation control approach for arm exoskeleton based on human muscular manipulability". *IEEE International Conference on Robotics and Automation*, pages 5929–5934, 2017.

[198] Tadej Petrič, Luka Peternel, Jun Morimoto, and Jan Babič. "Assistive arm-exoskeleton control based on human muscular manipulability". *Frontiers in Neurorobotics*, 13:30, 2019.

[199] Kim Wansoo, Marta Lorenzini, Balatti Pietro, Wu Yuqiang, and Arash Ajoudani. "Towards ergonomic control of collaborative effort in multi-human mobile-robot teams". *IEEE/RSJ International Conference on Intelligent Robots and Systems*, 2019.

[200] Johannes Lachner, Vincenzo Schettino, Felix Allmendinger, Mario Daniele Fiore, Fanny Ficuciello, Bruno Siciliano, and Stefano Stramigioli. "The influence of coordinates in robotic manipulability analysis". *Mechanism and Machine Theory*, 146:103722, 2020.

[201] Johannes Lachner, Felix Allmendinger, Stefano Stramigioli, and Neville Hogan. "Shaping impedances to comply with constrained task dynamics". *IEEE Transactions on Robotics*, 2022.

[202] Toru Tsumugiwa, Ryuichi Yokogawa, and Kei Hara. "Variable impedance control with regard to working process for man-machine cooperation-work system". *IEEE/RSJ International Conference on Intelligent Robots and Systems*, 3:1564–1569, 2001.

[203] Heon Park and JangMyung Lee. "Adaptive impedance control of a haptic interface". *Mechatronics*, 14(3):237–253, 2004.

[204] Isura Ranatunga, Frank L Lewis, Dan O Popa, and Shaikh M Tousif. "Adaptive admittance control for human-robot interaction using model reference design and adaptive inverse filtering". *IEEE Transactions on Control Systems Technology*, 25(1):278–285, 2016.

[205] Zhijun Li, Junqiang Liu, Zhicong Huang, Yan Peng, Huayan Pu, and Liang Ding. "Adaptive impedance control of human-robot cooperation using reinforcement learning". *IEEE Transactions on Industrial Electronics*, 64(10):8013–8022, 2017.

[206] Luka Peternel, Cheng Fang, Nikos Tsagarakis, and Arash Ajoudani. "Online human muscle force estimation for fatigue management in human-robot co-manipulation". *IEEE/RSJ International Conference on Intelligent Robots and Systems*, pages 1340–1346, 2018.

[207] Pascal D Labrecque and Clément Gosselin. "Variable admittance for phri: from intuitive unilateral interaction to optimal bilateral force amplification". *Robotics and Computer-Integrated Manufacturing*, 52:1–8, 2018.

[208] Alexandre Lecours, Boris Mayer-St-Onge, and Clément Gosselin. "Variable admittance control of a four-degree-of-freedom intelligent assist device". *IEEE International Conference on Robotics and Automation*, pages 3903–3908, 2012.

[209] Fotios Dimeas and Nikos Aspragathos. "Reinforcement learning of variable admittance control for human-robot co-manipulation". *IEEE/RSJ International Conference on Intelligent Robots and Systems*, pages 1011–1016, 2015.

[210] Abdel-Nasser Sharkawy, Panagiotis N Koustournpardis, and Nikos Aspragathos. “Variable admittance control for human-robot collaboration based on online neural network training”. *IEEE/RSJ International Conference on Intelligent Robots and Systems*, pages 1334–1339, 2018.

[211] Connie W Tsao, Aaron W Aday, Zaid I Almarzooq, Cheryl AM Anderson, Pankaj Arora, Christy L Avery, Carissa M Baker-Smith, Andrea Z Beaton, Amelia K Boehme, and Alfred E Buxton. “Heart disease and stroke statistics—2023 update: a report from the american heart association”. *Circulation*, 147(8):e93–e621, 2023.

[212] J G. BROEKS, GJ Lankhorst, K Rumping, and AJH Prevo. “The long-term outcome of arm function after stroke: results of a follow-up study”. *Disability and Rehabilitation*, 21(8):357–364, 1999.

[213] Kay Wing, James V Lynskey, and Pamela R Bosch. “Whole-body intensive rehabilitation is feasible and effective in chronic stroke survivors: a retrospective data analysis”. *Topics in Stroke Rehabilitation*, 15(3):247–255, 2008.

[214] Roberta Shepherd and Janet Carr. “Reflections on physiotherapy and the emerging science of movement rehabilitation”. *Australian Journal of Physiotherapy*, 40:39–47, 1994.

[215] Peter Langhorne, Julie Bernhardt, and Gert Kwakkel. “Stroke rehabilitation”. *The Lancet*, 377(9778):1693–1702, 2011.

[216] Meg E Morris and Robert Iansek. “Characteristics of motor disturbance in parkinson’s disease and strategies for movement rehabilitation”. *Human Movement Science*, 15(5):649–669, 1996.

[217] L Oujamaa, I Relave, J Froger, D Mottet, and J-Y Pelissier. “Rehabilitation of arm function after stroke. literature review”. *Annals of Physical and Rehabilitation Medicine*, 52(3):269–293, 2009.

[218] James R Carey, Teresa J Kimberley, Scott M Lewis, Edward J Auerbach, Lisa Dorsey, Peter Rundquist, and Kamil Ugurbil. “Analysis of fmri and finger tracking training in subjects with chronic stroke”. *Brain*, 125(4):773–788, 2002.

[219] Noriyuki Tejima. “Rehabilitation robotics: a review”. *Advanced Robotics*, 14(7):551–564, 2001.

[220] Won Hyuk Chang and Yun-Hee Kim. “Robot-assisted therapy in stroke rehabilitation”. *Journal of stroke*, 15(3):174, 2013.

[221] Hermano Igo Krebs and Bruce T. Volpe. “Rehabilitation robotics”. *Handbook of clinical neurology*, 110:283–294, 2013.

[222] Daniel Lynch, Mark Ferraro, Jenifer Krol, Christine M Trudell, Paul Christos, and Bruce T Volpe. “Continuous passive motion improves shoulder joint integrity following stroke”. *Clinical Rehabilitation*, 19(6):594–599, 2005.

[223] Neville Hogan, Hermano I Krebs, Brandon Rohrer, Jerome J Palazzolo, Laura Dipietro, Susan E Fasoli, Joel Stein, Richard Hughes, Walter R Frontera, and Danie Lynch. "Motions or muscles? some behavioral factors underlying robotic assistance of motor recovery". *Journal of Rehabilitation Research and Development*, 43(5), 2006.

[224] Hermano Igo Krebs, Bruce T. Volpe, and Neville Hogan. "A working model of stroke recovery from rehabilitation robotics practitioners". *Journal of NeuroEngineering and Rehabilitation*, 6:1–8, 2009.

[225] Eric J Lenze, Michael C Munin, Tanya Quear, Mary Amanda Dew, Joan C Rogers, Amy E Begley, and Charles F Reynolds III. "Significance of poor patient participation in physical and occupational therapy for functional outcome and length of stay". *Archives of Physical Medicine and Rehabilitation*, 85(10):1599–1601, 2004.

[226] Sara Morghen, Alessandro Morandi, Andrew A Guccione, Michela Bozzini, Fabio Guerini, Roberto Gatti, Francesco Del Santo, Simona Gentile, Marco Trabucchi, and Giuseppe Bellelli. "The association between patient participation and functional gain following inpatient rehabilitation". *Aging Clinical and Experimental Research*, 29(4):729–736, 2017.

[227] Laura Marchal-Crespo and David J Reinkensmeyer. "Review of control strategies for robotic movement training after neurologic injury". *Journal of NeuroEngineering and Rehabilitation*, 6(1):1–15, 2009.

[228] Eric T Wolbrecht, Vicky Chan, David J Reinkensmeyer, and James E Bobrow. "Optimizing compliant, model-based robotic assistance to promote neurorehabilitation". *IEEE Transactions on Neural Systems and Rehabilitation Engineering*, 16(3):286–297, 2008.

[229] Hermano Igo Krebs, Jerome Joseph Palazzolo, Laura Dipietro, Mark Ferraro, Jennifer Krol, Keren Rannekleiv, Bruce T Volpe, and Neville Hogan. "Rehabilitation robotics: Performance-based progressive robot-assisted therapy". *Autonomous robots*, 15:7–20, 2003.

[230] Urs Keller, Georg Rauter, and Robert Riener. "Assist-as-needed path control for the pascal rehabilitation robot". *IEEE International Conference on Rehabilitation Robotics*, pages 1–7, 2013.

[231] Lance L Cai, Andy J Fong, Chad K Otoshi, Yongqiang Liang, Joel W Burdick, Roland R Roy, and V Reggie Edgerton. "Implications of assist-as-needed robotic step training after a complete spinal cord injury on intrinsic strategies of motor learning". *Journal of Neuroscience*, 26(41):10564–10568, 2006.

[232] Alexander Duschau-Wicke, Joachim Von Zitzewitz, Andrea Caprez, Lars Lunenburger, and Robert Riener. "Path control: a method for patient-cooperative robot-aided gait rehabilitation". *IEEE Transactions on Neural Systems and Rehabilitation Engineering*, 18(1):38–48, 2009.

[233] Tatsuya Teramae, Tomoyuki Noda, and Jun Morimoto. “EMG-based model predictive control for physical human-robot interaction: Application for assist-as-needed control”. *IEEE Robotics and Automation Letters*, 3(1):210–217, 2017.

[234] Guan De Lee, Wei-Wen Wang, Kai-Wen Lee, Sheng-Yen Lin, Li-Chen Fu, Jin-Shin Lai, Wen-Shiang Chen, and Jer-Junn Luh. “Arm exoskeleton rehabilitation robot with assistive system for patient after stroke”. *International Conference on Control, Automation and Systems*, pages 1943–1948, 2012.

[235] Jean-Jacques E Slotine and Weiping Li. “Applied nonlinear control”. *Prentice Hall*, 199(1), 1991.

[236] Kai Gui, U-Xuan Tan, Honghai Liu, and Dingguo Zhang. “Electromyography-driven progressive assist-as-needed control for lower limb exoskeleton”. *IEEE Transactions on Medical Robotics and Bionics*, 2(1):50–58, 2020.

[237] C Bower, H Taheri, and E Wolbrecht. “Adaptive control with state-dependent modeling of patient impairment for robotic movement therapy”. *IEEE International Conference on Rehabilitation Robotics*, pages 1–6, 2013.

[238] Robert Riener, Lars Lunenburger, Saso Jezernik, Martin Anderschitz, Gery Colombo, and Volker Dietz. “Patient-cooperative strategies for robot-aided treadmill training: first experimental results”. *IEEE Transactions on Neural Systems and Rehabilitation Engineering*, 13(3):380–394, 2005.

[239] Robert Riener, Lars Lünenburger, and Gery Colombo. “Human-centered robotics applied to gait training and assessment”. *Journal of Rehabilitation Research and Development*, 43(5), 2006.

[240] Neville Hogan. “Impedance control: An approach to manipulation: Part II–implementation”. *Journal of Dynamic Systems, Measurement, and Control*, 1985.

[241] Shahid Hussain, Sheng Q Xie, and Prashant K Jamwal. “Adaptive impedance control of a robotic orthosis for gait rehabilitation”. *IEEE Transactions on Cybernetics*, 43(3):1025–1034, 2013.

[242] Kyle Hunte, Siyu Chen, Jingang Yi, and Hao Su. “Assist-as-needed control of a wearable lightweight knee robotic device”. *IEEE/ASME International Conference on Advanced Intelligent Mechatronics*, pages 1477–1482, 2020.

[243] Quy-Thinh Dao and Shin-ichiroh Yamamoto. “Assist-as-needed control of a robotic orthosis actuated by pneumatic artificial muscle for gait rehabilitation”. *Applied Sciences*, 8(4):499, 2018.

[244] Eugenia Papaleo, Loredana Zollo, Luca Spedaliere, and Eugenio Guglielmelli. “Patient-tailored adaptive robotic system for upper-limb rehabilitation”. *IEEE International Conference on Robotics and Automation*, pages 3860–3865, 2013.

[245] Shawgi Younis Ahmed Mounis, Norsinnira Zainul Azlan, and Fatai Sado. “Assist-as-needed control strategy for upper-limb rehabilitation based on subject’s functional ability”. *Measurement and Control*, 52(9-10):1354–1361, 2019.

[246] Yin-Yu Su, Ying-Lung Yu, Ching-Hui Lin, and Chao-Chieh Lan. “A compact wrist rehabilitation robot with accurate force/stiffness control and misalignment adaptation”. *International Journal of Intelligent Robotics and Applications*, pages 45–58, 2019.

[247] Michael A Arbib. “The handbook of brain theory and neural networks”. *MIT press*, 2003.

[248] Neville Hogan. “Contact and physical interaction”. *Annual Review of Control, Robotics, and Autonomous Systems*, 5:179–203, 2022.

[249] Neville Hogan, Hermano Igo Krebs, Jain Charnnarong, Padmanabhan Srikrishna, and Andre Sharon. “MIT-Manus: a workstation for manual therapy and training”. *IEEE International Workshop on Robot and Human Communication*, pages 161–165, 1992.

[250] Alin Albu-Schäffer, Christian Ott, and Gerd Hirzinger. “A unified passivity-based control framework for position, torque and impedance control of flexible joint robots”. *The International Journal of Robotics Research*, 26(1):23–39, 2007.

[251] Christian Ott. ”Cartesian impedance control of redundant and flexible-joint robots”. *Springer*, 2008.

[252] Alexander Dietrich, Xuwei Wu, Kristin Bussmann, Marie Harder, Maged Iskandar, Johannes Englsberger, Christian Ott, and Alin Albu-Schäffer. “Practical consequences of inertia shaping for interaction and tracking in robot control”. *Control Engineering Practice*, 114:104875, 2021.

[253] Jun Nakanishi, Rick Cory, Michael Mistry, Jan Peters, and Stefan Schaal. “Operational space control: A theoretical and empirical comparison”. *The International Journal of Robotics Research*, 27(6):737–757, 2008.

[254] Shamel Fahmi and Thomas Hulin. “Inertial properties in haptic devices: Non-linear inertia shaping vs. force feedforward”. *International Federation of Automatic Control*, 51(22):79–84, 2018.

[255] Hassan K Khalil. “Lyapunov stability”. *Control Systems, Robotics and Automation*, 12:115, 2009.

[256] Wen-Hong Zhu and Septimiu E Salcudean. “Stability guaranteed teleoperation: an adaptive motion/force control approach”. *IEEE Transactions on Automatic Control*, 45(11):1951–1969, 2000.

[257] Vincent Duchaine and Clement M Gosselin. “Investigation of human-robot interaction stability using lyapunov theory”. *IEEE International Conference on Robotics and Automation*, pages 2189–2194, 2008.

[258] Mojtaba Sharifi, Saeed Behzadipour, and Gholamreza Vossoughi. “Model reference adaptive impedance control in cartesian coordinates for physical human–robot interaction”. *Advanced Robotics*, 28(19):1277–1290, 2014.

[259] Mojtaba Sharifi, Saeed Behzadipour, and Gholamreza Vossoughi. “Nonlinear model reference adaptive impedance control for human–robot interactions”. *Control Engineering Practice*, 32:9–27, 2014.

[260] Xiang Li, Guoyi Chi, Stephen Vidas, and Chien Chern Cheah. “Human-guided robotic comanipulation: Two illustrative scenarios”. *IEEE Transactions on Control Systems Technology*, 24(5):1751–1763, 2016.

[261] Zhijun Li, Junqiang Liu, Zhicong Huang, Yan Peng, Huayan Pu, and Liang Ding. “Adaptive impedance control of human–robot cooperation using reinforcement learning”. *IEEE Transactions on Industrial Electronics*, 64(10):8013–8022, 2017.

[262] Dongseok Ryu, J-B Song, Sungchul Kang, and Munsang Kim. “Frequency domain stability observer and active damping control for stable haptic interaction”. *IET Control Theory and Applications*, 2(4):261–268, 2008.

[263] Fotios Dimeas and Nikos Aspragathos. “Online stability in human-robot cooperation with admittance control”. *IEEE Transactions on Haptics*, 9(2):267–278, 2016.

[264] Federica Ferraguti, Chiara Talignani Landi, Lorenzo Sabattini, Marcello Bonfe, Cesare Fantuzzi, and Cristian Secchi. “A variable admittance control strategy for stable physical human–robot interaction”. *The International Journal of Robotics Research*, 38(6):747–765, 2019.

[265] Cristovao Sousa, Rui Cortesao, and Pedro Queirós. “Compliant comanipulation control for medical robotics”. *Conference on Human System Interactions*, pages 265–271, 2009.

[266] Toru Tsumugiwa, Yasunori Fuchikami, Atsushi Kamiyoshi, Ryuichi Yokogawa, and Kazunobu Yoshida. “Stability analysis for impedance control of robot in human-robot cooperative task system”. *Journal of Advanced Mechanical Design, Systems, and Manufacturing*, 1(1):113–121, 2007.

[267] Luca Bascetta and Gianni Ferretti. “Ensuring safety in hands-on control through stability analysis of the human-robot interaction”. *Robotics and Computer-Integrated Manufacturing*, 57:197–212, 2019.

[268] Fanny Ficuciello, Amedeo Romano, Luigi Villani, and Bruno Siciliano. “Cartesian impedance control of redundant manipulators for human-robot co-manipulation”. *IEEE/RSJ International Conference on Intelligent Robots and Systems*, pages 2120–2125, 2014.

[269] Romeo Ortega and Mark W Spong. “Adaptive motion control of rigid robots: A tutorial”. *Automatica*, 25(6):877–888, 1989.

[270] Bernard Brogliato, Ioan-Doré Landau, and Rogelio Lozano-Leal. "Adaptive motion control of robot manipulators: A unified approach based on passivity". *International Journal of Robust and Nonlinear Control*, 1(3):187–202, 1991.

[271] Yu Tang and Marco A Arteaga. "Adaptive control of robot manipulators based on passivity". *IEEE Transactions on Automatic Control*, 39(9):1871–1875, 1994.

[272] D Youla, L Castriota, and H Carlin. "Bounded real scattering matrices and the foundations of linear passive network theory". *IRE Transactions on Circuit Theory*, 6(1):102–124, 1959.

[273] Katsuya Kanaoka and Tsuneo Yoshikawa. "Passivity monitor and software limiter which guarantee asymptotic stability of robot control systems". *IEEE International Conference on Robotics and Automation*, 3:4366–4373, 2003.

[274] Takeshi Hatanaka, Nikhil Chopra, Masayuki Fujita, and Mark W Spong. "Passivity-based control and estimation in networked robotics". *Springer*, 2015.

[275] Cristian Secchi, Stefano Stramigioli, and Cesare Fantuzzi. "Position drift compensation in port-hamiltonian based telemanipulation". *IEEE/RSJ International Conference on Intelligent Robots and Systems*, pages 4211–4216, 2006.

[276] Yasuyoshi Yokokohji, Takashi Imaida, and Tsuneo Yoshikawa. "Bilateral control with energy balance monitoring under time-varying communication delay". *IEEE International Conference on Robotics and Automation*, 3:2684–2689, 2000.

[277] Blake Hannaford and Jee-Hwan Ryu. "Time-domain passivity control of haptic interfaces". *IEEE Transactions on Robotics and Automation*, 18(1):1–10, 2002.

[278] Michel Franken, Stefano Stramigioli, Sarthak Misra, Cristian Secchi, and Alessandro Macchelli. "Bilateral telemanipulation with time delays: A two-layer approach combining passivity and transparency". *IEEE Transactions on Robotics*, 27(4):741–756, 2011.

[279] Antonio Franchi, Cristian Secchi, Hyoung Il Son, Heinrich H Bulthoff, and Paolo Robuffo Giordano. "Bilateral teleoperation of groups of mobile robots with time-varying topology". *IEEE Transactions on Robotics*, 28(5):1019–1033, 2012.

[280] Nikhil Chopra and Mark W Spong. "Passivity-based control of multi-agent systems". *Advances in Robot Control: From Everyday Physics to Human-Like Movements*, pages 107–134, 2006.

[281] Cristian Secchi, Antonio Franchi, Heinrich H Bulthoff, and Paolo Robuffo Giordano. "Bilateral teleoperation of a group of UAVs with communication delays and switching topology". In *IEEE International Conference on Robotics and Automation*, pages 4307–4314, 2012.

[282] Marco Tognon, Chiara Gabellieri, Lucia Pallottino, and Antonio Franchi. "Aerial co-manipulation with cables: The role of internal force for equilibria, stability, and passivity". *IEEE Robotics and Automation Letters*, 3(3):2577–2583, 2018.

[283] Christian Ott, Alin Albu-Schaffer, Andreas Kugi, S Stamigioli, and Gerd Hirzinger. "A passivity based cartesian impedance controller for flexible joint robots-part i: Torque feedback and gravity compensation". *IEEE International Conference on Robotics and Automation*, 3:2659–2665, 2004.

[284] Alin Albu-Schaffer, Christian Ott, and Gerd Hirzinger. "A passivity based cartesian impedance controller for flexible joint robots-part II: Full state feedback, impedance design and experiments". *IEEE International Conference on Robotics and Automation*, 3:2666–2672, 2004.

[285] Christian Ott, Alin Albu-Schaffer, Andreas Kugi, and Gerd Hirzinger. "On the passivity-based impedance control of flexible joint robots". *IEEE Transactions on Robotics*, 24(2):416–429, 2008.

[286] Dimitrios Papageorgiou, Theodora Kastritsi, and Zoe Doulgeri. "A passive robot controller aiding human coaching for kinematic behavior modifications". *Robotics and Computer-Integrated Manufacturing*, 61:101824, 2020.

[287] Min Jun Kim, Woongyong Lee, Christian Ott, and Wan Kyun Chung. "A passivity-based admittance control design using feedback interconnections". *IEEE/RSJ International Conference on Intelligent Robots and Systems*, pages 801–807, 2016.

[288] Yong-Duk Kim, Bum-Joo Lee, Jee-Hwan Ryu, and Jong-Hwan Kim. "Landing force control for humanoid robot by time-domain passivity approach". *IEEE Transactions on Robotics*, 23(6):1294–1301, 2007.

[289] Sang-Ho Hyon and Gordon Cheng. "Passivity-based full-body force control for humanoids and application to dynamic balancing and locomotion". *IEEE/RSJ International Conference on Intelligent Robots and Systems*, pages 4915–4922, 2006.

[290] Chengxu Zhou, Zhibin Li, Juan Castano, Houman Dallali, Nikos G Tsagarakis, and Darwin G Caldwell. "A passivity based compliance stabilizer for humanoid robots". *IEEE International Conference on Robotics and Automation*, pages 1487–1492, 2014.

[291] Brad Paden and Ravi Panja. "Globally asymptotically stable PD+ controller for robot manipulators". *International Journal of Control*, 47(6):1697–1712, 1988.

[292] Bruno Siciliano and Luigi Villani. "A passivity-based approach to force regulation and motion control of robot manipulators". *Automatica*, 32(3):443–447, 1996.

[293] Vincent Duindam and Stefano Stramigioli. "Port-based asymptotic curve tracking for mechanical systems". *European Journal of Control*, 10(5):411–420, 2004.

[294] Cristian Secchi, Stefano Stramigioli, and Cesare Fantuzzi. "Position drift compensation in port-hamiltonian based telemanipulation". *IEEE/RSJ International Conference on Intelligent Robots and Systems*, pages 4211–4216, 2006.

[295] Michel Franken, Stefano Stramigioli, Rob Reilink, Cristian Secchi, Alessandro Macchelli, et al. "Bridging the gap between passivity and transparency". *Robotics: Science and Systems*, 2009.

[296] Michel Franken, Stefano Stramigioli, Sarthak Misra, Cristian Secchi, and Alessandro Macchelli. “Bilateral telemanipulation with time delays: A two-layer approach combining passivity and transparency”. *IEEE Transactions on Robotics*, 27(4):741–756, 2011.

[297] Alexander Dietrich, Xuwei Wu, Kristin Bussmann, Christian Ott, Alin Albu-Schäffer, and Stefano Stramigioli. “Passive hierarchical impedance control via energy tanks”. *IEEE Robotics and Automation Letters*, 2(2):522–529, 2016.

[298] Antonio Franchi, Cristian Secchi, Hyoung Il Son, Heinrich H Bulthoff, and Paolo Robuffo Giordano. “Bilateral teleoperation of groups of mobile robots with time-varying topology”. *IEEE Transactions on Robotics*, 28(5):1019–1033, 2012.

[299] Cristian Secchi, Antonio Franchi, Heinrich H Bülthoff, and Paolo Robuffo Giordano. “Bilateral teleoperation of a group of uavs with communication delays and switching topology”. *IEEE International Conference on Robotics and Automation*, pages 4307–4314, 2012.

[300] Giuseppe Riggio, Cesare Fantuzzi, and Cristian Secchi. “On the use of energy tanks for multi-robot interconnection”. *IEEE/RSJ International Conference on Intelligent Robots and Systems*, pages 3738–3743, 2018.

[301] Federica Ferraguti, Cristian Secchi, and Cesare Fantuzzi. “A tank-based approach to impedance control with variable stiffness”. *IEEE international Conference on Robotics and Automation*, pages 4948–4953, 2013.

[302] Tadele Shiferaw Tadele, Theo JA De Vries, and Stefano Stramigioli. “Combining energy and power based safety metrics in controller design for domestic robots”. *IEEE International Conference on Robotics and Automation*, pages 1209–1214, 2014.

[303] Alexander Toedtheide, Erfan Shahriari, and Sami Haddadin. “Tank based unified torque/impedance control for a pneumatically actuated antagonistic robot joint”. In *2017 IEEE International Conference on Robotics and Automation (ICRA)*, pages 1255–1262. IEEE, 2017.

[304] Klas Kronander and Aude Billard. “Stability considerations for variable impedance control”. *IEEE Transactions on Robotics*, 32(5):1298–1305, 2016.

[305] Youssef Michel, Christian Ott, and Dongheui Lee. “Passivity-based variable impedance control for redundant manipulators”. *International Federation of Automatic Control*, 53(2):9865–9872, 2020.

[306] Ramy Rashad, Johan BC Engelen, and Stefano Stramigioli. “Energy tank-based wrench/impedance control of a fully-actuated hexarotor: A geometric port-hamiltonian approach”. *International Conference on Robotics and Automation*, pages 6418–6424, 2019.

[307] Federica Ferraguti, Nicola Preda, Auralius Manurung, Marcello Bonfe, Olivier Lambercy, Roger Gassert, Riccardo Muradore, Paolo Fiorini, and Cristian Secchi. “An

energy tank-based interactive control architecture for autonomous and teleoperated robotic surgery". *IEEE Transactions on Robotics*, 31(5):1073–1088, 2015.

[308] Tadele Shiferaw Tadele, Theo J. A. de Vries, and Stefano Stramigioli. "Combining energy and power based safety metrics in controller design for domestic robots". *IEEE International Conference on Robotics and Automation*, pages 1209–1214, 2014.

[309] Mahdi Khoramshahi and Aude Billard. "A dynamical system approach for detection and reaction to human guidance in physical human-robot interaction". *Autonomous Robots*, 44(8):1411–1429, 2020.

[310] Chiara Talignani Landi, Federica Ferraguti, Lorenzo Sabattini, Cristian Secchi, and Cesare Fantuzzi. "Admittance control parameter adaptation for physical human-robot interaction". *IEEE International Conference on Robotics and Automation*, pages 2911–2916, 2017.

[311] Hsieh-Yu Li, Ishara Paranawithana, Liangjing Yang, Terence Sey Kiat Lim, Shaohui Foong, Foo Cheong Ng, and U-Xuan Tan. "Stable and compliant motion of physical human–robot interaction coupled with a moving environment using variable admittance and adaptive control". *IEEE Robotics and Automation Letters*, 3(3):2493–2500, 2018.

[312] Pengfei Cao, Yahui Gan, Jinjun Duan, and Xianzhong Dai. "Passivity-based stable human-robot cooperation with variable admittance control". *IEEE International Conference on Advanced Robotics and Mechatronics*, pages 446–451, 2019.

[313] Cristian Secchi and Federica Ferraguti. "Energy optimization for a robust and flexible interaction control". *IEEE International Conference on Robotics and Automation*, pages 1919–1925, 2019.

[314] Chiara Talignani Landi, Federica Ferraguti, Lorenzo Sabattini, Cristian Secchi, Marcello Bonfé, and Cesare Fantuzzi. "Variable admittance control preventing undesired oscillating behaviors in physical human-robot interaction". *IEEE/RSJ International Conference on Intelligent Robots and Systems*, pages 3611–3616, 2017.

[315] Chiara Talignani Landi, Federica Ferraguti, Cesare Fantuzzi, and Cristian Secchi. "A passivity-based strategy for coaching in human-robot interaction". *IEEE International Conference on Robotics and Automation*, pages 1–6, 2018.

[316] Federica Ferraguti, Chiara Talignani Landi, Lorenzo Sabattini, Marcello Bonfè, Cesare Fantuzzi, and Cristian Secchi. "A variable admittance control strategy for stable physical human–robot interaction". *The International Journal of Robotics Research*, 38(6):747–765, 2019.

[317] Francesco Cordoni, Luca Di Persio, and Riccardo Muradore. "A variable stochastic admittance control framework with energy tank". *IFAC-PapersOnLine*, 53(2):9986–9991, 2020.

[318] Jee-Hwan Ryu, Blake Hannaford, Carsten Preusche, and Gerd Hirzinger. "Time domain passivity control with reference energy behavior". *IEEE/RSJ International Conference on Intelligent Robots and Systems*, 3:2932–2937, 2003.

[319] Jee-Hwan Ryu and Jong-Hwan Kim. "Stable and high performance teleoperation with time domain passivity control: reference energy following scheme". *International Conference on Advanced Robotics*, pages 782–787, 2005.

[320] Romeo Ortega and Mark W Spong. "Stabilization of underactuated mechanical systems via interconnection and damping assignment". *International Federation of Automatic Control*, 33(2):69–74, 2000.

[321] Romeo Ortega, Arjan J Van Der Schaft, Iven Mareels, and Bernhard Maschke. "Putting energy back in control". *IEEE Control Systems Magazine*, 21(2):18–33, 2001.

[322] Arantza Sanz and Victor Etxebarria. "Experimental control of a single-link flexible robot arm using energy shaping". *International Journal of Systems Science*, 38(1):61–71, 2007.

[323] David Navarro-Alarcon, Peng Li, and Hiu Man Yip. "Energy shaping control for robot manipulators in explicit force regulation tasks with elastic environments". *IEEE/RSJ International Conference on Intelligent Robots and Systems*, pages 4222–4228, 2011.

[324] Lucas C Neves, Gabriel V Paim, Isabelle Queinnec, Ubirajara F Moreno, and Edson R De Pieri. "Passivity and power based control of a robot with parallel architecture". *International Federation of Automatic Control*, 44(1):14608–14613, 2011.

[325] Milad Geravand, Erfan Shahriari, Alessandro De Luca, and Angelika Peer. "Port-based modeling of human-robot collaboration towards safety-enhancing energy shaping control". *IEEE International Conference on Robotics and Automation*, pages 3075–3082, 2016.

[326] Stefan S Groothuis, Gerrit A Folkertsma, and Stefano Stramigioli. "A general approach to achieving stability and safe behavior in distributed robotic architectures". *Frontiers in Robotics and AI*, 5:108, 2018.

[327] Johannes Lachner, Felix Allmendinger, Eddo Hobert, Neville Hogan, and Stefano Stramigioli. "Energy budgets for coordinate invariant robot control in physical human–robot interaction". *The International Journal of Robotics Research*, 40(8-9):968–985, 2021.

[328] Stefano Stramigioli. "Energy-aware robotics". *Springer*, pages 37–50, 2015.

[329] Domen Novak, Jaka Ziherl, Andrej Olenšek, Maja Milavec, Janez Podobnik, Matjaž Mihelj, and Marko Munih. "Psychophysiological responses to robotic rehabilitation tasks in stroke". *IEEE Transactions on Neural Systems and Rehabilitation Engineering*, 18(4):351–361, 2010.

[330] Johanna Wagner, Teodoro Solis-Escalante, Peter Grieshofer, Christa Neuper, Gernot Müller-Putz, and Reinhold Scherer. "Level of participation in robotic-assisted treadmill walking modulates midline sensorimotor EEG rhythms in able-bodied subjects". *Neuroimage*, 63(3):1203–1211, 2012.

[331] Ali Utku Pehlivan, Dylan P Losey, Chad G Rose, and Marcia K O'Malley. "Maintaining subject engagement during robotic rehabilitation with a minimal assist-as-needed (mAAN) controller". *International Conference on Rehabilitation Robotics*, pages 62–67, 2017.

[332] Jun-ichiro Furukawa, Tomoyuki Noda, Tatsuya Teramae, and Jun Morimoto. "Estimating joint movements from observed emg signals with multiple electrodes under sensor failure situations toward safe assistive robot control". *IEEE International Conference on Robotics and Automation*, pages 4985–4991, 2015.

[333] Yuanjie Fan and Yuehong Yin. "Active and progressive exoskeleton rehabilitation using multisource information fusion from EMG and force-position EPP"". *IEEE Transactions on Biomedical Engineering*, 60(12):3314–3321, 2013.

[334] Rakesh Pilkar, Kamyar Momeni, Arvind Ramanujam, Manikandan Ravi, Erica Garbarini, and Gail F Forrest. "Use of surface EMG in clinical rehabilitation of individuals with SCI: barriers and future considerations. *Frontiers in Neurology*, 11:578559, 2020.

[335] Raphael Banz, Marc Bolliger, Gery Colombo, Volker Dietz, and Lars Lünenburger. "Computerized visual feedback: an adjunct to robotic-assisted gait training". *Physical therapy*, 88(10):1135–1145, 2008.

[336] Bo Ding, Qingsong Ai, Quan Liu, and Wei Meng. "Path control of a rehabilitation robot using virtual tunnel and adaptive impedance controller". *International Symposium on Computational Intelligence and Design*, 1:158–161, 2014.

[337] Ali Utku Pehlivan, Fabrizio Sergi, and Marcia K O'Malley. "A subject-adaptive controller for wrist robotic rehabilitation". *IEEE/ASME Transactions on Mechatronics*, 20(3):1338–1350, 2014.

[338] Ali Utku Pehlivan, Dylan P Losey, and Marcia K O'Malley. "Minimal assist-as-needed controller for upper limb robotic rehabilitation". *IEEE Transactions on Robotics*, 32(1):113–124, 2015.

[339] Hamed Jabbari Asl, Masashi Yamashita, Tatsuo Narikiyo, and Michihiro Kawanishi. "Field-based assist-as-needed control schemes for rehabilitation robots". *IEEE/ASME Transactions on Mechatronics*, 25(4):2100–2111, 2020.

[340] Lukas Zimmerli, Carmen Krewer, Roger Gassert, Friedemann Müller, Robert Riener, and Lars Lünenburger. "Validation of a mechanism to balance exercise difficulty in robot-assisted upper-extremity rehabilitation after stroke". *Journal of Neuroengineering and Rehabilitation*, 9(1):1–13, 2012.

[341] Juan C Perez-Ibarra, Adriano AG Siqueira, Marcela A Silva-Couto, Thiago L de Russo, and Hermano I Krebs. "Adaptive impedance control applied to robot-aided neuro-rehabilitation of the ankle". *IEEE Robotics and Automation Letters*, 4(2):185–192, 2018.

[342] Marc G Carmichael and Dikai Liu. "Estimating physical assistance need using a musculoskeletal model". *IEEE Transactions on Biomedical Engineering*, 60(7):1912–1919, 2013.

[343] Homayoon Kazerooni. "Human-robot interaction via the transfer of power and information signals". *IEEE Transactions on Systems, Man, and Cybernetics*, 20(2):450–463, 1990.

[344] Christopher Schindlbeck and Sami Haddadin. "Unified passivity-based cartesian force/impedance control for rigid and flexible joint robots via task-energy tanks". *IEEE International Conference on Robotics and Automation*, 2015.

[345] Sami Haddadin. "Vorrichtung und verfahren zur steuerung und regelung eines robotermanipulators". *German Patent DE102015102642A1*, 2015.

[346] Sami Haddadin, Sven Parusel, Lars Johannsmeier, Saskia Golz, Simon Gabl, Florian Walch, Mohamadreza Sabaghian, Christoph Jähne, Lukas Hausperger, and Simon Haddadin. "The franka emika robot: A reference platform for robotics research and education". *IEEE Robotics & Automation Magazine*, 29(2):46–64, 2022.

[347] Gary Bradski and Adrian Kaehler. "Learning opencv: Computer vision with the OpenCV library". *O'Reilly Media, Inc.*, 2008.

[348] Kim K Peper, Dinmukhamed Zardykhan, Marion Egger, Martina Steinböck, Friedemann Müller, Xavier Hildenbrand, Alexander Koenig, Elisabeth R Jensen, and Sami Haddadin. "Testing robot-based assist-as-needed therapy for improving active participation of a patient during early neurorehabilitation: a case study". *IEEE International Conference on Rehabilitation Robotics*, 2022.

[349] European Robotics Forum. "euRobotics Technology Transfer Award 2021". $https://old.eu-robotics.net/robotics_forum/awards/index.html$, 2021.

[350] Sami Haddadin and Erfan Shahriari. "Unified force-impedance control". *The International Journal of Robotics Research*, 43(13):2112–2141, 2024.

[351] Erfan Shahriari, Seyed Ali Baradaran Birjandi, and Sami Haddadin. "Passivity-based adaptive force-impedance control for modular multi-manual object manipulation". *IEEE Robotics and Automation Letters*, 7(2):2194–2201, 2022.

[352] Erfan Shahriari, Aljaz Kramberger, Andrej Gams, Ales Ude, and Sami Haddadin. "Adapting to contacts: Energy tanks and task energy for passivity-based dynamic movement primitives". *IEEE International Conference on Humanoid Robots*, pages 136–142, 2017.

[353] Aljaz Kramberger, Erfan Shahriari, Andrej Gams, Bojan Nemec, Ales Ude, and Sami Haddadin. "Passivity based iterative learning of admittance-coupled dynamic movement primitives for interaction with changing environments". *IEEE/RSJ International Conference on Intelligent Robots and Systems*, pages 6023–6028, 2018.

[354] Dinmukhamed Zardykhan, Petr Svarny, Matej Hoffmann, Erfan Shahriari, and Sami Haddadin. “Collision preventing phase-progress control for velocity adaptation in human-robot collaboration”. *IEEE International Conference on Humanoid Robots*, pages 266–273, 2019.

[355] Erfan Shahriari, Petr Svarny, Seyed Ali Baradaran Birjandi, Matej Hoffmann, and Sami Haddadin. “Path-constrained haptic motion guidance via adaptive phase-based admittance control”. *IEEE Transactions on Robotics*, 41:1039–1058, 2024.

[356] Erfan Shahriari, Kim Kristin Peper, Matej Hoffmann, and Sami Haddadin. “Enhancing robustness in manipulability assessment: The pseudo-ellipsoid approach”. *IEEE/RSJ International Conference on Intelligent Robots and Systems*, pages 1329–1336, 2024.

[357] Erfan Shahriari, Dinmukhamed Zardykhan, Alexander Koenig, Elisabeth Jensen, and Sami Haddadin. “Energy-based adaptive control and learning for patient-aware rehabilitation”. *IEEE/RSJ International Conference on Intelligent Robots and Systems*, pages 5671–5678, 2019.

[358] Erfan Shahriari, Johannes Lachner, Sami Haddadin, and Neville Hogan. “Minimally-back-drivable robots for rehabilitation: Path-adherent permissiveness control via trajectory adaptation”. *IEEE Robotics and Automation Letters*, 2025.

[359] Marion Egger, Martina Steinböck, Erfan Shahriari, and Friedemann Müller. “Robotergestützte mobilisierungstherapie mit künstlicher intelligenz”. *neuroreha*, 13(01):27–31, 2021.

[360] Erfan Shahriari, Sami Haddadin, Dinmukhamed Zardykhan, Alexander Koenig, Helfried Peyrl, and Xavier Hildenbrand. “Method for the open-loop and closed-loop control of a device including a movement module during the interaction of the device with a human, and device controlled in such a manner”. *World Intellectual Property Organization*, WO2021089087A1, 2021.

[361] Erfan Shahriari, Lars Johannsmeier, and Sami Haddadin. “Valve-based virtual energy tanks: A framework to simultaneously passify controls and embed control objectives”. *American Control Conference*, pages 3634–3641, 2018.

[362] Erfan Shahriari and Sami Haddadin. “Einbestellung von regelzielen in virtuelle energietanks in der passivitatsbasierten regelung”. *egelungstechnisches Kolloquium*, 2018.

[363] Erfan Shahriari, Lars Johannsmeier, Elisabeth Jensen, and Sami Haddadin. “Power flow regulation, adaptation, and learning for intrinsically robust virtual energy tanks”. *IEEE Robotics and Automation Letters*, 5(1):211–218, 2019.

[364] Elisabeth R Jensen, Kim K Peper, Marion Egger, Friedemann Müller, Erfan Shahriari, and Sami Haddadin. “Monitoring active patient participation during robotic rehabilitation: comparison between a robot-based metric and an emg-based metric”. *IEEE Transactions on Neural Systems and Rehabilitation Engineering*, 31:4156–4166, 2023.

[365] Bruno Siciliano, Oussama Khatib, and Torsten Kröger. “Handbook of robotics”. *Springer*, 200, 2008.

[366] Brian C Hall and Brian C Hall. “Lie groups, Lie algebras, and representations”. *Springer*, 2013.

[367] Richard M. Murray, Zexiang Li, and S. Shankar Sastry. “A mathematical introduction to robotic manipulation”. *CRC Press*, 1994.

[368] Oussama Khatib. “Inertial properties in robotic manipulation: An object-level framework”. *The International Journal of Robotics Research*, 14(1):19–36, 1995.

[369] João Carlos Alves Barata and Mahir Saleh Hussein. “The Moore–Penrose pseudoinverse: A tutorial review of the theory”. *Brazilian Journal of Physics*, 42(1):146–165, 2012.

[370] Mark W Spong. “Modeling and control of elastic joint robots”. *Journal of Dynamic Systems, Measurement, and Control*, 1987.

[371] Alessandro De Luca and Wayne J Book. “Robots with flexible elements”. *Springer Handbook of Robotics*, pages 243–282, 2016.

[372] Harold Alden Wheeler and David Dettinger. *Wheeler Monograph*, volume 9. Wheeler Labs., Inc. NY, 1949.

[373] Don D Roberts. “The existential graphs of Charles S. Peirce (approaches to semiotics)”. *De Gruyter Mouton*, 1973.

[374] Bernhard M Maschke and Arjan J van der Schaft. “Port-controlled hamiltonian systems: modelling origins and systemtheoretic properties”. *Nonlinear Control Systems Design 1992*, pages 359–365, 1993.

[375] David Morin. “Introduction to classical mechanics: with problems and solutions”. *Cambridge University Press*, 2008.

[376] Goran Golo, Arjan van der Schaft, Peter C Breedveld, and Bernhard M Maschke. “Hamiltonian formulation of bond graphs”. *Nonlinear and Hybrid Systems in Automation Control*, pages 351–372, 2003.

[377] Arjan Van Der Schaft. “Port-hamiltonian systems: an introductory survey”. *Proceedings of the international congress of mathematicians*, 3:1339–1365, 2006.

[378] Wisama Khalil and Etienne Dombre. “Modeling identification and control of robots”. *CRC Press*, 2002.

[379] Richard M Murray, Zexiang Li, and S Shankar Sastry. “A mathematical introduction to robotic manipulation”. *CRC press*, 2017.

[380] Alessandro De Luca, Alin Albu-Schäffer, Sami Haddadin, and Gerd Hirzinger. “Collision detection and safe reaction with the DLR-III lightweight manipulator arm”. *IEEE/RSJ International Conference on Intelligent Robots and Systems*, pages 1623–1630, 2006.

[381] Alin Albu-Schäffer, Christian Ott, Udo Frese, and Gerd Hirzinger. “Cartesian impedance control of redundant robots: Recent results with the DLR-light-weight-arms”. *IEEE International Conference on Robotics and Automation*, 3:3704–3709, 2003.

[382] Zhe Cao, Tomas Simon, Shih-En Wei, and Yaser Sheikh. “OpenPose”. *GitHub repository*, 2018.

[383] Auke Jan Ijspeert, Jun Nakanishi, Heiko Hoffmann, Peter Pastor, and Stefan Schaal. “Dynamical movement primitives: learning attractor models for motor behaviors”. *Neural Computation*, 25(2):328–373, 2013.

[384] Kamal Kant and Steven W Zucker. “Toward efficient trajectory planning: The path-velocity decomposition”. *The International Journal of Robotics Research*, 5(3):72–89, 1986.

[385] Ahmed Hussein, Mohamed Medhat Gaber, Eyad Elyan, and Chrisina Jayne. “Imitation learning: A survey of learning methods”. *ACM Computing Surveys*, 50(2):1–35, 2017.

[386] Martin Dietrich Buhmann. “Radial basis functions”. *Acta numerica*, 9:1–38, 2000.

[387] Intell. “Intel RealSense SDK 2.0”. *https://github.com/IntelRealSense/librealsense*, 2018.

[388] Zhe Cao, Tomas Simon, Shih-En Wei, and Yaser Sheikh. “Realtime multi-person 2d pose estimation using part affinity fields”. *Conference on Computer Vision and Pattern Recognition*, pages 7291–7299, 2017.

[389] Oussama Khatib, Luis Sentis, Jaeheung Park, and James Warren. “Whole-body dynamic behavior and control of human-like robots”. *International Journal of Humanoid Robotics*, 1(01):29–43, 2004.

[390] Brian A Garner and Marcus G Pandy. “A kinematic model of the upper limb based on the visible human project (VHP) image dataset”. *Computer Methods in Biomechanics and Biomedical Engineering*, 2(2):107–124, 1999.

[391] Erwin Kreyszig. “Advanced engineering mathematics: 2d Ed. *J. Wiley*, 1967.

[392] Jadran Lenarcic and Andreja Umek. “Simple model of human arm reachable workspace”. *IEEE Transactions on Systems, Man, and Cybernetics*, 24(8):1239–1246, 1994.

[393] Paolo De Leva. “Adjustments to zatsiorsky-seluyanov’s segment inertia parameters”. *Journal of biomechanics*, 29(9):1223–1230, 1996.

[394] Erfan Shahriari, Sami Haddadin, Dinmukhamed Zardykhan, Alexander Koenig, and Helfried Peyrl. “Verfahren zur steuerung und regelung einer vorrichtung umfassend ein bewegungsmodul in ihrer interaktion mit einem menschen, sowie eine derart gesteuerte vorrichtung”. *German Patent Office*, DE102020102351A1, 2021.

[395] Archibald Vivian Hill. “The heat of shortening and the dynamic constants of muscle”. *Proceedings of the Royal Society of London. Series B-Biological Sciences*, 126(843):136–195, 1938.

[396] Matthew Millard, Thomas Uchida, Ajay Seth, and Scott L Delp. “Flexing computational muscle: modeling and simulation of musculotendon dynamics”. *Journal of biomechanical engineering*, 135(2), 2013.

[397] Thiago Yukio Fukuda, Jorge Oliveira Echeimberg, José Eduardo Pompeu, Paulo Roberto Garcia Lucareli, Silvio Garbelotti, Rafaela Okano Gimenes, and Adilson Apolinário. “Root mean square value of the electromyographic signal in the isometric torque of the quadriceps, hamstrings and brachial biceps muscles in female subjects. *J Appl Res*, 10(1):32–39, 2010.

[398] Catherine Disselhorst-Klug, Thomas Schmitz-Rode, and Günter Rau. “Surface electromyography and muscle force: Limits in semg–force relationship and new approaches for applications”. *Clinical biomechanics*, 24(3):225–235, 2009.

[399] Kotaro Sasaki, Richard R Neptune, and Steven A Kautz. “The relationships between muscle, external, internal and joint mechanical work during normal walking”. *Journal of Experimental Biology*, 212(5):738–744, 2009.

[400] Takumi Jiroumaru, Toshiyuki Kurihara, and Tadao Isaka. “Measurement of muscle length-related electromyography activity of the hip flexor muscles to determine individual muscle contributions to the hip flexion torque”. *Springerplus*, 3:1–9, 2014.

[401] Scott L Delp, Frank C Anderson, Allison S Arnold, Peter Loan, Ayman Habib, Chand T John, Eran Guendelman, and Darryl G Thelen. “OpenSim: open-source software to create and analyze dynamic simulations of movement”. *IEEE transactions on biomedical engineering*, 54(11):1940–1950, 2007.

[402] James Hermus, Joseph Doeringer, Dagmar Sternad, and Neville Hogan. “Separating neural influences from peripheral mechanics: The speed-curvature relation in mechanically constrained actions”. *Journal of Neurophysiology*, 123(5):1870–1885, 2020.

[403] Brandon Rohrer, Susan Fasoli, Hermano Igo Krebs, Bruce Volpe, Walter R Frontera, Joel Stein, and Neville Hogan. “Submovements grow larger, fewer, and more blended during stroke recovery”. *Motor control*, 8(4):472–483, 2004.

[404] Laura Dipietro, Hermano I Krebs, Susan E Fasoli, Bruce T Volpe, Joel Stein, C Bever, and Neville Hogan. “Changing motor synergies in chronic stroke”. *Journal of neurophysiology*, 98(2):757–768, 2007.